Theoretische Physik

Statistical and Dynamical Properties of Convecting Systems

Inaugural-Dissertation
zur Erlangung des Doktorgrades
der Naturwissenschaften im Fachbereich Physik
der Mathematisch-Naturwissenschaftlichen Fakultät
der Westfälischen Wilhelms-Universität Münster

vorgelegt von

Johannes Lülff

aus Coesfeld

— 2015 —

v1.01 – Abgabeversion (für Publikation aufbereitet)

Umschlagabbildung: Siehe Abbildung 8.1 auf Seite 61.

Dieses Dokument wurde mit $\LaTeX\,2_{\varepsilon}$ und KOMA-Script erstellt.

Die verwendeten Schriften sind:
URW Garamond
URW Classico
`URW Nimbus Mono`

Dekan: Prof. Dr. Christian Weinheimer

Erster Gutachter: Prof. Dr. Ulrich Hansen

Zweiter Gutachter: Prof. Dr. Detlef Lohse

Tag der mündlichen Prüfung: 27. Januar 2016

Tag der Promotion: 27. Januar 2016

Kurzzusammenfassung

Diese Dissertation behandelt die Analyse der statistischen und dynamischen Eigenschaften von konvektiven Systemen sowie der darin auftretenden kohärenten Strukturen. Konvektion ist ein Phänomen, welches auftritt, wenn die Bewegung eines Fluids von Auftriebskräften angetrieben wird, wie es für viele Arten von Strömungen der Fall ist, die in der Natur auftreten. Die Bewegung der tektonischen Platten, der Ozeane, der Atmosphäre sowie der Sonnenoberfläche können auf derartige Auftriebskräfte zurückgeführt werden. Das Paradebeispiel dieses Phänomens wird als Rayleigh–Bénard-Konvektion bezeichnet: Ein sich zwischen zwei horizontalen Platten befindendes Fluid wird von unten geheizt und von oben gekühlt, was einen Stoff- und damit Wärmetransport durch die Fluidschicht zur Folge hat. Das Spektrum der verschiedenen Regime und Strukturen, die sich in der Strömung beobachten lassen, reicht von stabiler laminarer Konvektion bis zu hochturbulenten Strömungen, die bei großer Temperaturdifferenz zwischen den beiden horizontalen Platten auftreten.

Die sprunghafte und verworrene Struktur turbulenter Konvektion macht eine statistische Beschreibung unumgänglich, da auf der einen Seite eine punktweise Vorhersage einer einzelnen Strömungskonfiguration nicht in greifbarer Nähe ist, auf der anderen Seite aber auch aufgrund des chaotischen Verhaltens nicht sehr aufschlussreich wäre. Nichtsdestoweniger treten in konvektiven Strömungen oft kohärente Strukturen mit einer charakteristischen Dynamik auf, die wiederum die Statistik beeinflussen und somit für ein tiefergehendes Verständnis des Systems essentiell sind. Gemäß dieses Gedankengangs schlagen wir den folgenden Weg zur Analyse der Statistik und der Dynamik von konvektiven Strömungen ein:

Im ersten Teil der Arbeit untersuchen wir die Temperaturfluktuationen in turbulenter Rayleigh–Bénard-Konvektion und deren Statistik mit Hilfe ihrer Verteilungsfunktion (englisch: *probability density function*, PDF). Ausgehend von den Grundgleichungen leiten wir eine Bewegungsgleichung her, die die Form der Temperatur-PDF festlegt. Des Weiteren schlagen wir eine Methode vor, wie sich die Entwicklung der PDF mit den durchschnittlichen Transporteigenschaften der turbulenten Strömung in Verbindung bringen lässt. Dadurch können wir die Statistik mit der Dynamik des Systems verknüpfen. So lassen sich die Vorgänge im System aufgeschlüsselt nach ihrer Temperatur betrachten, und wir können die verschiedenen Verhaltensweisen von Fluid unterschiedlicher Temperatur an unterschiedlichen Stellen in der Konvektionszelle analysieren. Der hier vorgeschlagene Ansatz macht es nötig, ungeschlossene Terme aus numerischen Simulationen zu gewinnen.

Wir verwenden Daten, die in drei verschiedenen Geometrien berechnet wurden, und sind so in der Lage, allgemeine Mechanismen sowie subtile Unterschiede herauszuarbeiten.

Der zweite Teil beschäftigt sich damit, kohärente Strukturen und deren Zusammensetzung in turbulenter RAYLEIGH–BÉNARD-Konvektion zu erfassen. Dazu benutzen wir die sogenannte *proper orthogonal decomposition* (POD), ein etabliertes Verfahren, welches die Konstruktion von orthogonalen Basismoden zu einem gegebenen Datensatz erlaubt. Die Basismoden lassen sich hierarchisch nach der in ihnen enthaltenen Energie einordnen. Mit diesen Moden kann ein Basiswechsel durchgeführt werden, was eine besser an turbulente Konvektion angepasste Beschreibung erlaubt, und es ist möglich, die Dynamik der großskaligen kohärenten Strukturen vom Hintergrund der feinskaligen Turbulenz zu trennen. Anschließend argumentieren wir, dass die Energie keine geeignete Größe ist, um das System zu beschreiben, und dass stattdessen eine Charakterisierung mit Hilfe des Wärmetransports physikalisch sinnvoller ist. Dementsprechend schlagen wir eine Modifikation des POD-Verfahrens vor, die an konvektive Strömungen angepasst ist und die die auftretenden Strukturen entsprechend der von ihnen transportierten Wärmemenge klassifizieren kann. Anhand von Daten aus einer numerischen Simulation zweidimensionaler Konvektion demonstrieren wir dann, dass dieser neue Ansatz besser geeignet ist, um den Wärmetransport und dessen Zeitserie sowie Verteilungsfunktion zu beschreiben.

Im dritten Teil der Arbeit entfernen wir uns von turbulenten Strömungen und untersuchen stattdessen die Statistik und die Strukturen, die sich beim Eintreten von Konvektion zeigen. Das Verhalten in diesem Regime kann durch die stochastische SWIFT–HOHENBERG-Gleichung modelliert werden, einer nichtlinearen Bewegungsgleichung für einen Ordnungsparameter, der dem Temperaturfeld in horizontalen Schnitten durch ein Konvektionsexperiment entspricht. Dabei werden Störstellen im System durch eine stochastisch fluktuierende Kraft nachgebildet, was eine statistische Beschreibung nahelegt. Wir leiten eine Bewegungsgleichung für die Verteilungsfunktion des Ordnungsparameters her, die die Form einer FOKKER–PLANCK-Gleichung besitzt. Dadurch können wir die Form der Verteilungsfunktion zu den Termen der SWIFT–HOHENBERG-Gleichung in Beziehung setzen, wobei ungeschlossene Terme durch numerische Simulationen bestimmt werden. Als ein Nebenprodukt der numerischen Simulation entwickeln wir eine Methode, mit der sich schnell statistische Ensembles des stochastischen SWIFT–HOHENBERG-Systems generieren lassen. Dieses Verfahren lässt sich auf beliebige ausgedehnte Gradientensysteme erweitern, die unter dem Einfluss von Rauschen stehen.

Abstract

This thesis deals with the analysis of the statistics and the dynamics as well as of coherent structures that are found in convecting systems. Convection is a phenomenon that occurs whenever a fluid is driven by buoyancy forces, as is the case for many types of flows encountered in nature. The motion of the tectonic plates, the oceans, the atmosphere and the outer layers of the sun can all be traced back to buoyancy. The prime example of this principle is the so-called Rayleigh–Bénard convection: A fluid enclosed between two horizontal plates is heated from below and cooled from above, which induces a transport of mass and thereby of heat energy through the horizontal fluid layer. The spectrum of different flow regimes and structures that this system displays ranges from stable laminar convection to highly turbulent flows which occur when the temperature difference between the horizontal plates is increased.

The erratic and tangled structure of turbulent convection necessitates a statistical description, as a pointwise prediction of a single realization of the flow is on the one hand out of reach, and on the other hand not very insightful due to the chaotic behavior. Nevertheless, the typical dynamics and coherent structures that are found in convective flows influence the statistics, and their behavior is crucial for a deeper understanding of the system. Along these lines, we pursue the following approach in analyzing the statistics and dynamics of convection:

In the first part of the thesis, we examine the statistics of temperature fluctuations in turbulent Rayleigh–Bénard convection with the help of their *probability density function* (PDF). We derive an evolution equation from first principles that determines the shape of the temperature PDF. Furthermore, we propose a method to link the evolution of the PDF to the mean transport properties in the convection cell, thus connecting the statistics and the average dynamics in turbulent convection. This results in a temperature-resolved view of Rayleigh–Bénard convection that describes the distinct dynamics of fluid of different temperatures in different regions of the convection cell. The appearing unclosed terms are estimated from direct numerical simulations of convection in three different geometries. We are thus able to work out the general picture as well as subtle differences between the three convection cases we consider.

The second part concentrates on the detection and composition of coherent structures in turbulent Rayleigh–Bénard convection. To this end, we apply a technique known as *proper orthogonal decomposition* (POD), which is able to build a hierarchical set of orthogonal basis modes from data, and the modes can be organized by the energy that they contain. These modes can then be used to transform the data into a basis that is more adapt in describing the turbulent flows, and it becomes possible to separate the dynamics of the large-scale coherent structures from the small-scale background turbulence acting as noise. We then argue that instead of the energy, the physically more relevant quantity to describe the system is the heat transport through the fluid layer. Thus, we propose a modification of the usual POD approach that is able to grasp the structures classified by the heat they carry. A numerical data set of two-dimensional convection is then used as a test case to show that this new approach consistently performs better in describing the heat transport and its time series as well as its distribution function.

For the third part, we depart from turbulent states and instead investigate the structures and statistics that are found near the onset of convection. The behavior in this regime can be modeled by the stochastic SWIFT–HOHENBERG equation, a nonlinear order parameter equation that describes the temperature field in horizontal slices of convection experiments, and impurities are included as a fluctuating force. The noise term that influences the dynamics suggests a stochastic treatment, and we derive an evolution equation of FOKKER–PLANCK-type for the probability density function of the order parameter. We then show how the shape of the PDF can be related to the terms of the SWIFT–HOHENBERG equation, where unclosed terms have to be estimated from direct numerical simulations. In passing we propose a fast numerical method of generating ensembles of the stochastic SWIFT–HOHENBERG equation that can be extended towards arbitrary spatially extended gradient systems subjected to noise.

Contents

Kurzzusammenfassung iii

Abstract v

Contents vii

1 Introduction 1
1.1 Convection 1
1.2 Mathematical Formulation 4
1.3 The Necessity of a Statistical Description 6
1.4 The Importance of Dynamics and Coherent Structures 7
1.5 Roadmap of the Thesis 8

I Statistical Description of Heat Transport and Average Dynamics in RAYLEIGH–BÉNARD Convection 11

2 Introduction 15

3 Statistical Description of Heat Transport 17
3.1 PDF Methods 17
3.2 Method of Characteristics 18

4 Results from DNS 21
4.1 Three-dimensional Convection with Periodic Horizontal Boundaries . . 21
4.2 Two-dimensional Convection with Periodic Horizontal Boundaries . . . 28
4.3 Three-dimensional Convection in a Cylindrical Vessel 31

5 Summary 39

II Optimal Modes of Heat Transport Obtained by Proper Orthogonal Decomposition 41

6 Introductory Example – The Idea Behind POD 45

7 Mathematical Description of POD 47
- 7.1 Formulation as Variational Principle 47
- 7.2 Matrix Formulation for Discrete Numerical Data 49
- 7.3 Method of Snapshots 52
- 7.4 Direct Method or Method of Snapshots? 55
- 7.5 Lower-Dimensional Projection 55
  - 7.5.1 Direct Method 56
  - 7.5.2 Method of Snapshots 56
  - 7.5.3 Quantifying the Quality of the Projection 57
- 7.6 Summary of Mathematical Description 58

8 POD of Turbulent Convection 61
- 8.1 Data Set 62
- 8.2 POD Eigenvalue Spectrum and Modes 62

9 New Approach that Optimizes the Heat Transport 69
- 9.1 Theory 70
  - 9.1.1 Consequences of Indefinite **S** 71
- 9.2 Results from DNS Data 73
  - 9.2.1 Eigenvalues and Modes 73
  - 9.2.2 Comparing the Heat Transport of Nu- and E-Modes 75
  - 9.2.3 Time Series of Projections 79
  - 9.2.4 Statistics of Local Convective Heat Transport 82
  - 9.2.5 Amplitudes of the POD Modes 87

10 Summary and Outlook 91

III Statistical Analysis of the Forced SWIFT–HOHENBERG Equation 93

11 Introduction 97
- 11.1 Pattern Formation in Convection 97
- 11.2 Randomly Forced SWIFT–HOHENBERG Equation 98

12 Numerics 101
- 12.1 Pseudospectral Scheme 101
- 12.2 Semi-Implicit Time-Stepping 102

13 Linear Stability Analysis and LYAPUNOV Functional 105
- 13.1 Linear Stability Analysis 105
- 13.2 Variational Formulation of the SWIFT–HOHENBERG Eq.: The LYAPUNOV Functional 106

    - 13.2.1 Plane Waves and LYAPUNOV Functional 107
    - 13.2.2 Plane Waves Compared to Stationary Solutions 109
  - 13.3 The Functional FOKKER–PLANCK Equation 110
  - 13.4 Construction of Statistical Ensembles 112
  - 13.5 Summary of LYAPUNOV Formalism and Ensemble Construction 117

14 Statistical Analysis 119
  - 14.1 PDF Equation 119
    - 14.1.1 Symmetry Considerations 120
  - 14.2 Numerical Results 121
    - 14.2.1 Model for the Conditional Averages 123
    - 14.2.2 Model for the PDF Using GAUSSian Convolution 126

15 Summary and Conclusion 129

IV Summary and Conclusion of the Thesis 131

Publications in the Context of this Thesis 137

Appendix 139

A PDF Description of RAYLEIGH–BÉNARD Convection: In-depth Analyses 141
  - A.1 Improvement of the Numerics 141
  - A.2 Comparison of Limit Cycle and Family of Closed Curves 142

B Proper Orthogonal Decomposition: Proofs and Remarks 145
  - B.1 From Maximization to Eigenvalue Problem 145
  - B.2 Mean Energy of the Data Ensemble 146
  - B.3 Positive Definiteness of $\mathbf{XTX}^\dagger\mathbf{S}$ 147
  - B.4 Eigenvalues of $\mathbf{AB}$ and $\mathbf{BA}$ 147
  - B.5 Comments on the Calculation of Covariance Matrices and its Implementation 148
  - B.6 Energy Contained in the Projection of a Single Snapshot 149
  - B.7 Heat Transport Maximizing POD in Three Dimensions 150

C SWIFT–HOHENBERG Equation: Additional Comments 153
  - C.1 Quadratic Nonlinearity in the SWIFT–HOHENBERG Equation and the Connection to the RAYLEIGH–BÉNARD System 153
  - C.2 Creating GAUSSian Noise with Correlation 154
  - C.3 Variational Calculus in a Nutshell 155

List of Figures I

List of Tables V

Bibliography VII

Mephistopheles:
Der ganze Strudel strebt nach oben;
Du glaubst zu schieben, und du wirst geschoben.

Faust I, Goethe

1 Introduction

Convection – the motion of a liquid or a gas that is driven by temperature differences – is the major mechanism at work for a wide range of flows that are found in nature and engineering. It has been one of the first and until today remain among the classical systems of fluid dynamics research, and despite of more than a century worth of effort, the profound understanding of convection remains as one key ingredient in the greater goal of *the turbulence problem*.[1]

1.1 Convection

The phenomenon of convection occurs when a fluid (i. e., a liquid or a gas) in a downwards-acting gravity field is destabilized by temperature and thus density differences: Fluid of lower density rises upwards, while higher densities fall down. One of the most prominent and also the prime example for this phenomenon is called Rayleigh–Bénard convection: A layer of fluid is confined between two horizontal plates, where a hot plate is at the bottom and a cold plate is at the top. When the temperature difference between the hot bottom and the cold top is high enough, the heated fluid at the bottom plate is able to overcome its inner friction (i. e., viscosity) and starts to move up towards the cold top plate. The system thus transports the heat that is injected at the bottom towards the top by convection, where it is emitted from the system. This macroscopic fluid motion is able to transport much more heat through the fluid layer than what would be possible by pure heat conduction, i. e. when the fluid only moves on an atomic scale but not macroscopically. The name of this system goes back to the first experiments of Bénard (1901) and the theoretical description of the onset of convection by Rayleigh (1916). Examples of the temperature field of Rayleigh–Bénard convection in different settings are shown in figures 1.1 and 1.2.

This seemingly simple process – fluid motion induced by a temperature gradient – is at the heart of nearly all the complex flows of fluid that occur in nature: Starting from the plate tectonics in the mantle of the earth, which are caused by the motion of magma between the hot core and the cold crust, it is also the principle driving force behind the

---

[1] *The turbulence problem* is deemed by some to be that nobody precisely knows what “the” turbulence problem is, although the Navier–Stokes existence and smoothness proof, the phenomenon of intermittency and its interplay with the small-scale statistics, as well as the infamous *closure problem* of turbulence seem to be constantly recurring unsolved components.

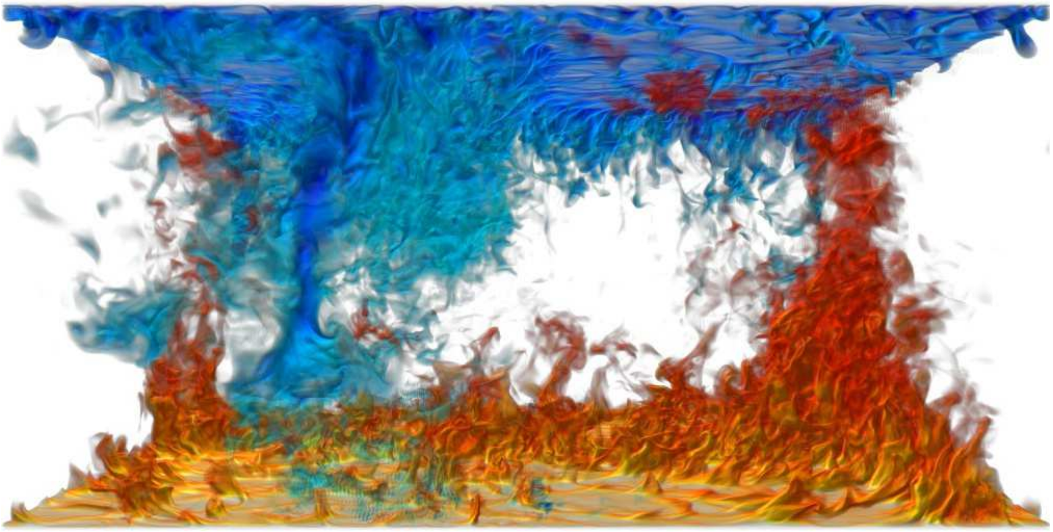

Figure 1.1: *Numerical simulation of three-dimensional convection with periodic horizontal boundaries. The parameters are* $\mathrm{Ra} = 10^9$ *and* $\mathrm{Pr} = 1$. *The temperature field is shown, with red corresponding to hot and blue to cold fluid; the mean temperature is made translucent. Image adapted from* Lülff *(2011, sec. 1.1), where also details can be found.*

circulation of the oceans and the atmosphere that both exhibit a temperature gradient because heat is emitted at the top side. Further examples include the convection of plasma in the outer layers of the sun as well as more down-to-earth examples borrowed from engineering applications, e. g. the heat distributed into a room by a radiator or convection patterns observed in solidifying liquid metals.

The flow structures and patterns that the system displays depend mainly on the temperature difference between the two horizontal plates as well as the properties of the fluid. The relevant quantities are condensed in two dimensionless control parameters, the Rayleigh and the Prandtl number:

$$\mathrm{Ra} = \frac{\alpha g \delta T L^3}{\nu\kappa} \quad \text{and} \quad \mathrm{Pr} = \frac{\nu}{\kappa} \tag{1.1}$$

The Rayleigh number is proportional to the temperature difference δT between bottom and top and also strongly dependent on the distance L between the horizontal plates, and the Prandtl number is defined as the ratio of inertia diffusion to heat diffusion. The remaining quantities are the thermal expansion coefficient α, the gravitational acceleration g, the kinematic viscosity ν and the thermal diffusivity κ. Loosely speaking, the Rayleigh

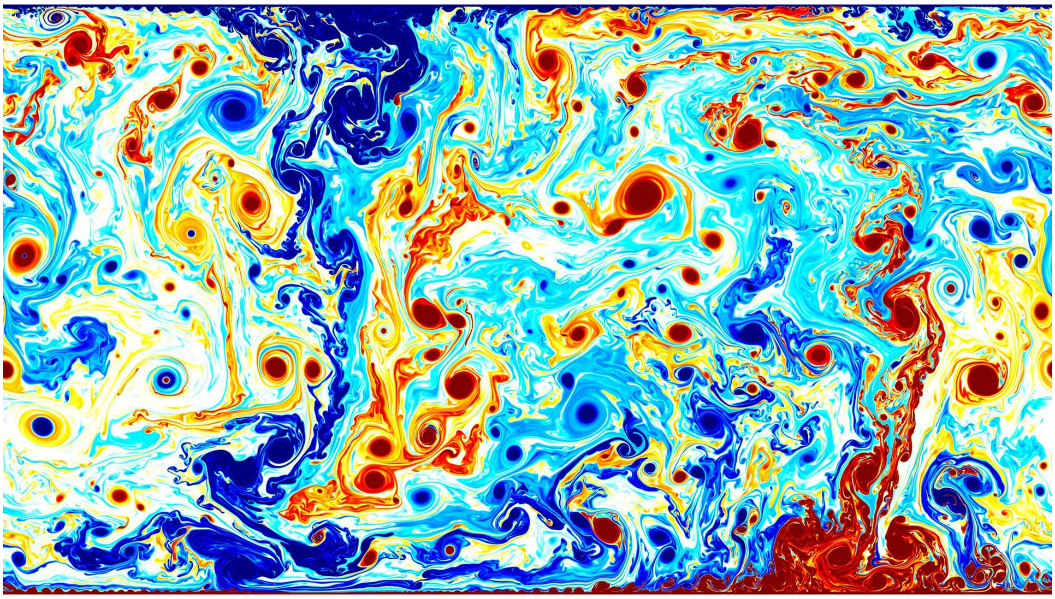

Figure 1.2: *Snapshot of two-dimensional convection with periodic horizontal boundaries obtained from numerical simulation. Hot fluid is represented by reddish colors, cold fluid is blue, and fluid of average temperature is white. The parameters of this simulation are* $\mathrm{Ra} = 10^{13}$ *and* $\mathrm{Pr} = 1$, *and at the bottom and top are no-slip plates of constant temperature.*

number describes the experimental setup, while the PRANDTL number characterizes the fluid. A third control parameter that is often included is the aspect ratio

$$\Gamma = \frac{\text{lateral extent}}{\text{vertical extent}} \tag{1.2}$$

that relates to the geometry of the fluid volume.

When the RAYLEIGH number is gradually increased, the system exhibits a wide range of different flow configurations with distinct features: For low Ra, the fluid remains at rest, and heat is transported through the system only by diffusion. At $\mathrm{Ra} \approx 1707$ (with no-slip – i. e., sticky – plates), the first instability occurs, and the fluid starts a macroscopic motion in the form of parallel convection rolls. When the RAYLEIGH number is increased further, the rolls start to deform and oscillate, and after $\mathrm{Ra} \gtrsim 10^5$ a chaotic rearrangement of convection rolls sets in. After this regime, the fluid state departs from its relatively clear roll-like structure, and more unstructured turbulence starts to form. With rising Ra the smallest scales of turbulence become smaller and smaller, and thus the influence of the boundary layers near the horizontal plates decreases. Finally, in the so-called *ultimate regime* at $\mathrm{Ra} \gtrsim 10^{14}$, the flow is expected to be largely determined by the behavior in the bulk of the fluid volume.

The PRANDTL number mainly influences the size and shape of the structures that are found in the flow: For low PRANDTL numbers (i. e., $\mathrm{Pr} \ll 1$), the temperature field shows large, blurred structures, while at large $\mathrm{Pr} \gg 1$, the observed patterns (denoted as *plumes*, i. e. vertically elongated, mushroom-like structures) become thinner and more filament-like.

The turbulent temperature fields in three and two dimensions that are shown in figures 1.1 and 1.2 give an impression of the generic mechanism of RAYLEIGH–BÉNARD convection: Fluid that heats up at the hot bottom plate moves upwards due to buoyancy until it arrives at the cold upper plate. At this point the fluid cools down and falls towards the lower plate again. Due to this constant exchange of fluid between the plates, the flow organizes in the large-scale structure of a convection cell (rotating counter-clockwise in both figures), and it is found that its shape strongly depends on Γ. The large-scale circulation that sweeps fluid along the horizontal plates also prevents hot fluid to arbitrarily rise in a straight vertical line; instead the fluid mainly moves upwards in bundles of hot fluid where the horizontal large-scale currents of two neighboring cells collide head-on and are thus deflected in the vertical direction. These bundles of hot fluid are denoted as *plume hot spots*,[2] and the interplay between the large-scale current and the plumes and hot spots can be perceived best from figure 1.2.

1.2 Mathematical Formulation

Although the first results on RAYLEIGH–BÉNARD convection have been the experimental observations by BÉNARD, and also until today many insights about the system are gained through experiments, still a lot has been and can be learned from the basic equations of motion, the OBERBECK–BOUSSINESQ equations for velocity field $\boldsymbol{u}(\boldsymbol{x}, t)$ and temperature field $T(\boldsymbol{x}, t)$:

$$\frac{\partial}{\partial t}\boldsymbol{u} + \boldsymbol{u} \cdot \nabla \boldsymbol{u} = -\nabla p + \mathrm{Pr}\,\Delta \boldsymbol{u} + \mathrm{Pr}\,\mathrm{Ra}\,T\boldsymbol{e}_z \tag{1.3a}$$

$$\nabla \cdot \boldsymbol{u} = 0 \tag{1.3b}$$

$$\frac{\partial}{\partial t}T + \boldsymbol{u} \cdot \nabla T = \Delta T \tag{1.3c}$$

Here the quantities have been non-dimensionalized with respect to the distance and the temperature difference between the horizontal plates and the time scale of heat diffusion;

---

[2] As the RAYLEIGH–BÉNARD system is mirror-symmetric in the vertical direction (at least for symmetric boundary conditions), the same picture holds for cold fluid being swept along the upper plate and aggregating in “hot spots” of cold fluid, as can be seen in the figures. However, due to the aforementioned symmetry, from now on the reversed “cold” process is implied for every “hot” process that is described (and vice versa).

$p(x,t)$ is the pressure field. Equations (1.3a)–(1.3b) are the incompressible NAVIER–STOKES equations for the velocity field $\boldsymbol{u}$ with an additional temperature-dependent buoyancy force acting in vertical direction; the strength of the buoyancy force is proportional to the RAYLEIGH number and thus also to the temperature difference between the plates. Equation (1.3c) is an advection-diffusion equation for the temperature field T that describes how the temperature is transported by the velocity field.

The OBERBECK–BOUSSINESQ equations have to be supplemented by boundary conditions for the temperature and velocity fields at the plates located at $z = 0$ and $z = 1$ and at possible sidewalls. Throughout this thesis, we will use DIRICHLET conditions at the horizontal plates, i. e. the temperature of the plates is fixed to $T = 1$ at the bottom and $T = 0$ at the top, and the velocity obeys no-slip conditions $\boldsymbol{u} = \boldsymbol{0}$. Sidewalls are most commonly assumed to be insulating, i. e. there is no flux of heat into the walls; this corresponds to NEUMANN boundary conditions, where the derivative of the temperature field in the direction of the wall normal $\boldsymbol{n}$ is zero, i. e. $\boldsymbol{n} \cdot \nabla T = 0$. Other possible boundary conditions, like a stress-free velocity field or a prescribed heat flux at the horizontal plates (both corresponding to NEUMANN boundaries), will not be detailed in this thesis.

The name of the evolution equations (1.3) relates to OBERBECK (1879), who formulated the equations of motion for the advection of a temperature field, and to BOUSSINESQ (1903). The latter introduced and examined the approximation that the temperature dependence of all material constants can be neglected, and also the temperature dependence of density is relevant only in the buoyancy term. Because the OBERBECK–BOUSSINESQ equations are based on the NAVIER–STOKES equations, they share a number of properties: Both consist of a set of nonlinear partial differential equations that are nonlocal due to the pressure term, and therefore the same complications are encountered when analyzing convection and “pure” fluid turbulence.

As the system is driven by a temperature gradient, it answers with a macroscopic fluid motion and thus an enhanced heat transport. It is measured in terms of the dimensionless NUSSELT number, which specifies the total heat transport in multiples of the conductive heat transport:

$$\mathrm{Nu} = \frac{\text{total heat transport}}{\text{conductive heat transport}} = \left\langle u_z T' \right\rangle_V + 1 \tag{1.4}$$

The last identity holds due the non-dimensionalization we are using, where $T' = T - \left\langle T \right\rangle_V$ is the shifted temperature field so that $\left\langle T' \right\rangle_V = 0$, and $\langle \cdot \rangle_V$ denotes averaging over the whole fluid volume. Thus, the NUSSELT number can be understood as the mean correlation between vertical velocity and temperature, and $\mathrm{Nu} = 1$ signifies that the fluid transports heat through the system only by conduction, i. e. when the fluid is at rest.

1.3 The Necessity of a Statistical Description

From the tangled, erratic structure of the turbulent convection flows shown in figures 1.1 and 1.2 it becomes clear that a pointwise prediction of the flow fields from first principles, i. e. by solving the OBERBECK–BOUSSINESQ equations, is virtually impossible. Furthermore, the nonlinear and nonlocal nature of the equations of motion has proven to be a major challenge when trying to solve the equations analytically. Lastly, from the mathematical side not even general existence proofs for the NAVIER–STOKES equations have been found so far. Thus, an analytical and pointwise solution for arbitrary initial conditions is not in prospect.

On the other hand, though, a microscopic description of all the small-scale turbulent fluctuations may be way beyond what is needed for a physical understanding of the system. To this end, we bring to mind the description of an ideal gas with its typically $\mathcal{O}(10^{23})$ particles, where it is impossible to know and thus predict the vast amount of all microscopic degrees of freedom. However, this detailed knowledge is not needed in order to understand macroscopic variables like temperature and pressure, which are the more relevant quantities in physics. Thus, for an ideal gas, it is possible to directly derive the macroscopic behavior with the help of the microscopic equations of motion of the single particles.

It is clear that the analysis of RAYLEIGH–BÉNARD convection would benefit from a similar approach, where the analogue of the microscopic level is the description of all turbulent scales in terms of the OBERBECK–BOUSSINESQ equations.[3] To give an example, a great deal of RAYLEIGH–BÉNARD research is focused on understanding and predicting the average heat transport through the system in dependence of the control parameters, i. e. to find a functional dependence $\mathrm{Nu}(\mathrm{Ra}, \mathrm{Pr}, \Gamma)$ from first principles. While there has been great progress in recent years – among the most notable the scaling theory by GROSSMANN and LOHSE (2000) that can adequately predict the heat transport on the basis of average dissipation rates –, still these theories rely on modeling assumptions based on experimental observations that as yet could not be derived rigorously from the basic equations of motion.

Further examples include turbulent quantities like velocity and temperature fluctuations, where the understanding of the higher moments and ultimately the probability density functions is more important than a microscopic prediction of a single realization. Although in this case the description is subjected to the notorious *closure problem* of turbulence, this macroscopic, statistical description of convection and turbulence in general is still more promising than a microscopic, pointwise prediction of the fluid.

---

[3] Obviously this analogy between an ideal gas and turbulent convection is not very profound and therefore has to be taken with a grain of salt, as it compares a HAMILTONian system with a dissipative system far from equilibrium.

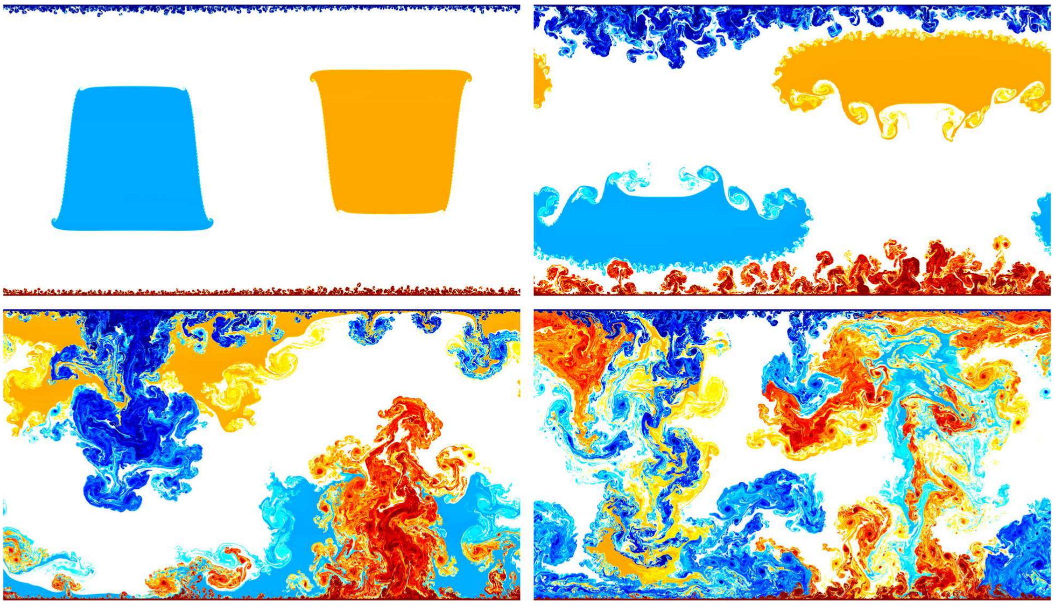

Figure 1.3: *Four consecutive snapshots of two-dimensional convection with periodic horizontal boundaries, starting from an initial condition with two large hot respectively cold patches of fluid. The parameters are* $\mathrm{Ra} = 10^{14}$ *and* $\mathrm{Pr} = 1$, *and the snapshots are taken* 5 *free-fall time units apart. The color scale is the same as in figure* 1.2.

1.4 The Importance of Dynamics and Coherent Structures

In the previous section we elaborated how a description of turbulent convection on a statistical level is on the one hand sufficient to understand macroscopic variables like the heat transport, and on the other hand inevitable due to the complex structure of the fluid flows and the underlying equations of motion. However, among the complex behavior of the convective flows in both space and time, coherent structures that possess characteristic dynamics still emerge. Examples of these coherent structures are the large-scale current and plumes that aggregate in hot spots, as already described in the previous sections. In figure 1.3 four consecutive snapshots of two-dimensional convection exemplify the dynamical behavior of coherent structures, especially plumes. Also the convection rolls that are found in a linear stability analysis of the OBERBECK–BOUSSINESQ equations can be understood as coherent structures that appear near the onset of convection. The dynamics of these structures also cover a wide range of different time scales: The cessation and reorientation of the large-scale circulation happens on the longest time scales and may take place during many re-circulations of the convection cell; in contrast, the change of the small-scale turbulent fluctuations is usually the fastest time scale the system has. Both processes still have a significant influence on quantities like the heat transport through the fluid layer.

While the statistical description is desirable, as argued in the previous section, it only describes e. g. the heat transport in a statistical sense, and most of the coherent structures and their dynamics get lost due to the coarse-grained view the statistics provide. Nevertheless, convective flows and turbulence in general can be imagined as being built from a hierarchical cascade of coherent structures of different sizes that all possess their own dynamical behavior, as can be conceived from figures 1.1–1.3 in this chapter: Due to the slow, large-scale dynamics of the convection cell, small-scale shear instabilities near the boundary layer as well as plumes emerge and gather in the form of hot spots; these in turn are build from big plumes that interact with smaller plumes and vortices that finally decay into the "background" turbulence of the smallest and fastest scales. All these structures influence the heat transport in a unique way, sometimes attenuating and sometimes enhancing it, and this fine-grained view is missing in a purely statistical description. Thus, this hierarchical picture of the building blocks of convective flows suggests that the identification and understanding of coherent structures and their dynamics – either from first principles, e. g. in the spirit of a linear stability analysis, or from an empirical point of view – is essential for a comprehensive insight of convection.

1.5 Roadmap of the Thesis

The previous sections as well as the title of this thesis suggests the following roadmap in order to examine the statistical and dynamical properties of structures that are found in convective flows as well as their mutual interaction:

In part I we analyze the temperature statistics of turbulent Rayleigh–Bénard convection by deriving an evolution equation for the probability density function and supplementing this ansatz with data obtained from direct numerical simulations of the Oberbeck–Boussinesq equations. We thus achieve a temperature-resolved view of the average dynamics and structures in the flow, which enables us to examine how fluid of different temperatures behaves in different parts of the convection cell and how this in turn influences the heat transport. This method is then applied to numerical data generated in three different settings and vessel geometries in order to work out differences and generic behaviors. Part I closely follows the results that have already been published in Lülff *et al.* (2015).

Part II deals with the empirical detection of coherent structures in turbulent convective flows. For this purpose, we apply the known technique of proper orthogonal decomposition to a numerical data set of two-dimensional convection to obtain a set of basis modes that describe convection in an optimal way. We then extend this already established, general ansatz and adapt it towards Rayleigh–Bénard convection to obtain an optimal description of the heat transport. Thereby, we can identify a hierarchy of modes, starting from the large-scale structures and going down to the smallest fluctuating scales, and classify them in terms of their heat transport. We then show that this new ansatz achieves better results in describing the heat transport compared to the usual approach. The essential results of this part have been condensed in the publication LÜLFF (2015), where also further analysis can be found that goes beyond the scope of part II.

In part III we describe the behavior of the large-scale structures found in convection in a more abstract sense. To this end, we analyze the SWIFT–HOHENBERG equation, which is an order parameter equation for a two-dimensional horizontal cut through the temperature field of RAYLEIGH–BÉNARD convection. This equation describes the formation of convection rolls and cell patterns from a more coarse-grained point of view. When adding a stochastic driving force to this system, which can be thought of as imperfections found in experimental settings, the behavior of the structures has to be analyzed by statistical methods. We will combine tools borrowed from the analysis of stochastic processes as well as a gradient-dynamics approach to yield a description of the probability density function of the full order parameter field and the values it can take.

In the end, part IV will summarize and connect the main results of the three parts, put them into a scientific context, and give an outlook on open questions that should be revisited in further research.

Part I

Statistical Description of Heat Transport and Average Dynamics in RAYLEIGH–BÉNARD Convection

Rayleigh–Bénard convection, i. e. the flow of a fluid between two parallel plates that is driven by a temperature gradient, is an idealized setup to study thermal convection. Of special interest are the statistics of the turbulent temperature field, which we are investigating and comparing for three different geometries, namely convection with periodic horizontal boundary conditions in three and two dimensions as well as convection in a cylindrical vessel, in order to work out similarities and differences. To this end, we derive an exact evolution equation for the temperature probability density function (PDF). Unclosed terms are expressed as conditional averages of velocities and heat diffusion, which are estimated from direct numerical simulations. This framework lets us identify the average behavior of a fluid particle by revealing the mean evolution of fluid of different temperatures in different parts of the convection cell. We connect the statistics to the dynamics of Rayleigh–Bénard convection, giving deeper insights into the temperature statistics and transport mechanisms. In all three cases we find that the average behavior is described by closed cycles in phase space that reconstruct the typical Rayleigh–Bénard cycle of fluid heating up at the bottom, rising up to the top plate, cooling down and falling down again. The detailed behavior shows subtle differences between the three cases.

The work presented here has already been published (Lülff *et al.*, 2015), and the content of part I has been adapted in large parts from this publication; additional analysis and remarks that are not part of the publication are given as footnotes or in the appendix of this thesis. It represents original research that builds upon the foundation that was laid in previous publications (Lülff, 2011, Lülff *et al.*, 2011). The cylindrical data used in section 4.3 was provided by Stevens (2011).

2 Introduction

In Rayleigh–Bénard convection, a fluid that is enclosed between two horizontal plates is heated from below and cooled from above, which induces a flow and thereby enhanced heat transport between the plates. This simple setup is the benchmark system to study thermal convection, which is important in nature and technical applications. Prominent examples include convection in the oceans and the atmosphere or plate tectonics in the mantle of the earth. Depending on the control parameters, the Rayleigh–Bénard system displays a variety of different patterns and flow regimes, ranging from laminar to highly turbulent flows.

Apart from special cases like laminar convection, an analytical solution does not exist as turbulent flows are remarkably hard to handle analytically. Because of their importance, a deeper understanding of turbulent convective flows is still desired, despite the inability to solve the basic equations analytically. To achieve this, many different approaches have been pursued. The heat transport as a function of the control parameters is of particular interest and is well described by the Grossmann–Lohse theory (Grossmann and Lohse, 2000, 2001, Ahlers *et al.*, 2009, Grossmann and Lohse, 2011, 2012, Petschel *et al.*, 2013, Stevens *et al.*, 2013). There have also been studies on the turbulence properties of Rayleigh–Bénard convection, by e. g. characterizing the statistics of temperature readings of thermal probes in the convection cell (Yakhot, 1989, Ching, 1993, Ching *et al.*, 2004, Shang *et al.*, 2008) or by examining the heat transport mechanisms and the large-scale circulation by Eulerian (Bailon-Cuba *et al.*, 2010, Petschel *et al.*, 2011, van der Poel *et al.*, 2011, Ahlers *et al.*, 2012) or Lagrangian (Gasteuil *et al.*, 2007, Schumacher, 2009) approaches. An overview of recent progress on Rayleigh–Bénard convection can be found in Ahlers *et al.* (2009), Lohse and Xia (2010), Chillà and Schumacher (2012).

In the present part of the thesis, we will describe Rayleigh–Bénard convection with the full single-point temperature statistics using the temperature probability density function (PDF). This in turn gives us information about the dynamics of the convecting fluid. To this end, we will derive an evolution equation for the temperature PDF, feed in numerical data to complete our ansatz and obtain through the statistics a description of the mean dynamics of fluid particles that travel around in the convection cell. A similar method has been used to describe the statistics in homogeneous isotropic turbulence before, see Wilczek and Friedrich (2009), Wilczek *et al.* (2011), Friedrich *et al.* (2012).

In this part, we will generalize and extend the work presented by Lülff *et al.* (2011), where we first introduced the aforementioned method to Rayleigh–Bénard convection.

We start by deriving the framework in the most general form. Since Rayleigh–Bénard setups usually contain a number of symmetries that can be utilized to simplify the problem, we will apply our framework to three different showcases of three- and two-dimensional convection with homogeneous horizontal directions (i. e., periodic boundaries) and three-dimensional convection in a cylinder. All three cases have different statistical symmetries and show slightly different dynamics. The differences between two- and three-dimensional convection and also between fixed sidewalls and periodic horizontal boundaries are discussed, for example, in van der Poel *et al.* (2013, 2014). We will use the PDF methods presented here to further work out similarities and differences between these three cases and give a comprehensive description of the statistics and the dynamics of Rayleigh–Bénard convection.

Since the derivation of our framework utilizes the basic equations of Rayleigh–Bénard convection, it can be considered as an ansatz from first principles. The basic equations that govern Rayleigh–Bénard convection are the Oberbeck–Boussinesq equations (Oberbeck, 1879, Boussinesq, 1903) for the velocity $\boldsymbol{u}(\boldsymbol{x},t)$ and temperature field $T(\boldsymbol{x},t)$:

$$\frac{\partial}{\partial t}\boldsymbol{u} + \boldsymbol{u}\cdot\nabla\boldsymbol{u} = -\nabla p + \mathrm{Pr}\,\Delta\boldsymbol{u} + \mathrm{Pr}\,\mathrm{Ra}\,T\boldsymbol{e}_z \tag{2.1a}$$

$$\nabla\cdot\boldsymbol{u} = 0 \tag{2.1b}$$

$$\frac{\partial}{\partial t}T + \boldsymbol{u}\cdot\nabla T = \Delta T \tag{2.1c}$$

Here, the equations have been non-dimensionalized by the heat diffusion time $\frac{L^2}{\kappa}$, the vertical height L and the heat difference δT between the upper and lower plate. This introduces the Rayleigh number $\mathrm{Ra} = \frac{\alpha g \delta T L^3}{\nu\kappa}$ and the Prandtl number $\mathrm{Pr} = \frac{\nu}{\kappa}$ as the control parameters. The vertical coordinate lies in the range $z \in [0,1]$ and the temperature takes values $T \in [0,1]$. Another control parameter that is often taken into account is the aspect ratio Γ which indicates the lateral over the vertical extent of the system.

The remainder of this part of the thesis is structured as follows. In chapter 3 we will briefly recount our method, i. e. derive an equation for the temperature PDF and connect it to the description of the dynamics of the system. This general theory is then applied to three different Rayleigh–Bénard geometries in chapter 4, namely three- and two-dimensional convection with homogeneous horizontal directions, and three-dimensional convection in a closed cylindrical vessel with $\Gamma = 1$. Chapter 5 closes part I with an interpretation and discussion of the findings.

3 Statistical Description of Heat Transport

Our idea to describe Rayleigh–Bénard convection is to start from the temperature PDF. Therefore we want to derive an equation that describes the temperature PDF and use it to gain insights into the dynamics of the system. This ansatz is generally referred to as *PDF methods* (Pope, 1984, 2000) or the *Lundgren–Monin–Novikov hierarchy* (Lundgren, 1967, Monin, 1967, Novikov, 1968). We now give a short overview of this derivation; a more detailed discussion of the framework can be found in Lülff *et al.* (2011), Wilczek and Friedrich (2009), Wilczek *et al.* (2011), Friedrich *et al.* (2012). Similar equations have been derived for turbulent reactive flows by Pope (1985). However, there the unclosed terms are modeled instead of estimated from the numerics as in our case.

3.1 PDF Methods

The starting point is the definition of the temperature PDF as an ensemble average,

$$f(T,\boldsymbol{x},t) = \left\langle \delta\left(T(\boldsymbol{x},t) - T\right)\right\rangle \quad , \tag{3.1}$$

where the PDF $f(T,\boldsymbol{x},t)$ describes the probability to find fluid of temperature T at position $\boldsymbol{x}$ and time t. Accordingly, T is the sample space variable, while $T(\boldsymbol{x},t)$ is a realization of the temperature field. The averaging process $\langle\cdot\rangle$ can be considered as an ensemble average; later on, ensemble averages are evaluated from the numerics by a suitable volume and time average.

Since the definition in (3.1) includes an actual realization $T(\boldsymbol{x},t)$ of the temperature field, it is now possible to calculate spatial and temporal derivatives of the PDF, i. e. $\nabla f(T,\boldsymbol{x},t)$ and $\frac{\partial}{\partial t} f(T,\boldsymbol{x},t)$. These derivatives contain unclosed terms in the form of conditional averages $\langle\cdot|T,\boldsymbol{x},t\rangle$, where, e. g., the appearing conditionally averaged velocity $\langle\boldsymbol{u}|T,\boldsymbol{x},t\rangle$ is a function of the sample space variables T, $\boldsymbol{x}$ and t that tells us what the mean velocity is for fluid of given temperature, position and time.

Putting the aforementioned derivatives together and rearranging them gives the desired evolution equation that describes the temperature PDF:

$$\frac{\partial}{\partial t} f + \nabla \cdot \left(\langle \boldsymbol{u} | T, \boldsymbol{x}, t \rangle f \right) = -\frac{\partial}{\partial T} \left(\left\langle \frac{\partial}{\partial t} T + \boldsymbol{u} \cdot \nabla T \middle| T, \boldsymbol{x}, t \right\rangle f \right) \tag{3.2a}$$

$$= -\frac{\partial}{\partial T} \left(\langle \Delta T | T, \boldsymbol{x}, t \rangle f \right) \tag{3.2b}$$

The left-hand side of (3.2a) can be seen as the convective derivative of the PDF $f(T, \boldsymbol{x}, t)$, while the right-hand side of (3.2a) contains the conditional average of the convective derivative of the temperature field. Since $T(\boldsymbol{x}, t)$ is a realization of the temperature field, it obeys the OBERBECK–BOUSSINESQ equations, so in (3.2b) we replaced the convective derivative of the temperature field by the right-hand side of the OBERBECK–BOUSSINESQ equation (2.1c).

Above we obtained an evolution equation that links the shape of the temperature PDF to the conditionally averaged velocity $\langle \boldsymbol{u} | T, \boldsymbol{x}, t \rangle$ and heat diffusion $\langle \Delta T | T, \boldsymbol{x}, t \rangle$, which have to be supplied externally; in our case, we estimate them from simulations later on.

3.2 Method of Characteristics

The above evolution equation (3.2) that determines the temperature PDF is a first-order partial differential equation. That means that we can apply the method of characteristics (COURANT and HILBERT, 1962, SARRA, 2003) which lets us identify the average behavior of fluid as it travels through phase space.

In a nutshell, by applying the method of characteristics to the evolution equation, one can identify trajectories (the so-called *characteristic curves* or just *characteristics*) in phase space, along which the partial differential equation for the temperature PDF transforms into a set of ordinary differential equations for T and $\boldsymbol{x}$. The phase space is spanned by the variables that the temperature PDF depends upon, i. e. T, $\boldsymbol{x}$ and t. The characteristics are defined by the conditional averages,

$$\begin{pmatrix} \dot{T} \\ \dot{\boldsymbol{x}} \\ \dot{t} \end{pmatrix} = \begin{pmatrix} \langle \Delta T | T, \boldsymbol{x}, t \rangle \\ \langle \boldsymbol{u} | T, \boldsymbol{x}, t \rangle \\ 1 \end{pmatrix} \quad . \tag{3.3}$$

This states that the characteristics are solutions $\left(T, \boldsymbol{x}, t\right)^{\mathrm{T}}$ of (3.3) that follow the vector field on the right-hand side of the above equation; the vector field is regarded as the phase space velocity. From the last line of (3.3), $\dot{t} = 1$, it becomes clear that the parametrization of the characteristics in phase space, i. e. the arc length, is the same as the time of the system – a *fast* movement in phase space therefore really has to be seen in the temporal sense.

It is now important to notice that, since the characteristics are governed by the conditionally averaged vector field, they show the average behavior of a fluid parcel in phase space. In other words, the characteristics can be seen as the mean evolution of an ensemble of LAGRANGian particles that share the same coordinates in phase space. This is what POPE (1985, sec. 4.5) refers to as *conditional particles* – quasi-particles following the conditionally averaged vector field (3.3) that show the mean LAGRANGian evolution and that have the same statistics as LAGRANGian particles. By examining the conditionally averaged vector field and the resulting characteristic curves, one can investigate the mean transport properties of fluid through phase space and gain insight into the mean heat transport properties of RAYLEIGH–BÉNARD convection. Since the characteristics are trajectories in phase space, the framework can be seen as a quasi-LAGRANGian description, but it has to be stressed that it is achieved by utilizing the statistics of EULERian fields alone.

Along the characteristics, the partial differential equation (3.2) becomes an ordinary differential equation which can be integrated. Thus, the temperature PDF along a certain characteristic evolves according to

$$\begin{aligned} f(T(t),\boldsymbol{x}(t),t) = {} & f(T(t_0),\boldsymbol{x}(t_0),t_0)\times \\ & \exp\left(-\int_{t_0}^{t}\mathrm{d}t'\left(\nabla\cdot\langle\boldsymbol{u}|T,\boldsymbol{x},t\rangle+\frac{\partial}{\partial T}\langle\Delta T|T,\boldsymbol{x},t\rangle\right)_{T(t'),\boldsymbol{x}(t'),t'}\right) \quad . \end{aligned} \tag{3.4}$$

Here, the integral is a line integral along a characteristic from t_0 to t. The integral kernel is the phase space divergence $\nabla\cdot\langle\boldsymbol{u}|T,\boldsymbol{x},t\rangle+\frac{\partial}{\partial T}\langle\Delta T|T,\boldsymbol{x},t\rangle$ evaluated at the phase space position given by the characteristic for time t', i. e. $\left(T(t'),\boldsymbol{x}(t'),t'\right)^{\mathrm{T}}$. This equation tells us that the temperature PDF along the characteristic that connects the initial point $\left(T(t_0),\boldsymbol{x}(t_0),t_0\right)^{\mathrm{T}}$ with the point $\left(T(t),\boldsymbol{x}(t),t\right)^{\mathrm{T}}$ in phase space changes according to the integrated phase space divergence. As an alternative interpretation, (3.4) determines how the temperature PDF for time t is traced back to the PDF for t_0. While we will not further investigate (3.4) in the numerical results of the next chapter, we included it for the sake of completeness.

Up to now, we have kept the description as general as possible. But usually, a RAYLEIGH–BÉNARD setup has a number of statistical symmetries which simplify the problem, i. e. the phase space dimension is reduced and the estimation of the unknown conditional averages from numerical simulation is simplified. In the next chapter, we will apply the framework that has been outlined in this chapter to three different RAYLEIGH–BÉNARD geometries with different symmetries and discuss the findings.

4 Results from DNS

This chapter will focus on three Rayleigh–Bénard geometries, i. e. three-dimensional convection with periodic horizontal boundaries (section 4.1), two-dimensional convection with periodic horizontal boundaries (section 4.2), and three-dimensional convection in a cylindrical vessel with $\Gamma = 1$ (section 4.3).

4.1 Three-dimensional Convection with Periodic Horizontal Boundaries

First, we consider three-dimensional convection with periodic horizontal boundaries in the statistically stationary state. A snapshot of the instantaneous temperature field taken from the numerics can be seen in figure 4.1. The parameters of the simulation are $\mathrm{Ra} = 2.4 \times 10^7$, $\mathrm{Pr} = 1$, and the aspect ratio of the periodic box is $\Gamma = 4$. The two horizontal plates have a constant temperature and a no-slip velocity boundary condition. The numerical setup is a tri-periodic pseudospectral direct numerical simulation, where the boundary conditions are enforced by volume penalization methods (Lülff *et al.*, 2011,

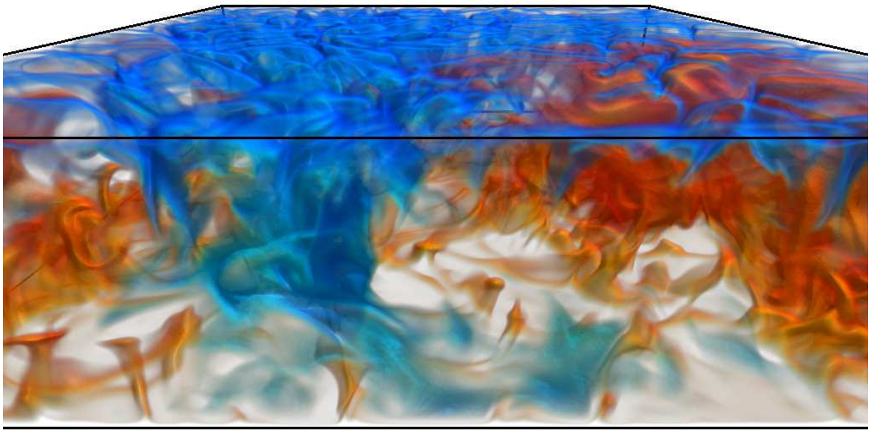

Figure 4.1: *Snapshot of the temperature field in three-dimensional Rayleigh–Bénard convection. Hot fluid rising up from the bottom plate is reddish, while cold fluid falling down from the top is dyed blue.*

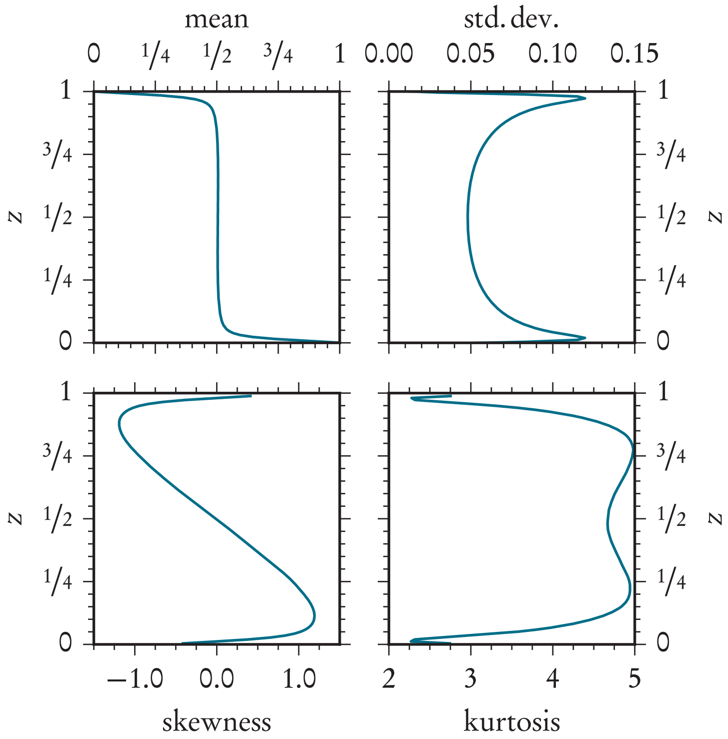

Figure 4.2: *Height-resolved profiles of the mean, standard deviation, skewness and kurtosis of the temperature distribution (row-major from upper-left panel) for three-dimensional convection with periodic horizontal boundaries. The skewness and kurtosis are defined as the third and fourth standardized moment.* G*aussian distributions have skewness of* 0 *and a kurtosis of* 3.

Angot *et al.*, 1999, Schneider, 2005, Keetels *et al.*, 2007). The equidistant resolution in x, y and z direction is 512 × 512 × 128 grid points, and in the vertical direction 5 grid points fall into the boundary layers, according to the criteria given by Shishkina *et al.* (2010). We calculated the statistical quantities from an ensemble consisting of 571 snapshots, and the snapshots were taken 3.75 free-fall time units apart.

Statistically stationary Rayleigh–Bénard convection in this geometry is homogeneous in horizontal directions. This means that the statistical quantities only depend on the temperature T and the vertical coordinate z and not on the horizontal coordinates x and y or time t. Thus, the temperature PDF and the conditional averages read $f(T,z)$ and $\langle\cdot|T,z\rangle$, and the phase space becomes two-dimensional.

In figure 4.2, the height-resolved mean, standard deviation, skewness and kurtosis of the temperature field are shown. As is well known, the mean temperature is almost constant in the bulk and has a steep gradient towards the hot and cold boundaries at $z=0$ and $z=1$. The standard deviation takes its highest values close to the boundaries and decreases towards the center of the bulk, indicating a temperature PDF that is broadening towards the boundaries. The height-resolved skewness takes its highest absolute values near the boundaries and decreases linearly as function of height in the bulk. This can be interpreted as hot fluid that is beginning to cool down on its way from the lower to the upper plate (and vice versa). The kurtosis indicates that, apart from the boundaries, the temperature PDF is more peaked and shows stronger tails than the Gaussian distribution.

When the simplifications resulting from the statistical symmetries are incorporated into the general framework presented in chapter 3, (3.2) that defines the PDF becomes

$$\frac{\partial}{\partial z}\left(\langle u_z|T,z\rangle f\right) = -\frac{\partial}{\partial T}\left(\langle \Delta T|T,z\rangle f\right) \quad , \tag{4.1}$$

while the vector field (3.3) of the characteristics reads

$$\begin{pmatrix} \dot{T} \\ \dot{z} \end{pmatrix} = \begin{pmatrix} \langle \Delta T|T,z\rangle \\ \langle u_z|T,z\rangle \end{pmatrix} \quad . \tag{4.2}$$

The PDF and the characteristic curves are therefore defined by the conditional averages of vertical velocity and heat diffusion. The next step is to estimate the conditional averages from the numerics while taking the statistical symmetries into account. Subsequently, the characteristics are obtained by integrating (4.2) for arbitrary initial conditions $\left(T_0, z_0\right)^{\mathrm{T}}$ in phase space. Obviously only initial conditions where the PDF and the conditional averages are defined, i. e. where there have been any events at all, can be considered.

When integrating the characteristics for many starting positions, we observed that they tended to converge to what at first seems to be similar to a limit cycle. In contrast, though, one would expect that the characteristics form concentric closed curves: To see this, let the phase space be densely seeded by the conditional particles described in section 3.2. As the density of the conditional particles following the characteristics is proportional to the temperature PDF, and a limit cycle acts as an attractor for the conditional particles, the temperature PDF should converge towards a δ-function that is non-vanishing on the cycle and zero everywhere else. This in turn stands in contrast to the fact that we are considering statistically stationary systems and that the temperature PDF is clearly not a δ-function, and thus it follows that the characteristics cannot converge to a limit cycle but must form concentric closed curves.

We find that the observed erroneous convergence is caused by the flawed conditionally averaged vector field estimated from the numerics by a binning process. The noise inherent to the binning violates the solenoidality of the probability flux (phase space velocity times PDF) as demanded by (4.1), and thus the imperfect binned vector field contains many localized sinks where the characteristics converge.

By smoothing the binned data through a convolution with a Gaussian kernel and projecting the vector field onto the solenoidal part (i. e., enforcing the validity of (4.1)), we are indeed able to find the expected concentric closed curves, as exemplified in figure 4.3.[1] Here the horizontal axis corresponds to the temperature coordinate T and the vertical axis to the vertical coordinate z of the phase space; the background color coding gives

---

[1] Details of this post-processing are given in section A.1.

Figure 4.3: *Concentric closed characteristics found for three-dimensional convection after removing the imperfections from the binned conditionally averaged vector field, cf. text. The temperature PDF $f(T, z)$ is color coded.*

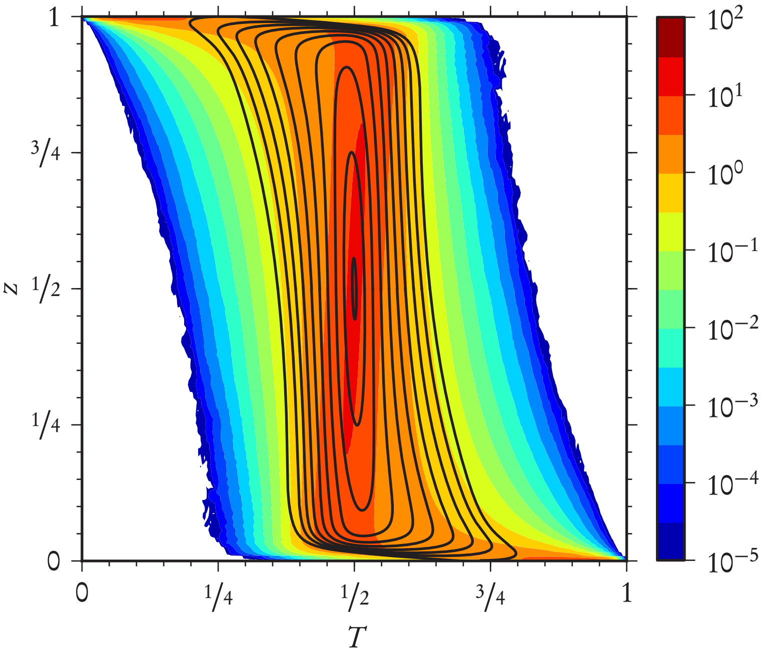

the temperature PDF $f(T, z)$. For every starting point located on the $z = 0.5$-axis, the characteristics perform a closed loop in counter-clockwise direction that shows how particles on average evolve through phase space. By tracing its course, one is able to reconstruct the typical Rayleigh–Bénard cycle a conditional particle undergoes: A fluid element near the lower plate first heats up and then starts to move up towards the cold plate. During its upward travel it slowly cools down and then becomes much colder when it is close to the top plate before it falls down again towards the lower plate while beginning to heat up and starting what we call the RB cycle all over again. The cycles for fluid starting at more moderate temperatures (i. e., near $T = 0.5$) show a smaller amplitude in both T- and z-direction. We do not find closed circles located further outwards, because the characteristics would visit areas of the phase space where no events are recorded in the numerics, and thus the vector field is undefined there. This usually happens near the vertical boundaries of the phase space (i. e., near the plates) where the support of the vector field becomes very narrow. Furthermore, we remark that the precise appearance of the closed cycles slightly varies with the parameters of the post-processing described above (e. g., the amount of smoothing); nevertheless, the description of the qualitative behavior we are aiming at is found to be robust.

Without the aforementioned projection to keep the vector field solenoidal in the presence of noise, the characteristics converge in some parts of the phase space. To study this behavior, and also the near-wall regions, we seed characteristics on the $\{T > 0.5, z = 0.5\}$-line and integrate them backwards in time, as shown in figure 4.4. The comparison of

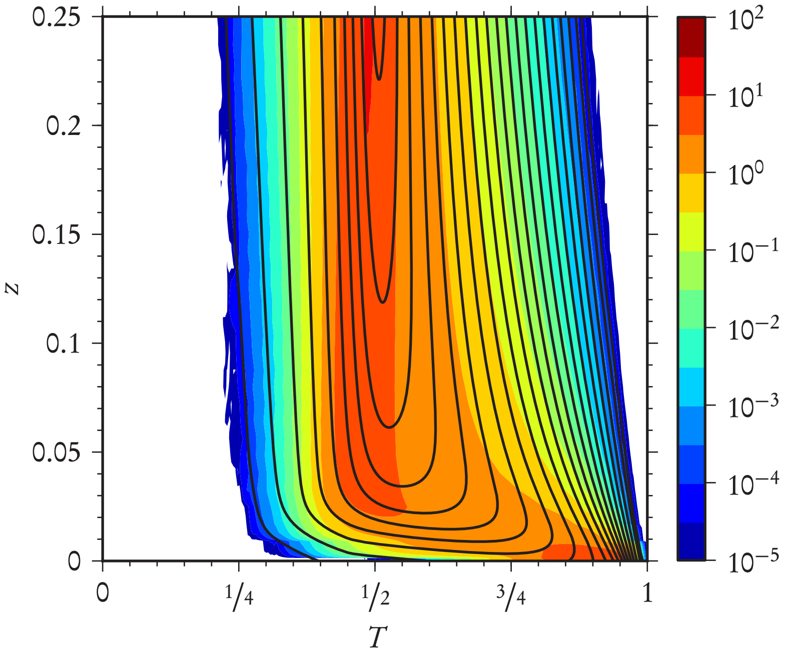

Figure 4.4: *Characteristics seeded on the $\{T > 0.5, z = 0.5\}$-line and followed backwards in time for three-dimensional convection. A zoom into the bottom region $0 \leq z \leq 0.25$ is shown. The divergences of the vector field have not been removed here. The temperature PDF $f(T,z)$ is color coded.*

the characteristics in the regions $T < 0.5$ and $T > 0.5$ immediately reveals the convergence for the non-solenoidal case, because the density of the characteristics on the right side (i. e., at later times) is higher than on the left side. Furthermore, the characteristics on the far right enter the boundary at $z = 0$ when integrated backwards in time, or, to put it in other words, characteristics leave the boundaries very close to each other and then become less dense when following them forward in time. This corresponds to the fact that at $z = 0$, the temperature PDF becomes a δ-function located at $T = 1$ due to the DIRICHLET boundary condition. In fact, the characteristics should end precisely in this point, but this behavior is not resolved here. Likewise, by symmetry considerations, the characteristics approaching the boundary from the far left side should also enter the point $\{T = 1, z = 0\}$, which we do not observe. We speculate that a numerical resolution that goes beyond what is demanded by the criterion of SHISHKINA *et al.* (2010) may be needed to capture the correct behavior of the characteristics in this singular region of phase space.

The cycle to which the characteristics converge in the presence of noise is shown in figure 4.5. This cycle is very similar to the closed curves shown in figure 4.3; in fact, it is almost completely embedded between two adjacent closed curves.[2] While the solenoidal projection helps to find the required closed curves, the conditionally averaged vector field still containing the noise gives the same general picture of the RB cycle. Additionally, the projection may introduce unpredictable systematic errors, especially in regions of the phase space where the support of the conditional averages and the PDF changes

---

[2] See also section A.2.

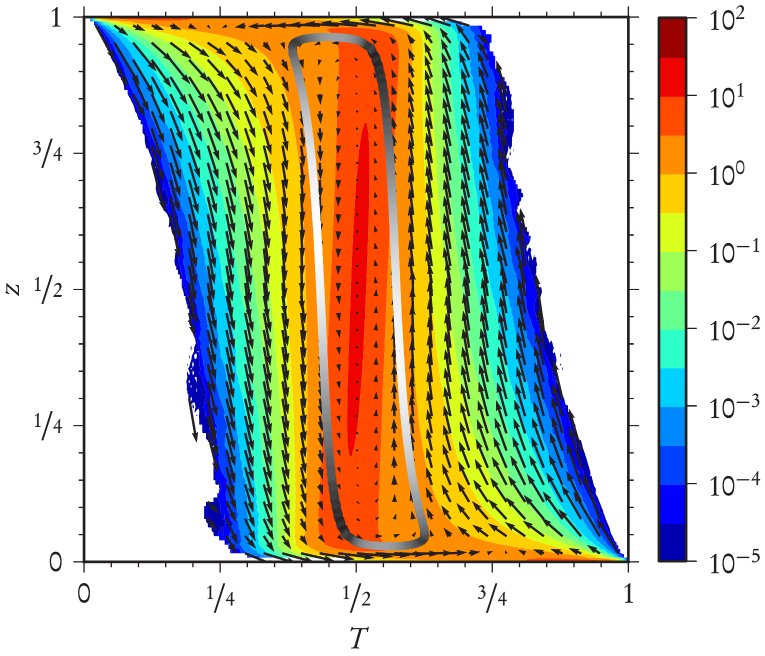

Figure 4.5: *RB cycle of the characteristics for three-dimensional convection. The phase space speed along the cycle shown as solid thick line is coded in black and white, i. e. the norm of the phase space velocity appearing in* (4.2). *The color coding in the background shows the temperature PDF* $f(T, z)$. *The arrows show the phase space velocity field, where the length of the arrows has been rescaled to arbitrary units for visualization purposes. Note that around the lower-left and upper-right corners, no events were recorded (e. g., there is no fluid of temperature* $T \approx 1$ *near the upper plate).*

rapidly. Therefore, as we want to focus on the qualitative features of Rayleigh–Bénard convection that the RB cycle as well as the vector field represent, we will from now on only consider the cases without the solenoidal projection and use the found cycle as one generic representative of the family of closed concentric curves. The same applies to the convection cases discussed in sections 4.2 and 4.3 where the characteristics also tend to converge due to imperfections induced by noise.

We now come back to the discussion of the qualitative features that the conditionally averaged phase space velocity and the RB cycle describe. In figure 4.5, the RB cycle is shown together with the temperature PDF and in figure 4.6 together with the phase space velocity. From the first-mentioned figure, it is interesting to see that hot fluid on the RB cycle has the highest phase space speed in the range $0.25 < z < 0.5$, i. e. hot rising fluid is fastest in the lower half of the convection vessel, and likewise for cold fluid in the upper half due to the up-down symmetry of Rayleigh–Bénard convection. As a side note,

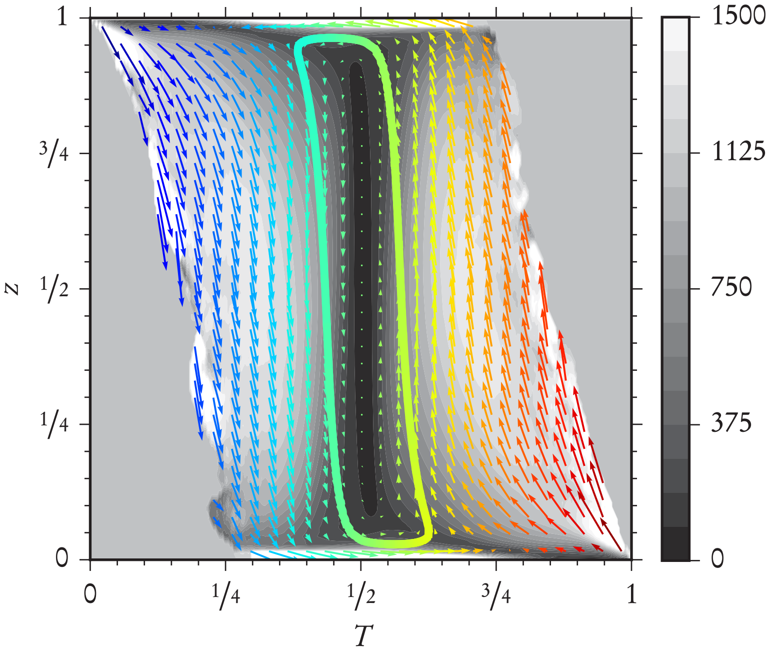

Figure 4.6: *RB cycle of the characteristics for three-dimensional convection as function of height and temperature. The color of the arrows (with blue corresponding to $T = 0$ and red to $T = 1$) indicates the temperature. The black and white background color shows the phase space speed.*

from now on, whenever we describe a fluid process, the *reversed* process – interchanging hot⟷cold, bottom⟷top, up⟷down etc. – is also implied.

The temperature PDF in figure 4.5 shows that the temperature distribution changes with the vertical coordinate and contracts to a δ-function at the fixed temperature boundaries. Furthermore, one can map the shape of the distribution to the higher moments in figure 4.2, i. e. the peaks of the standard deviation near the boundaries and the linear dependence of the skewness on the height in the bulk region. We note that the isocontours of the PDF do not lie tangent to the vector field or the RB cycle because the divergence of the phase space velocity, $\frac{\partial}{\partial z}\langle u_z|T,z\rangle + \frac{\partial}{\partial T}\langle \Delta T|T,z\rangle$, is non-vanishing.

In figure 4.6, the black and white background color corresponds to the phase space speed, and the temperature is given by the color of the arrows. This display lets us identify how fluid behaves in different parts of the phase space. Near the boundaries, fluid of all temperatures displays high phase space speeds, while in the bulk only fluid of *intense* temperature (i. e., deviating strongly from the mean) has high speeds. This supports the previous finding that hot fluid on the RB cycle has its highest speed in the lower half. Fluid that has the mean temperature (cf. upper-left panel of figure 4.2) is found to be at rest because no buoyancy acts on it and it does not heat up or cool down. As can be expected *a priori*, the vector field shows that the main movement in T-direction, i. e. heating and cooling, takes place near the boundaries, while the main movement in vertical direction happens in the bulk.

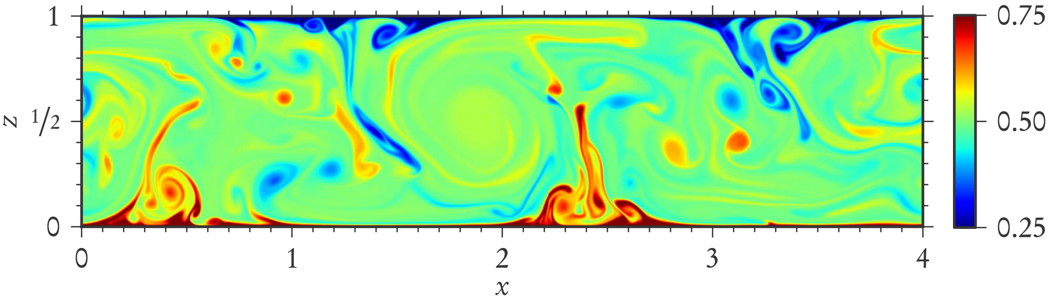

Figure 4.7: *Temperature field for two-dimensional convection with periodic horizontal boundary conditions. The color scale for T is shown on the right.*

4.2 Two-dimensional Convection with Periodic Horizontal Boundaries

The next case to investigate is two-dimensional RAYLEIGH–BÉNARD convection with periodic horizontal boundaries. The parameters are $\mathrm{Ra} = 5 \times 10^8$, $\mathrm{Pr} = 1$ and $\Gamma = 4$, and the numerical scheme that is used is identical to the one from section 4.1. Again, the two horizontal plates are no-slip walls of fixed temperature. The numerical resolution is 1536×384 equidistant grid points with 7 grid points in the vertical direction falling into the boundary layers (cf. SHISHKINA *et al.* (2010)), and the ensemble consists of 3891 snapshots separated by 3.75 free-fall time units.

A snapshot of the temperature field is shown in figure 4.7, and one can see coherent structures in the form of four plume hot spots (two at the top, two at the bottom) and four convection rolls, even at this intermediate RAYLEIGH number. Also, localized round blobs of hot and cold fluid can be found. The statistical symmetries in this system are identical to the ones for the three-dimensional periodic case discussed before, which means the phase space becomes two-dimensional and the statistics depend on T and z only.

Figure 4.8 shows the first four height-resolved standardized moments of temperature. While the mean temperature profile has the same shape as the one from three-dimensional convection (cf. figure 4.2), the higher moments show subtle new features. For the three-dimensional case the moment profiles as function of the height are smoother than for the two-dimensional case. Especially the skewness shows transitions and is in the bulk not as linear as for the three-dimensional case. We link this to the coherent structures in the form of plume hot spots in the two-dimensional case because the position of the transitions in the moments corresponds to the vertical size of the plume hot spots (cf. figure 4.7). In the plume hot spots, there is a re-cycling of hot fluid, which means that fluid that is hotter than the mean temperature profile is trapped near the hot bottom plate for some time instead of being advected upwards directly, cf. SUGIYAMA *et al.* (2010). This

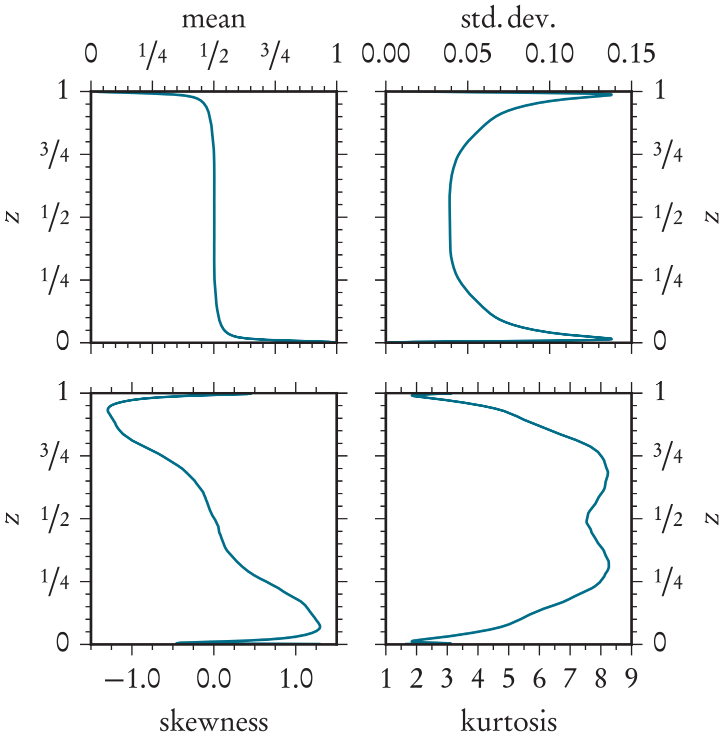

Figure 4.8: *First four standardized moments of temperature for two-dimensional convection, analogous to figure* 4.2.

hot trapped fluid causes a temperature distribution that is near the lower plate strongly skewed towards higher temperatures. Above the hot spot, only a sharp jet of hot fluid remains which results in a flatter profile of the skewness. In three-dimensional convection the trapping mechanism of plume hot spots is missing: Loosely speaking, in three-dimensional convection, there is another lateral dimension into which the fluid can escape and be advected away, forming the sheet-like plumes that can also be found in figure 4.1 (SCHMALZL *et al.* (2004) and VAN DER POEL *et al.* (2013) also discuss differences in flow structures between two- and three-dimensional convection). Therefore, the entrapment seen in two-dimensional convection does not occur in three dimensions, which means that a strong mechanism that in two dimensions traps hot fluid near the bottom is missing for the three-dimensional case.

When we estimate the conditional averages for two-dimensional convection from the simulation and then numerically calculate the characteristics, we again find that the dynamics in phase space resemble a closed cycle. This RB cycle is shown in figures 4.9 and 4.10. While the RB cycle displays the same basic cycle of fluid heating up at the

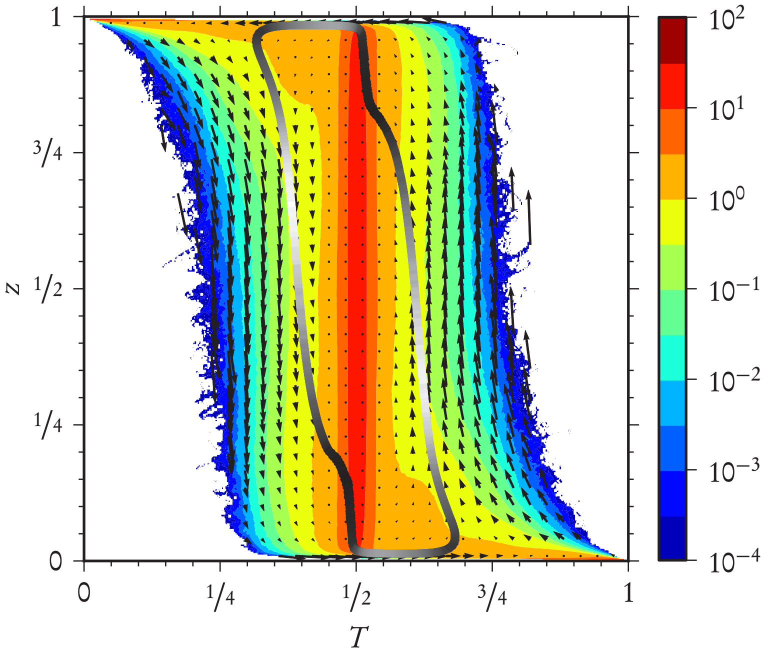

Figure 4.9: *RB cycle of the characteristics for two-dimensional convection, together with the temperature PDF. Illustration analogous to figure* 4.5.

bottom, moving upwards, cooling down at the top plate and falling down again, there are some differences as compared to the three-dimensional case (figures 4.5 and 4.6).

The most striking new feature is a kink in the RB cycle in the lower left and upper right corners. As can be seen from the color coding of the cycle, this is also the region of the lowest phase space speed. Therefore, we also link this region to the re-cycling areas discussed above because fluid trapped in the plume hot spots undergoes almost no net vertical movement and needs more time to heat up in comparison to fluid that is in direct contact with the much hotter bottom plate. A similar argument is discussed by van der Poel *et al.* (2013).

Another difference with the three-dimensional case is that there is a bulge in the temperature PDF towards higher temperatures (around $T \approx 0.6$, $z \approx 0.15$). This bulge is due to hotter-than-average fluid that gathers near the bottom plate and is therefore compatible with the interpretation of the re-cycling fluid from above; also, this bulge gives a direct impression of the high skewness values found in this region (cf. figure 4.8).

Figure 4.10 shows the vector field of the phase space velocities together with its norm (coded in black and white). The phase space velocities are more heterogeneously distributed as compared to the three-dimensional case, e. g. the high speeds in the bulk for intense temperatures are more pronounced (cf. figure 4.5). These strong vertical

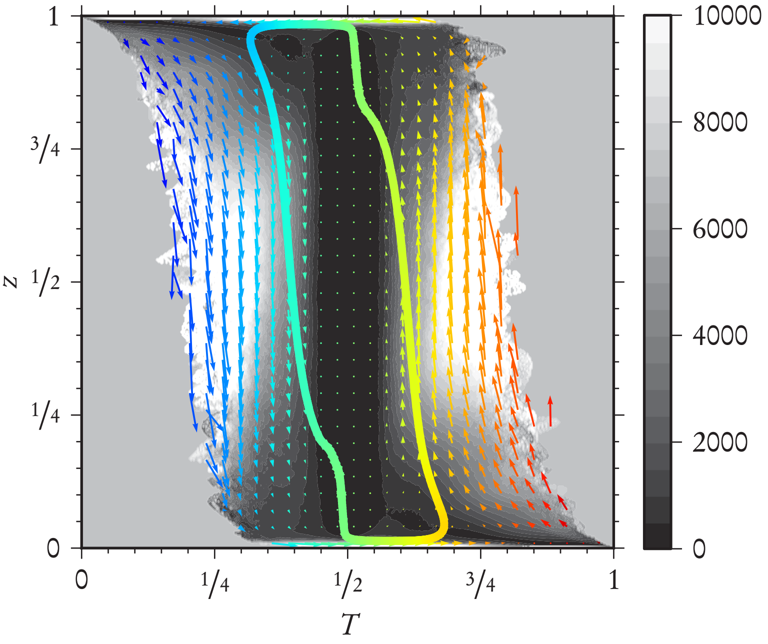

Figure 4.10: *RB cycle of the characteristics for two-dimensional convection, together with the phase space speed. Illustration analogous to figure* 4.6.

movements in the bulk lead to higher phase space speeds as compared to three dimensions (see the color scale in figures 4.6 and 4.10). We think this can only in part be attributed to the difference in Rayleigh numbers (2.4×10^7 vs. 5×10^8), but is also due to the coherent structures found in two dimensions, i. e. plume hot spots as localized events of intense temperature. It is also found that in the kink region the RB cycle passes through the region of lowest phase space speed, which can be understood as the average dynamics being slowed down in the re-circulating plume hot spots.

4.3 Three-dimensional Convection in a Cylindrical Vessel

The last Rayleigh–Bénard geometry under investigation is a closed cylindrical vessel. The control parameters are $\mathrm{Ra} = 2 \times 10^8$, $\mathrm{Pr} = 1$ and $\Gamma = 1$ (diameter over height). All the walls are no-slip, and the horizontal plates are of constant temperature while the sidewalls are thermally insulating. The ensemble consists of 870 snapshots that are obtained from direct numerical simulation using a second-order finite difference scheme on a staggered cylindrical grid (Verzicco and Camussi, 2003) with a resolution of $N_\varphi \times N_r \times N_z = 384 \times 192 \times 384$ grid points (with φ, r and z being the azimuthal, radial and vertical coordinate, respectively). The boundary layer contains 17 grid points in the

Figure 4.11: *Snapshot of the temperature field in three-dimensional* Rayleigh–Bénard *convection in a* $\Gamma = 1$*-cylinder. In the upper left corner, the color and opacity scale is shown; fluid around the mean temperature is translucent.*

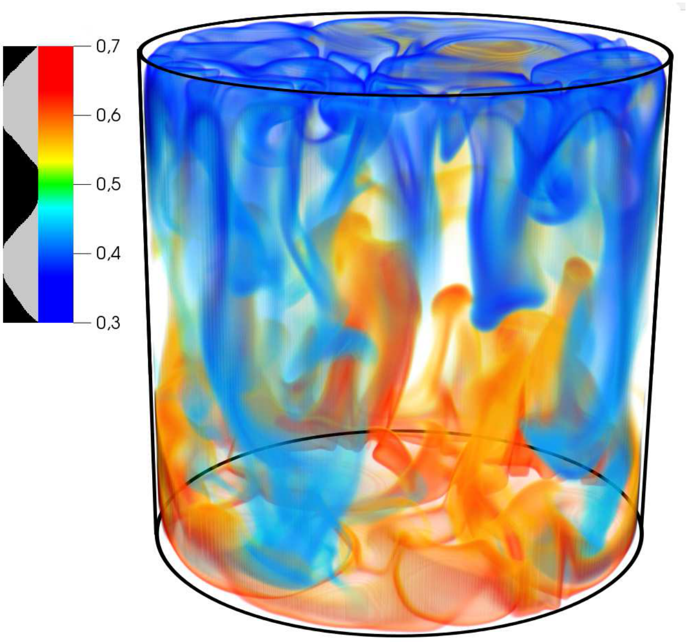

vertical direction. The snapshots are separated by 1 free-fall time unit. Figure 4.11 shows a snapshot of the temperature field.

Rayleigh–Bénard convection in a cylinder has statistical symmetries that are different from the former two cases of horizontally homogeneous convection. In addition to the temperature T and vertical position z the statistics now also depend on the radial position r in the cylinder. Here $r = 0$ corresponds to the cylinder axis and the sidewall is at $r = 1/2$.

In figure 4.12 the r-z-resolved first four standardized moments of the temperature distribution are shown. The horizontal and vertical axes correspond to the radial coordinate r and the vertical coordinate z, respectively. The mean temperature profile is almost constant in the bulk, and only near the hot and cold plate (and to a lesser extent near the sidewalls) a deviation can be seen. Like in the former cases, the standard deviation of the temperature takes its highest values near the horizontal plates and falls off towards the middle of the convection cell with a local minimum at $z = 0.5$. Also, it can be seen that this local minimum is less pronounced near the sidewalls, i. e. for high r. After rising up to its maximum value at $z \approx 0.1$, the skewness varies monotonically with increasing z. This has also been found for the former two cases. Regarding the radial dependence, the skewness falls off towards the sidewalls, indicating a less asymmetric temperature distribution there, while its highest values are found near the cylinder axis. Although the statistics are less converged for the kurtosis (especially near $r = 0$ due to the cylindrical geometry), one can see that the highest values correspond roughly to the extrema of

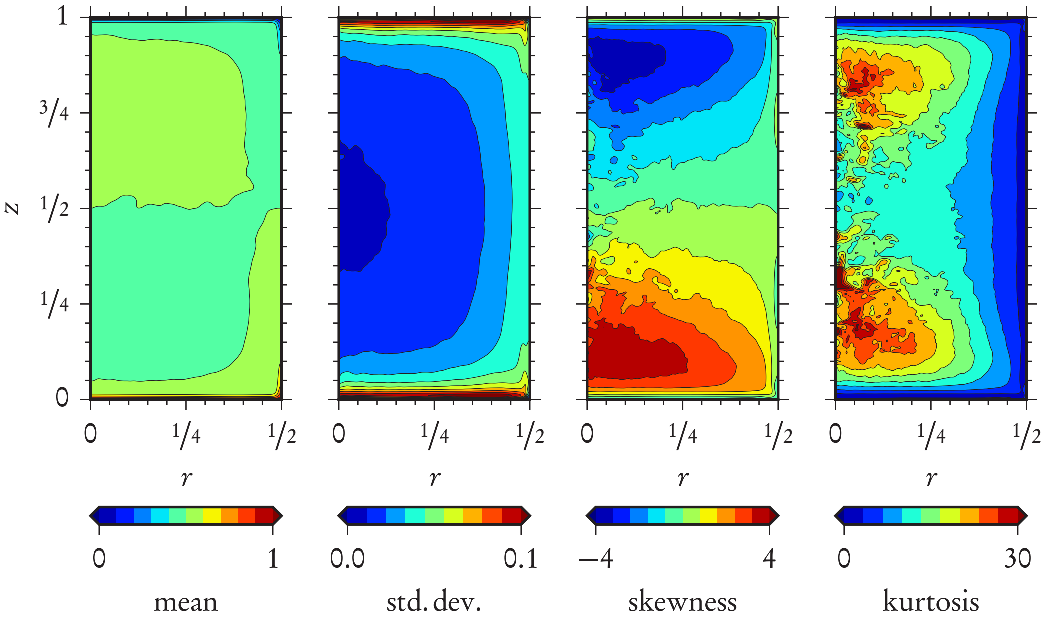

Figure 4.12: *First four standardized* r-z*-resolved moments of the temperature distribution, i. e. mean value, standard deviation, skewness and kurtosis (from left to right). Here the convection is in a cylinder with* $\Gamma = 1$.

the skewness. These high values of skewness and kurtosis near the bottom wall can be attributed to hot localized plumes detaching from the hot bottom plate and piercing into the colder fluid of the bulk. We also note that the absolute values of skewness and kurtosis are higher than in the former two cases (figures 4.2 and 4.8), which can be understood on dimensional grounds: In horizontally periodic convection, we averaged over all horizontal directions and therefore averaged out the sharp maxima that can be seen in the cylindrical case (figure 4.12) where the statistics are resolved additionally in the horizontal coordinate r.

When inserting the temperature PDF $f(T,r,z)$ and the conditional averages $\langle\cdot|T,r,z\rangle$ into the general framework from chapter 3, the PDF-defining equation (3.2) becomes

$$\frac{1}{r}\frac{\partial}{\partial r}\Big(r\langle u_r|T,r,z\rangle f\Big)+\frac{\partial}{\partial z}\Big(\langle u_z|T,r,z\rangle f\Big)=-\frac{\partial}{\partial T}\Big(\langle\Delta T|T,r,z\rangle f\Big)\quad, \tag{4.3}$$

while the characteristics (3.3) read

$$\begin{pmatrix}\dot{T}\\ \dot{r}\\ \dot{z}\end{pmatrix}=\begin{pmatrix}\langle\Delta T|T,r,z\rangle\\ \langle u_r|T,r,z\rangle\\ \langle u_z|T,r,z\rangle\end{pmatrix}\quad. \tag{4.4}$$

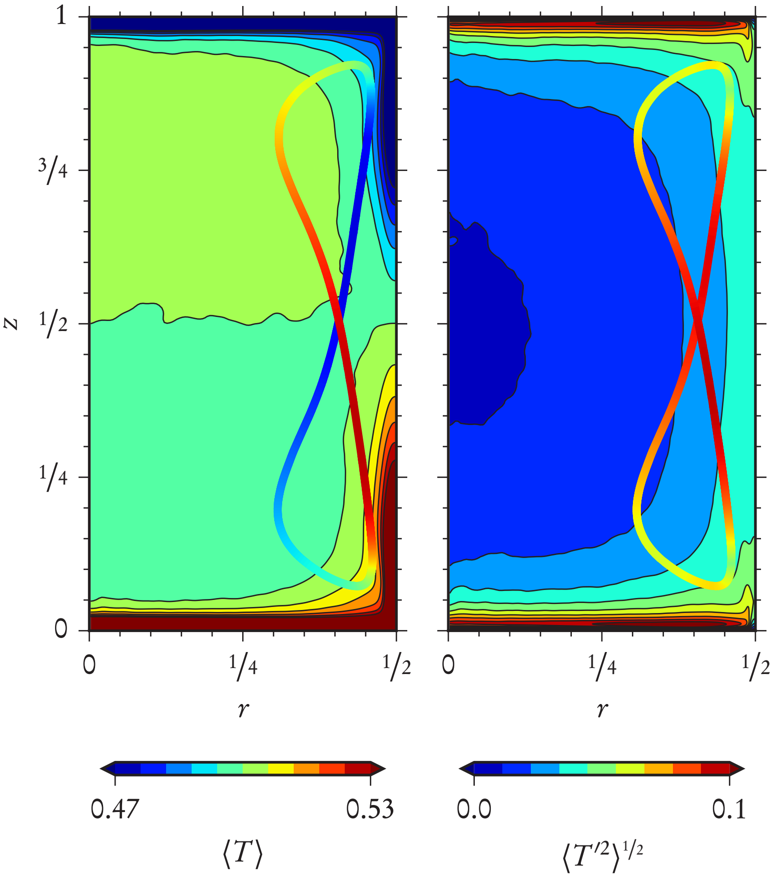

Figure 4.13: *RB cycle of the characteristics for convection in a $\Gamma = 1$-cylinder. Left: Temperature of the cycle (figure-eight) and r-z-resolved mean temperature color coded. Right: The r-z-resolved standard deviation of temperature where $T' = T - \langle T \rangle$. The color of the figure-eight-shaped cycle indicates its absolute temperature difference with respect to the background temperature.*

In comparison to the former two cases, we now deal with a three-dimensional phase space where the additional dimension is related to the radial movement. From (4.4) one sees that the radial coordinate r of the characteristics evolves according to the conditional average of radial velocity u_r.

We now again turn to the integration of the characteristics, following (4.4). Although cylindrical convection is intrinsically different from the former two cases of horizontally periodic convection (due to three- vs. two-dimensional phase space), we still find that the average dynamics of fluid parcels are described by a closed, twisted loop in phase space that shares common features with the former two. The cycle is shown in figures 4.13 and 4.14 as the slender figure-eight-shaped curve.

In the left panel of figure 4.13, the background shows the mean temperature (cf. figure 4.12) and the figure-eight-shaped curve shows a projection of the RB cycle into the r-z-plane. The third coordinate of the RB cycle, the temperature T, is color coded. The temperature scale corresponds to the minimal and maximal temperature ($T = 0.47$

and $T = 0.53$) the RB cycle takes. When tracing the cycle, one can again identify the RAYLEIGH–BÉNARD cycle of the horizontally periodic convection cases, superposed with an additional inwards and outwards motion: Starting with fluid of mean temperature that is quickly heating up at the bottom, it then begins to rise up and move inwards into the bulk until $z \approx 0.8$ and $r \approx 0.3$, where it goes outwards and starts to cool down. At the maximal z, the fluid cools down quickly and then falls towards the lower plate while moving inwards, thus starting the RB cycle all over again. Additionally, one can see that the hot fluid rising from the lower plate steadily cools down when it crosses the bulk of almost uniform temperature; this is related to the monotonically decreasing skewness of temperature that can be seen in figure 4.12.

The difference of the temperature of the RB cycle and the background temperature (cf. color coding of these two in figure 4.13 (left)) shows that the regions where the temperature of the RB cycle deviates most from the mean background temperature are the regions of high buoyancy and correspond to the regions of main vertical movement in the bulk. To elaborate on this, the right panel of figure 4.13 shows the standard deviation of the temperature field in the background, and the color coding of the cycle shows the absolute deviation of its temperature coordinate T from the mean temperature. The deviation of the temperature of a fluid particle on the cycle from the surrounding mean temperature determines its mean buoyancy, so the right panel tells us how strong the buoyancy acts; the highest values for hot rising fluid are found in the lower half of the convection cell. In comparison, the mean deviation of fluid from the mean temperature profile (shown in the background as the standard deviation of temperature) is much weaker. To summarize, from the left panel of figure 4.13 one can see in which direction the buoyancy acts, while the right panel shows its strength.

The vector field of the characteristics is shown in figure 4.14. Due to the difficulty to display a vector field in three-dimensional phase space, we show slices of the phase space velocity in the r-z plane at different T. The panels **I–VIII** show one cycle of a fluid parcel traveling along the RB cycle, with its temperature color coded as in figure 4.13 (left). Additionally to the RB cycle described above, figure 4.14 also reveals the average behavior of fluid in different parts of the convection cell, conditioned on its temperature. The arrows show an r-z slice of the vector field of the characteristics (4.4) at the T coordinate of the cycle. Also, the black and white background color indicates the phase space speed, i. e. how fast a fluid parcel travels through phase space (with white being the fastest movement). The arrows indicate the mean movement of fluid of a given temperature in different regions of the convection cell.

Panel **I** shows that cold fluid (here, $T = 0.475$) has the highest speeds in the bulk and near the sidewall. Near the cold top plate, cold fluid is mainly transported towards the outer wall. For $z < 0.75$, the direction of movement is slightly tilted towards the cylinder axis. Cold fluid that falls down along the sidewall is deflected towards the inner cylinder at around $z \approx 0.25$ due to a corner flow that propels cold fluid upwards along the sidewall; notice that at $r \approx 0.45$ and $z \approx 0.25$, up- and downwelling cold fluid collides.

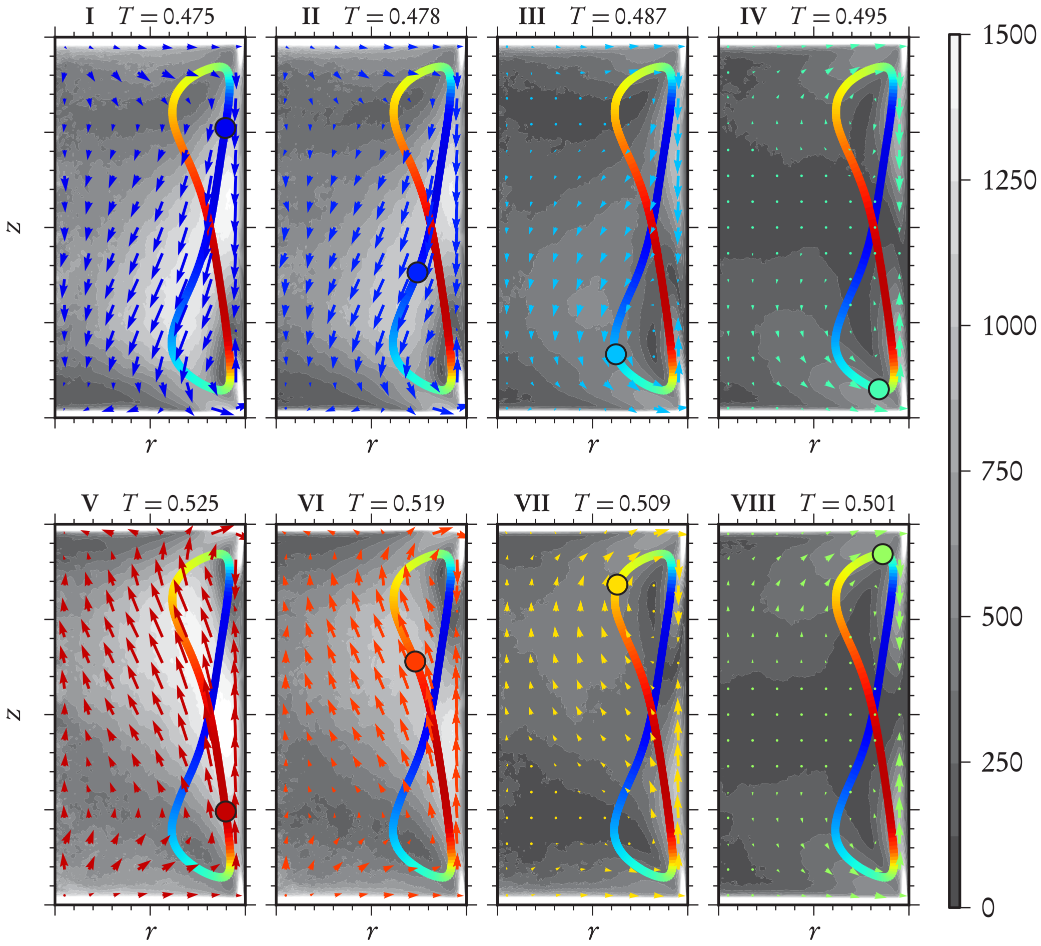

Figure 4.14: *Vector field governing the characteristics in phase space for convection in a* $\Gamma = 1$-*cylinder, cf.* (4.4). *Extents of horizontal and vertical axes as in figure* 4.13, *i. e.* $0 \leq r \leq 1/2$ *and* $0 \leq z \leq 1$. *The RB cycle is the slender figure-eight-shaped curve at the right side. The temperature of the vector field and the RB cycle is color coded as in figure* 4.13 *(left), and the phase space speed (i. e., norm of velocity) is coded in black and white in the background (with white being high velocity). The eight panels* ***I–VIII*** *follow a fluid parcel (circle on the cycle, with the color showing its temperature) along the RB cycle and show a slice of the vector field of the phase space velocity in the* r-z *plane at the* T *coordinate of the fluid parcel (with* $T \in \{0.475, 0.478, 0.487, 0.495, 0.525, 0.519, 0.509, 0.501\}$ *from left to right). The vector fields show the average movement in different regions of the convection cell of fluid of a particular temperature.*

This feature can be understood as cold plumes that are formed at the upper plate and are swept towards the sidewalls. The plumes then fall down along the sidewall until they hit the hot fluid at the bottom plate where they are directed inwards. These cold plumes that fall down along the sidewall can also be seen in figure 4.11.

The fluid from panel **III** is less cold ($T = 0.487$) and has overall lower speeds, but still shows the same features as in panel **I**, e. g. cold fluid is swept along the upper plate outwards and falls down along the sidewall until it hits the upwelling corner flow. The vector fields for fluid of mean temperature ($T \approx 0.5$, panel **IV** and **VIII**) are symmetric around $z = 0.5$ and show an almost vanishing velocity in the bulk. Near the horizontal plates, fluid is swept towards the sidewalls and from there vertically towards the $z = 0.5$-line.

The rest of the panels complete one run of the RB cycle and due to the up-down symmetry contain the same information already described. Still, from all eight panels it can be seen that fluid for all temperatures has high phase space speed near the sidewalls, which can be attributed to plumes that are guided along the outer walls of the cylinder, and also has high speeds near the bottom and top plate which is due to the vigorous temperature contrast between fluid and horizontal plates that leads to high speeds regarding the T coordinate. Also, we have to stress here that the corner flows show up due to the investigation being conditioned on the temperature and not due to some large-scale structure that may be present in the fields; this structure is lost in the azimuthal averaging process when obtaining the vector field from (4.4). Therefore, in our analysis the corner flows are statistical structures that are not necessarily related to structures in the flow.

5 Summary

Part I of this thesis analyzed the turbulent flow in Rayleigh–Bénard convection on the basis of statistical quantities like the temperature PDF and conditionally averaged fields. We derived that the mean path a fluid particle takes through phase space (spanned by temperature and spatial coordinates) is defined by so-called *characteristics*, i. e. trajectories in phase space that follow the conditionally averaged vector field composed of heat diffusion and fluid velocities. Thereby, we could characterize the dynamics and flow features that occur in turbulent convection cells from a statistical point of view, i. e. from averaged quantities like the temperature distribution and its moments as well as statistics conditioned on temperature and spatial position.

By estimating the aforementioned vector fields for three different Rayleigh–Bénard geometries while utilizing their symmetries and then integrating the characteristics we described the mean dynamics that fluid particles undergo, i. e. we could describe how fluid of different temperatures behaves in different regions of the convection volume. We also distinguished regions of high and low transport through phase space. For all geometries there are high phase space speeds for intense temperatures in the bulk (which we attribute to localized events of intense temperatures and high speeds, i. e. plumes) as well as high speeds near the horizontal plates for all temperatures, while for the case of cylindrical convection the phase space speed also takes high values near the wall of the cylinder. This we interpret as plumes that are directed along the insulating sidewalls. In the conditionally averaged vector field of the cylinder, we could furthermore identify corner flows near the sidewalls for fluid of different temperatures. Cold fluid experiences a corner flow near the bottom plate while showing no corner flow near the upper plate and vice versa. Additionally, we described the higher moments of the temperature distributions, where we could link features of the moments to coherent structures that appear in turbulent flows.

When we then obtained the characteristics by integrating trajectories through the conditionally averaged vector field, we found that for all different convection setups, the characteristics form closed cycles in phase space. These cycles reconstruct the typical Rayleigh–Bénard cycle a fluid particle undergoes on average, i. e. fluid is heated up at the bottom and rises upwards while slightly cooling down until it hits the upper plate, where it cools down fast and falls down to the lower plate while slightly heating up, thus starting the cycle all over again. In the cylindrical case, where there is another phase space dimension corresponding to horizontal movement, the fluid shows an additional inwards and outwards movement while following the RB cycle. The method thus allows to further pin-point and quantify the differences and similarities between Rayleigh–Bénard convection in two- and three-dimensional periodic boxes and in three-dimensional convection in a cylindrical cell.

For so-called homogeneous Rayleigh–Bénard convection (Lohse and Toschi, 2003, Calzavarini *et al.*, 2005) – thermal convection with horizontally periodic boundary conditions as well as periodic boundary conditions in vertical direction together with an imposed temperature gradient driving the flow – we would expect quite different behavior as such a system does not have boundary layers, but represents pure bulk turbulence. Furthermore, the statistics do not depend on the spatial coordinates and the phase space becomes one-dimensional, which is fundamentally different from the three cases considered in the present part of this thesis. The analysis of homogeneous Rayleigh–Bénard convection would actually be more in line with the work by Yakhot (1989) and Ching (1993), who analyze with the help of conditional averages the PDF of experimental time series obtained from temperature probe measurements. In these works, in a sense the phase space is also one-dimensional due to the lack of any spatial coordinate. Thus, while their ansatz can be used to e. g. describe the transition from soft to hard turbulence, no information about the dynamics and spatial structures can be obtained from the statistics, contrary to the method we proposed here.

Part II

Optimal Modes of Heat Transport Obtained by Proper Orthogonal Decomposition

Coherent structures play a key role in Rayleigh–Bénard convection. Although turbulence is characterized by many different length scales that fluctuate on different time scales, still patterns like a stable large-scale circulation or plumes emerge from convective flows. These building blocks of convective turbulence are what we think of as *coherent structures*.

The above-mentioned examples for coherent structures are readily conceivable – one can easily make out the main structures that form the convective flows in the pictures of the introductory chapter of this thesis (e. g., the plumes and large-scale circulations in figures 1.1 and 1.2 on pages 2 and 3). But how can one formalize this detection of structures that seem evident to the naked eye? And can one also identify a cascade of subsequent *higher-order* structures that build turbulent flows in a *top-down* fashion, starting from the large-scale structures and going down to finer and finer turbulent filaments?

To this end, we apply a technique known as *proper orthogonal decomposition* (POD). Given an ensemble of flow fields, this methods yields a set of empirical spatial modes that give the *best* approximation of the system. Here, “best” means that the modes are optimal in capturing the energy. Also, the modes may be ordered by the energy that they contain. Our new ansatz is then to extend this well-known technique so that the modes give the best approximation of the heat transport instead of the energy, as this is the more relevant quantity in Rayleigh–Bénard convection.

This part of the thesis is structured as follows: After introducing the idea behind POD at a low-dimensional example in chapter 6, we give an overview of the mathematics behind this procedure in chapter 7 and express the methods in a way that is most suited to the application we are aiming for – namely, the POD of high-dimensional turbulent convection data, as shown in chapter 8. Chapter 9 introduces our new ansatz that can optimally describe the heat transport of the system, which is then used in a lower-dimensional statistical analysis of convective flows.

The contents of the present part have been published in a modified form in Lülff (2015). The publication was produced after this part of the thesis has been written and contains additional analysis not presented here.

6 Introductory Example – The Idea Behind POD

When applying *proper orthogonal decomposition*[1], one seeks a set of modes or basis vectors that characterize the essentials of a data set better than any other basis. A transformation of the data set into the basis of POD modes gives then a more insightful representation of the ensemble. Before presenting a more mathematically sound description in chapter 7 (where also a formal definition of the colloquial terms *better*, *optimally* etc. is given), we explain the idea behind POD at a low-dimensional example.

In figure 6.1 (left), a two-dimensional data set is shown, with blue circles representing ensemble members. The data set consists of random samples from a bivariate Gaussian distribution. Since the covariance matrix has off-diagonal elements, the cloud of data points is not rotationally symmetric but skewed; also, the data has an anisotropic standard deviation, resulting in a rotated ellipsoidal form. The right graph of figure 6.1 shows the same data transformed into the POD basis. Here, the cloud of data points is rotationally symmetric and has the same standard deviation in all directions; thus, the POD basis allows for a *better* description of the data.

The calculation of the POD modes and the subsequent transformation between data basis (left graph) and POD basis (right graph) is done as follows: First, the 2×2 covariance matrix of the data set is estimated.[2] In the next step, the two eigenvalues and corresponding eigenvectors of the covariance matrix are calculated. The eigenvectors can be thought of as the principal axes of the data set (hence the alternative name *principal component analysis*), while the eigenvalues give the variance of the data in the corresponding directions. In the left graph of figure 6.1, the two brown arrows show the eigenvectors, with their lengths scaled to be the corresponding standard deviation (i. e., square root of eigenvalue). Thus, the brown arrows give a visual representation of the principal axes of the data and its

---

[1] Proper orthogonal decomposition goes under many names, depending on the field of study, e. g. *principal component analysis* in signal processing (Pearson, 1901), *Karhunen–Loève transformation* (stochastic processes (Karhunen, 1946, Loève, 1945)) or *singular value decomposition* in linear algebra. We denote it as *proper orthogonal decomposition (POD)* since this is the preferred term in fluid dynamics and mechanical engineering.

[2] In our example, it is know *a priori* due to the generation of the random sample, but in general it has to be computed from the data.

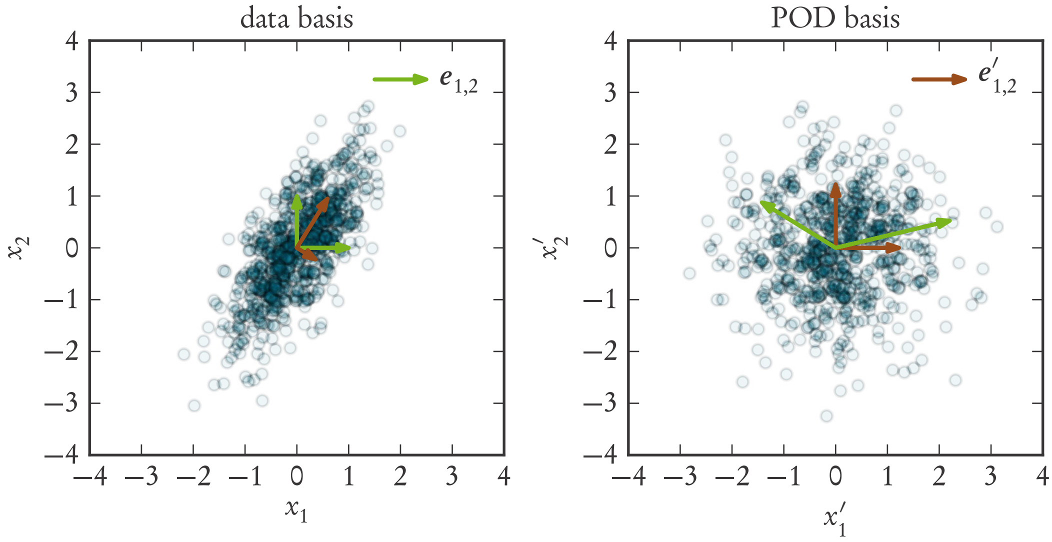

Figure 6.1: *Proper orthogonal decomposition in two dimensions. Both plots show the same random samples following a bivariate Gaussian distribution with covariance matrix* $\begin{pmatrix} 1/2 & 1/2 \\ 1/2 & 1 \end{pmatrix}$ *and zero mean. Green arrows show basis vectors of the data (i. e.,* canonical*) basis, brown arrows show basis vectors of the POD basis.*

extend along these axes. The green arrows show the canonical basis vectors $\boldsymbol{e}_1$ and $\boldsymbol{e}_2$ of the data basis.

In this example, the brown arrows are the POD modes of the data set. In order to describe the data in the POD basis, one has to find a linear transformation that converts the POD modes into unit vectors $\boldsymbol{e}'_1$ and $\boldsymbol{e}'_2$. This suggests that the transformation is readily found as the inverse of the matrix that contains the eigenvectors as columns, followed by dividing each row of the matrix by the square root of the eigenvalues. To put it in other words, the transformation consists of a rotation followed by a rescaling to unit variance (i. e., unit standard deviation). One can easily imagine how this transforms the green and brown arrows between left and right graph of figure 6.1.

When the transformation is applied to each member of the data set, the data is transformed into the POD basis. In this basis, the data distribution becomes symmetric, and the covariance matrix is now the 2 × 2 identity matrix. Thus, proper orthogonal decomposition gives an easier and more convenient view of the data.

7 Mathematical Description of POD

For the low-dimensional introductory example from the prior chapter, the ensemble members of the data set were two-dimensional points, and also the POD modes were vectors in two dimensions. Since we want to use proper orthogonal decomposition to analyze the spatial modes of Rayleigh–Bénard convection, where a single ensemble member is represented by a volumetric snapshot of the temperature and flow fields, we will now give a mathematically rigor description of the method that can also be applied to high- or even *infinite*-dimensional modes. For a more in-depth reading, the interested reader is referred to the textbook literature (see, e. g., Holmes *et al.* (1996, chap. 3)) or to Smith *et al.* (2005) for a tutorial-like introduction into the topic aimed at an application to fluid dynamics. Authors that use POD to analyze Rayleigh–Bénard convection include Lumley and Poje (1997), Bailon-Cuba *et al.* (2010) and Bailon-Cuba and Schumacher (2011).

7.1 Formulation as Variational Principle

In this section, we will describe how to calculate POD modes from a data ensemble of scalar functions $\{q(x)\}$. The proper orthogonal decomposition then gives a set of basis functions $\{\phi(x)\}$ of the data ensemble. To keep the description as general as possible, we allow the scalar functions to be complex valued. Also, the functions are chosen from a Hilbert space such that a scalar product

$$(f, g) := \int \mathrm{d}x\, \overline{f}(x) g(x) \tag{7.1}$$

exists that also induces an L^2-norm via $||f||^2 = (f, f)$. The overbar $\overline{\cdot}$ denotes complex conjugation.

As outlined in chapter 6, the POD modes are optimal in describing the data set. Mathematically this means that the mean projection of the data onto the POD modes is maximized:

$$\max_{\phi} \left\langle |(q, \phi)|^2 \right\rangle \tag{7.2}$$

In other words, proper orthogonal decomposition captures the most energy (i. e., squared L^2-norm) from the data set. Here, $\langle \cdot \rangle$ indicates an average over the data ensemble. While this expression strictly speaking yields only one ϕ, the remaining local maxima of (7.2) give the rest of the POD modes.[1]

Thus, the estimation of POD modes becomes a variational problem: Find a function ϕ that maximizes the functional $\left\langle |(q,\phi)|^2 \right\rangle$ under the constraint $||\phi||^2 = 1$ (since the basis should be orthonormal).[2] According to variational calculus, solutions of (7.2) obey an EULER–LAGRANGE type equation, which can be recast as an integral equation for ϕ:[3]

$$\int \mathrm{d}x' \left\langle q(x)\overline{q}(x') \right\rangle \phi(x') = \lambda \phi(x) \tag{7.3}$$

The basis modes $\phi(x)$ are therefore eigenfunctions of the (spatial) covariance function (or “matrix”) $\left\langle q(x)\overline{q}(x') \right\rangle$, and λ are the corresponding eigenvalues. Since the covariance matrix has HERMITian property, spectral theory assures that eigenfunctions are orthonormal.

The eigenvalue λ gives the mean energy of the data ensemble in ϕ-direction, which can be seen as follows: Multiplication of (7.3) by $\overline{\phi}(x)$ and integration over x gives

$$\int \mathrm{d}x \int \mathrm{d}x' \left\langle q(x)\overline{q}(x') \right\rangle \phi(x')\overline{\phi}(x) = \lambda \int \mathrm{d}x\, \phi(x)\overline{\phi}(x) \quad , \tag{7.4}$$

which after reordering and identifying scalar products reads[4]

$$\lambda \underbrace{(\phi,\phi)}_{=1} = \lambda = \left\langle |(q,\phi)|^2 \right\rangle \quad . \tag{7.5}$$

The eigenvalue λ is therefore the average squared L^2-norm (i. e., energy) of the data ensemble projected onto the corresponding ϕ-direction.

Given a data ensemble $\{q^i(x)\}$, which may contain a finite or (un)countable infinite number of member functions indexed by i, the solutions of the eigenvalue problem (7.3) give a set of orthonormal functions $\{\phi^i(x)\}$ that form a basis of the data ensemble,[5] as well as a spectrum $\{\lambda_i\}$ of corresponding energies. The representation of the data set in the POD basis is then

$$q^j(x) = \sum_k \xi_{kj} \phi^k(x) \tag{7.6}$$

---

[1] Alternatively, to obtain the other POD modes one could think of a projection approach: After obtaining the first mode through (7.2), one projects the data set onto this mode and calculates the next mode from the residuum between projection and full data set. Iterating this step gives all POD modes.

[2] In the literature, this is often summarized as $\max\limits_{\phi} \frac{\left\langle |(q,\phi)|^2 \right\rangle}{||\phi||^2}$.

[3] For a detailed presentation, see section B.1 or HOLMES *et al.* (1996, sec. 3.1).

[4] It is assumed that the ensemble average commutes with the spatial integration.

[5] Or, to be more precise, a basis of the linear hull of the data ensemble.

with amplitudes ξ_{ij} that may be obtained by scalar multiplication with ϕ^i:

$$\xi_{ij} = \left(\phi^i, q^j\right) \tag{7.7}$$

With an uncountable POD basis, the sum in (7.6) has to be replaced by an integration over a continuous index.

According to (7.5), the mean energy contained in mode ϕ^i is given by λ_i. The mean energy contained in the whole data ensemble is $\sum_i \lambda_i$. This can be seen by inserting (7.5) and utilizing the completeness of the POD basis, i. e. $\sum_i \phi^i(x)\overline{\phi^i}(x') = \delta(x - x')$ (cf. section B.2 for a detailed calculation).

In the representation of the data in the POD basis, it is also possible to reduce the dimensionality of the data ensemble. This is done by taking only certain modes in (7.6) into account, i. e. by truncating the sum. For example, one could use only the N_p POD modes with the highest energies, thus projecting the data set onto the subspace spanned by the most energetic modes. The optimality of the POD modes assures that this projection is the *best* among all N_p-dimensional projections (in an L^2- or energetic sense).

7.2 Matrix Formulation for Discrete Numerical Data

In the application we are aiming for, the data ensemble consists of N_t member functions (or snapshots) $\{q^i(x)\}$ with $i \in \{1, \ldots, N_t\}$, which may have been obtained by sampling a dynamical system at discrete times t_i. The ensemble average then can be thought as an average over time. Also, since we want to deal with numerical or experimental data, we will not have continuous functions but vectors of N_x real or complex numbers that correspond to a finite sampling in space. These sampling points may not only be points on the real line but also come from a higher-dimensional space, so that a snapshot can e. g. represent a three-dimensional snapshot of the temperature field of a numerical simulation of convection or even a “mixed” snapshot of temperature and velocity fields. Therefore, one ensemble member is now a vector $\boldsymbol{q}^i \in \mathbb{C}^{N_x}$, and the scalar product between two vectors $\boldsymbol{v}$ and $\boldsymbol{w}$ reads

$$(\boldsymbol{v}, \boldsymbol{w}) = \boldsymbol{v}^\dagger \mathbf{S} \boldsymbol{w} \quad , \tag{7.8}$$

where the row vector $\boldsymbol{v}^\dagger \in \mathbb{C}^{1\times N_x}$ is the conjugate transpose of the column vector $\boldsymbol{v} \in \mathbb{C}^{N_x(\times 1)}$. The matrix $\mathbf{S} \in \mathbb{C}^{N_x \times N_x}$ induces the scalar product of two snapshots. The simplest case would be $\mathbf{S} = \frac{1}{N_x}\mathbb{1}$ for an equidistant discretization of the scalar product (7.1);[6] likewise, by choosing $\mathbf{S}$ as a diagonal matrix with appropriate weights on the diagonal, one could account for a non-equidistant spatial sampling of the snapshots (e. g., the cylindrical grid used in section 4.3). In general though, **S** could be any positive definite Hermitian matrix, which would induce an arbitrary spatial scalar product.

---

[6] Here and likewise from now on, $\mathbb{1}$ is the identity matrix of appropriate size. Whenever its size is unclear from the context, it will be given as a subscript, e. g. in this case $\mathbb{1}_{N_x \times N_x}$. The same applies to the zero matrix $\mathbb{0}_{n\times n}$, which may also be rectangular ($\mathbb{0}_{n\times m}$).

The whole ensemble of N_t snapshots is assembled as columns in the data matrix

$$\mathbf{X} = \left(\boldsymbol{q}^1 \boldsymbol{q}^2 \cdots \boldsymbol{q}^{N_t}\right) = \begin{pmatrix} q_1^1 & \cdots & q_1^{N_t} \\ \vdots & \ddots & \vdots \\ q_{N_x}^1 & \cdots & q_{N_x}^{N_t} \end{pmatrix} \in \mathbb{C}^{N_x \times N_t} \quad . \tag{7.9}$$

In the rightmost "full" matrix representation, upper indices are temporal and lower indices are spatial ones. This matrix representation is especially useful, because it allows for a compact notation of operations on the whole data set.

We will now show what the steps to obtain the POD modes from the prior section look like when performed for discrete numerical data: Calculating the spatial covariance matrix means correlating all pairs of grid points and averaging over time; in a matrix representation of the data ensemble, one can easily see that

$$\mathbf{XTX}^\dagger = \begin{pmatrix} q_1^1 & \cdots & q_1^{N_t} \\ \vdots & \ddots & \vdots \\ q_{N_x}^1 & \cdots & q_{N_x}^{N_t} \end{pmatrix} \begin{pmatrix} \beta_1 & & \\ & \ddots & \\ & & \beta_{N_t} \end{pmatrix} \begin{pmatrix} \overline{q}_1^1 & \cdots & \overline{q}_{N_x}^1 \\ \vdots & \ddots & \vdots \\ \overline{q}_1^{N_t} & \cdots & \overline{q}_{N_x}^{N_t} \end{pmatrix} \in \mathbb{C}^{N_x \times N_x} \tag{7.10}$$

is the discretized version of the covariance matrix $\left\langle q(x)\overline{q}(x')\right\rangle$ from (7.3). Similar to the matrix **S** before, the matrix $\mathbf{T} \in \mathbb{C}^{N_t \times N_t}$ is the diagonal matrix that contains the temporal weights β_i of the snapshots $\boldsymbol{q}^i$. In the most simple cases, e. g. for equidistant sampling in time or uncorrelated snapshots, it would be $\frac{1}{N_t}\mathbb{1}$, but again, any positive definite Hermitian matrix could be used, corresponding to an arbitrary temporal scalar product.

The eigenvalue equation (7.3) in a discrete formulation then reads

$$\mathbf{XTX}^\dagger \mathbf{S} \boldsymbol{\phi}^i = \lambda_i \boldsymbol{\phi}^i \tag{7.11}$$

for one pair of eigenvector and eigenvalue, where the matrix **S** accounts for the spatial weights of the integral (i. e., the scalar product) in (7.3).[7] More compact, the eigenvalue problem (7.11) reads

$$\mathbf{XTX}^\dagger \mathbf{S} \mathbf{\Phi} = \mathbf{\Phi\Lambda} \tag{7.12}$$

---

[7] In general, **S** performs the spatial scalar product between the covariance matrix $\mathbf{XTX}^\dagger \in \mathbb{C}^{N_x \times N_x}$ and the eigenvector $\boldsymbol{\phi}^i \in \mathbb{C}^{N_x}$, cf. Rowley *et al.* (2004) or Rowley (2001, sec. 4.1).

with the matrix

$$\mathbf{\Phi} = \left(\boldsymbol{\phi}^1 \ldots \boldsymbol{\phi}^{N_x} \right) \in \mathbb{C}^{N_x \times N_x} \tag{7.13}$$

containing the POD modes as columns and

$$\mathbf{\Lambda} = \operatorname{diag}(\lambda_1, \ldots, \lambda_{N_x}) \in \mathbb{R}^{N_x \times N_x} \tag{7.14}$$

as the diagonal matrix that contains the corresponding eigenvalues.

It is crucial that the matrix $\mathbf{A} = \mathbf{XTX}^\dagger\mathbf{S}$ is self-adjoint with respect to the scalar product (7.8) induced by $\mathbf{S}$:

$$(\mathbf{A}\boldsymbol{v}, \boldsymbol{w}) = (\mathbf{A}\boldsymbol{v})^\dagger \mathbf{S}\boldsymbol{w} \tag{7.15a}$$

$$= \boldsymbol{v}^\dagger \mathbf{A}^\dagger \mathbf{S}\boldsymbol{w} \tag{7.15b}$$

$$= \boldsymbol{v}^\dagger \mathbf{S}^\dagger \mathbf{X}\mathbf{T}^\dagger \mathbf{X}^\dagger \mathbf{S}\boldsymbol{w} \tag{7.15c}$$

$$= \boldsymbol{v}^\dagger \mathbf{SXTX}^\dagger \mathbf{S}\boldsymbol{w} \quad (\mathbf{S}, \mathbf{T} \text{ are } \textsc{Hermitian}) \tag{7.15d}$$

$$= \boldsymbol{v}^\dagger \mathbf{SA}\boldsymbol{w} \tag{7.15e}$$

$$= (\boldsymbol{v}, \mathbf{A}\boldsymbol{w}) \tag{7.15f}$$

Thus, the eigenvectors $\mathbf{\Phi}$ can be chosen to be orthonormal with respect to the same scalar product:[8]

$$\mathbf{\Phi}^\dagger \mathbf{S} \mathbf{\Phi} = \mathbb{1} \tag{7.16}$$

Therefore, the solution $\mathbf{\Phi}$ of (7.12) gives N_x orthonormal vectors, which form a basis of the data ensemble (i. e., a basis of $\mathbb{C}^{N_x}$).[9] Also, the eigenvalues λ_i are real and non-negative, cf. section B.3, so that the interpretation of the eigenvalues as energies or L^2-norms holds.

For a finite data set, the transformation of the data into the POD basis, i. e. (7.6)–(7.7), reads

$$\mathbf{X} = \mathbf{\Phi}\mathbf{\Xi} \quad , \tag{7.17}$$

with the amplitudes

$$\mathbf{\Xi} = \begin{pmatrix} \xi_{11} & \cdots & \xi_{1N_t} \\ \vdots & \ddots & \vdots \\ \xi_{N_x 1} & \cdots & \xi_{N_x N_t} \end{pmatrix} \in \mathbb{C}^{N_x \times N_t} \quad . \tag{7.18}$$

---

[8] In the numerical implementation, this has to be ensured by hand *a posteriori* (i. e., by dividing every column of $\mathbf{\Phi}$ by its norm), as the eigenproblem algorithm does not know about the matrix $\mathbf{S}$, but only “sees” the whole matrix $\mathbf{XTX}^\dagger\mathbf{S}$.

[9] At least for well-behaved matrices, i. e. when the matrix $\mathbf{XTX}^\dagger\mathbf{S}$ has full rank or, equivalently, if all eigenvalues are non-zero; also cf. section 7.4.

Here, ξ_{ij} gives the contribution of POD mode $\boldsymbol{\phi}^i$ to snapshot $\boldsymbol{q}^j$; accordingly, the i-th row of Ξ is the time series of mode $\boldsymbol{\phi}^i$, and the j-th column represents the partition of snapshot $\boldsymbol{q}^j$. Multiplying (7.17) from the left with $\boldsymbol{\Phi}^\dagger\mathbf{S}$ gives the calculation of the amplitudes as

$$\Xi = \boldsymbol{\Phi}^\dagger\mathbf{S}\mathbf{X} \tag{7.19}$$

which is the discretized version of (7.7). The following verification shows that the transformation of the data into the POD basis is exact:[10]

$$\begin{aligned}\mathbf{X} &= \boldsymbol{\Phi}\Xi && (7.20\text{a})\\ &= \underbrace{\boldsymbol{\Phi}\boldsymbol{\Phi}^\dagger\mathbf{S}}_{=\boldsymbol{\Phi}^\dagger\mathbf{S}\boldsymbol{\Phi}=\mathbb{1}}\ \mathbf{X} && (7.20\text{b})\\ &= \mathbf{X} && (7.20\text{c})\end{aligned}$$

With this matrix formulation of the relevant equations (sometimes referred to as the *direct method*), it is easy to calculate the POD modes and corresponding energies from a numerical data set (equation (7.12)) and also obtain the time series or amplitudes that reconstruct the data set in the basis of the POD modes (equation (7.19)).

7.3 Method of Snapshots

Although the direct method to obtain POD modes described in the previous section is exact, it may be infeasible in practice. The reason is that in fluid dynamics, the number of grid points is usually much higher than the number of snapshots in a data set. For example, the data sets of three-dimensional turbulent convection used in part I consist of $N_t = \mathcal{O}(10^3)$ snapshots, while the number of grid points is roughly $N_x = \mathcal{O}(10^8)$. Thus, the spatial covariance matrix has $\mathcal{O}(10^{16})$ entries, which means it is far too big to be handled numerically.[11]

As a solution, SIROVICH (1987a) suggested the *method of snapshots* to deal with data sets where there are more grid points than snapshots. This ansatz boils down to calculating the $N_t \times N_t$ temporal instead of the $N_x \times N_x$ spatial covariance matrix, which is favorable when $N_t \ll N_x$. In the following, we will outline this method.

We want the method of snapshots to give essentially the same POD modes $\boldsymbol{\phi}^i$ and eigenvalue spectrum λ_i as the direct method, but avoid the calculation of the spatial covariance matrix $\mathbf{XTX}^\dagger$. So the goal is to obtain $\mathbf{\Phi}$ and $\mathbf{\Lambda}$ from the temporal covariance matrix

---

[10] The identity $\boldsymbol{\Phi}\boldsymbol{\Phi}^\dagger\mathbf{S} = \boldsymbol{\Phi}^\dagger\mathbf{S}\boldsymbol{\Phi}$ in (7.20b) holds because for square matrices $\mathbf{A}$ and $\mathbf{B}$, the relation $\mathbf{A}\mathbf{B} = \mathbb{1}$ implies $\mathbf{B} = \mathbf{A}^{-1}$, and thus $\mathbf{A}\mathbf{B} = \mathbf{B}\mathbf{A}$ because an invertible matrix commutes with its inverse.

[11] As an example, the spatial covariance matrix of the data set from section 4.1 would consume $\mathcal{O}(2^{52})$ bytes, which would be roughly 4.5 petabytes.

$$\mathbf{X}^\dagger\mathbf{SX} \in \mathbb{C}^{N_t \times N_t} \quad , \tag{7.21}$$

where the entry $(\mathbf{X}^\dagger\mathbf{SX})_{i,j}$ gives the spatially averaged correlation of snapshots $\boldsymbol{q}^i$ and $\boldsymbol{q}^j$.

The eigenvalue problem of the temporal covariance matrix reads

$$\mathbf{X}^\dagger\mathbf{SXT}\boldsymbol{c}^i = \lambda_i \boldsymbol{c}^i \quad \text{or} \quad \mathbf{X}^\dagger\mathbf{SXTC} = \mathbf{C\Lambda} \tag{7.22}$$

with eigenvectors $\boldsymbol{c}^i \in \mathbb{C}^{N_t}$ respectively $\mathbf{C} \in \mathbb{C}^{N_t \times N_t}$ and eigenvalues $\mathbf{\Lambda} \in \mathbb{R}^{N_t \times N_t}$. Similar to (7.11), the matrix $\mathbf{T}$ here accounts for the temporal weights of the snapshots. A calculation analogous to (7.15) shows that $\mathbf{X}^\dagger\mathbf{SXT}$ is self-adjoint with respect to the scalar product induced by $\mathbf{T}$, which implies that the eigenvectors $\mathbf{C}$ are orthonormal under the same scalar product:[12]

$$\mathbf{C}^\dagger\mathbf{TC} = \mathbb{1} \tag{7.23}$$

Also, it has to be stressed that the matrices $\mathbf{X}^\dagger\mathbf{SXT} = (\mathbf{X}^\dagger\mathbf{S})(\mathbf{XT})$ and $\mathbf{XTX}^\dagger\mathbf{S} = (\mathbf{XT})(\mathbf{X}^\dagger\mathbf{S})$ share the same non-zero eigenvalues, which is a general result for the eigenvalues of matrix products (cf. section B.4); therefore the eigenvalues obtained by the direct method (7.12) and by the method of snapshots (7.22) were both denoted by $\mathbf{\Lambda}$.

To relate the eigenvectors $\mathbf{C}$ to the desired POD modes $\mathbf{\Phi}$, we multiply the eigenvalue problem (7.22) of the spatial covariance matrix from the left with $\mathbf{XT}$ and with $\mathbf{\Lambda}^{-1/2}$ from the right[13]:

$$\mathbf{XTX}^\dagger\mathbf{SXTC\Lambda}^{-1/2} = \mathbf{XTC\Lambda\Lambda}^{-1/2} \tag{7.24a}$$

$$= \mathbf{XTC\Lambda}^{-1/2}\mathbf{\Lambda} \tag{7.24b}$$

$$\Rightarrow \quad \mathbf{XTX}^\dagger\mathbf{S\Phi} = \mathbf{\Phi\Lambda} \tag{7.24c}$$

In the last step, we arrived at the direct method (7.12) by identifying the POD modes as

$$\mathbf{\Phi} = \mathbf{XTC\Lambda}^{-1/2} \quad . \tag{7.25}$$

Indeed, it is readily seen that this choice assures orthonormal POD modes:

$$\mathbf{\Phi}^\dagger\mathbf{S\Phi} = \mathbf{\Lambda}^{-1/2}\mathbf{C}^\dagger\mathbf{T}^\dagger \underbrace{\mathbf{X}^\dagger\mathbf{SXTC}}_{=\mathbf{C\Lambda}} \mathbf{\Lambda}^{-1/2} \tag{7.26a}$$

$$= \mathbf{\Lambda}^{-1/2} \underbrace{\mathbf{C}^\dagger\mathbf{T}^\dagger\mathbf{C}}_{=\mathbf{C}^\dagger\mathbf{TC}=\mathbb{1}} \mathbf{\Lambda\Lambda}^{-1/2} \tag{7.26b}$$

$$= \mathbb{1} \tag{7.26c}$$

---

[12] Also see footnote 8 on page 51 regarding the normalization of the eigenvectors $\mathbf{C}$.

[13] The matrix $\mathbf{\Lambda}^{-1/2}$ can be calculated trivially because $\mathbf{\Lambda}$ is diagonal with strictly positive diagonal entries (for the well-behaved case).

Equation (7.25) states that the POD modes $\mathbf{\Phi}$ are expressed as a linear combination (determined in large part by $\mathbf{C}$) of the data snapshots $\mathbf{X}$.[14] Therefore, the POD modes inherit any linear constraints that the snapshots have, e. g. boundary conditions or incompressibility, cf. ROWLEY (2001, sec. 4.1).

Contrary to the direct method, the matrix $\mathbf{\Phi} \in \mathbb{C}^{N_x \times N_t}$ contains only N_t POD modes, which is the most one can expect from a data set that consists of N_t snapshots (also in an information-theoretical sense). Thus, the POD modes $\mathbf{\Phi}$ do not span the full $\mathbb{C}^{N_x}$ but only the linear hull of the data set. Of course, the more linearly independent snapshots are used, the bigger the space spanned by the POD modes becomes.

The transformation of the data set $\mathbf{X}$ into the POD basis $\mathbf{\Phi}$ in principle looks alike to the direct method, i. e. $\mathbf{X} = \mathbf{\Phi}\mathbf{\Xi}$ with the amplitudes $\mathbf{\Xi} = \mathbf{\Phi}^\dagger\mathbf{S}\mathbf{X} \in \mathbb{C}^{N_t \times N_t}$. One can avoid the calculations involving the big $N_x \times N_t$ matrices $\mathbf{\Phi}$ and $\mathbf{X}$, though:

$$\mathbf{\Xi} = \mathbf{\Phi}^\dagger\mathbf{S}\mathbf{X} \tag{7.27a}$$

$$= \mathbf{\Lambda}^{-1/2}\underbrace{\mathbf{C}^\dagger\mathbf{T}^\dagger\mathbf{X}^\dagger\mathbf{S}\mathbf{X}}_{=(\mathbf{C}\mathbf{\Lambda})^\dagger} \tag{7.27b}$$

$$= \mathbf{\Lambda}^{1/2}\mathbf{C}^\dagger \tag{7.27c}$$

The amplitudes can therefore be obtained in passing because they are calculated from small $N_t \times N_t$ matrices that are available anyhow. As in the direct method, one can verify the transformation of the data into the POD basis as follows:[15]

$$\mathbf{X} = \mathbf{\Phi}\mathbf{\Xi} \tag{7.28a}$$

$$= \mathbf{X}\mathbf{T}\mathbf{C}\mathbf{\Lambda}^{-1/2}\mathbf{\Lambda}^{1/2}\mathbf{C}^\dagger \tag{7.28b}$$

$$= \mathbf{X}\underbrace{\mathbf{T}\mathbf{C}\mathbf{C}^\dagger}_{=\mathbf{C}^\dagger\mathbf{T}\mathbf{C}=\mathbb{1}} \tag{7.28c}$$

$$= \mathbf{X} \tag{7.28d}$$

In the method of snapshots, the matrices of the eigenvalue problem have only N_t rows and columns, so the eigenvalue problem can readily be solved numerically. The computation of the covariance matrix $\mathbf{X}^\dagger\mathbf{S}\mathbf{X}$ is now possible, contrary to the direct method for $N_x \gg N_t$.[16]

---

[14] In fact, most authors begin the derivation of the method of snapshots by inserting a linear combination of the snapshots into the direct method.

[15] For the justification of the relation $\mathbf{T}\mathbf{C}\mathbf{C}^\dagger = \mathbf{C}^\dagger\mathbf{T}\mathbf{C}$ in (7.28c), see footnote 10 on page 52.

[16] Though the calculation is possible *per se*, it is still computationally challenging; comments on this are given in section B.5.

7.4 Direct Method or Method of Snapshots?

As mentioned before, the spatial covariance matrix of the direct method and the temporal covariance matrix of the method of snapshots have the same number of non-zero eigenvalues and thus the same rank. This means that the same number of energy-containing eigenvectors and thus the same number of POD modes $\boldsymbol{\phi}^i$ can be obtained with both methods. Thus, in general one will choose the method that leads to smaller matrices and is computationally more feasible, i. e. the method of snapshots whenever $N_x > N_t$, as is the case here.

The rank of the temporal covariance matrix of the method of snapshots can be estimated as

$$N_t \geq \operatorname{rank}(\mathbf{X}^\dagger \mathbf{S} \mathbf{X} \mathbf{T}) = \min(\operatorname{rank}\mathbf{X}, \operatorname{rank}\mathbf{T}) \quad , \tag{7.29}$$

assuming that $\mathbf{S}$ has full rank with $\operatorname{rank}\mathbf{S} > \operatorname{rank}\mathbf{T}$. Because $\operatorname{rank}\mathbf{X} \leq N_t$ and $\operatorname{rank}\mathbf{T} \leq N_t$, the covariance matrix has full rank N_t whenever $\mathbf{X}$ and $\mathbf{T}$ have full rank, i. e. when all snapshots $\boldsymbol{q}^i$ in $\mathbf{X}$ are linearly independent and all temporal weights are non-vanishing[17]. If this should not be the case, the corresponding snapshots can simply be omitted from the data set, thus assuring that all matrices have full rank. This reasoning also justifies why we could assume well-behaved matrices earlier on.

A similar reasoning can also be applied to the direct method: If either $\mathbf{X}$ or $\mathbf{S}$ is rank deficient, i. e. has rank smaller than N_x, then either some spatial dimensions of the data set are not linearly independent (e. g., the data set consists of snapshots of the form $\boldsymbol{q}^i = (x, y, 2y)^{\mathrm{T}} \in \mathbb{R}^3$), or some dimensions are given zero weights by the scalar product $\mathbf{S}$. In both cases the respective dimensions can be omitted from the data set, which results in matrices with full rank.

7.5 Lower-Dimensional Projection

The transformation of the data set into the POD basis is an exact relation, as shown in (7.20) and (7.28). But the POD basis can also be used to obtain a lower-dimensional projection of the data-set, i. e. by projecting only onto a range of POD modes. Since the ordering of the single POD modes in $\boldsymbol{\Phi}$ (and the corresponding ordering of eigenvalues in $\boldsymbol{\Lambda}$) is arbitrary, we will assume that the data set should be projected onto the first N_p modes.[18]

---

[17] Strictly speaking, this is already guaranteed by the positive definiteness of $\mathbf{T}$.

[18] Usually the modes are sorted by descending eigenvalues, which means the first N_p modes are the most energetic ones.

7.5.1 Direct Method

We want to obtain the matrix $\widetilde{\mathbf{\Phi}}$ that contains only the first N_p modes of $\mathbf{\Phi}$. This is formally achieved by multiplication with an appropriate matrix $\mathbf{R}^{N_p} \in \mathbb{R}^{N_x \times N_p}$ that retains only the first N_p columns of $\mathbf{\Phi}$:

$$\begin{aligned} \widetilde{\mathbf{\Phi}} &= \mathbf{\Phi}\mathbf{R}^{N_p} && (7.30a)\\ &:= \mathbf{\Phi} \begin{pmatrix} \mathbb{1}_{N_p \times N_p} \\ \mathbb{0}_{(N_x - N_p) \times N_p} \end{pmatrix} \in \mathbb{C}^{N_x \times N_p} && (7.30b) \end{aligned}$$

With this matrix and (7.20), the projected data set reads

$$\begin{aligned} \widetilde{\mathbf{X}} &= \widetilde{\mathbf{\Phi}}\widetilde{\mathbf{\Phi}}^{\dagger}\mathbf{S}\mathbf{X} && (7.31a)\\ &=: \mathbf{P}_d \mathbf{X} \quad . && (7.31b) \end{aligned}$$

Thus, in the direct method the projected data set $\widetilde{\mathbf{X}}$ is easily obtained by left-multiplying the full data set $\mathbf{X}$ with the projection matrix $\mathbf{P}_d = \widetilde{\mathbf{\Phi}}\widetilde{\mathbf{\Phi}}^{\dagger}\mathbf{S} \in \mathbb{C}^{N_x \times N_x}$, which is constructed from the first N_p POD modes. A simple calculation shows that $\mathbf{P}_d$ fulfills the required idempotence $\mathbf{P}_d^2 = \mathbf{P}_d$ of a projection.

The action of the projection matrix and its different constituents

$$\begin{aligned} \mathbf{P}_d\mathbf{X} &= \widetilde{\mathbf{\Phi}}\widetilde{\mathbf{\Phi}}^{\dagger}\mathbf{S}\mathbf{X} && (7.32a)\\ &= \underbrace{\mathbf{\Phi}}_{\text{IV}}\ \underbrace{\mathbf{R}^{N_p}\left(\mathbf{R}^{N_p}\right)^{\dagger}}_{\text{III}}\ \underbrace{\mathbf{\Phi}^{\dagger}}_{\text{II}}\ \underbrace{\mathbf{S}}_{\text{I}}\ \mathbf{X} && (7.32b) \end{aligned}$$

can intuitively be interpreted as a weighting of the spatial dimensions (I) followed by a rotation into the POD basis (II). In this basis the data is projected onto an N_p-dimensional subspace (III) and then rotated back into the original basis (IV).

7.5.2 Method of Snapshots

In the method of snapshots, the subset $\widetilde{\mathbf{\Phi}}$ of POD modes (cf. (7.25)) is obtained by keeping only the first N_p eigenvalues in $\mathbf{\Lambda}$ and correspondingly the first N_p columns in $\mathbf{C}$ (this is achieved in the same way as before, i. e. by $\widetilde{\mathbf{C}} = \mathbf{C}\mathbf{R}^{N_p}$). Therefore, the projected data set in the method of snapshots reads

$$\begin{aligned} \widetilde{\mathbf{X}} &= \mathbf{X}\mathbf{T}\widetilde{\mathbf{C}}\widetilde{\mathbf{C}}^{\dagger} && (7.33a)\\ &=: \mathbf{X}\mathbf{P}_s \quad , && (7.33b) \end{aligned}$$

cf. (7.28). Again, the projection is readily obtained by right-multiplying $\mathbf{X}$ with the projection matrix $\mathbf{P}_s = \mathbf{T}\widetilde{\mathbf{C}}\widetilde{\mathbf{C}}^\dagger \in \mathbb{C}^{N_t \times N_t}$ (with $\mathbf{P}_s^2 = \mathbf{P}_s$). The projected snapshots therefore are linear combinations of the initial snapshots, and so they obey the same linear constraints, as discussed in section 7.3.

It has to be stressed that for the projection in the method of snapshots, the actual POD basis (which is a big $N_x \times N_t$ matrix) does not have to be calculated explicitly: The projection can instead be achieved by utilizing rather small $N_t \times N_t$ matrices that are already available (i. e., $\mathbf{T}$ and $\mathbf{C}$).

7.5.3 Quantifying the Quality of the Projection

In both methods, it can be shown that the residuum between full and projected data set is related to the eigenvalues. To this end, we observe that the weighted Frobenius norm of $\mathbf{X}$ may be defined as the temporal average of the norm of every snapshot, i. e.

$$||\mathbf{X}||_{\mathrm{F}}^2 = \sum_{i=1}^{N_t} ||\boldsymbol{q}^i||^2 \beta_i = \sum_{i=1}^{N_t} \left(\boldsymbol{q}^i\right)^\dagger \mathbf{S} \boldsymbol{q}^i \beta_i \tag{7.34a}$$

$$= \mathrm{tr}(\mathbf{X}^\dagger \mathbf{S} \mathbf{X} \mathbf{T}) = \sum_{i=1}^{N_t} \lambda_i \tag{7.34b}$$

for the method of snapshots,[19] which means that the squared Frobenius norm is the mean energy of the data set (cf. section B.2).

By utilizing the invariance of the trace under cyclic permutations and inserting the definition of $\widetilde{\mathbf{X}}$, one can easily find that

$$||\widetilde{\mathbf{X}}||_{\mathrm{F}}^2 = \sum_{i=1}^{N_p} \lambda_i \quad , \tag{7.35}$$

which is reasonable: Since $\widetilde{\mathbf{X}}$ is the data set projected onto N_p modes, it should also contain only the energy represented by these modes. Reversely, this means that the norm of the residuum between projected and full data set is given by the energy contained in the POD modes that are removed from the system:

$$||\mathbf{X} - \widetilde{\mathbf{X}}||_{\mathrm{F}}^2 = \sum_{i=N_p+1}^{N_t} \lambda_i \tag{7.36}$$

With these relations, one can easily quantify the quality of the projection by examining the eigenvalues (instead of, e. g., directly calculating norms of the full data set).

---

[19] The same is found for the direct method because $\mathbf{X}^\dagger \mathbf{S} \mathbf{X} \mathbf{T}$ and $\mathbf{X} \mathbf{T} \mathbf{X}^\dagger \mathbf{S}$ have the same non-zero eigenvalues and the trace is cyclic.

It has to be stressed, though, that the eigenvalues relate to the *overall* quality of the projection; however, the lower-dimensional projection of a *single* snapshot cannot be assessed from the eigenvalues alone. Indeed, the projection quality of a certain snapshot may be significantly worse than the overall quality, e. g. when one snapshot differs strongly from all the others.

7.6 Summary of Mathematical Description

In this section, we gave an introduction into the mathematics behind proper orthogonal decomposition. We outlined the direct method and the method of snapshots, the latter being preferred when the spatial dimension is bigger than the temporal dimension. Both methods are deeply connected with the eigenvalue problem of the covariance matrix of the data ensemble, i. e. the correlation between two spatial dimensions for the direct method and the correlation between two snapshots in time for the method of snapshots. We gave the formulas to obtain a set of orthonormal POD modes in a concise form, and also showed the easiest ways to perform a transformation into this basis or a projection onto a number of basis vectors.

We want to emphasize, though, that POD methods are known for a long time and have become a standard tool in many fields of application; thus, we do not claim we presented any new insights in the present chapter. Instead, we tried to give an accessible formulation, that on the one hand is kept as general as possible; on the other hand, we derived all relations using matrix calculus, as this greatly simplifies the numerical implementation we are aiming for. Also, we elaborated on the estimation of time series (i. e., transformation into the POD basis) as well as on the lower-dimensional projection aspect of POD. This, as well as a rigorous matrix formulation leaned towards a numerical implementation, is understudied by most authors – at least to the knowledge of the author of these lines.

We want to finish with two closing remarks: First, we deliberately did not subtract the temporal mean from the snapshots, which would amount to an *affine-linear transformation*, as Rowley (2001, sec. 4.1.4) puts it. Though this is in principle possible, we considered it inconvenient, as then the matrix $\mathbf{X}$ would be rank deficient[20] and one eigenvalue in $\mathbf{\Lambda}$ would be zero – this would lead to problems, e. g. when calculating the matrix $\mathbf{\Lambda}^{-1/2}$ in (7.25) (cf. also section 7.4). Also the interpretation of eigenvalues and modes would become less insightful, as they would relate to the fluctuations about the mean and not directly to the flow itself.

Second, in POD analysis it is generally also possible to expand the data ensemble by utilizing symmetries, and there are techniques that allow to do so with little additional numerical cost (Sirovich and Park, 1990)[21]. We decided not to take discrete or even continuous symmetries into account, though, because this would “destroy” spatial structures that are present in convective flows: Consider for example two-dimensional convection with a stable clockwise large-scale circulation (this is actually the situation we will discuss in the next chapter). Employing the horizontal reflectional symmetry of this system would result in POD modes that do not show a large scale circulation – for every “clockwise” snapshot, the data ensemble would also contain the corresponding “anti-clockwise” snapshot due to symmetries, and their contribution would average out. Likewise, the continuous azimuthal symmetry of convection in a cylindrical vessel destroys information about the reorientation of the large-scale circulation. In other words, by taking into account the symmetries of the system one may lose information about symmetry-breaking flows that are present in the data ensemble (a similar argument is also discussed by Holmes *et al.* (1996, sec. 3.3.3) in the context of ergodicity). Therefore we decided against utilizing symmetries, although in certain situations, symmetries do make sense; the interested reader is referred to the pivotal overview provided by Sirovich (1987b).

---

[20] It can easily be seen that the mean-subtracted snapshots are not linearly independent: Since their mean is zero, we have found a linear combination that produces the null vector, which implies that the mean-subtracted snapshots are linearly dependent.

---

[21] In this reference, there are 16 possible discrete symmetries (i. e., reflections and rotations), but the numerical cost for incorporating these symmetries in the POD calculation can be as low as a factor of 2^2 instead of the factor of 16^2 one would naively assume.

8 POD of Turbulent Convection

We now will apply the methods that where outlined before to a data set of two-dimensional convection. To this end, we will compute the eigenvalue spectrum and the POD modes from the data ensemble and also examine lower-dimensional projections of the data.

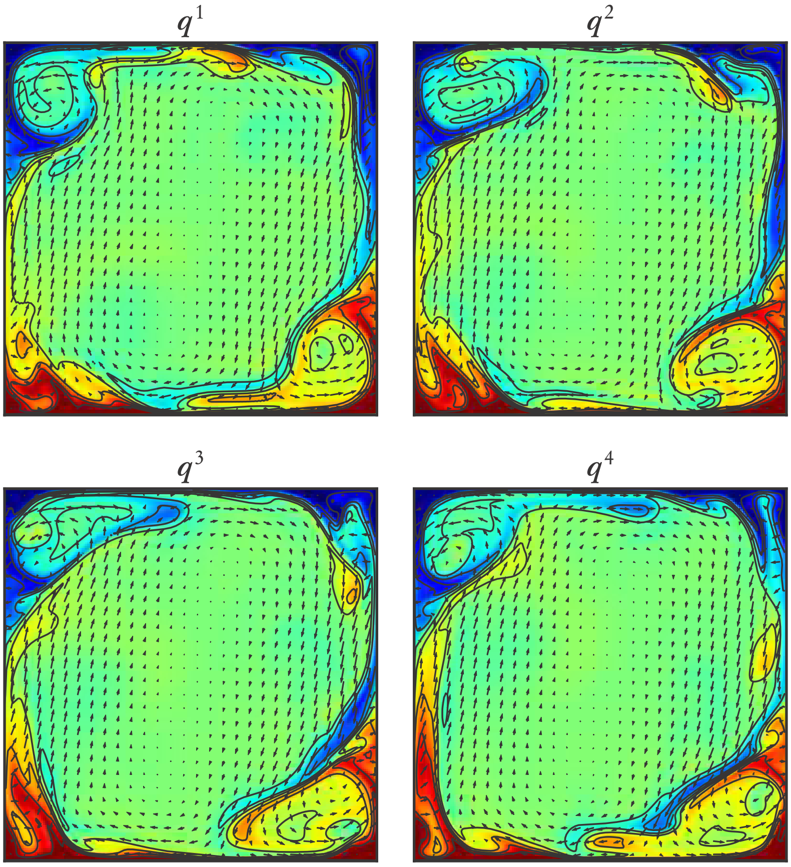

Figure 8.1: *Four subsequent snapshots of the two-dimensional data set used in this chapter. The temperature is color-coded and additionally shown with* 8 *equidistant isothermals for* $0.25 \leq T \leq 0.75$*, and the velocity field is indicated by the arrows. The axis labels and ticks have been omitted (horizontal axis:* $0 \leq x \leq 1$*, vertical axis:* $0 \leq z \leq 1$*).*

8.1 Data Set

The data set consists of 500 snapshots of the temperature field $T(\boldsymbol{x}, t_i)$ and the velocity field $\boldsymbol{u}(\boldsymbol{x}, t_i) = \binom{u_x(\boldsymbol{x},t_i)}{u_z(\boldsymbol{x},t_i)}$ of two-dimensional convection in a box with aspect ratio $\Gamma = 1$, obtained from DNS (cf. also section 4.2). The snapshots are separated by half a free-fall time unit, and the temperature and velocity fields are non-dimensionalized by the temperature difference as well as the distance of the plates and with respect to diffusive time scales. The bottom and top plate have a fixed temperature of $T = 1$ respectively $T = 0$, and the side walls are adiabatic; all walls obey no-slip conditions. RAYLEIGH and PRANDTL numbers are $\mathrm{Ra} = 1.46 \times 10^8$ and $\mathrm{Pr} = 1$.

Four consecutive snapshots of the temperature and velocity fields are shown in figure 8.1. This system forms a stable convection cell with the main turbulence occurring near the side walls and especially in the counter-rotating corner rolls. In the data ensemble there is no reversal of the large-scale circulation, in accordance with the findings of SUGIYAMA *et al.* (2010) for the parameters considered here.

The fields are each resolved with $n_x = 224 \times 224$ equidistant grid points $\boldsymbol{x}_1, \dots, \boldsymbol{x}_{n_x}$, so one snapshot would in principle be a vector consisting of all three fields sampled at the grid point, i. e. a vector with $3n_x$ entries. Since we are dealing with incompressible fluids, though, u_x is already fully determined by u_z, so we can restrict our snapshots to be vectors

$$\boldsymbol{q}^i = \left(T(\boldsymbol{x}_1, t_i), \dots, T(\boldsymbol{x}_{n_x}, t_i), u_z(\boldsymbol{x}_1, t_i), \dots, u_z(\boldsymbol{x}_{n_x}, t_i)\right)^{\mathrm{T}} \in \mathbb{R}^{2n_x} \quad . \tag{8.1}$$

The total spatial dimension of the grid points is therefore $N_x = 2 \times 224 \times 224 = 100\,352$. With $N_t = 500$ snapshots, we definitely will apply the method of snapshots.

8.2 POD Eigenvalue Spectrum and Modes

We choose the spatial scalar product simply as $\mathbf{S} = \frac{1}{n_x}\mathbb{1}$, and the temporal weighting matrix as $\mathbf{T} = \frac{1}{N_t}\mathbb{1}$, which corresponds to an equidistant sampling in space and time. Thus, the squared norm of one snapshot will be the "generalized" energy averaged over the whole fluid volume:

$$||\boldsymbol{q}^i||^2 = \left(\boldsymbol{q}^i, \boldsymbol{q}^i\right) = \frac{1}{n_x}\sum_{j=1}^{n_x} T(\boldsymbol{x}_j, t_i)^2 + \frac{1}{n_x}\sum_{j=1}^{n_x} u_z(\boldsymbol{x}_j, t_i)^2 \tag{8.2a}$$

$$= \left\langle T(t_i)^2 \right\rangle_V + \left\langle u_z(t_i)^2 \right\rangle_V \tag{8.2b}$$

Likewise, the eigenvalue λ_i gives the energy contained in mode $\boldsymbol{\phi}^i$, i. e. temperature squared plus vertical velocity squared. The mean energy content of the data ensemble is $\left\langle ||\boldsymbol{q}||^2 \right\rangle \approx 1\,770\,976$.

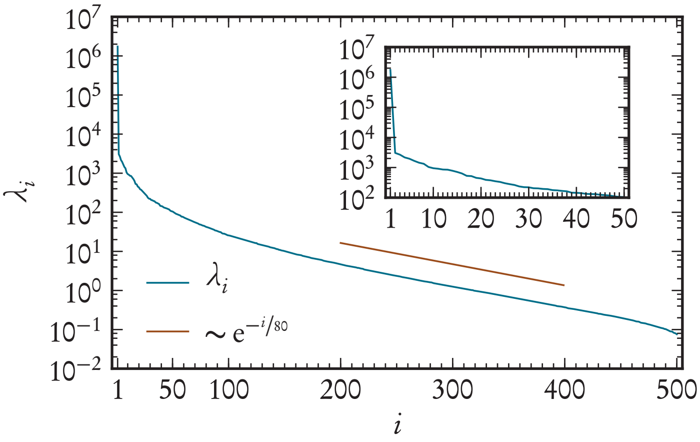

Figure 8.2: *Eigenvalues λ_i of the POD modes, with the first eigenvalues magnified in the inset. As a guide to the eye, the brown line indicates an exponential decay.*

Figure 8.2 shows the eigenvalues, determined by solving the eigenvalue problem (7.22) numerically. One observes that the first mode contains a large part of the energy, with the drop to the second eigenvalue being almost 3 orders of magnitude, as is seen in the inset. The higher eigenvalues show an almost exponential decay, which has also been observed for turbulent convection by Bailon-Cuba *et al.* (2010)[1].

In figure 8.3, some exemplary POD modes are shown. Since the modes are scaled to be orthonormal, the absolute value of the temperature (as well as the velocity) fields becomes more or less meaningless; therefore the temperature part of each mode has been rescaled in the color coding. The first mode $\boldsymbol{\phi}^1$ looks like the flow fields averaged over time (cf. figure 8.1), while modes $\boldsymbol{\phi}^2$, $\boldsymbol{\phi}^3$ and $\boldsymbol{\phi}^4$ have their main contribution near the corners. This indicates that they are responsible for the deformation and oscillation of the corner rolls. The higher modes become more erratic and noise-like, which can be seen in mode $\boldsymbol{\phi}^{90}$.

The energy content of the first modes relative to the total energy content is displayed in figure 8.4. This confirms that the first mode contains almost all the energy, namely 98.1 %. From there the energy rises quickly to almost 100 % (e. g., the first 10 modes contain 99 %, and the first 90 modes contain 99.9 % of the energy). The higher modes contribute less and less to the total energy, so in the end the curve converges slowly towards the 100 % contained in the 500 modes of the full data set. This graph can also be used to determine the desired dimension of the projection, as one can readily read of the number of modes needed to achieve a certain amount of energy.

In figure 8.5, a projection of the snapshot $\boldsymbol{q}^1$ onto a different number of modes is shown. It is seen that already a few modes (say, 10 or even as few as 4 modes) suffice to reproduce the general picture of a stable roll with "broken" corner flows. For the finer structures, though, more modes are needed: For example, the small patch of hot fluid

---

[1] In this reference, a norm similar to ours is used, namely $\left\langle T^2 \right\rangle + \left\langle u^2 \right\rangle$.

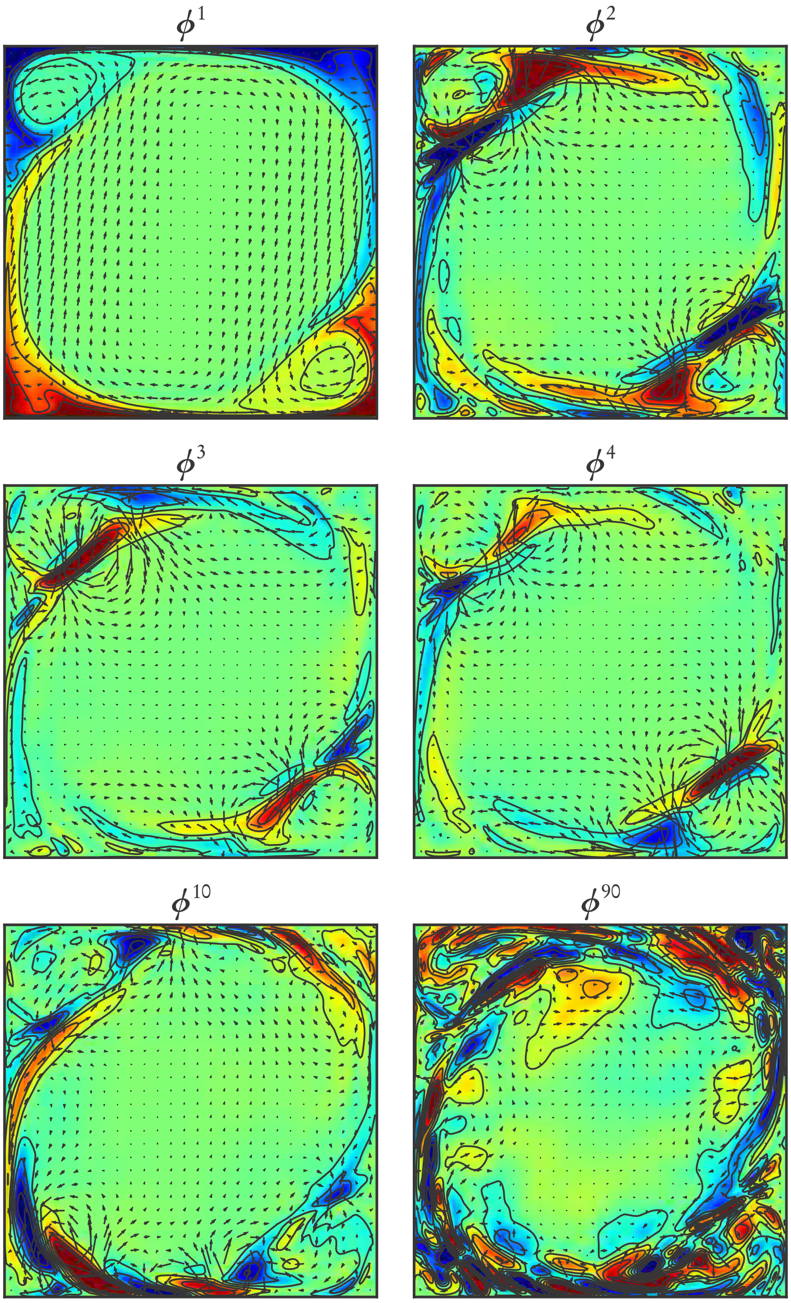

ϕ^1 ϕ^2

ϕ^3 ϕ^4

ϕ^{10} ϕ^{90}

Figure 8.3: *Examples of the POD modes of the data set. In each mode, the temperature part has been rescaled according to its minimal and maximal values, and the* 8 *equidistant isothermals as well as the color scale cover a temperature range* $\left[\frac{T_{\min}}{2}, \frac{T_{\max}}{2}\right]$.

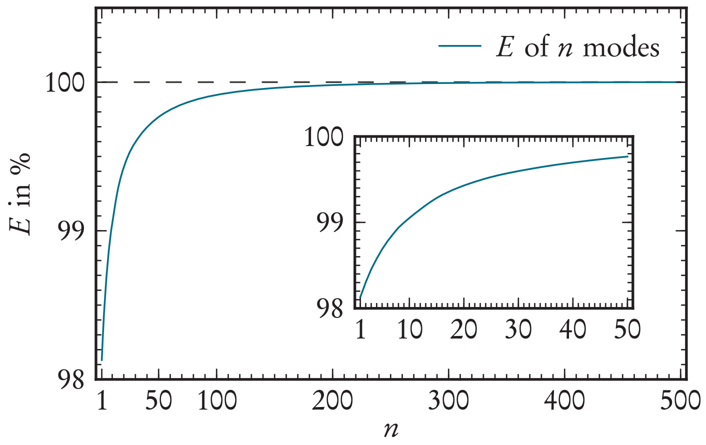

Figure 8.4: *Sum of the first n eigenvalues, which is the energy contained in the first n POD modes, normalized by the total energy, i. e.* $100\,\% \times \sum_{i=1}^{n} \lambda_i / \sum_{i=1}^{N_t} \lambda_i$. *The total energy is indicated by the dashed line.*

that is swept clockwise along the top plate is barely visible with 10 modes, but already quite pronounced when using 90 modes (i. e., less that 20 % of the available modes).

We can also inspect the time series of the energies, i. e. the norm of each (projected) snapshot. It is straightforward to see that the time series of the full data set is given by the diagonal entries of the temporal covariance matrix $\mathbf{X}^\dagger \mathbf{S} \mathbf{X}$, while the time series of the projected data corresponds to the diagonal of

$$\tilde{\mathbf{X}}^\dagger \mathbf{S} \tilde{\mathbf{X}} = \mathbf{P}_s^\dagger \mathbf{X}^\dagger \mathbf{S} \mathbf{X} \mathbf{P}_s \quad . \tag{8.3}$$

Since the full covariance matrix is calculated anyhow, the time series of the projected data is quickly obtained by multiplying this matrix with the projection matrix $\mathbf{P}_s^\dagger$ respectively $\mathbf{P}_s$, constructed as given in (7.33) – this means that we do not need to construct the whole projected data set in order to obtain the projected time series. The resulting time series of some of the projections from before (cf. figure 8.5) are shown in figure 8.6. We see that already one mode describes the full time series quite well, while of course more modes reproduce the full signal better and better.

In section 7.5.3 we discussed how the *mean* energy captured by a lower-dimensional projection monotonically rises with increasing mode count. In the right panel of figure 8.6 we can see that this also seems to be true for the projection of every *single* snapshot. This is not evident *a priori*: The mean energy captured is monotonically rising because it corresponds to the sum of non-negative eigenvalues; the more modes are used for the projection, the more non-negative eigenvalues are summed up. This simple argument does not hold for every single snapshot, though, as the energy of a projection of a single snapshot does not depend on the eigenvalues alone. To this end, we present a rigorous proof of this observation in section B.6.

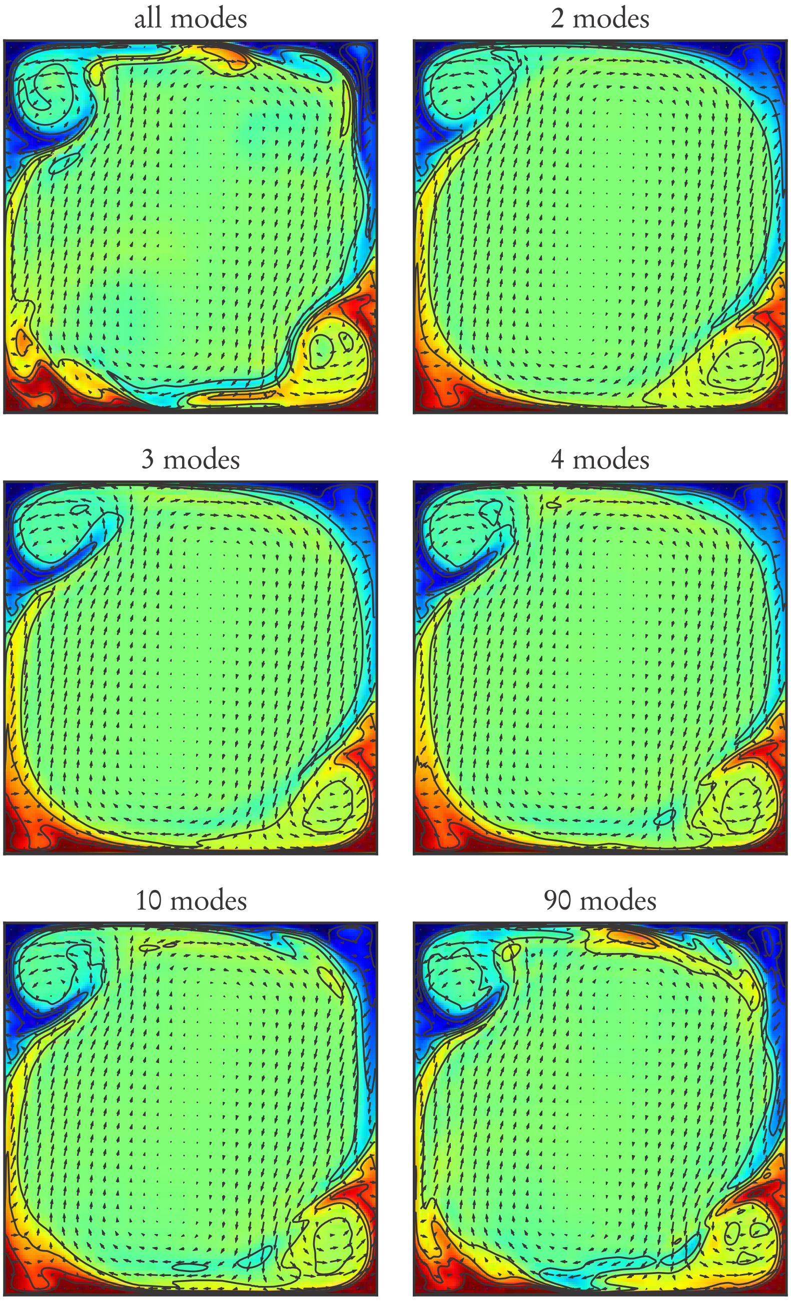

Figure 8.5: *The snapshot* $\boldsymbol{q}^1$ *projected onto the first* $\{2, 3, 4, 10, 90\}$ *modes, with representation as in figure* 8.1. *The projection onto only the first mode has been omitted since it looks precisely as the mode* $\boldsymbol{\phi}^1$ *itself, cf. figure* 8.3. *Instead, the upper left panel shows a projection using all modes, i. e. the full snapshot* $\boldsymbol{q}^1$.

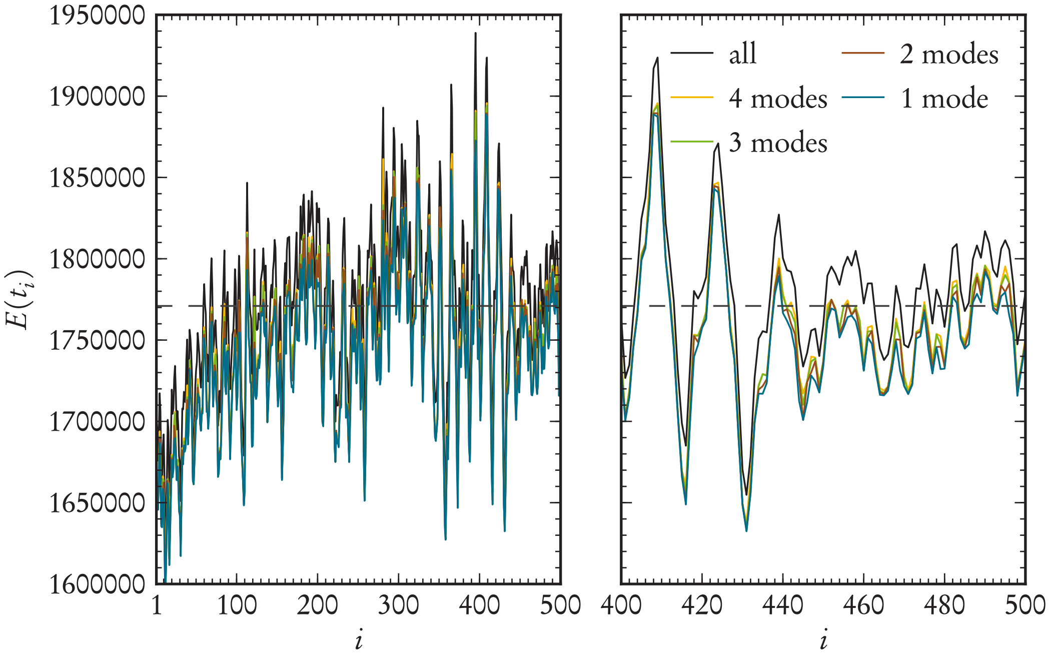

Figure 8.6: *Time series of the energies (i. e., the energy of the i-th snapshot) of the full data set and projections onto the first $\{1,2,3,4\}$ modes. The dashed line indicates the mean energy of $\left\langle ||\boldsymbol{q}||^2 \right\rangle \approx 1\,770\,976$. In the right panel, time steps 400–500 have been magnified.*

9 New Approach that Optimizes the Heat Transport

As yet we have shown the standard POD analysis of two-dimensional convection in the last chapter. The modes and eigenvalues were representing the generalized energy $E = \left\langle T^2 \right\rangle_V + \left\langle u_z^2 \right\rangle_V$, which was a consequence of the chosen scalar product. This generalized energy does not have a meaningful physical significance though, as quantities measured in different units are added. Even when non-dimensionalized quantities are used, this issue persists, as the relative weight given to temperature respectively velocity depends on the way the non-dimensionalization is achieved. For example, the velocities non-dimensionalized according to free-fall time scales are typically of order $\mathcal{O}(1)$, while for diffusive time scales (as we are using), velocities for the parameters considered here are of order $\mathcal{O}(1000)$. If the temperature is in both cases non-dimensionalized with respect to the plate temperatures and is therefore typically of order $\mathcal{O}(1)$, this means that one non-dimensionalization gives a factor of $\mathcal{O}(1000)$ more weight to the velocity than the other. Introducing a weighting factor in front of the velocity would also not solve this problem but merely shift it, because then the question arises of how to determine a “good” choice for this external factor. All in all, the problem boils down to the fact that it is not a good idea to compare temperatures and velocities. The generalized energy is therefore not an appropriate measure for convective systems.

In contrast, what *is* a good measure of convection is the heat transport through the system, measured in terms of the Nusselt number

$$\mathrm{Nu} = 1 + \left\langle T u_z \right\rangle_V \quad , \tag{9.1}$$

assuming that the temperature field has been shifted to $\left\langle T \right\rangle_V = 0$. The Nusselt number and its dependencies on the system parameters (i. e., Rayleigh and Prandtl number and fluid geometry) is one of the most studied quantities in Rayleigh–Bénard convection (see e. g. Ahlers *et al.* (2009), Grossmann and Lohse (2001)). Also, it has been found that the Nusselt number depends strongly on the flow configurations, for example the shape and dynamics of the large-scale current circulation (Petschel *et al.*, 2011, van der Poel *et al.*, 2011). Thus, it would be insightful to learn about the “building blocks” from which the spatial structures are constructed, and also to quantify the heat transport of these building blocks.

To this end, we adapt the POD technique to allow for modes that are optimal in capturing the convective heat transport of the system, instead of the generalized energy. The average convective heat transport is the average correlation between vertical velocity and temperature, which we define as the convective NUSSELT number

$$\mathrm{Nu}^{\mathrm{c}} = \left\langle T u_z \right\rangle_V \quad , \tag{9.2}$$

with $\mathrm{Nu} = 1 + \mathrm{Nu}^{\mathrm{c}}$. We will show in the next section how the previous methods have to be modified in order to achieve a proper orthogonal decomposition that maximizes Nu^{c}. The description will be restricted to the method of snapshots, as this will be the preferred choice in virtually all applications.

9.1 Theory

In the matrix formulation of section 7.2, the quantity that the POD method maximizes hinges on the choice of the scalar-product-inducing matrix $\mathbf{S}$. The choice $\mathbf{S} \sim \mathbb{1}$ resulted in the generalized energy that does not contain any mixed terms, as are needed to obtain the NUSSELT number.

With the snapshots as in (8.1), here abbreviated in a blockwise fashion[1] as $\boldsymbol{q}^i = \begin{pmatrix} T^i \\ u_z^i \end{pmatrix} \in \mathbb{R}^{2n_x}$, the matrix

$$\mathbf{S} = \frac{1}{2n_x} \begin{pmatrix} \mathbb{0} & \mathbb{1} \\ \mathbb{1} & \mathbb{0} \end{pmatrix} \in \mathbb{R}^{2n_x \times 2n_x} \tag{9.3}$$

results in the representation of the heat transport of a single snapshot as

$$\left(\boldsymbol{q}^i\right)^\dagger \mathbf{S} \boldsymbol{q}^i = \frac{1}{2n_x} \left(T^i u_z^i\right) \begin{pmatrix} \mathbb{0} & \mathbb{1} \\ \mathbb{1} & \mathbb{0} \end{pmatrix} \begin{pmatrix} T^i \\ u_z^i \end{pmatrix} = \frac{1}{2n_x} \left(T^i u_z^i\right) \begin{pmatrix} u_z^i \\ T^i \end{pmatrix} \tag{9.4a}$$

$$= \frac{1}{2} \left(\left\langle T^i u_z^i \right\rangle_V + \left\langle u_z^i T^i \right\rangle_V \right) = \mathrm{Nu}^{\mathrm{c}}(t_i) \quad . \tag{9.4b}$$

By utilizing this matrix $\mathbf{S}$ and the scalar product it induces, it becomes possible for the POD method to optimize for the convective heat transport and also to obtain the spatial structures (i. e., modes) that achieve the most heat transport.

There is a slight complication, though, as the matrix $\mathbf{S}$ is HERMITian, but not positive definite – its eigenvalues are $\pm 1/2n_x$. Thus, the scalar product of a vector with itself, i. e. the squared norm, is not guaranteed to be non-negative. Speaking in physical terms, this is the case when a snapshot has a negative convective heat transport, which can happen if e. g. strong hot plumes are swept downwards by the large-scale current.

---

[1] That is, T^i and u_z^i are blocks of n_x values that represent the temperature and velocity fields at time t_i.

Since the requirement of positive definiteness, $(q, q) \geq 0$, is not fulfilled, the matrix $\mathbf{S}$ does not define a proper scalar product, but rather a non-degenerate symmetric bilinear form[2], which is sometimes denoted as a pseudo scalar product; likewise, the pseudo scalar product of a vector with itself defines a pseudo norm that may become negative. At first glance, this definition of a pseudo scalar product and a pseudo norm may seem unintuitive and artificial. But in physics, there exists a well-known concept that has similar properties, namely the MINKOWSKI space of special relativity. Here, the distance or MINKOWSKI metric[3] between two events in space-time can be positive or negative, which categorizes distances in space-like or time-like. Moreover, the MINKOWSKI space is a special case of a pseudo-EUCLIDean space that also generalizes the concept of norms and distances to allow for negative measures; this is also achieved by general symmetric (not necessarily positive definite) bilinear forms, just as in our case. The interested reader is referred to textbooks leaned towards the mathematics of special relativity, e. g. FLIESSBACH (1992, chap. IX), or to the mathematical literature relating to linear algebra. For the rest of this section, we will sloppily drop the "pseudo" for reasons of simplicity and just refer to scalar products or norms – e. g., the reader should be aware that whenever we discuss the norm of a snapshot, it is not to be meant in the strict mathematical sense but in the sense of a measure assigned to the snapshot.

9.1.1 Consequences of Indefinite S

In the matrix formulation of sections 7.3ff., we did not rely on $\mathbf{S}$ defining a proper scalar product, but rather on properties of the matrix itself, e. g. that it is positive definite and HERMITian. Thus, we will now analyze how the methods have to be adapted for the indefinite matrix (9.3).

The matrix $\mathbf{X}^\dagger\mathbf{S}\mathbf{X}$ is still self-adjoint with respect to $\mathbf{T}$, so there still exist eigenvectors $\mathbf{C}$ and real eigenvalues $\boldsymbol{\Lambda}$ with $\mathbf{X}^\dagger\mathbf{S}\mathbf{X}\mathbf{T}\mathbf{C} = \mathbf{C}\boldsymbol{\Lambda}$ and $\mathbf{C}^\dagger\mathbf{T}\mathbf{C} = \mathbb{1}$. However, the eigenvalues in $\boldsymbol{\Lambda}$ are not strictly positive, as $\mathbf{S}$ is not positive definite.[4] This agrees with the eigenvalues measuring the convective heat transfer Nu^c which may become negative. Thus, calculating the POD modes $\boldsymbol{\Phi}$ from $\mathbf{C}$ as given in (7.25) could result in complex modes, as it involves the inverse square root $\boldsymbol{\Lambda}^{-1/2}$ of the eigenvalues. To prevent complex POD modes (as for real input data, real POD modes should be obtained), we can take the absolutes of the eigenvalues, i. e.

$$\boldsymbol{\Lambda}_+ := \operatorname{diag}\left(|\lambda_1|, \ldots, |\lambda_{N_t}|\right) \quad , \tag{9.5}$$

---

[2] In our context, this means that (i) $v^\dagger\mathbf{S}w = w^\dagger\mathbf{S}v$ and (ii) for every non-zero v, there exists a w with $v^\dagger\mathbf{S}w \neq 0$.

[3] We are aware that the term "MINKOWSKI metric" is a misnomer, as it is not a metric in the strict mathematical sense; terms like this are established in the physical jargon, though – albeit being imprecise.

[4] This can be seen from a reasoning similar to the one given in section B.3: Multiplying the eigenvalue problem $\mathbf{X}^\dagger\mathbf{S}\mathbf{X}\mathbf{T}c = \lambda c$ from the left with $c^\dagger\mathbf{T}^\dagger$ gives $\lambda = c^\dagger\mathbf{T}^\dagger\mathbf{X}^\dagger\mathbf{S}\mathbf{X}\mathbf{T}c =: v^\dagger\mathbf{S}v \lesseqgtr 0$.

for which $\mathbf{\Lambda}_+^{-1/2}$ and therefore also the POD modes

$$\mathbf{\Phi} = \mathbf{XTC}\mathbf{\Lambda}_+^{-1/2} \tag{9.6}$$

are real.

The apparent "drawback" of using $\mathbf{\Lambda}_+$ instead of $\mathbf{\Lambda}$ is that now the POD modes are not orthonormal anymore:

$$\begin{aligned}
\mathbf{\Phi}^\dagger\mathbf{S}\mathbf{\Phi} &= \mathbf{\Lambda}_+^{-1/2}\mathbf{C}^\dagger\mathbf{T}^\dagger \underbrace{\mathbf{X}^\dagger\mathbf{S}\mathbf{X}\mathbf{T}\mathbf{C}}_{=\mathbf{C\Lambda}} \mathbf{\Lambda}_+^{-1/2} && \text{(9.7a)}\\
&= \mathbf{\Lambda}_+^{-1/2}\mathbf{\Lambda}\mathbf{\Lambda}_+^{-1/2} && \text{(9.7b)}\\
&= \operatorname{diag}\left(\frac{\lambda_1}{|\lambda_1|},\ldots,\frac{\lambda_{N_t}}{|\lambda_{N_t}|}\right) =: \mathbf{\Lambda}_s && \text{(9.7c)}
\end{aligned}$$

Therefore, the POD modes are not normalized to 1 but to ±1, i. e. the signs of the eigenvalues as contained in $\mathbf{\Lambda}_s$; modes with positive heat transport are normalized to $+1$, and modes with negative heat transport are normalized to -1. The drawback can therefore rather be interpreted as a grouping of the modes into positive and negative convective heat transport.[5]

Due to $\mathbf{\Phi}^\dagger\mathbf{S}\mathbf{\Phi} = \mathbf{\Lambda}_s$, the amplitudes of the transformation into the POD basis, i. e. $\mathbf{X} = \mathbf{\Phi\Xi}$, have to be modified: Multiplication with $\mathbf{\Lambda}_s\mathbf{\Phi}^\dagger\mathbf{S}$ from the left yields

$$\mathbf{\Lambda}_s\mathbf{\Phi}^\dagger\mathbf{S}\mathbf{X} = \mathbf{\Lambda}_s\mathbf{\Phi}^\dagger\mathbf{S}\mathbf{\Phi}\mathbf{\Xi} = \mathbf{\Lambda}_s\mathbf{\Lambda}_s\mathbf{\Xi} = \mathbf{\Xi} \quad , \tag{9.8}$$

because $\mathbf{\Lambda}_s^2 = \mathbb{1}$. After inserting $\mathbf{\Phi}$ from (9.6), the amplitudes finally read

$$\begin{aligned}
\mathbf{\Xi} &= \mathbf{\Lambda}_s\mathbf{\Lambda}_+^{-1/2} \underbrace{\mathbf{C}^\dagger\mathbf{T}^\dagger\mathbf{X}^\dagger\mathbf{S}\mathbf{X}}_{=(\mathbf{C\Lambda})^\dagger=\mathbf{\Lambda}\mathbf{C}^\dagger} && \text{(9.9a)}\\
&= \mathbf{\Lambda}_s\mathbf{\Lambda}_+^{-1/2}\mathbf{\Lambda}_+\mathbf{\Lambda}_s\mathbf{C}^\dagger \quad (\text{because } \mathbf{\Lambda} = \mathbf{\Lambda}_+\mathbf{\Lambda}_s) && \text{(9.9b)}\\
&= \mathbf{\Lambda}_+^{1/2}\mathbf{C}^\dagger \quad . && \text{(9.9c)}
\end{aligned}$$

One can quickly verify the self-consistency of the transformation,

$$\mathbf{X} = \mathbf{\Phi\Xi} = \mathbf{XTC}\mathbf{\Lambda}_+^{-1/2}\mathbf{\Lambda}_+^{1/2}\mathbf{C}^\dagger = \mathbf{XTCC}^\dagger = \mathbf{X} \quad , \tag{9.10}$$

---

[5] We want to remark here that the normalization of the modes to ±1 is not a consequence of the choice of $\mathbf{\Lambda}_+$ over $\mathbf{\Lambda}$ in (9.6): Had we instead chosen to use the complex $\mathbf{\Lambda}^{-1/2}$ (where $(\mathbf{\Lambda}^{-1/2})^\dagger \neq \mathbf{\Lambda}^{-1/2}$), (9.7) would read $\mathbf{\Phi}^\dagger\mathbf{S}\mathbf{\Phi} = (\mathbf{\Lambda}^{-1/2})^\dagger\mathbf{\Lambda}\mathbf{\Lambda}^{-1/2} = \operatorname{diag}\left({}^{\lambda_1}/_{|\lambda_1|},\ldots,{}^{\lambda_{N_t}}/_{|\lambda_{N_t}|}\right)$, i. e. the same as it is now – complex POD modes would therefore also result in normalization to ±1. Thus, we could conveniently opt for real POD modes.

cf. (7.28). The lower-dimensional projection from section 7.5.2 depends only on the eigenvectors and the temporal weighting matrix, so the formulas presented there are still valid for the new **S** considered here.

Summarizing this section, we have seen that the methods developed for a positive definite **S** may be extended to indefinite matrices – as the one we use to describe the convective heat transport – by almost trivial modifications like splitting the eigenvalues into sign and absolute value.

9.2 Results from DNS Data

We will now apply the newly developed methods to the same data set as before and compare the performance to the prior results. In order to distinguish between the modes that optimize the generalized energy and the ones that optimize the convective heat transport, we will refer to them as E-modes and Nu-modes whenever otherwise confusion is to be feared, or add subscripts to the variables and matrices.

9.2.1 Eigenvalues and Modes

Figure 9.1 shows the eigenvalue spectrum of the Nu-modes, sorted in descending order; the eigenvalue λ_i is the convective heat transport of mode $\boldsymbol{\phi}^i$. Due to the logarithmic vertical axis, we plot the absolute of the eigenvalues. As for the energy case, we see that the first mode transports most of the heat, and the drop from the first to the second eigenvalue is almost 2 orders of magnitude. There are 324 modes with positive heat transport, and a big share of the eigenvalues show an exponential decay. Correspondingly, there are 176 modes with negative heat transport, and the most negative one is about a factor of 5 to the second to last (best seen in the inset of the figure). The sum of the eigenvalues, i. e. the mean convective heat transport of the data set, is $\mathrm{Nu}^{\mathrm{c}} = \left\langle \|q\|^2 \right\rangle \approx 27.39$.

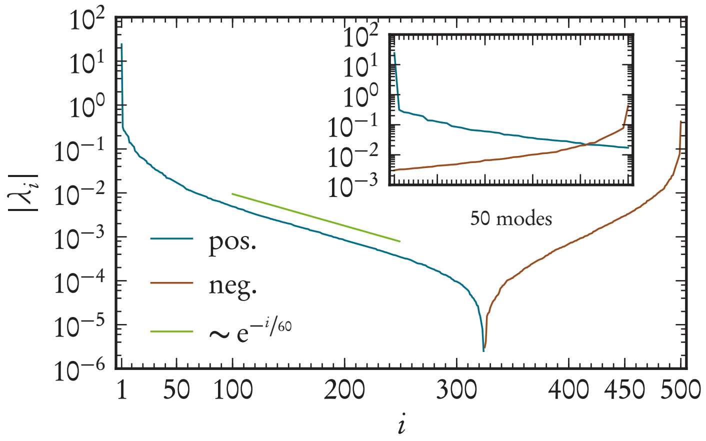

Figure 9.1: *Eigenvalues of the* Nu-*modes sorted in descending order, grouped into positive and negative ones. The green line acts as a guide to the eye for an exponential decay. The inset magnifies the first* 50 *most positive modes in blue and the last* 50 *most negative modes in brown.*

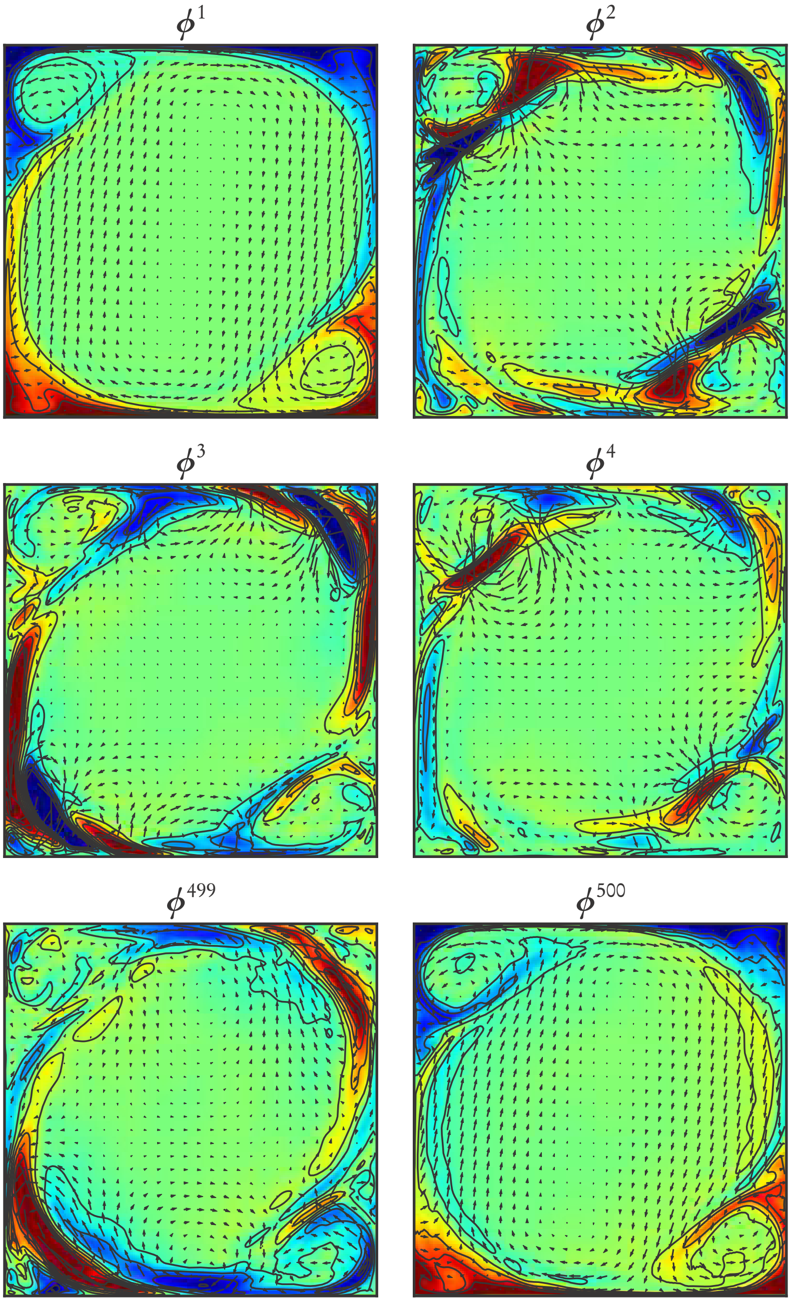

$\boldsymbol{\phi}^1$ $\boldsymbol{\phi}^2$

$\boldsymbol{\phi}^3$ $\boldsymbol{\phi}^4$

$\boldsymbol{\phi}^{499}$ $\boldsymbol{\phi}^{500}$

Figure 9.2: *Examples of the* Nu*-modes of the data set; the representation is in line with the one in figure* 8.3*. The mode* $\boldsymbol{\phi}^1$ *corresponds to the most positive eigenvalue, and* $\boldsymbol{\phi}^{500}$ *to the most negative one.*

The corresponding modes are shown in figure 9.2. As expected, the first mode $\boldsymbol{\phi}^1$ represents the mean large-scale circulation, and it looks virtually identical to the first E-mode, cf. figure 8.3. The second mode is concentrated near the corner flows and is thought to trigger their deformation, similar to the second E-mode. However, the third Nu-mode differs from the respective E-mode, as it shows elongated vertical structures of high absolute temperature values near the side walls that correspond to events of high convective heat transport – these are missing from the third E-mode, as there the method is in a sense insensitive to the convective heat transport.

The last mode $\boldsymbol{\phi}^{500}$ which corresponds to the most negative eigenvalue looks almost like $\boldsymbol{\phi}^1$, i. e. the mean flow – upon closer inspection, though, it clearly shows signatures of negative heat transport: On the left side, there is a patch of cold fluid moving upwards, which is the signature of cold plumes that are swept towards the upper plate by the large scale current; likewise on the right side, hot fluid is swept down. Also at the boundary between the corner flows and the main circulation cell one can find cold fluid being swept upwards respectively hot fluid being swept downwards, and this appears to be much more pronounced than in the analogue regions of $\boldsymbol{\phi}^1$. These flow structures all have a negative convective heat transport.

9.2.2 Comparing the Heat Transport of Nu- and E-Modes

Next we want to compare the convective heat transport of the Nu and E-modes (the time series of the convective heat transport of the data ensemble is shown in figure 9.3). The convective heat transport of the Nu-modes is simply given by the respective eigenvalues. For the heat transport of the E-modes, a more intricate processing is needed, as their eigenvalues give the generalized energy instead of the heat transport. In principle one could project the data set onto the E-modes and calculate the heat transport of these projections to obtain the heat transport of the E-modes. But as before, the projections do not have to be calculated explicitly:

First we note that the heat transport of the full data set $\mathbf{X}$ can be expressed as $\mathrm{Nu}^c = \mathrm{tr}(\mathbf{X}^\dagger \mathbf{S}_{\mathrm{Nu}} \mathbf{X} \mathbf{T})$. The heat transport represented by $\boldsymbol{\phi}_E^i$ (the i-th E-mode) can then be calculated by inserting a projection of $\mathbf{X}$ onto $\boldsymbol{\phi}_E^i$ into this relation. According to (7.33), this projection is given by

$$\tilde{\mathbf{X}} = \mathbf{X}\mathbf{T}\boldsymbol{c}_E^i \left(\boldsymbol{c}_E^i\right)^\dagger \quad , \tag{9.11}$$

Figure 9.3: *Time series of the convective heat transport of the full data set. The dashed line marks the mean of the full data set,* $\mathrm{Nu}^{\mathrm{c}} \approx 27.39$.

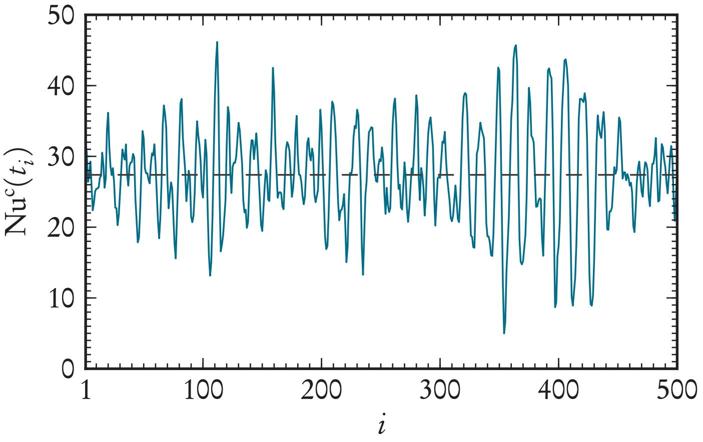

where $\boldsymbol{c}_E^i$ denotes the i-th eigenvector of the E-covariance matrix $\mathbf{X}^\dagger \mathsf{S}_E \mathbf{X}\mathbf{T}$, corresponding to the i-th E-eigenvalue. Inserting this projection into the trace from before, we obtain the heat transport of $\boldsymbol{\phi}_E^i$ as

$$\mathrm{Nu}^{\mathrm{c}}(\boldsymbol{\phi}_E^i) = \mathrm{tr}\left(\widetilde{\mathbf{X}}^\dagger \mathsf{S}_{\mathrm{Nu}} \widetilde{\mathbf{X}}\mathbf{T}\right) \tag{9.12a}$$

$$= \mathrm{tr}\left(\boldsymbol{c}_E^i \left(\boldsymbol{c}_E^i\right)^\dagger \mathbf{T}^\dagger \mathbf{X}^\dagger \mathsf{S}_{\mathrm{Nu}} \mathbf{X}\mathbf{T} \boldsymbol{c}_E^i \left(\boldsymbol{c}_E^i\right)^\dagger \mathbf{T}\right) \tag{9.12b}$$

$$= \mathrm{tr}\left(\left(\boldsymbol{c}_E^i\right)^\dagger \mathbf{T}^\dagger \mathbf{X}^\dagger \mathsf{S}_{\mathrm{Nu}} \mathbf{X}\mathbf{T} \boldsymbol{c}_E^i\right) \tag{9.12c}$$

$$= \left(\boldsymbol{c}_E^i\right)^\dagger \mathbf{T}^\dagger \mathbf{X}^\dagger \mathsf{S}_{\mathrm{Nu}} \mathbf{X}\mathbf{T} \boldsymbol{c}_E^i \quad . \tag{9.12d}$$

From (9.12b) to (9.12c) we have used that the trace is cyclic and $\boldsymbol{c}_E^i$ is orthonormal with respect to $\mathbf{T}$, i. e. $\left(\boldsymbol{c}_E^i\right)^\dagger \mathbf{T} \boldsymbol{c}_E^i = 1$, and in the last step we used the fact that the argument of the trace is actually already a scalar. To put the expression (9.12d) in colloquial terms, the heat transport of the E-modes is obtained from the Nu-covariance matrix by simply utilizing the eigenvectors of the E-eigenvalue problem – again, all necessary information is already contained in the covariance matrices and their eigenvectors.

In (9.12), we calculated the heat transport of one single mode $\boldsymbol{\phi}_E^i$; as is evident, this is actually given by the i-th diagonal entry of the matrix $\mathbf{C}_E^\dagger \mathbf{T}^\dagger \mathbf{X}^\dagger \mathsf{S}_{\mathrm{Nu}} \mathbf{X}\mathbf{T}\mathbf{C}_E$, which means that the diagonal of this matrix contains the heat transport of all the E-modes.[6] Also, the heat transport of a projection onto a range of E-modes is obtained simply as the sum of the respective diagonal elements.

Figure 9.4 compares the convective heat transport spectra of the Nu- and E-modes. The heat transport of the E-modes is found to be generally decreasing, though not mono-

---

[6] The matrix can be computed rather quickly, as it consists of products of the already known covariance matrix and the small $N_t \times N_t$ matrices $\mathbf{T}$ and $\mathbf{C}$.

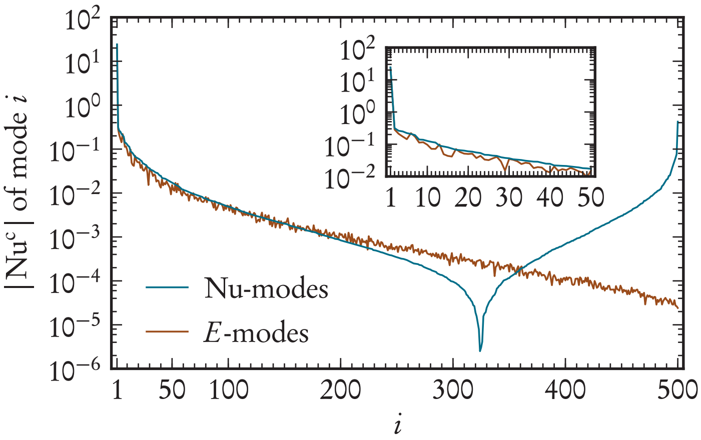

Figure 9.4: *Heat transport that is contained in the i-th* Nu- *respectively E-mode. In the inset, the first* 50 *modes are shown.*

Figure 9.5: *Heat transport of a projection onto n* Nu- *respectively E-modes, given in percent of the heat transport of the full system. In the inset, the first* 50 *modes are shown. Also cf. table* 9.1.

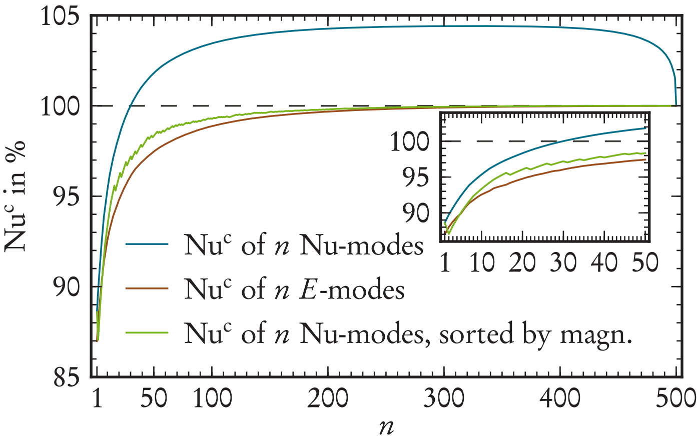

tonically but superimposed with noise. For the higher modes, the two spectra deviate strongly, because the Nu-modes show a zero crossing towards negative heat transport while all E-modes have a positive convective heat transport. This seems reasonable, because positive convective heat transport is in a sense the prevalent flow structure (cf. figure 9.3, where all time steps have $\mathrm{Nu}^c > 0$); thus, only a method that is sensitive to the heat transport is able to filter out the structures with negative heat transport.

In figure 9.5, the heat transported by a projection onto n modes (i. e., the integrated eigenvalue spectrum) is shown in percent of the total heat transport. The transport of the E-modes is always positive, which means that the 100 % heat transport of the full data is an upper bound that is reached for $n = 500$, i. e. when there is in fact no projection at all (cf. figure 8.4 for the integrated spectrum of the generalized energy). For the Nu-modes, though, the picture is rather different: Since there are positive and negative Nu-eigenvalues, their sum can rise above 100 % (i. e., when only positive modes are used), and it shows a maximum at $n = 324$ of 104.4 %, before again dropping towards 100 % at

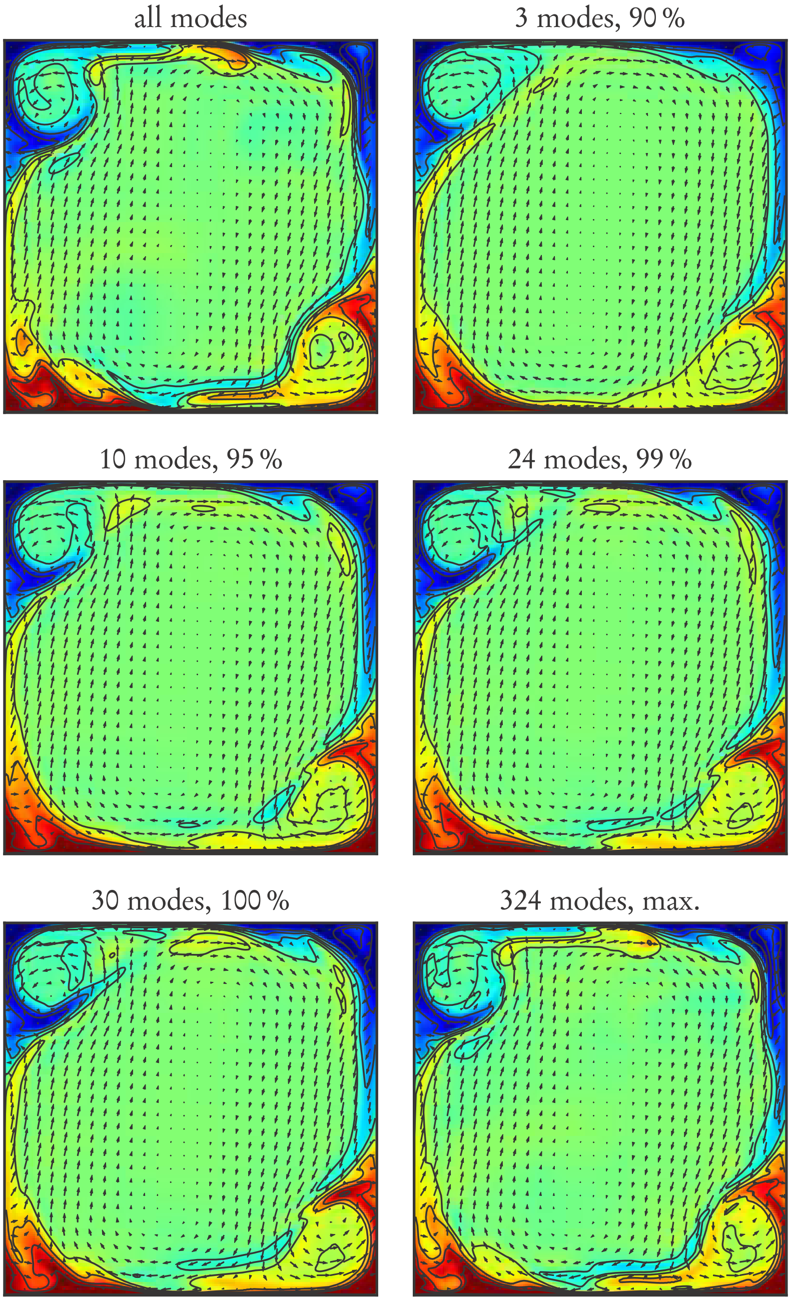

all modes

3 modes, 90 %

10 modes, 95 %

24 modes, 99 %

30 modes, 100 %

324 modes, max.

Figure 9.6: *One snapshot projected onto* $\{3, 10, 24, 30, 324\}$ Nu-*modes, with the convective heat transport of the projected data ensemble given in percent, cf. table* 9.1.

	90 %	95 %	99 %	100 %	max.
E	6	22	109	(500)	(500)
Nu	3	10	24	30	324

Table 9.1: *Number of modes needed to obtain a specified percentage of convective heat transport, distinguished into E- and* Nu-*modes.*

$n = 500$. Therefore, by omitting the modes with negative Nu^c from the projection, the heat transport of the projected system is actually increased above 100 %. Likewise, as few as 30 modes are needed to obtain the same heat transport as is contained in the full system. Of course, these 30 modes will not be able to reconstruct all the fine structures of the full data set, but as long as only the heat transport is regarded, the Nu-modes allow for a vast dimensional reduction. Table 9.1 summarizes the number of modes needed to obtain a projection that contains a certain percentage of the convective heat transport, and the corresponding visualizations of the projections are given in figure 9.6. As before, it is seen that few modes suffice to obtain the general picture of a stable convection cell, but more modes are needed to reproduce the finer structures. The convective heat transport, i. e. an averaged quantity, is still reasonably well described with a lower-dimensional projection.

As was pointed out in section 7.5, the modes that are used for the projection may be chosen arbitrarily. Up to now we considered the n modes with the highest heat transport, and this resulted in the increased heat transport of 104.4 %. Instead, one could also consider to sort the modes by the absolute value of the heat transport, as also the strong negative modes are part of “the physics” of the system. The integrated heat transport spectrum of this alternate sorting is shown as the green line in figure 9.5. The curve now converges to 100 % strictly from below, and it is not monotonous but jagged as it is the sum of alternating positive and negative values. However and most importantly, the percentage of Nu^c contained in a lower-dimensional projection is still above the E-modes for all values of n, thus indicating that the Nu-modes give a better description of the heat transport independent of the ordering. From now on we will only consider the direct sorting of the modes by descending value of Nu^c.

9.2.3 Time Series of Projections

Figure 9.7 shows the time series of the convective heat transport calculated after projecting onto subsets of Nu-modes, compared to the one of the full data set. It is seen that the lower-dimensional projections describe the full data very well, and that the projections chosen here (i. e., sets of modes corresponding to 90 %, 95 % and 99 % of the full Nu^c) capture also an increasing amount of heat transport *per snapshot*. Unlike the generalized energy (see discussion of figure 8.6), though, the convective heat transport is in general not monotonically rising with the number of modes used; e. g., the full heat transport can lie above, below or in between the lower-dimensional projections, as is seen in the right graph of figure 9.7. This is due to the Nu-eigenvalues being not strictly positive, as it is not *a priori* clear how the heat transport of a single snapshot is composed from the linear

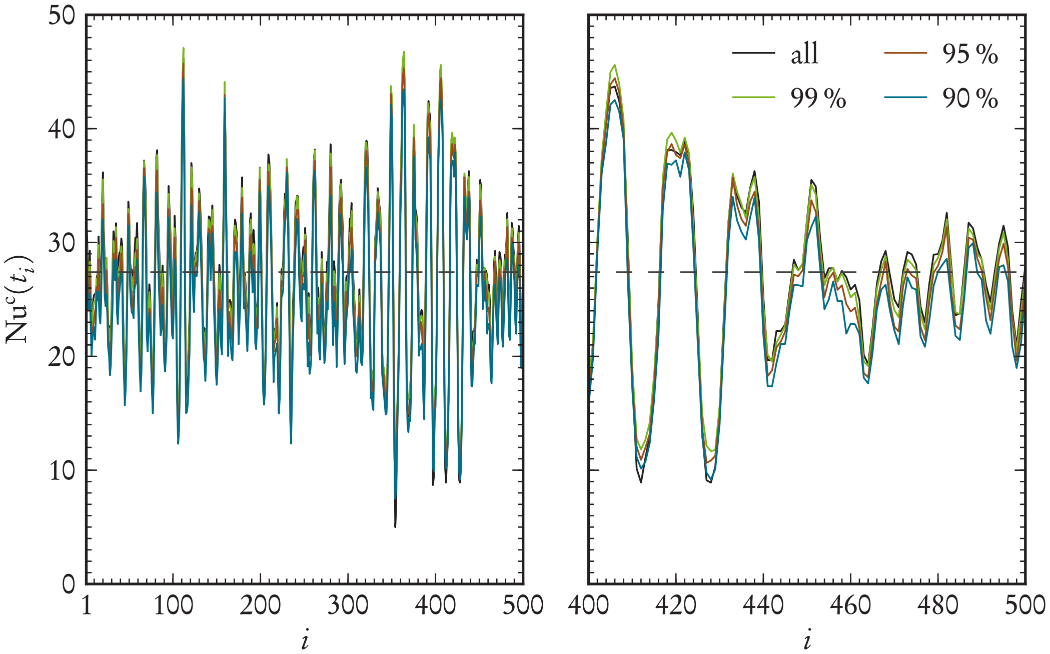

Figure 9.7: *Time series of the convective heat transport of the full data set and projections onto the first* $\{3, 10, 24\}$ Nu-*modes, cf. table* 9.1. *The dashed line indicates the mean convective heat transport. Time steps* 400–500 *have been magnified in the right panel.*

Figure 9.8: *Time series of the convective heat transport of projections onto the* 324 Nu-*modes that have a positive eigenvalue and onto* 30 *modes corresponding to* 100 % Nu^c. *Only the last* 100 *time steps are shown, as in the magnified time series from the plots before.*

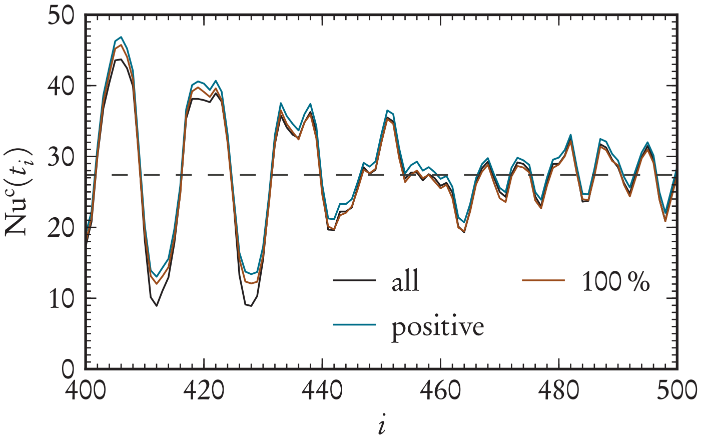

combination of the positive and negative Nu-eigenvalues (cf. (B.21), section B.6). When only considering projections onto positive modes, though, then the argument given for the generalized energy holds again – i. e., the convective heat transport of the projection of every *single* snapshot rises monotonically with the number of *positive* modes used for

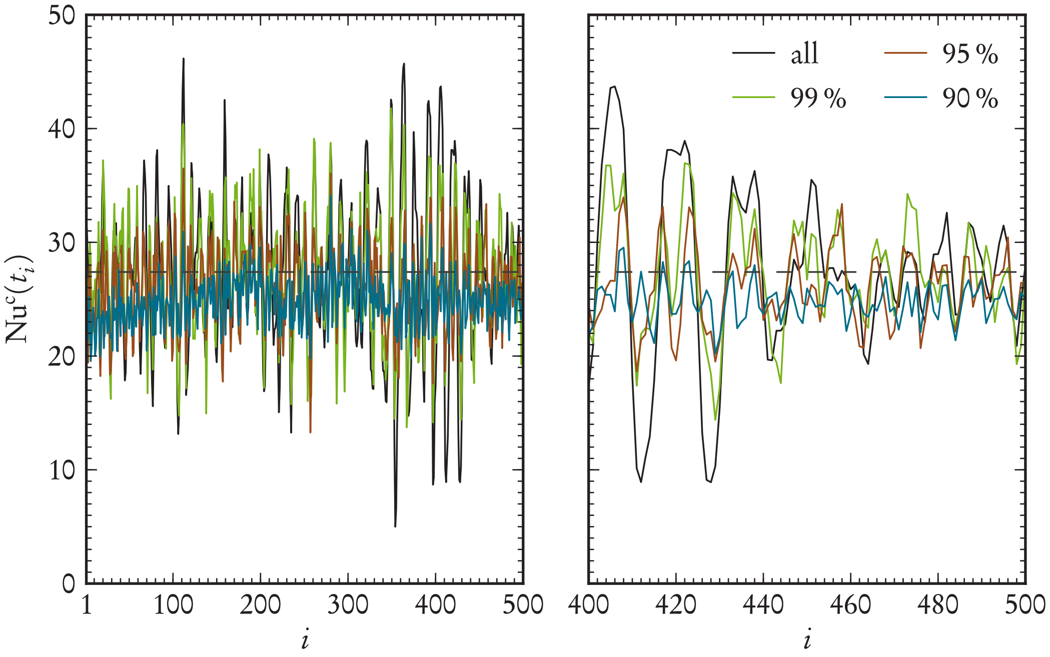

Figure 9.9: *Time series of the convective heat transport of the full data set and projections onto the first* $\{6, 22, 109\}$ *E-modes, cf. table* 9.1. *The mean convective heat transport is given by the dashed line.*

the projection. In this regard, figure 9.8 compares the full time series with the one of a projection onto the 324 positive Nu-modes, and it is seen that the projected time series always has a higher convective heat transport than the full time series.

The comparison with the projections onto the number of E-modes that achieve the same heat transport as the Nu-modes (cf. table 9.1) is rather striking: Figure 9.9 shows the Nu^c-time series of projections onto $\{6, 22, 109\}$ E-modes, corresponding to $\{90\,\%, 95\,\%, 99\,\%\}$ of convective heat transport, i. e. the same shares of the total heat transport as in figure 9.7 for the Nu-modes. Although more E-modes are used for the respective projections, one can directly see that the full time series differs strongly from the lower-dimensional ones; especially the big swings are not reproduced. This is best seen at the time series corresponding to 90 %, which shows much less pronounced peaks. Also in general the deviation from the true time series is not systematic at all: Sometimes the projection is above the true value, sometimes below, sometimes one projection is above while the other is below etc. To conclude, when compared to the E-modes, the

Figure 9.10: *Difference between* Nu^{c}*-time series obtained from a projection onto* n Nu- *respectively* E*-modes and the full time series, measured in terms of the* L^2*-norm, cf. text.*

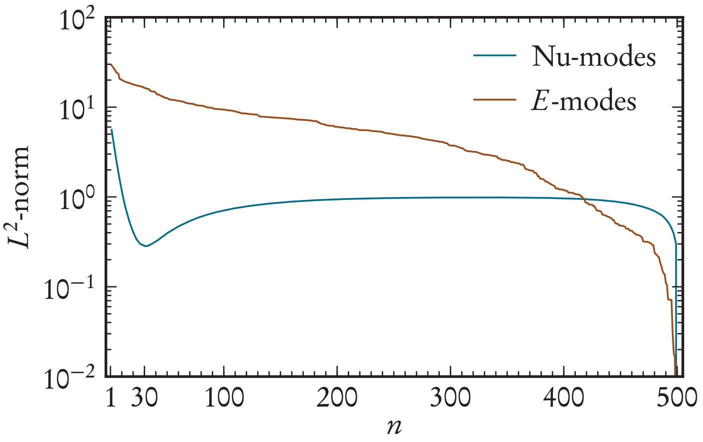

Nu-modes show a *better performance* with *fewer modes* in reconstructing the time series of the convective heat transport.[7]

The performance with regard to time series is quantified in figure 9.10. Here, the difference of the full time series $\mathrm{Nu}^{\mathrm{c}}(t_i)$ and the one projected onto n modes, say $\widetilde{\mathrm{Nu}^{\mathrm{c}}}^{n}(t_i)$, is compared in terms of the L^2-norm, i. e. $\sqrt{\frac{1}{N_t}\sum_{i=1}^{N_t}\left(\mathrm{Nu}^{\mathrm{c}}(t_i)-\widetilde{\mathrm{Nu}^{\mathrm{c}}}^{n}(t_i)\right)^2}$ for equal temporal weights as are considered here. For $n \lesssim 420$, the L^2-difference of the Nu-modes is up to an order of magnitude below the E-modes. The Nu-modes show a local minimal deviation from the true time series at $n = 30$, which seems reasonable as this corresponds exactly to 100 % Nu^{c}; cf. also figure 9.8 for this case. Also, it is clear that the difference of the Nu-modes is not monotonically falling with rising mode number n, because, as we have seen, lower-dimensional projections onto Nu-modes can actually *increase* the heat transport, thus resulting in a difference (i. e., increasing L^2-norm) compared to the full case. In contrast, the L^2-norm of the E-modes is monotonically falling (cf. the monotonically rising heat transport in figure 9.5); this is also the reason for the seemingly better performance of the E-modes for $n \gtrsim 420$. Of course, in the end for $n = 500$, in both cases the L^2-norm vanishes.

9.2.4 Statistics of Local Convective Heat Transport

The convective heat transport Nu^{c} is defined as a volume-averaged quantity. In order to achieve a better understanding of the spatial structures involved and how these structures

---

[7] We want to remark here that the “benchmark” of describing the heat transport is on the one hand slightly biased, because the Nu-modes were specifically tailored to do so; conversely, the E-modes would perform better than the Nu-modes in describing the generalized energy. On the other hand, though, the argument still holds that the NUSSELT number is a physically relevant quantity, while the generalized energy is not.

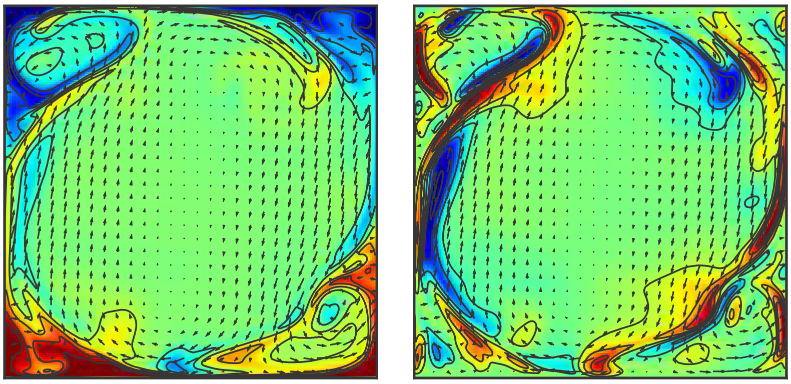

Figure 9.11: *Color plots of temperature field* $T(\boldsymbol{x})$ *(left) and local convective heat transport* $\mathrm{Nu}^{\mathrm{c}}(\boldsymbol{x})$ *(right) of a single snapshot, cf.* (9.13). *The color scale of* $\mathrm{Nu}^{\mathrm{c}}(\boldsymbol{x})$ *in the right panel is the same as in figure* 9.12.

are represented by our new ansatz, we will now investigate the statistics of the *local* convective heat transport, defined as (Bailon-Cuba *et al.*, 2010)

$$\mathrm{Nu}^{\mathrm{c}}(\boldsymbol{x}) = u_z(\boldsymbol{x})\theta(\boldsymbol{x}) \tag{9.13a}$$

$$= u_z(\boldsymbol{x})\left(T(\boldsymbol{x}) - \langle T(\boldsymbol{x})\rangle_{A,t}\right) \quad , \tag{9.13b}$$

where θ are the temperature fluctuations about the horizontally and temporally averaged temperature profile $\langle T(\boldsymbol{x})\rangle_{A,t}(z)$. Obviously, the mean local convective heat transport gives the total convective heat transport, i. e. $\langle \mathrm{Nu}^{\mathrm{c}}(\boldsymbol{x})\rangle_{V,t} = \mathrm{Nu}^{\mathrm{c}}$.

A color plot of the local convective heat transport is compared to the respective temperature field in figure 9.11. While also the temperature representation gives an impression of the convective structures that have a big impact on the heat transport (e. g., the hot plume being swept downwards in the upper right corner), the same structures can be identified much easier in the color plot of the local convective heat transport – in this case, one can for example make out roughly three big blue patches that correspond to negative heat transport, i. e. plumes being swept in the “wrong” vertical direction. Due to them, the snapshot has a convective heat transport way below the average, namely $\mathrm{Nu}^{\mathrm{c}} \approx 13.15$.

The projection of this snapshot onto all 324 positive Nu-modes is shown in figure 9.12; the convective heat transport of the projection is enhanced by 22 %. The color plot of $\mathrm{Nu}^{\mathrm{c}}(\boldsymbol{x})$ makes it clear that this enhancement is achieved by removing the big blue patches, i. e. localized events of negative heat transport, from the snapshot, while the positive structures are only marginally smaller in amplitude, compared to the full snapshot (figure 9.11 right).

To attain a more quantitative understanding of this enhancement mechanism, we will now investigate the probability density function (PDF) of the local convective heat

Figure 9.12: *Local convective heat transport of a projection onto the* 324 *positive* Nu-*modes, with the same snapshot as used in figure* 9.11. *While in this projection in general the high values are missing, the negative events are much more diminished compared to the positive ones. The mean convective heat transport of the full snapshot is* $\mathrm{Nu}^{\mathrm{c}} \approx 13.15$, *while the projection presented here has* $\mathrm{Nu}^{\mathrm{c}} \approx 15.99$, *which is* 22 % *higher than the value without projection.*

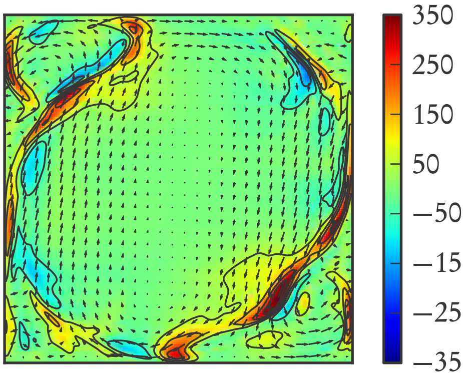

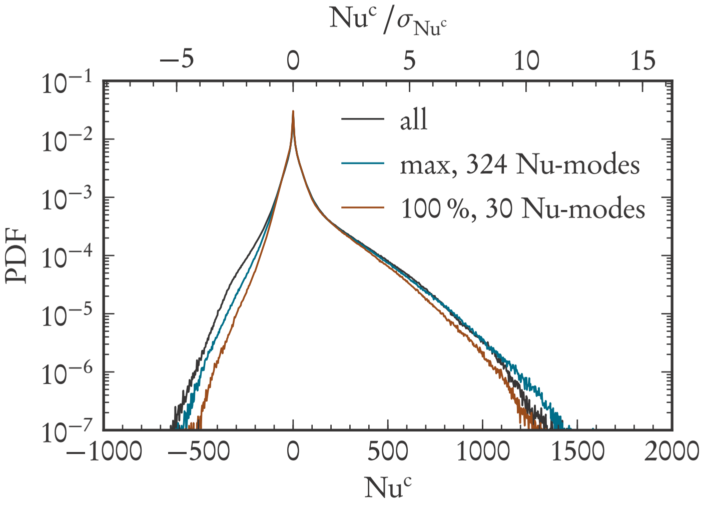

Figure 9.13: *Probability density function of the local convective heat transport* $\mathrm{Nu}^{\mathrm{c}}(\boldsymbol{x})$ *of the full ensemble (black) and of projections onto the first* 30 *and* 324 Nu-*modes. The upper abscissa is rescaled with respect to the standard deviation* $\sigma_{\mathrm{Nu}^{\mathrm{c}}} \approx 122.9$ *of the full PDF.*

transport. The PDF of the full data in figure 9.13 is asymmetric and has stronger tails towards positive values, which is not surprising, as positive heat transport is in a sense the generic behavior of the RAYLEIGH–BÉNARD system. The blue curve shows the PDF of the data set projected onto the 324 positive Nu-modes that maximize the heat transport, and it is seen that the negative tails are less pronounced, while the positive tails actually lie above the ones of the full data. Thus, the projection onto the positive modes optimizes the convective heat transport in a two-fold way – by enhancing the events of positive heat transport while reducing the negative ones. Likewise, 100 % heat transport with as few as 30 modes (which is a remarkable result) can be achieved by strongly reducing the negative tails of the PDF while capturing almost all positive events, as the respective tails of the PDF reveal (cf. brown curve).

We will now compare the PDFs of projections onto Nu- and E-modes that represent a certain percentage of the total convective heat transport: In line with the observations from before, the PDFs of the local convective heat transport of the Nu-projection

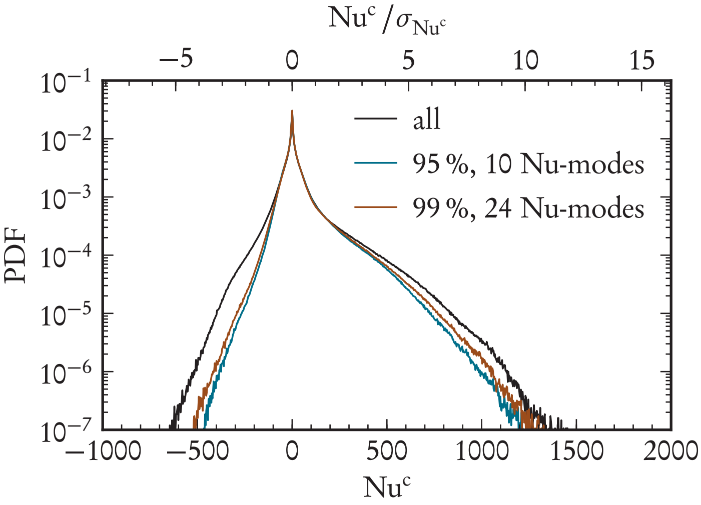

Figure 9.14: *Probability density function of the local convective heat transport* $\mathrm{Nu^c}(\boldsymbol{x})$ *of the full ensemble (black) and of projections onto the first* 10 *and* 24 Nu-*modes, corresponding to* 95 % *and* 99 % *of the full heat transport.*

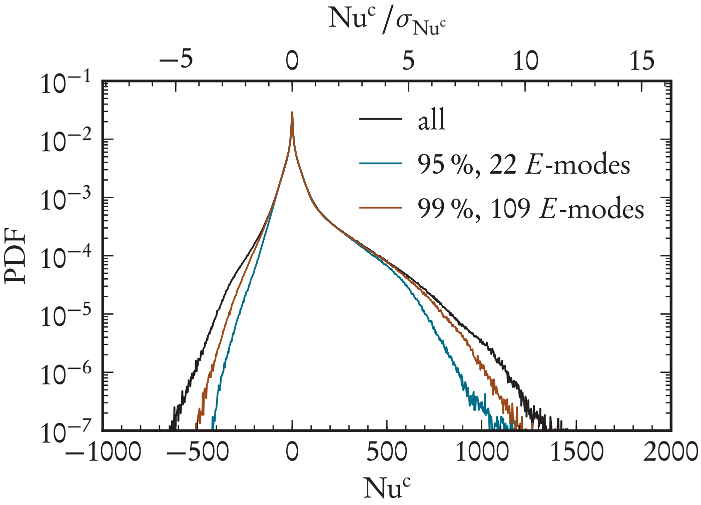

Figure 9.15: *Probability density function of the local convective heat transport* $\mathrm{Nu^c}(\boldsymbol{x})$ *of the full ensemble (black) and of projections onto the first* 22 *and* 109 E*-modes, corresponding to* 95 % *and* 99 % *of the full heat transport.*

corresponding to 95 % and 99 % in figure 9.14 have strongly falling negative tails; also the shoulder seen in the full PDF is missing. The positive tails, though, remain almost as strong as in the full case; one can indeed see that in the far positive end, the full PDF even has a steeper slope than the projected PDFs, although this is obscured by noise. Thus, the reason only 10 (24) modes are needed to obtain 95 % (99 %) of $\mathrm{Nu^c}$ is because the respective modes contain many positive, but few negative events of convective heat transport – after all, this is what the newly developed method was tailored for.

The picture is rather different for the PDFs of the same share of $\mathrm{Nu^c}$ obtained from E-modes, cf. figure 9.15. Here the extreme events in the positive and negative tails of the projected PDFs are equally reduced; in comparison to the Nu-case, the negative tails are slightly bigger, while the positive tails fall of much more steeply. This results in fewer

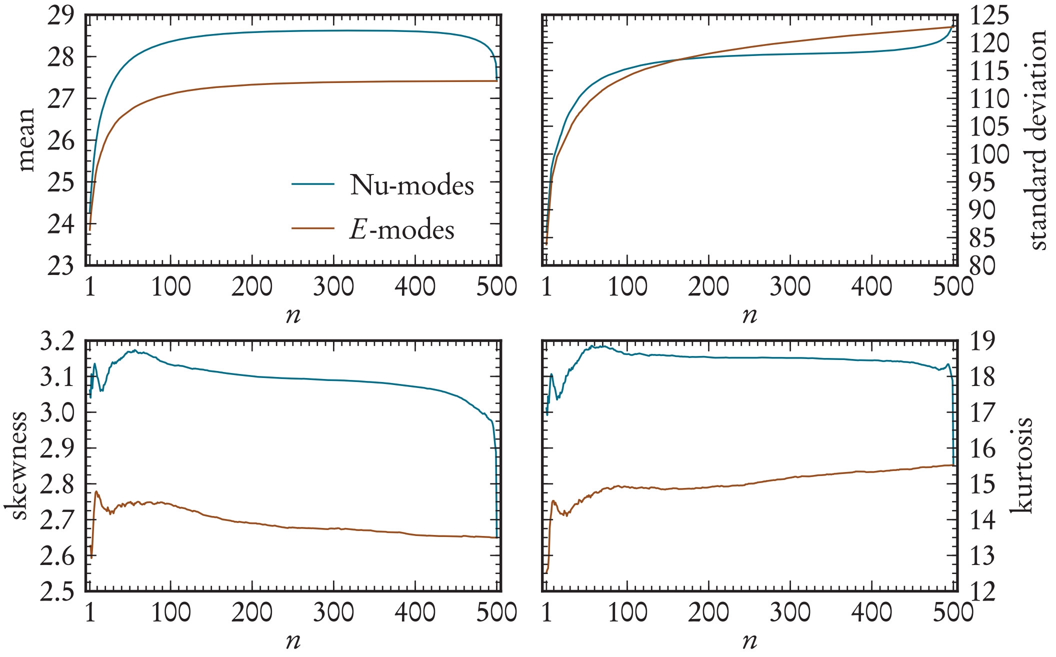

Figure 9.16: *Higher moments – i. e. mean, standard deviation* σ_{Nu^c}*, skewness (centralized third moment over* $\sigma^3_{\mathrm{Nu}^c}$*) and kurtosis (centralized fourth moment over* $\sigma^4_{\mathrm{Nu}^c}$*) – of the PDFs of the local convective heat transport relative to the number* n *of* Nu- *and* E*-modes used for the projection.*

positive and more negative events when compared to the Nu-case, and thus, 120 % (354 %) more E-modes are needed to obtain the same share of the heat transport as the Nu-modes.

Instead of discussing the form and especially the tails of the PDFs of certain projections, we can also quantify the shapes of the PDFs of all projections by their higher moments. To this end, we calculate the projections onto $n \in \{1, \dots, 500\}$ Nu- respectively E-modes and then estimate the first four moments of the PDFs of the local convective heat flux. The higher moments are more sensitive to changes in the tails of the PDF, and therefore the different behavior of the Nu- and E-projections with respect to the tails should manifest in the moments. As the Nu-modes favor the positive tails and therefore introduce an asymmetry, especially the comparison of the skewness between Nu- and E-modes is expected to be insightful.

The results are shown in figure 9.16: Obviously the mean is equivalent to figure 9.5. The monotonically rising standard deviation simply indicates that with increasing mode count, the PDFs of Nu^c become broader and in general more events are captured by the projection. Although the Nu- and the E-curves differ, this is mainly due to the ordering of the modes; for the Nu-case, at $n \gtrsim 400$ the modes with the biggest negative heat transport begin to kick in, thus resulting in the increasing slope of the standard deviation towards $n = 500$ (also cf. figure 9.4). As was predicted before, the skewness of the Nu-PDF is higher than that of the E-PDF (about 15 %), which again shows the asymmetry of the Nu-modes with respect to the heat transport. The skewness of the Nu-PDF displays a maximum when utilizing $n \approx 55$ modes. Likewise, the kurtosis of the Nu-PDF is about $20 - 25$ % higher than the one of the E-PDF, which is a signature of the enhanced tails when a projection onto Nu-modes is utilized (as we have seen in figure 9.13, the positive tails of the projected PDF can actually overshoot the ones of the full PDF). As before for the skewness, the Nu-kurtosis shows a maximum at $n \approx 55$ modes.

To conclude, the PDF analysis of the convective heat transport has shown the difference between Nu- and E-modes when it comes to capturing the heat transport: The E-modes do not distinguish between positive and negative convective heat transport, and thus, in a lower-dimensional projection both tails of the PDF of $\mathrm{Nu}^c(\boldsymbol{x})$ are missing. On the other hand, the Nu-modes we developed can distinguish between positive and negative heat transport; when using a projection onto the modes with on average positive heat transport, the PDF of $\mathrm{Nu}^c(\boldsymbol{x})$ can actually have stronger positive tails than the full PDF, while the negative tails are weakened. Therefore, we confirmed the presumed mechanism of how a projection onto the positive Nu-modes increases the heat transport – by amplifying the positive and diminishing the negative extreme events of convective heat transport.

9.2.5 Amplitudes of the POD Modes

In this section, we want to investigate the amplitudes Ξ of the transformation into the POD basis of the Nu-modes, cf. sections 7.2f. Figure 9.17 displays the time series of the amplitudes of a choice of modes. As we have seen before, the first mode contributes the most, and it is not surprising that the mean amplitude of the first mode is around 5 – the heat transport is the squared norm of the snapshots, i. e. the scalar product of a snapshot with itself, and the heat transport of the first mode is approximately 25 (cf. figure 9.16 upper left). In general, it is found that the standard deviations of the time series are decreasing for the higher modes.

To scrutinize on this, we calculate the cross-correlation between the time series of the amplitudes of two modes, say $\boldsymbol{\phi}^i$ and $\boldsymbol{\phi}^j$. As the time series of the amplitude of mode $\boldsymbol{\phi}^i$ is the i-th row of Ξ, denoted here as ξ_i, the cross-correlation is the temporally weighted scalar product between the two time series, i. e. $\xi_i^\dagger \mathbf{T} \xi_j$. It can easily be seen that this is actually the i, j-th element of the matrix[8] $\Xi \mathbf{T} \Xi^\dagger$, and thus, this matrix contains

---

[8] The adjoint dagger $(\cdot)^\dagger$ switching sides here is not a typing error, but because ξ_i is the i-th *row*, not *column* of Ξ.

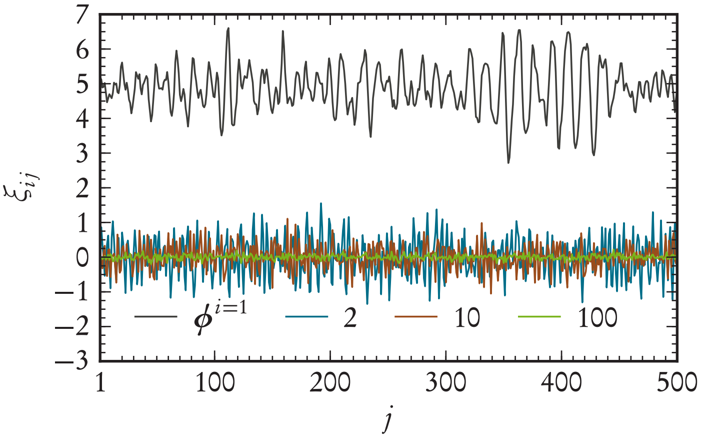

Figure 9.17: *Time series of the amplitudes of the transformation into the POD basis. The coefficient ξ_{ij} gives the contribution of mode i to snapshot j. Only the amplitudes of four exemplary modes are shown, i. e. $\boldsymbol{\phi}^1$, $\boldsymbol{\phi}^2$, $\boldsymbol{\phi}^{10}$ and $\boldsymbol{\phi}^{100}$.*

the cross-correlations between all pairs of time series. By inserting the definition of the amplitudes from (9.9), the cross-correlation matrix becomes

$$\boldsymbol{\Xi}\mathbf{T}\boldsymbol{\Xi}^\dagger = \boldsymbol{\Lambda}_+^{1/2}\underbrace{\mathbf{C}^\dagger\mathbf{T}\mathbf{C}}_{=\mathbb{1}}\boldsymbol{\Lambda}_+^{1/2} = \boldsymbol{\Lambda}_+ \quad . \tag{9.14}$$

Thus, we see that the time series of the amplitude of a mode has a *root-mean-square* value that is directly related to the respective eigenvalue, and that time series of different modes are uncorrelated, which is a remarkable observation – the proper *orthogonal* decomposition does not only yield spatially orthogonal modes, but also the time series of the amplitudes are temporally orthogonal.

It is easy to see that the mean value $\langle\boldsymbol{\Xi}\rangle_t$ of the time series of the amplitudes corresponds to the amplitudes of the transformation of the temporal average $\langle\mathbf{X}\rangle_t$ of the snapshots into the POD basis:[9]

$$\langle\boldsymbol{\Xi}\rangle_t = \boldsymbol{\Xi}\mathbf{T}\boldsymbol{v}_1 \tag{9.15a}$$

$$= \boldsymbol{\Lambda}_s\boldsymbol{\Phi}^\dagger\mathbf{S}\mathbf{X}\mathbf{T}\boldsymbol{v}_1 \quad \text{(deploying (9.8))} \tag{9.15b}$$

$$= \boldsymbol{\Lambda}_s\boldsymbol{\Phi}^\dagger\mathbf{S}\langle\mathbf{X}\rangle_t \tag{9.15c}$$

This compares to (9.8), i. e. $\boldsymbol{\Xi} = \boldsymbol{\Lambda}_s\boldsymbol{\Phi}^\dagger\mathbf{S}\mathbf{X}$. To put it in concise terms, the temporally averaged amplitudes are the amplitudes of the temporal average. Thus, the temporal mean of the amplitudes has to be calculated from $\boldsymbol{\Xi}$ itself, because it cannot be related to the eigenvalues as was the case for the temporal standard deviations.

In figure 9.18, we have calculated PDFs of the time series of each amplitude rescaled to zero mean and unit standard deviation. The PDFs of all the time series are close to a

---

[9] Here, the vector $\langle\mathbf{A}\rangle_t$ is the temporal average, i. e. the weighted sum of the columns of the matrix $\mathbf{A}$ with the temporal weights as contained in $\mathbf{T}$; in a matrix formulation, this can be written as $\langle\mathbf{A}\rangle_t := \mathbf{A}\mathbf{T}\boldsymbol{v}_1$ with the one-vector $\boldsymbol{v}_1 = (1,1,\dots,1)^\mathrm{T}$.

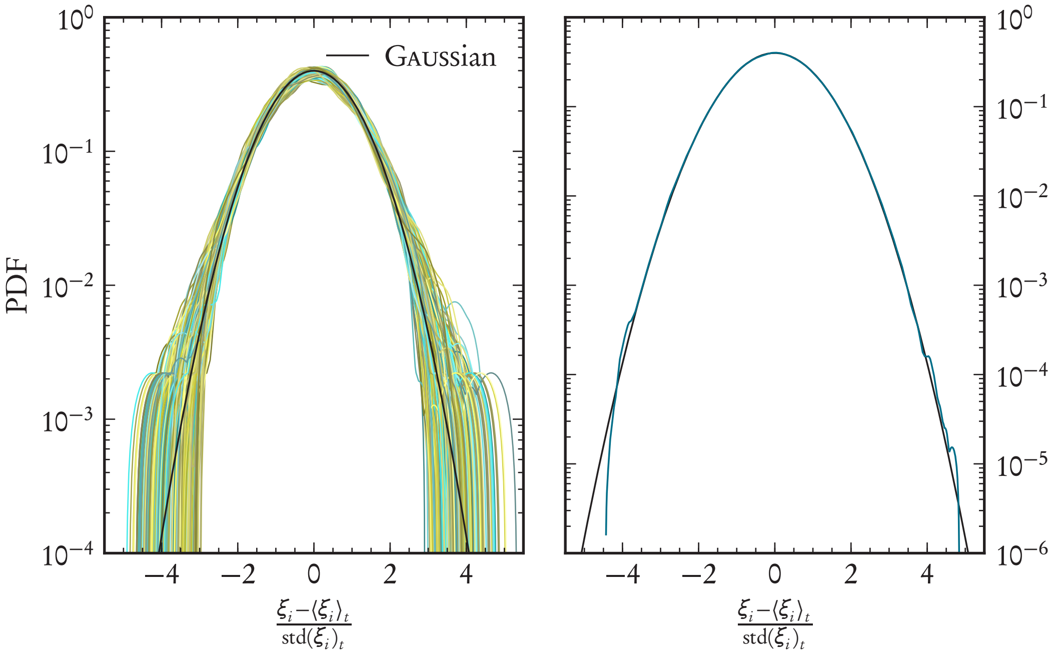

Figure 9.18: *PDFs of the time series of the amplitudes* Ξ, *rescaled to mean of* 0 *and standard deviation of* 1*. The left graph shows* 500 *PDFs for every time series, the right graph all time series condensed in a single PDF; the black curve is a* GAUSSIAN *distribution, also with mean of* 0 *and standard deviation of* 1*. Due to the small amount of data (a single time series consists of only* 500 *data points), the PDFs were calculated using* kernel density estimation, *see, e. g.,* HÄRDLE *et al.* (2004).

GAUSSian shape, but the data quality of 500 samples per PDF results in noisy statistics. Condensing all the data in the single PDF of the right graph creates a better GAUSSian curve with less noise, which suggests that the time series of the amplitudes are normally distributed.

The amplitude of the first mode ξ_1 as well as the time series of the NUSSELT number seem to have characteristic time scales of roughly 15 snapshots or 7.5 free-fall times per oscillation (cf. figures 9.17 and 9.3). To this end, we investigate the frequency power spectrum of some exemplary amplitudes in figure 9.19. The power spectrum of the amplitude of the first mode shows a peak around wave number $j \approx 35$, which indeed corresponds to a time scale of $^{500}/_{35} \approx 14.3$ snapshots per oscillation. For lower wave numbers, the spectrum could be thought of as rather flat, while after the peak, it exhibits an algebraic decay; due to the noise inherent to the power spectra, this is rather ambiguous, though. The power spectra of the higher modes feature peaks at higher wave numbers, albeit being less pronounced (ξ_2: $j \approx 80$ and $j \approx 130$; ξ_{10}: $j \approx 150$); this is in line with

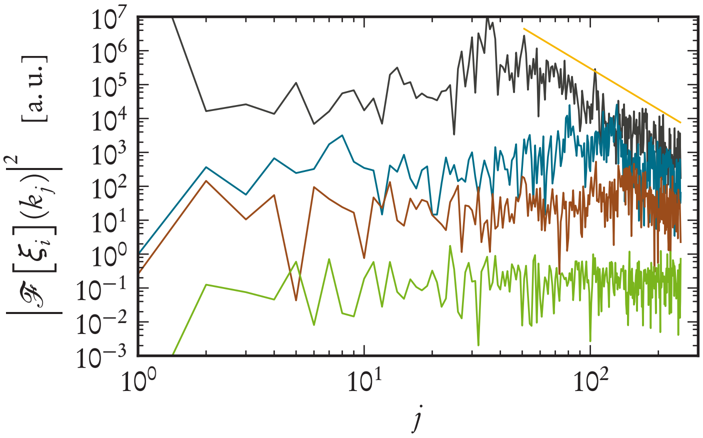

Figure 9.19: *Power spectra of the time series of the amplitudes, i. e. squared norm of the* Fourier *transform of the rows ξ_i of Ξ, with k_j being the wave number; the yellow line indicates an algebraic decay $\sim j^{-4}$. Only spectra corresponding to time series from figure* 9.17 *are shown, also with the same colors. The spectra are shifted vertically for illustration purposes.*

the assumption from before that the higher modes are responsible for the smaller-scale features that fluctuate on a faster time scale, e. g. the deformation and oscillation of the corner rolls. The spectrum of ξ_{100} is completely flat and thus suggests a noise-like temporal behavior of the higher modes, which fits the general picture, as the higher modes are also spatially becoming more and more noise-like.

With the statistical analysis of the time series presented in this section, new possibilities present themselves to model a convective flow: As the temporal statistics (represented by PDF and spectrum, figures 9.18 and 9.19) and the importance (represented by the eigenvalues, figure 9.1) of the modes are known, one can artificially generate random time series of the amplitudes which have the same PDF and spectrum (or, at least, a representative band of wave numbers), and decide for an intended number of modes to generate a synthetic ensemble of snapshots of arbitrary size and arbitrary temporal spacing. As the eigenvalues, modes and temporal statistics are obtained from actual, "physical" data and the modes excel in maximizing the heat transport, this ansatz can be expected to produce physically sound artificial data with few modes – in a sense, "the physics" behind the Rayleigh–Bénard system also try to maximize the heat transport through the fluid layer. The implementation and analysis of the proposed procedure is beyond the scope of this thesis, though. Also, it has to be emphasized that this procedure is different from the lower-dimensional projection shown in the previous sections, as there the *true* time series of the modes where used instead of randomly generated ones.

10 Summary and Outlook

This part of the thesis started with an introduction into the topic of proper orthogonal decomposition, which is often used in fluid dynamics to investigate the predominant spatial structures of flow configurations. The idea behind POD is to obtain a set of orthonormal basis modes that can describe the flow in an optimal way; mathematically speaking, this optimality is achieved by means of a variational principle, which physically amounts to each mode capturing the most possible (generalized) energy. The variational principle boils down to solving the eigenvalue problem of the covariance function, where the eigenfunctions are the orthonormal basis modes and the eigenvalues are the corresponding energies. We then gave the relevant formulas for a discrete matrix formulation in a recipe-like fashion aimed towards a numerical implementation, and also presented the best way to calculate transformations and projections in the POD basis. Also, we introduced the method of snapshots as an alternate, numerically more feasible way to compute the modes from the high-dimensional data sets that are characteristic for fluid dynamics.

These general methods where then tested at a data set of two-dimensional Rayleigh–Bénard convection confined in a box. We obtained the modes and eigenvalue spectrum, and could relate them to spatial features of the flow, e. g. the large-scale circulation or corner flows.

As the generalized energy (i. e., kinetic energy plus temperature variance) is not a physically meaningful quantity, we then developed a way to adapt the POD technique so that it optimally describes the convective heat transport instead – the analysis of the related Nusselt number is physically highly relevant, as it is one of the key ingredients in Rayleigh–Bénard research. This new method hinges on the definition of a certain scalar product such that the induced squared norm of a snapshot represents its convective heat transport. Although the formulas had to be slightly modified due to mathematical complications, we could analyze the data set with the Nu-optimizing modes. It was found that the new method is able to extract spatial structures that amount to strong events of heat transport, e. g. plumes. Also, the POD modes can be grouped into positive and negative heat transport, which allowed for lower-dimensional projections that give the same or even an enhanced heat transport compared to the full system. We found that the Nu-modes perform significantly better in describing the heat transport when compared to the E-modes; this could be traced back to the new method being sensitive to the local convective heat transport, which we proved by examining its PDF. In the end, we analyzed the temporal statistics of the time series obtained by transforming the data set into the POD basis, which suggested an ansatz to generate arbitrarily large, artificial data sets from relatively few modes. This had to remain as future work, though.

In a further outlook, the methods should be applied to larger data sets – e. g., cylindrical three-dimensional data to further understand the structures that contribute the most to the convective heat transport or hinder it in this changed geometry. The numerical cost rises quadratically with the number of degrees of freedom, though; therefore we decided to analyze a longer time span of 500 snapshots for a two-dimensional data set instead of a short time span for a three-dimensional one (in comparison, BAILON-CUBA *et al.* (2010) could only use 100 three-dimensional snapshots due to computational limitations). The newly developed method should be able to cope with three-dimensional convection data as well, though care has to be taken, as the convective NUSSELT number we are optimizing only depends on one of the three velocity components. Comments on this are given in section B.7.[1]

As a distant goal, we expect it to be worthwhile to further analyze in detail how a stronger heat transport is achieved by lower-dimensional projections: We have seen that the heat transport may actually be enhanced when omitting the negative modes. By investigating projections onto only the negative modes, one could be able to identify typical flow configurations that reduce the heat transport. If there was a way to actively suppress these kind of flow configurations, e. g. by building appropriate barriers into the fluid vessel, it could perhaps be possible to actively enhance the heat transport in convection experiments. Of course, this adaption of our newly developed method aimed towards technical or industrial applications remains speculative, but still rather promising.

---

[1] Also, the publication LÜLFF (2015) that was produced in accordance to the present part implements the three-dimensional POD analysis that is only sketched here.

Part III

Statistical Analysis of the Forced SWIFT–HOHENBERG Equation

For the limit of small Rayleigh numbers, the Rayleigh–Bénard system displays stable coherent structures in the form of convection rolls. Depending on the chosen parameters, for example the applied temperature gradient, the convection rolls may lie parallel to each other or form tangled patterns when viewed from above. Frequently, one is not interested in the full three-dimensional structure of the velocity and temperature fields described by the full Oberbeck–Boussinesq equations, but only in the resulting patterns that the convection rolls form. This two-dimensional pattern forming behavior is described by the Swift–Hohenberg equation, a nonlinear partial differential equation that can be obtained from the full system in the limit of small Rayleigh numbers; the equation gives the temporal evolution of an order parameter that corresponds to a horizontal slice of the temperature field of Rayleigh–Bénard convection.

In this part, we will analyze the statistical behavior of the Swift–Hohenberg equation forced by noise, which may be thought of as temperature fluctuations induced by inhomogeneities of the horizontal plates of the Rayleigh–Bénard system. To this end, we will derive an evolution equation for the probability density function (PDF) of the order parameter along the lines of the Lundgren–Monin–Novikov hierarchy already covered in part I of this thesis. The PDF equation contains unclosed terms in the form of conditional averages that are estimated from direct numerical simulations of the forced Swift–Hohenberg equation. Furthermore, as the system is described by gradient dynamics, the corresponding Lyapunov functional can be used in the analysis of the PDF equation as well as in the simplification of the numerics.

This part of the thesis is structured as follows: After introducing the Swift–Hohenberg equation and motivating its connection to the Rayleigh–Bénard system in chapter 11, we go into detail on the direct numerical simulation (chapter 12) and also give an alternative description in terms of the Lyapunov functional in chapter 13. We then outline the derivation of the PDF equation and present the obtained results in chapter 14 before ending with a conclusion (chapter 15).

11 Introduction

Here we will give an introduction to the behavior of the Rayleigh–Bénard system slightly above the onset of convection: Section 11.1 represents a phenomenological overview of the occurring pattern formation, while section 11.2 motivates how these patterns may be modeled by an order parameter equation – the Swift–Hohenberg equation – and how this is related to the full Oberbeck–Boussinesq equations that describe Rayleigh–Bénard convection.

11.1 Pattern Formation in Convection

When increasing the Rayleigh number, i. e. the control parameter that is connected to the temperature gradient between the horizontal plates in a Rayleigh–Bénard system, a variety of different flow regimes emerges. For high Rayleigh numbers, the fluid is turbulent and erratic, as was the case in the preceding parts of this thesis; cf. also figures 1.1 and 1.2 of the introduction on pages 2 and 3. On the other end of the spectrum, i. e. for Rayleigh numbers below the critical one, there is no convection at all, the fluid is at rest, and heat transport between the plates happens purely by conduction.

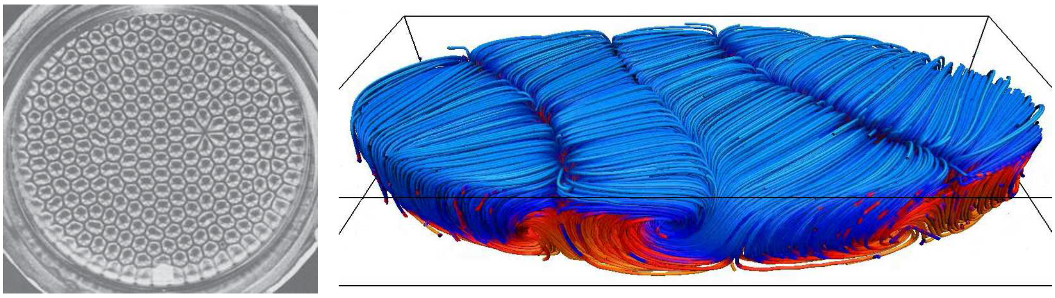

Figure 11.1: *Examples of pattern formation in convection. Left: Convection cells from the historic experiment conducted by Bénard; image borrowed from Bénard (1901). See also footnote 1 on page 98. Right: Numerical simulation of the full Rayleigh–Bénard system in an ellipsoidal vessel displaying four convection rolls. Streamlines of the velocity field are shown, with color coding according to the temperature (i. e., red corresponds to hot and blue to cold fluid). The Rayleigh number is* $\mathrm{Ra} = 10^4$, *which corresponds to* $\varepsilon = 4.9$, *cf.* (11.2). *For details, see Lülff (2011, sec. 3.7).*

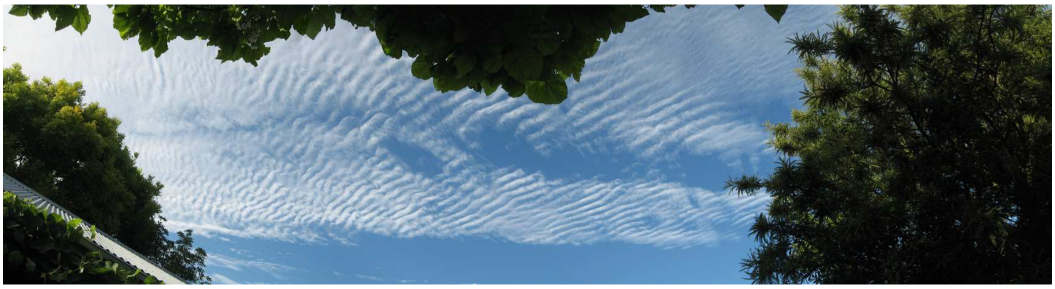

Figure 11.2: *Clouds of the* undulatus *type that show a stripe pattern. Image courtesy of O'Beirne (2009).*

In this part of the thesis, we are interested in the behavior in the intermediate flow regime when the Rayleigh number is slightly above the critical one. It is long known that in this flow regime, stable convection patterns emerge, as exemplified in figure 11.1, where an experimental and a numerical convection system are shown that form hexagons respectively stripes. In fact, the foundations of Rayleigh–Bénard research were laid by Bénard (1901) when studying these patterns experimentally and by their analytical description due to Rayleigh (1916).[1] This research continues until today, and recent developments and also examples of Rayleigh–Bénard convection near the onset are given in the review by Bodenschatz *et al.* (2000). Furthermore, many examples of pattern formation arise in convective systems that occur in nature, e. g. the distinct stripe pattern in clouds of the so-called *undulatus* type in figure 11.2; further examples are found in the review article by Cross and Hohenberg (1993).

11.2 Randomly Forced SWIFT–HOHENBERG Equation

The convection patterns in the figures above are prime examples of what Haken (1975) introduced as the *slaving principle*: The macroscopic, slowly varying modes – i. e., the convection patterns – determine or *enslave* the behavior of the fast, microscopic modes (e. g., the dynamics on the level of single fluid particles). Thus, only the dynamics of the macroscopic modes (also called *order parameters*) determine the behavior of the whole system, and the microscopic degrees of freedom quickly follow the order parameters (for an introduction into this topic, see Argyris *et al.* (2010, sec. 6.8)).

Following this reasoning, it often is not necessary to know the details of all microscopic degrees of freedom, i. e. the dynamics on the smallest scales as described by the Oberbeck–

---

[1] We note that the hexagonal pattern of figure 11.1 (left) is not an example of Rayleigh–Bénard convection in a strict sense, as the pattern is in part caused by surface effects – for example the Bénard–Marangoni effect, i. e. temperature dependence of the surface tension, see e. g. Chandrasekhar (1981, sec. 18) – that are not present in the Rayleigh–Bénard system. Still, the experiment of Bénard is an example of a pattern-forming convective system.

BOUSSINESQ equation. Instead, the pattern forming behavior of convective systems can be described by an evolution equation of a macroscopic order parameter field $\psi(\boldsymbol{x},t)$ with $\boldsymbol{x} \in \Omega \subset \mathbb{R}^2$. This thinking led SWIFT and HOHENBERG (1977) to introduce the following partial differential equation:

$$\frac{\partial}{\partial t}\psi(\boldsymbol{x},t) = \varepsilon\psi(\boldsymbol{x},t) - (\Delta+1)^2\psi(\boldsymbol{x},t) - \psi(\boldsymbol{x},t)^3 \tag{11.1}$$

The order parameter ψ is related to the temperature field in a horizontally extended plane in the RAYLEIGH–BÉNARD system. The terms on the right-hand side consist of a linear driving $\varepsilon\psi$ where ε can be seen as the temperature difference δT of hot bottom and cold top plate in units of the critical temperature difference δT_{c} at the onset of convection, i. e.

$$\varepsilon := \frac{\delta T}{\delta T_{\mathrm{c}}} - 1 = \frac{\mathrm{Ra}}{\mathrm{Ra}_{\mathrm{c}}} - 1 \quad , \tag{11.2}$$

cf. SWIFT and HOHENBERG (1977, equation (22a)). Here we have used that the RAYLEIGH number Ra is proportional to the temperature difference, cf. (1.1), and convection respectively pattern formation sets in for $\varepsilon > 0$. The linear driving is saturated by the cubic[2] nonlinearity $-\psi^3$, and the spatial linear operator $-(\Delta+1)^2$ selects patterns with a wave vector $|\boldsymbol{k}| \approx 1$ or equivalently a wave length of 2π.[3]

An example of the patterns that emerge from the SWIFT–HOHENBERG equation (11.1) is given in figure 11.3. It shows snapshots of a two-dimensional numerical simulation (cf. chapter 12), and a stripe pattern is obtained that reminds of convection rolls in a horizontally extended layer of fluid that is viewed from above. In the beginning, the system quickly establishes a pattern with a distinct wave length, and stripes are formed. The so-called *defects* (e. g., points where a convection roll ends or where two rolls merge) then wander around (cf. the shift of the defect in the upper-left corner from $t = 140$ to $t = 240$) and annihilate each other, while the dynamics gradually become slower and slower.

Equation (11.1) describes a deterministic evolution of the order parameter ψ obeying gradient dynamics,[4] i. e. the system dynamics slow down over time and come to rest in a stationary pattern of perfect parallel stripes for $t \to \infty$. On the other hand, when noise enters the equation, the system is pushed out of these stable configurations; this noise may be thought of as e. g. an irregular heating of the hot bottom and cold top plates in a

---

[2] Some authors also add a quadratic nonlinearity $\psi(\boldsymbol{x},t)^2$. We will not consider this case, but more details are given in section C.1.

[3] Usually the spatial operator is written as $\left(\Delta + k_{\mathrm{c}}^2\right)^2$, which instead selects patterns with wave vector $|\boldsymbol{k}| \approx k_{\mathrm{c}}$. By rescaling the spatial coordinates, though, it is possible to choose the critical wave number $k_{\mathrm{c}} = 1$ without loss of generality.

[4] We will go into detail on gradient dynamics in chapter 13.

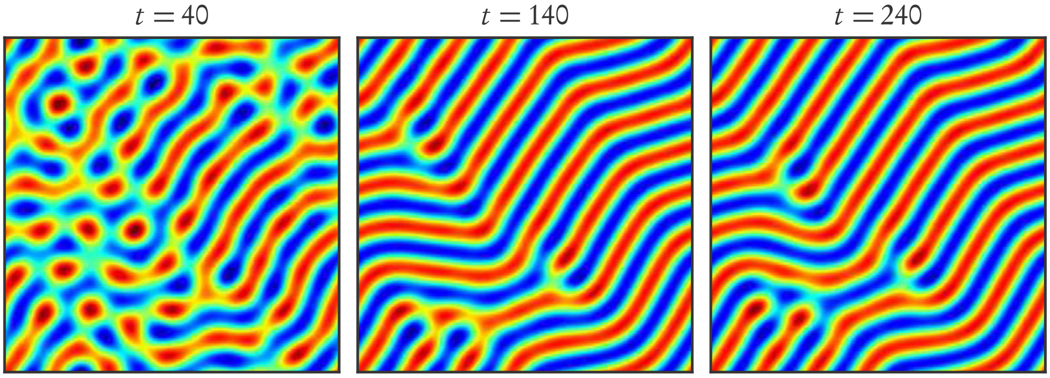

Figure 11.3: *Example of patterns formed by the* Swift–Hohenberg *equation at different times for $\varepsilon = 0.3$ and a simulation domain $\Omega = [0, 16\pi] \times [0, 16\pi]$ with periodic boundaries. The field $\psi(\boldsymbol{x})$ is color coded and varies between -0.8 (blue) and 0.8 (red). The initial condition is a noise field with small amplitude. Details of the numerics are given in chapter 12. The order parameter field $\psi(\boldsymbol{x})$ forms a pattern reminiscent of convection rolls with a predominant wavelength.*

Rayleigh–Bénard experiment or as fluctuating internal sources of heat. This leads to the stochastically driven Swift–Hohenberg equation:

$$\frac{\partial}{\partial t}\psi(\boldsymbol{x}, t) = \varepsilon\psi(\boldsymbol{x}, t) - (\Delta + 1)^2\psi(\boldsymbol{x}, t) - \psi(\boldsymbol{x}, t)^3 + \Gamma(\boldsymbol{x}, t) \tag{11.3}$$

Here, Γ is a stochastic force with zero mean that is δ-correlated in time and has a certain correlation function $c(|\boldsymbol{r}|)$ in space, i. e.

$$\left\langle \Gamma(\boldsymbol{x}, t) \right\rangle = 0 \tag{11.4a}$$

$$\left\langle \Gamma(\boldsymbol{x}, t)\Gamma(\boldsymbol{x} + \boldsymbol{r}, t') \right\rangle = c(|\boldsymbol{r}|)\,\delta(t - t') \tag{11.4b}$$

with $c(0) = C_0$ as a measure of the noise strength. Note that a stochastic force was already introduced in the fundamental publication by Swift and Hohenberg (1977).

The system described by (11.3)–(11.4) still displays gradient dynamics, but the “kicks” introduced by the stochastic force Γ enable the order parameter field $\psi(\boldsymbol{x}, t)$ to explore larger areas of the phase space. Also, due to the unpredictable nature of the force Γ, a certain realization of $\psi(\boldsymbol{x}, t)$ is of less interest than the statistics the order parameter obeys. We will come back to this when we analyze the probability density function (PDF) in chapter 14 after we go into the details of the numerical simulation of (11.3) in chapter 12.

12 Numerics

Due to its nonlinear nature, the Swift–Hohenberg equation in general cannot be solved analytically, and thus, we have to resort to direct numerical simulations of the forced system. The simulation involves two major topics: The calculation of the spatial operators, for which we will use the pseudospectral method as described in section 12.1, and the temporal integration of the equations (section 12.2), which needs extra care due to the form of the spatial operator and the stochastic force. We will keep the description of both the pseudospectral scheme as well as the time-stepping relatively short; a more elaborated portrayal of the general techniques may be found in Lülff (2011, sec. 2).

12.1 Pseudospectral Scheme

To handle the forced Swift–Hohenberg equation (11.3) with the pseudospectral method, we apply the Fourier transformation

$$\mathscr{F}\big[\psi(\boldsymbol{x},t)\big](\boldsymbol{k},t) = \frac{1}{2\pi}\int \mathrm{d}^2x\, \psi(\boldsymbol{x},t)\,\mathrm{e}^{-\mathrm{i}\boldsymbol{k}\cdot\boldsymbol{x}} =: \widetilde{\psi}(\boldsymbol{k},t) \tag{12.1a}$$

$$\mathscr{F}^{-1}\big[\widetilde{\psi}(\boldsymbol{k},t)\big](\boldsymbol{x},t) = \frac{1}{2\pi}\int \mathrm{d}^2k\, \widetilde{\psi}(\boldsymbol{k},t)\,\mathrm{e}^{\mathrm{i}\boldsymbol{k}\cdot\boldsymbol{x}} \quad = \psi(\boldsymbol{x},t) \tag{12.1b}$$

with $\widetilde{\psi}(\boldsymbol{k},t)$ denoting the time-dependent Fourier coefficients and $\boldsymbol{k} \in \mathbb{R}^2$ the wave number vector. As the Fourier transformation of a spatial derivative obeys the relation

$$\mathscr{F}\left[\nabla\psi\right] = \mathrm{i}\boldsymbol{k}\mathscr{F}\left[\psi\right] = \mathrm{i}\boldsymbol{k}\widetilde{\psi} \quad , \tag{12.2}$$

which can easily be seen through integration by parts, the forced Swift–Hohenberg equation in Fourier space reads

$$\frac{\partial}{\partial t}\widetilde{\psi} = \varepsilon\widetilde{\psi} - (-\boldsymbol{k}^2+1)^2\widetilde{\psi} - \mathscr{F}\left[\psi^3\right] + \mathscr{F}[\Gamma] \quad . \tag{12.3}$$

Thus, the partial differential equation (11.3) in real space is transformed into a set of ordinary differential equations in Fourier space.

The pseudospectral ansatz now means that instead of calculating the Fourier transform of the cubic term by convolutions of $\widetilde{\psi}$ in Fourier space, the calculation is instead carried out in real space by utilizing the inverse FOURIER transform, i. e. inserting $\psi = \mathscr{F}^{-1}\big[\widetilde{\psi}\big]$. Therefore, the full pseudospectral scheme reads

$$\frac{\partial}{\partial t}\widetilde{\psi} = \varepsilon\widetilde{\psi} - (-\boldsymbol{k}^2+1)^2\widetilde{\psi} - \mathscr{F}\left[\mathscr{F}^{-1}\big[\widetilde{\psi}\big]^3\right] + \mathscr{F}[\Gamma] \quad . \tag{12.4}$$

The cubic term introduces the so-called *aliasing* phenomenon when solving (12.4), cf. ORSZAG (1971): Due to the nonlinearity, the FOURIER modes that belong to different wave vectors interact and produce high frequencies that are not resolved by the numerical grid and therefore misinterpreted as lower frequencies. To prevent this, one usually *dealiases* the fields, i. e. removes frequencies from the system that would cause aliasing in the cubic nonlinearity. We found, though, that dealiasing is not necessary here, as the term $(-\boldsymbol{k}^2+1)^2\widetilde{\psi}$ favors wave numbers with $|\boldsymbol{k}| \approx 1$ while strongly damping all other (higher) wave numbers (the damping strength grows approximately with the fourth power of the distance from $|\boldsymbol{k}| = 1$ for big $|\boldsymbol{k}|$). Therefore, "the physics" of the system already make sure that no problematic high wave numbers are active, which renders dealiasing redundant.

12.2 Semi-Implicit Time-Stepping

After having dealt with the spatial terms by utilizing the pseudospectral scheme in the previous section, we now have to integrate (12.4) with a time-stepping scheme. It turns out that explicit schemes such as the classical RUNGE–KUTTA method of fourth order are unsuitable for the system at hand, because the strongly diffusing spatial operator $(\Delta+1)^2$ (or, thinking in FOURIER space, the high values that the prefactor $(-\boldsymbol{k}^2+1)^2$ of the corresponding term takes) imposes a severe restriction on the minimal time step.

To prevent this, we employ the semi-implicit EULER scheme to integrate the stochastic differential equation (12.4), cf. JENTZEN and KLOEDEN (2009). It treats the linear term implicitly by evaluating it in the future while handling the nonlinear term explicitly and the noise term in the ITŌ-sense, i. e. evaluating it at the beginning t of the time interval. Thus, after approximating the temporal derivative by finite differences with time step Δt, (12.4) reads

$$\begin{aligned} &\widetilde{\psi}(t+\Delta t) - \widetilde{\psi}(t) = \\ &\quad \Delta t\left(\varepsilon - (-\boldsymbol{k}^2+1)^2\right)\widetilde{\psi}(t+\Delta t) + \Delta t\,\mathscr{F}\left[\mathscr{F}^{-1}\big[\widetilde{\psi}(t)\big]^3\right] + \sqrt{\Delta t}\,\mathscr{F}\left[\Gamma(t)\right] \end{aligned} \tag{12.5}$$

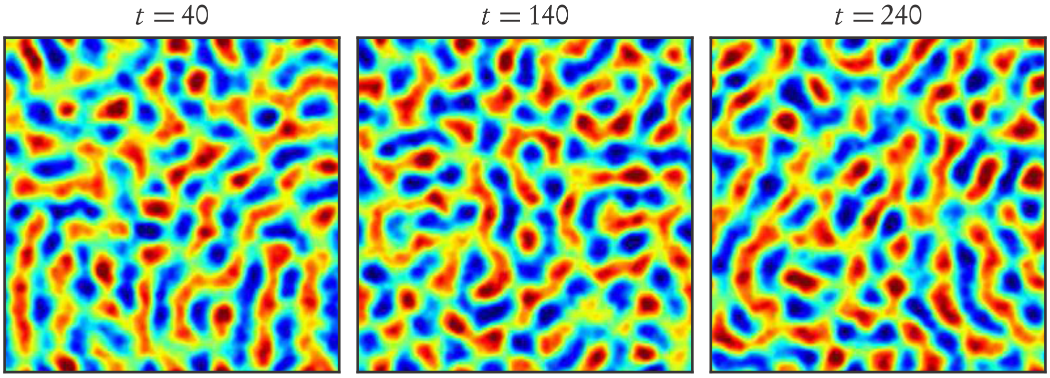

Figure 12.1: *Numerical solution of the stochastically driven Swift–Hohenberg equation* (11.3) *with* $\varepsilon = 0.3$ *and a simulation domain* $\Omega = [0, 16\pi] \times [0, 16\pi]$*. Color scale as described in figure* 11.3*. The noise strength is chosen as* $C_0 = 0.4$*, and the correlation length is* 1.5 *grid points, i. e.* $l = 16\pi\frac{1.5}{256} \approx 0.29$ *for a resolution of* 256×256 *grid points.*

where all $\widetilde{\psi}$ also depend on the wave vector $\boldsymbol{k}$. Equation (12.5) can easily be solved for $\widetilde{\psi}(t + \Delta t)$ to yield an explicit formula to calculate the next time step:

$$\widetilde{\psi}(t + \Delta t) = \frac{1}{1 - \Delta t\left(\varepsilon - (-\boldsymbol{k}^2 + 1)^2\right)} \left(\widetilde{\psi}(t) + \Delta t \mathscr{F}\left[\mathscr{F}^{-1}\left[\widetilde{\psi}(t)\right]^3\right] + \sqrt{\Delta t}\mathscr{F}\left[\Gamma(t)\right]\right) \tag{12.6}$$

As the diffusing term $(\Delta + 1)^2$ is now handled implicitly, it does not pose a restriction on the time step in order to obtain a stable temporal integration. Furthermore, the solution of a linear system that is usually needed when using implicit schemes is trivial here, because the linear operator $\varepsilon - (\Delta + 1)^2$ is diagonal in Fourier space.

Equation (12.6) is solved numerically by discretizing ψ and $\widetilde{\psi}$ on a two-dimensional uniform grid and utilizing the *fast Fourier transform*-algorithm (Cooley and Tukey, 1965), which results in periodic boundary conditions in both directions. In the following we use a resolution of 32 grid points per period of the stripe pattern, i. e. a grid spacing of $\Delta x = \frac{2\pi}{32}$, in accordance with Hernández-García *et al.* (1992). The noise $\Gamma(\boldsymbol{x}, t)$ is Gaussian distributed, δ-correlated in time, and the spatial correlation function is chosen to be a Gaussian bell curve with correlation length l, i. e.

$$\left\langle \Gamma(\boldsymbol{x}, t)\Gamma(\boldsymbol{x} + \boldsymbol{r}, t')\right\rangle = C_0 \mathrm{e}^{-\frac{r^2}{2l^2}}\, \delta(t - t') \quad . \tag{12.7}$$

This form of the spatial correlation ensures that the noise field $\Gamma(\boldsymbol{x}, t)$ is differentiable. Details on how to generate the correlated noise are given in section C.2.

An example of the stochastically forced SWIFT–HOHENBERG equation is shown in figure 12.1. The general picture of patterns with a distinct wavelength is comparable to figure 11.3, and also remnants of a labyrinth-like structure of elongated rolls or stripes can be found. However, the patterns are disturbed by the noise term, which causes them to change continuously; in contrast, the system settles in a stationary configuration when it is not subjected to noise.

13 Linear Stability Analysis and LYAPUNOV Functional

NOW WE WILL PERFORM a linear stability analysis of the SWIFT–HOHENBERG equation that explains the spatial structures that emerge from the system. Furthermore, we will recount a description in terms of the LYAPUNOV functional that connects to the linear stability analysis as well as to the gradient dynamics we mentioned earlier on. In the end, we will combine these two techniques to propose a new method to quickly generate ensembles of numerical data obtained from the stochastically forced SWIFT–HOHENBERG equation. This new method saves computational time by reducing the transient initial phase.

13.1 Linear Stability Analysis

A stationary solution of the unforced SWIFT–HOHENBERG equation is trivially given by $\psi(\boldsymbol{x},t) \equiv 0$. The stability of this solution is determined by adding perturbations and investigating their temporal behavior. As the perturbations are assumed to be small, the cubic term $-\psi^3$ can be neglected, which gives rise to the linearized SWIFT–HOHENBERG equation:

$$\frac{\partial}{\partial t}\psi = \left(\varepsilon - (\Delta + 1)^2\right)\psi \tag{13.1}$$

By inserting disturbances in the form of plane waves,

$$\psi(\boldsymbol{x},t) = \mathrm{e}^{\lambda t}\mathrm{e}^{\mathrm{i}\boldsymbol{x}\cdot\boldsymbol{k}} + \text{c. c.} \quad , \tag{13.2}$$

where the wave number vector $\boldsymbol{k} \in \mathbb{R}^2$ gives the direction of the mode, the $\boldsymbol{k}$-dependent growth rate

$$\lambda = \lambda(\boldsymbol{k}) = \varepsilon - (-\boldsymbol{k}^2 + 1)^2 \tag{13.3}$$

is obtained. The requirement for unstable modes, i. e. modes that grow when the stationary solution $\psi \equiv 0$ is subjected to arbitrarily small amounts of noise, is that the growth rate λ is positive, and therefore, only modes in the unstable wave number band

$$1 - \sqrt{\varepsilon} < \boldsymbol{k}^2 < 1 + \sqrt{\varepsilon} \tag{13.4}$$

can be excited for $\varepsilon > 0$. The biggest growth rate $\lambda = \varepsilon$ is obtained for $|\boldsymbol{k}| = 1$ (provided that such wave numbers can be realized[1]), and thus, patterns with a characteristic length scale of preferably $k = 1$ are formed by the SWIFT–HOHENBERG system. On the other hand, λ is always negative for $\varepsilon < 0$, and the trivial solution $\psi \equiv 0$ is stable against perturbations with arbitrary wavelength. The growth of the linear modes is saturated by the cubic nonlinearity for finite amplitudes. In the next section we will show that the amplitude of plane waves of the form (13.2) can be obtained by examining the LYAPUNOV functional.

13.2 Variational Formulation of the SWIFT–HOHENBERG Equation: The LYAPUNOV Functional

The deterministic part of the right-hand side of the SWIFT–HOHENBERG equation can be formulated as the variation of a functional, which yields an alternative and insightful view of the system. Especially, with the variational representation it will become possible to achieve analytical results in the statistical analysis of the SWIFT–HOHENBERG equation, as presented in sections 13.3 and 13.4.

For the SWIFT–HOHENBERG system there exists a LYAPUNOV functional

$$\mathscr{L}[\psi] : C^4(\Omega) \to \mathbb{R} \quad , \tag{13.5}$$

where $\mathscr{L}$ assigns a value to every field configuration $\psi(\boldsymbol{x}) \in C^4(\Omega)$ and $\mathscr{L}$ is bounded from below. Similar to elementary mechanics, where the overdamped (i. e., inertialess) one-dimensional movement in a potential $V(x)$ can be expressed as $\dot{x} = -\frac{\mathrm{d}}{\mathrm{d}x} V(x)$, the LYAPUNOV functional yields the right-hand side of the unforced SWIFT–HOHENBERG equation (11.1) in the form

$$\frac{\partial}{\partial t}\psi(\boldsymbol{x},t) = -\frac{\delta \mathscr{L}[\psi]}{\delta \psi(\boldsymbol{x},t)} \quad , \tag{13.6}$$

where $\frac{\delta \mathscr{L}[\psi]}{\delta \psi(\boldsymbol{x},t)}$ denotes the functional derivative of $\mathscr{L}[\psi]$ with respect to $\psi(\boldsymbol{x},t)$. An overview of variational calculus including rules of calculating functional derivatives is given in section C.3. With the tools presented there, it is easy to see that the choice

$$\mathscr{L}[\psi] = \int_\Omega \mathrm{d}^2x' \left(-\frac{\varepsilon}{2}\psi(\boldsymbol{x}')^2 + \frac{1}{4}\psi(\boldsymbol{x}')^4 + \frac{1}{2}\big(\Delta\psi(\boldsymbol{x}') + \psi(\boldsymbol{x}')\big)^2 \right) \tag{13.7}$$

results in the SWIFT–HOHENBERG equation. A variational formulation was already given in the pivotal publication by SWIFT and HOHENBERG (1977); their exact form of $\mathscr{L}$ differed

---

[1] For periodic boundary conditions, as are used in the numerics, the $\boldsymbol{k}$-vector can only take discrete values. However, choosing the system size as an integer multiple of 2π assures that plane waves with $k = 1$ can exist.

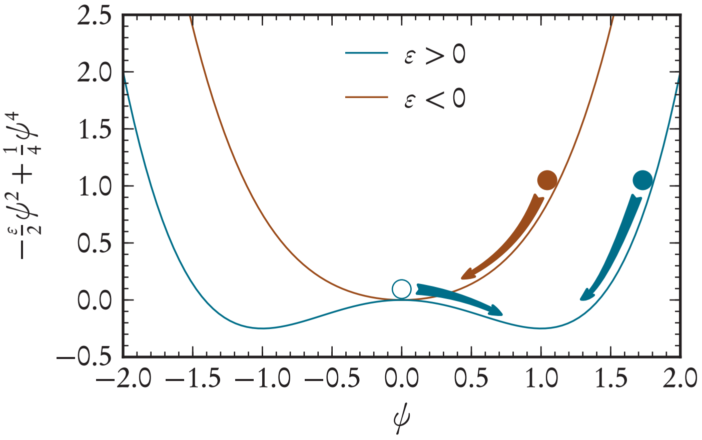

Figure 13.1: *Qualitative illustration of the competition of linear driving versus cubic saturation in the LYAPUNOV functional of the SWIFT–HOHENBERG equation. For $\varepsilon < 0$, $\psi = 0$ is the stable minimum, while for $\varepsilon > 0$, $\psi = 0$ is an unstable stationary point and additional stable minima appear at $\psi \neq 0$.*

slightly, though, as one has a certain freedom of choosing $\mathscr{L}$, provided that the functional derivative yields the correct right-hand side.

In the form of $\mathscr{L}$ chosen here, it becomes immediately clear that apart from the quadratic one related to the linear driving (i. e., $-\frac{\varepsilon}{2}\psi^2$), all terms are positive. Due to the positive quartic term that for sufficiently large amplitudes surpasses the quadratic term, $\mathscr{L}$ is bounded from below. Therefore, the evolution equation (13.6) states that the system moves in a *steepest descent*-manner towards (local) minima of $\mathscr{L}$ which correspond to stationary solutions of the problem; this behavior is referred to as *gradient dynamics*. For $\varepsilon < 0$, all terms in (13.7) are positive and $\mathscr{L} \geq 0$, and the system tends towards the global minimum $\mathscr{L} = 0$ at $\psi(\boldsymbol{x}) \equiv 0$. Contrary, for $\varepsilon > 0$, the minimum of $\mathscr{L} < 0$ is reached for $\psi(\boldsymbol{x}) \not\equiv 0$, and pattern formation occurs. These two cases agree with the observations made in the linear stability analysis in section 13.1. The different qualitative behavior for $\varepsilon \gtrless 0$ is also illustrated in figure 13.1, with arrows indicating the overdamped movement, and the open circle stands for an unstable stationary point.

13.2.1 Plane Waves and LYAPUNOV Functional

The optimal amplitude of plane waves, i. e. the one that minimizes $\mathscr{L}$, can be obtained by inserting the ansatz

$$\psi(\boldsymbol{x}) = \alpha e^{i\boldsymbol{k}\cdot\boldsymbol{x}} + \text{c. c.} \tag{13.8}$$

into the LYAPUNOV functional, which results in

$$\mathscr{L}\left[\alpha e^{i\boldsymbol{k}\cdot\boldsymbol{x}} + \text{c. c.}\right] = V(\Omega)\left(-\varepsilon\alpha^2 + \frac{3}{2}\alpha^4 + (-\boldsymbol{k}^2+1)^2\alpha^2\right) \tag{13.9a}$$

$$= V(\Omega)\left(-\lambda(\boldsymbol{k})\alpha^2 + \frac{3}{2}\alpha^4\right) \tag{13.9b}$$

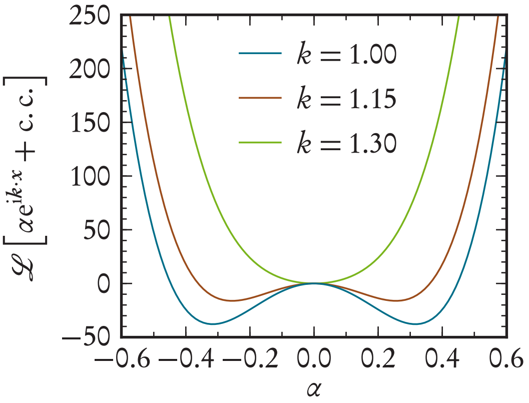

Figure 13.2: *Lyapunov functional of plane waves in dependence on their amplitude α for different wave numbers k and $\varepsilon = 0.3$. Plane waves with $k = 1$ and $k = 1.15$ are unstable, and $\mathscr{L}$ displays a minimum for $\alpha \neq 0$, with its position and value given by* (13.11) *and* (13.12), *respectively. The wave number $k = 1.3$ is outside the unstable wave number band* (13.4), *and the minimum of $\mathscr{L} = 0$ at $\alpha = 0$ corresponds to the stable trivial solution.*

with the growth rate $\lambda(\boldsymbol{k})$ as in (13.3) and $V(\Omega)$ the area of the spatial domain Ω. The optimal amplitudes α are then obtained by minimizing the above expression,

$$\frac{\partial}{\partial \alpha}\mathscr{L}\left[\alpha e^{i\boldsymbol{k}\cdot\boldsymbol{x}} + \text{c.c.}\right] \overset{!}{=} 0 \quad , \tag{13.10}$$

which yields the amplitudes

$$\alpha = \sqrt{\frac{1}{3}\lambda(\boldsymbol{k})} \quad \text{or} \quad \alpha = 0 \quad . \tag{13.11}$$

The trivial solution $\psi(\boldsymbol{x}) \equiv 0$ for $\alpha = 0$ with $\mathscr{L} = 0$ always exists, with the stability depending on $\lambda(\boldsymbol{k})$, while the non-trivial solution $\alpha_{\text{min}} = \sqrt{\frac{1}{3}\lambda(\boldsymbol{k})}$ with $\mathscr{L} < 0$ exists only for $\lambda(\boldsymbol{k}) > 0$, which is in agreement with the former observations. The Lyapunov functional takes the value

$$\mathscr{L}\left[\alpha_{\text{min}} e^{i\boldsymbol{k}\cdot\boldsymbol{x}} + \text{c.c.}\right] = -\frac{V(\Omega)}{6}\lambda(\boldsymbol{k})^2 \tag{13.12}$$

and is minimal for $|\boldsymbol{k}| = 1$, as can be expected *a priori* from the linear stability analysis. These findings are illustrated in figures 13.2 and 13.3.

By directly inserting the Fourier series ansatz[2]

$$\psi(\boldsymbol{x}) = \sum_{n=0}^{\infty} A_n \sin\big((2n+1)\,\boldsymbol{k}\cdot\boldsymbol{x}\big) \tag{13.13}$$

into the Swift–Hohenberg equation and sorting terms of different order, Viñals *et al.* (1991) reported the amplitude $A_0 = 2\sqrt{\frac{1}{3}\lambda(\boldsymbol{k})}$. This corresponds to our result (13.11), where the additional factor of 2 is due to the different ansatz functions used, i. e. $\sin(\boldsymbol{k}\cdot\boldsymbol{x})$ versus $e^{i\boldsymbol{k}\cdot\boldsymbol{x}} + \text{c.c.}$

---

[2] Due to symmetry considerations, only odd multiples of the wave number vector $\boldsymbol{k}$ make sense, as even multiples would result in fields that have no reflectional symmetry.

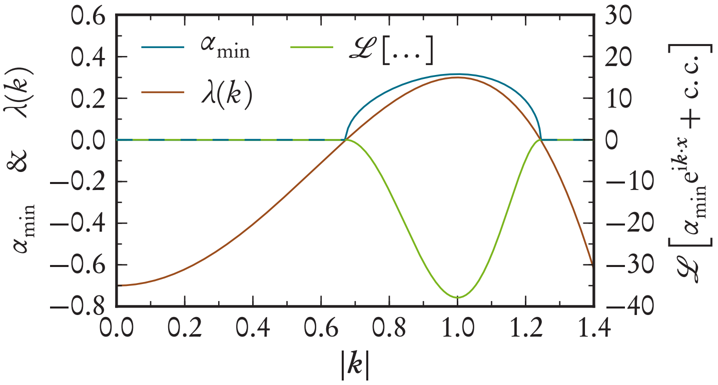

Figure 13.3: *LYAPUNOV functional $\mathscr{L}$* (13.12), *optimal amplitude $\alpha_{\min}$* (13.11) *and growth rate $\lambda(k)$* (13.3) *of plane waves in dependence on their wave number k and for $\varepsilon = 0.3$. Outside the unstable wave number band, $\alpha_{\min}$ and $\mathscr{L}$ are zero.*

13.2.2 Plane Waves Compared to Stationary Solutions

After the linear stability analysis resulted in the modes that become unstable and the LYAPUNOV functional gave their amplitude, the question remains how close these plane waves are to stationary solutions of the full nonlinear problem. It is stated by VIÑALS *et al.* (1991) that for stationary solutions of the SWIFT–HOHENBERG equation the coefficients A_n in (13.13) are of the order $\varepsilon^{n+1/2}$, provided that $|\boldsymbol{k}| \approx 1$. Also, the second coefficient is explicitly given as $A_1 = -\frac{A_0^3}{4\lambda(3\boldsymbol{k})}$. For $\varepsilon = 0.3$ and $|\boldsymbol{k}| = 1$, as is also used in the numerical simulations of this chapter, this results in the amplitudes $A_0 = 0.632$ and $A_1 = 0.993 \times 10^{-3}$ of the first two modes, i. e. already the first two modes differ by a factor of $\mathcal{O}(1000)$ in strength. The LYAPUNOV functional of the two-mode ansatz $\psi_2 = A_0 \sin(\boldsymbol{k}\cdot\boldsymbol{x}) + A_1 \sin(3\boldsymbol{k}\cdot\boldsymbol{x})$ can be calculated exactly:

$$\mathscr{L}[\psi_2] = -\frac{V(\Omega)}{6}\lambda(\boldsymbol{k})^2\left(1 - \frac{2}{9}\frac{\lambda(\boldsymbol{k})}{\lambda(3\boldsymbol{k})} - \left(\frac{2}{3}\frac{\lambda(\boldsymbol{k})}{\lambda(3\boldsymbol{k})}\right)^2 - \left(\frac{1}{3}\frac{\lambda(\boldsymbol{k})}{\lambda(3\boldsymbol{k})}\right)^4\right) \tag{13.14}$$

Numerical values for the one-mode ansatz (i. e., $\psi_1 = A_0 \sin(\boldsymbol{k}\cdot\boldsymbol{x})$) and the two-mode ansatz are

$$\mathscr{L}[\psi_1] = -37.8993 \quad \text{and} \quad \mathscr{L}[\psi_2] = -37.9386 \quad , \tag{13.15}$$

cf. (13.12) and (13.14), and the two values differ by 0.1 %.[3] As furthermore the higher modes in the FOURIER ansatz (13.13) contribute less and less to the LYAPUNOV functional, it can be expected that already the one- or two-mode ansatz is very close to actual stationary solutions of the SWIFT–HOHENBERG equation.

To further pinpoint the relation between plane waves and stationary solutions, we numerically solved the unforced SWIFT–HOHENBERG equation from initial conditions consisting of one mode and of two modes. The results are shown in figure 13.4, and it is seen

---

[3] As a comparison, the labyrinth-like structure in figure 11.3, corresponding to the same parameters, has a value of $\mathscr{L} = -34.51$.

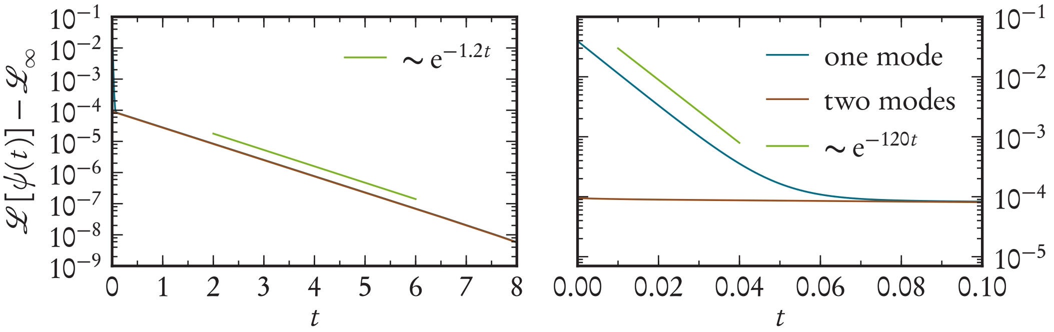

Figure 13.4: *Temporal evolution of the* LYAPUNOV *functional of the* SWIFT–HOHENBERG *equation, estimated from numerical simulations for* $\varepsilon = 0.3$. *Initial conditions consisted of one or two modes with* $|\boldsymbol{k}| = 1$, *cf. text and ansatz* (13.13). *The difference of* $\mathscr{L}[\psi(t)]$ *and the value* $\mathscr{L}_\infty \approx -37.9387$ *for large times, i. e. when the dynamics became stationary, is plotted logarithmically. The right panel magnifies the early times.*

that the value of the LYAPUNOV functional exponentially approaches the stationary value $\mathscr{L}_\infty$. From the magnification in the right panel of the figure, it also becomes clear that the difference when using ψ_1 or ψ_2 as initial conditions vanishes very quickly. Furthermore, the relative difference between $\mathscr{L}_\infty \approx -37.9387$ (estimated from the numerics) and the initial values of $\mathscr{L}[\psi_1]$ respectively $\mathscr{L}[\psi_2]$ amounts to $0.1\,\%$ respectively $0.26 \times 10^{-3}\,\%$. Therefore we conclude that an initial condition consisting of one or two modes is a very good approximation of a true stationary solution, as ψ_1 (and even slightly more so ψ_2) are in the direct vicinity of a deep minimum of the LYAPUNOV functional, which is reached exponentially fast.

13.3 The Functional FOKKER–PLANCK Equation

Up to now we only considered the unforced SWIFT–HOHENBERG equation in the LYAPUNOV functional formalism, and found that the evolution of the system is described by gradient dynamics. On the other hand, in the functional formulation of the *stochastically forced* SWIFT–HOHENBERG equation,

$$\frac{\partial}{\partial t}\psi(\boldsymbol{x},t) = -\frac{\delta\mathscr{L}[\psi]}{\delta\psi(\boldsymbol{x},t)} + \Gamma(\boldsymbol{x},t) \quad , \tag{13.16}$$

it becomes clear that the forced system does not show pure gradient dynamics: While traveling towards local minima, the noise kicks the solution around in phase space, and thus the evolution does not monotonously minimize $\mathscr{L}$. This in turn means that the forced SWIFT–HOHENBERG system can escape shallow local minima of $\mathscr{L}$, where the unforced system would get “trapped”. In general, the forced system is able to explore larger areas of the phase space, departing from the way of steepest descent that the unforced system follows.

As a consequence of the stochastic noise, a single solution $\psi(x,t)$ is not very informative, as it depends on the specific realization of the noise term. Later on, we will therefore examine the forced SWIFT–HOHENBERG equation in a statistical sense, i. e. by analyzing in chapter 14 the probability density function (PDF) of the different values the field $\psi(x,t)$ can take.

Instead of describing the different *values* of the field statistically, it is also possible to assign a probability to a whole field *configuration* $\psi(x,t)$. To this end, we observe that the stochastically forced SWIFT–HOHENBERG equation (13.16) can be considered as a functional LANGEVIN equation (i. e., with infinitely many degrees of freedom) for the field $\psi(x,t)$ with a deterministic force $-\frac{\delta}{\delta\psi}\mathscr{L}[\psi]$ and a noise term $\Gamma(x,t)$ that is GAUSSian distributed with zero mean and standard deviation C_0, cf. (12.7). The corresponding functional FOKKER–PLANCK equation describes how the corresponding PDF $P\big(\psi(x),t\big)$ changes over time under the influence of the deterministic and stochastic forces. It reads

$$\frac{\partial}{\partial t}P\big(\psi(x),t\big)=\frac{\delta}{\delta\psi}\left(\frac{\delta\mathscr{L}[\psi]}{\delta\psi}P\big(\psi(x),t\big)\right)+\frac{C_0}{2}\frac{\delta^2}{\delta\psi^2}P\big(\psi(x),t\big)\quad , \tag{13.17}$$

where $P\big(\psi(x),t\big)$ is proportional to the probability to find the field configuration $\psi(x)$ at time t, and $\frac{\delta}{\delta\psi}$ is shorthand for $\frac{\delta}{\delta\psi(x)}$. As the deterministic force in the LANGEVIN equation (13.16) is given by the functional derivative of $\mathscr{L}$, a stationary solution of the FOKKER–PLANCK equation can be calculated to yield

$$P\big(\psi(x)\big)=\mathfrak{N}\exp\left(-\frac{\mathscr{L}[\psi]}{C_0/2}\right)\quad , \tag{13.18}$$

which is easily confirmed by substituting $P\big(\psi(x)\big)$ into (13.17). Here, $\mathfrak{N}$ is a normalization constant.[4]

With the results from section 13.2.1,[5] we can therefore give the probability with which plane waves with a certain wave number are assumed by the system, and substituting (13.12) into (13.18) results in

$$P\left(\alpha_{\text{min}}\mathrm{e}^{\mathrm{i}\boldsymbol{k}\cdot\boldsymbol{x}}+\text{c. c.}\right)=\mathfrak{N}\,\mathrm{e}^{\frac{V(\Omega)}{3C_0}\lambda^2(k)}\quad . \tag{13.19}$$

---

[4] It is not readily possible to calculate the normalization constant $\mathfrak{N}$, as it is not clear how to average $P(\psi)$ for all possible fields $\psi\in C^4(\Omega)$. Thus, (13.18) can only be used to give *relative* probabilities, i. e. to compare probabilities of different field configurations.

[5] For the sake of simplicity, we will from now on restrict the analysis to the one-mode ansatz $\alpha_{\text{min}}\mathrm{e}^{\mathrm{i}\boldsymbol{k}\cdot\boldsymbol{x}}+$ c. c. As was noted earlier, already the second-order term in (13.14) amounts to only 0.1 % of $\mathscr{L}$, and furthermore figure 13.4 shows that the difference between one and two modes vanish quickly, and is expected to do so even faster in the presence of noise.

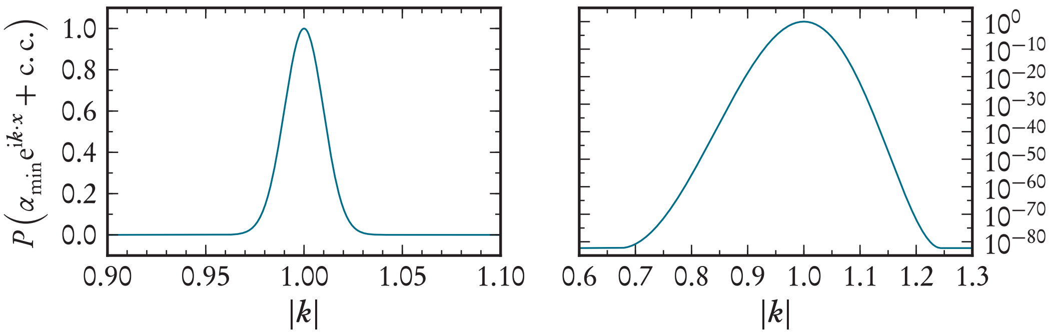

Figure 13.5: *Probability to obtain plane waves in the stochastically forced SWIFT–HOHENBERG equation, normalized to* $P(\dots)_{|k|=1}=1$, *cf.* (13.19). *Parameters are* $\varepsilon=0.3$, $C_0=0.4$ *and* $\Omega=[0,16\pi]\times[0,16\pi]$, *also cf. figure* 12.1. *The probability shows a strong peak at* $|k|=1$ *and falls off quickly (e. g.,* $P(\dots)_{|k|=0.9}=2.43\times10^{-19}$ *and* $P(\dots)_{|k|=1.1}=3.83\times10^{-23}$*); the standard deviation of the peak is* 9.97×10^{-3}. *The right panel gives a logarithmic representation over a larger* $|k|$*-range.*

Figure 13.5 shows that the probability to obtain plane waves with wave vector $\boldsymbol{k}$ is strongly peaked around $|\boldsymbol{k}|=1$. The width of this peak is related to the noise strength C_0: For higher C_0, the peak becomes broader, and roll configurations with $|\boldsymbol{k}|\neq1$ become more probable. This is in line with the remark from before that with a strong noise term, the system is able to explore more states and larger areas in phase space.

13.4 Construction of Statistical Ensembles

We will now utilize the findings of the previous sections to propose a new method how to save computational time when generating statistically stationary data sets of the forced SWIFT–HOHENBERG equation. These data sets are needed to estimate unclosed terms in the following chapter 14, where we derive an evolution equation for the PDF of ψ along the lines of the LUNDGREN–MONIN–NOVIKOV hierarchy, as already laid out in part I of this thesis.

When we ran simulations of the stochastically forced SWIFT–HOHENBERG equation starting from the homogeneous solution $\psi(\boldsymbol{x},t=0)\equiv0$, we found that after a long transient phase (corresponding examples of $\psi(\boldsymbol{x})$ are depicted in figure 12.1), the system ultimately settled in a roll-like state. The patterns are reminiscent of plane waves with slight deformations due to the noise, see the examples in figure 13.6. The noise term is responsible for the fact that in the long run, only parallel rolls instead of labyrinth- or patch-like structures survive: The latter ones correspond to shallow local minima of the LYAPUNOV functional where the unforced system would get trapped due to the gradient dynamics. On the other hand, with noise the system is able to leave these shallow minima;

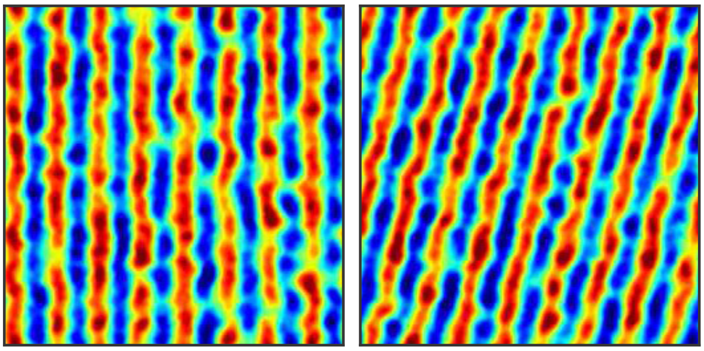

Figure 13.6: *Two different examples of the long-term behavior of the forced* SWIFT–HOHENBERG *equation, starting from* $\psi(\boldsymbol{x}) \equiv 0$*, with parameters* $\varepsilon = 0.3$, $C_0 = 0.4$ *and* $\Omega = [0, 16\pi] \times [0, 16\pi]$ *(likewise from now on for all results).*

e. g., the defects found in labyrinth-like structures are removed by simply "reconnecting" different rolls, and this process is induced respectively sped up by noise. Parallel rolls, on the other hand, are found in deeper local minima of $\mathscr{L}$ from which it is harder to escape. Also, the barriers between local minima of different patterns of parallel stripes are high and hard to overcome by noise; e. g., to transform the left stripe pattern in figure 13.6 into the right one, all the stripes have to tilt and reconnect in a regular fashion. The values of the LYAPUNOV functional given before ($\mathscr{L} \approx -34.5$ for labyrinth versus $\mathscr{L} \approx -37.9$ for parallel rolls with $|\boldsymbol{k}| \approx 1$) also support the finding that with noise, the system will settle in the deep parallel-stripe-minima of $\mathscr{L}$ in the long run.

Following this reasoning, it is not necessary to simulate the long transient (and thus not statistically stationary) descent from $\psi \equiv 0$ into the deep minima of parallel stripes where the system finally settles in a statistically stationary state. Instead it is possible to start the simulations directly from the plane waves we derived in section 13.2.1 and let the solution become statistically stationary, which requires considerably less time. To still ensure a statistically sound ensemble of different stripe patterns, we choose plane waves with different $\boldsymbol{k}$-vectors as prescribed by the probability distribution $P\left(\alpha_{\min} e^{i\boldsymbol{k}\cdot\boldsymbol{x}} + \text{c. c.}\right)$ from (13.19); if one would start many simulations from $\psi \equiv 0$ and let them become stationary, the $\boldsymbol{k}$-vectors of the different solutions would follow the same distribution.

The choice of the proper plane waves is further simplified due to the periodic boundary conditions we are dealing with, as only discrete $\boldsymbol{k}$-vectors (i. e., countably many, as opposed to uncountably many continuous vectors) are possible: Only an integer number of n_x respectively n_y plane waves in x- and y-direction can be fit into the periodic domain Ω, and thus, the possible $\boldsymbol{k}$-vectors may be parametrized as

$$\boldsymbol{k}(n_x, n_y) = \left(n_x \frac{2\pi}{L_x}, n_y \frac{2\pi}{L_y}\right)^{\mathrm{T}} \quad \text{with} \quad n_x, n_y \in \mathbb{N} \quad , \tag{13.20}$$

where $L_{x,y}$ is the extent of the periodic domain in x, y-direction. For example, the only wave vectors with $|\boldsymbol{k}| = 1$ that are possible for the domain $\Omega = [0, 16\pi] \times [0, 16\pi]$ used

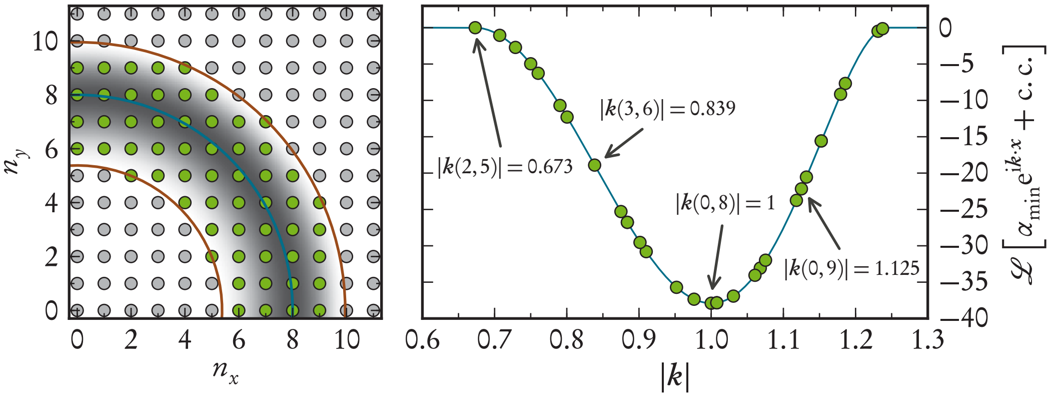

Figure 13.7: *Lyapunov functional of plane waves for the discrete wave vectors in a periodic domain. The possible wave vectors are represented as circles. Left: Green (gray) circles present unstable (stable) wave vectors, and the unstable wave number band is framed by the two brown lines (i. e.,* $|\boldsymbol{k}|^2 = 1 \pm \sqrt{\varepsilon}$*). The blue line gives the most unstable modes, i. e.* $|\boldsymbol{k}| = 1$*, which coincides with the minimum of* $\mathscr{L}$*; the Lyapunov functional is color coded, with black corresponding to the minimum and white to* $\mathscr{L} = 0$*. Right: The possible wave vectors and the corresponding* $\mathscr{L}$ *ordered by* $|\boldsymbol{k}|$ *are shown as green circles and range from* $|\boldsymbol{k}(2,5)| = 0.673$ *to* $|\boldsymbol{k}(7,7)| = 1.237$*. Only some wave vectors are given explicitly.*

Figure 13.8: *Probability to obtain plane waves in the forced Swift–Hohenberg equation for the possible discrete wave numbers, normalized to* $\max_{\boldsymbol{k}} P = 1$*. Only the most relevant wave numbers in the very narrow peak of* P *are shown, cf. figure* 13.5.

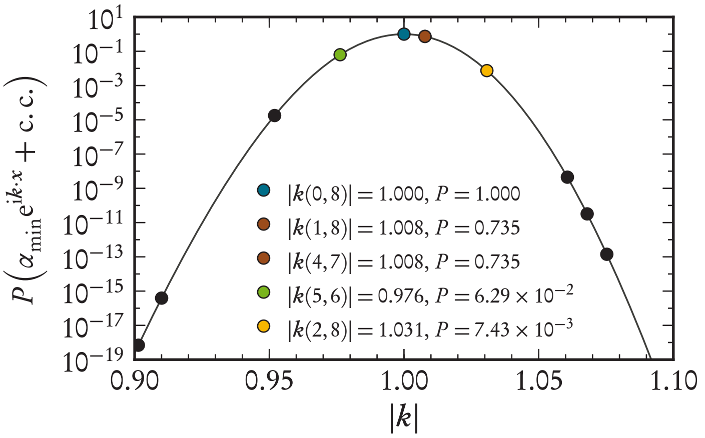

in the numerics are $\boldsymbol{k}(0,8)$ and $\boldsymbol{k}(8,0)$, which corresponds to 8 periods in x- respectively y-direction.[6]

Figure 13.7 shows the Lyapunov functional of the possible wave vectors and figure 13.8 the corresponding probability that plane waves with these wave vectors are assumed by

---

[6] Since the Swift–Hohenberg system is isotropic for the case $L_x = L_y$, these two wave vectors can of course be considered to be equivalent.

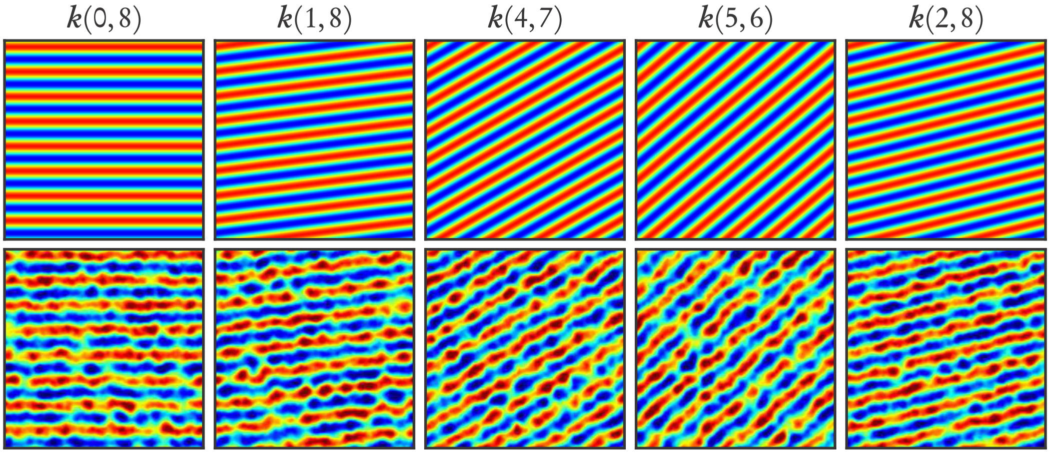

Figure 13.9: *Order parameter field* $\psi(\boldsymbol{x})$ *of the five most probable plane waves (modulo reflection, rotation and translation) which are used as initial conditions (upper row), and the corresponding fields at the end of the numerical simulation (lower row).*

	$\boldsymbol{k}(0,8)$	$\boldsymbol{k}(1,8)$	$\boldsymbol{k}(4,7)$	$\boldsymbol{k}(5,6)$	$\boldsymbol{k}(2,8)$	$\boldsymbol{k}(3,7)$
$\lvert\boldsymbol{k}\rvert$	1.000	1.008	1.008	0.976	1.031	0.952
$\mathscr{L}$	−37.899	−37.838	−37.838	−37.349	−36.919	−35.711
N_{ens}	3937	2893	2893	248	29	0.07

Table 13.1: *Number of ensemble members* N_{ens} *for each mode when the total number of members is* $N_{\text{total}} = 10000$*; only five modes are realized. The sixth most common mode* $\boldsymbol{k}(3,7)$ *would contribute with only a fraction of* 0.07 *of a single snapshot. Additionally, the* LYAPUNOV *functional of the corresponding plane wave is indicated.*

the forced system. It is seen that only a small number of wave vectors is found in the unstable wave number band – to be exact, there are 58 different wave vectors with 28 distinct lengths. Even fewer wave vectors are actually realized in the stochastically forced system with a noteworthy probability; for example, already the tenth most common plane wave with wave vector $|\boldsymbol{k}(2,7)| = 0.91$ has a relative probability of $P < 10^{-15}$, cf. figure 13.8.[7]

With the relative probability P, it is now easy to generate statistically sound ensembles of arbitrary size from the numerics. For 10000 ensemble members, only the 5 most probable plane waves are realized. These initial conditions and the order parameter field $\psi(\boldsymbol{x})$ at the end of the simulations are shown in figure 13.9, and table 13.1 gives the number

---

[7] The precise quantitative behavior of course depends on the parameters of the numerical simulation; in a larger spatial domain and for larger ε, fewer different wave vectors are realized, while for a stronger noise term more plane waves have a considerable probability.

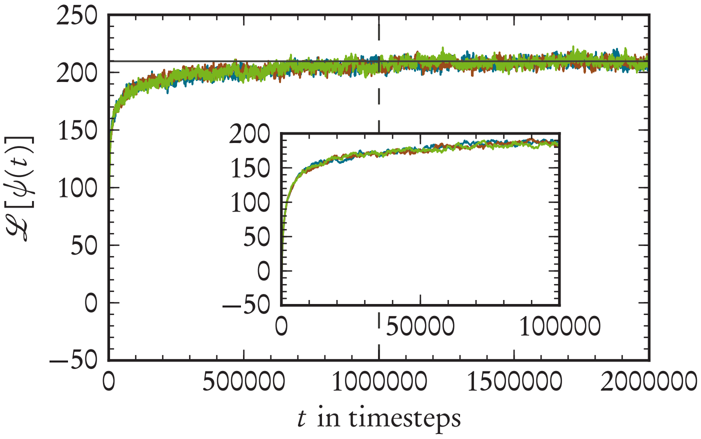

Figure 13.10: *Three exemplary time series of the Lyapunov functional, obtained from numerical simulations of the forced Swift–Hohenberg equation. The value of $\mathscr{L}$ quickly rises and saturates after approximately 10^6 time steps. The horizontal line gives the mean value of $\mathscr{L} = 209.7$, and the inset shows a zoom of the first time steps.*

ε	C_0	l	$L_{x,y}$	Δt	$N_{x,y}$	N_t	N_{total}
0.3	0.4	1.5	16π	10^{-6}	256	2×10^6	10000

Table 13.2: *Details of the numerical simulations for the ensemble calculation. The spatial correlation length l of the noise term is given in gridpoints. $N_{x,y}$ is the equidistant grid resolution in x- respectively y-direction. N_t is the number of time steps, and Δt their time interval. N_{total} gives the total number of ensemble members, with the shares of the different initial conditions as in table* 13.1.

of snapshots that are generated for each $\boldsymbol{k}$-vector (we again assume "mirrored" $\boldsymbol{k}$-vectors – e. g., $\boldsymbol{k}(0,8)$ and $\boldsymbol{k}(8,0)$ – to be equal due to the symmetries of the Swift–Hohenberg system). We then ran a number of simulations from different initial conditions and generated the required number of snapshots as outlined above.[8] Exemplary time series of the Lyapunov functional are shown in figure 13.10, and it is seen that in the beginning $\mathscr{L}$ quickly rises from its plane-wave value $\mathscr{L} \approx -37$ and then continues to grow more slowly until the system approaches a statistically stationary state. We consider the simulations to be stationary after 10^6 time steps when the Lyapunov functional saturates at a value of $\mathscr{L} \approx 209.7$. The snapshots are then taken 10^4 time steps apart. Details of the ensemble calculations that we performed are presented in table 13.2.

---

[8] To speed up the overall computation, we opted to run e. g. 40 simulations in parallel for $\boldsymbol{k}(0,8)$, each producing approximately 100 snapshots; this takes considerably less time than running one simulation that produces 3937 snapshots.

13.5 Summary of LYAPUNOV Formalism and Ensemble Construction

In this chapter, we started from two well-established tools – the linear stability analysis and the formulation of the problem in terms of the LYAPUNOV functional. With the linear stability analysis, we recounted the known result that the SWIFT–HOHENBERG system tends to form patterns with a distinct wave length of $|\boldsymbol{k}| = 1$. We furthermore showed that the system obeys gradient dynamics, and from the corresponding LYAPUNOV functional we could tell that stationary solutions of the system are close to plane waves with a known amplitude. Also, by utilizing the variational formulation of the stochstastically forced SWIFT–HOHENBERG equation, it was straight-forward to give a FOKKER–PLANCK equation for the probability distribution of configurations of the order parameter field, and a stationary solution was readily obtained.

We then combined these concepts to propose a method to quickly generate valid numerical ensembles of the stochastically forced SWIFT–HOHENBERG equation. To this end, we skipped the lengthy descent of the order parameter, i. e. the process of starting from the homogeneous solution and ending in the plane-wave-minima of the LYAPUNOV functional. As the patterns that are assumed in the minima are approximately known from the linear stability analysis as well as the LYAPUNOV functional, and the relative probability of the minima is known from the FOKKER–PLANCK equation, we are instead able to start the numerical simulations directly from plane waves and let them reach a statistically stationary state; this requires much less computational time.

The method relies on the fact that we can enumerate the plane-wave-minima of the LYAPUNOV functional, because they are parametrized by only a single discrete parameter, i. e. the $\boldsymbol{k}$-vector. This can be seen as a weakness of the proposed approach, because patterns in local minima that are harder to parametrize (e. g., the labyrinth-like structure in figure 11.3 that requires the interplay of many degrees of freedom) cannot be generated easily. Although all the minima of plane waves that we considered are deeper than the labyrinth-like-minimum from before, it is not guaranteed that there are minima corresponding to more complicated patterns that lie in between the plane-wave-minima from section 13.4 and that should thus be included in the ensemble. However, we remark that we did only find roll-like final patterns instead of more complicated ones when we ran long simulations starting from homogeneous initial conditions.

The methods presented in sections 13.1–13.4 can readily be extended towards the SWIFT–HOHENBERG equation with an additional quadratic nonlinearity (cf. section C.1), as there still exists a LYAPUNOV functional that is bounded from below; the exact calculations performed in section 13.2 may become a bit cumbersome, though, as the characterization of the unstable modes requires more cases to be differentiated (e. g., the stability of hexagonal versus stripe patterns, cf. BESTEHORN (2006, sec. 9.4.5)). Also, generating the patterns corresponding to the hexagonal minima of the LYAPUNOV functional requires more rigor, as more modes and thus less symmetry is involved.

As an outlook, the proposed ansatz of generating statistical ensembles may readily be extended to any gradient system with an additional stochastic force, as the stationary solution of the FOKKER–PLANCK equation does not depend on the precise form of the LYAPUNOV functional. Thus, the same method can be used to generate ensembles of the stochastically driven GINZBURG–LANDAU equation (HOHENBERG and HALPERIN, 1977, ARANSON and KRAMER, 2002) or thin-film equations under the influence of noise, e. g. MECKE and RAUSCHER (2005).

14 Statistical Analysis

After having introduced all the prerequisites, we will now derive an evolution equation for the probability density function (PDF) of the order parameter ψ along the lines of the Lundgren–Monin–Novikov hierarchy that was already outlined in part I. As the derivation for the Swift–Hohenberg system is in large parts analogous to the one for Rayleigh–Bénard convection, we will keep the description in section 14.1 relatively short. In section 14.2, we will use data obtained from DNS to solve the PDF equation and compare the reconstructed PDF with the directly estimated one, and also present models that are able to describe the PDF.

14.1 PDF Equation

Similar to the temperature PDF in chapter 3, the derivation of the evolution equation for the PDF $f(\psi, \boldsymbol{x}, t)$ of the order parameter field $\psi(\boldsymbol{x}, t)$ starts from the definition

$$f(\psi, \boldsymbol{x}, t) = \left\langle \delta\left(\psi(\boldsymbol{x}, t) - \psi\right) \right\rangle \quad , \tag{14.1}$$

where ψ is the sample space variable and $\langle\cdot\rangle$ is an ensemble average over the realizations $\psi(\boldsymbol{x}, t)$ of the order parameter field. Thus, f is defined as the ensemble-average of the fine-grained PDF $\delta\left(\psi(\boldsymbol{x}, t) - \psi\right)$. Without noise, it is straightforward to derive the following evolution equation for f by calculating the temporal derivative of (14.1) and inserting the Swift–Hohenberg equation (11.1) (cf. also chapter 3 for details):

$$\frac{\partial}{\partial t} f(\psi, \boldsymbol{x}, t) = -\frac{\partial}{\partial \psi}\left(\left\langle \varepsilon\psi - (\Delta+1)^2\psi - \psi^3 \middle| \psi, \boldsymbol{x}, t\right\rangle f(\psi, \boldsymbol{x}, t)\right) \tag{14.2a}$$

$$= -\frac{\partial}{\partial \psi}\left(\left(\varepsilon\psi - \psi^3 - \langle(\Delta+1)^2\psi|\psi, \boldsymbol{x}, t\rangle\right) f(\psi, \boldsymbol{x}, t)\right) \tag{14.2b}$$

The evolution of the PDF is therefore determined by the conditionally averaged right-hand side $\langle\ldots|\psi, \boldsymbol{x}, t\rangle$ of the Swift–Hohenberg equation, where the linear and the cubic term can be evaluated explicitly.

The evolution equation for the stochastically forced Swift–Hohenberg equation (11.3) is a bit more cumbersome to derive, though, because it is not immediately clear how to evaluate the conditional average of the fluctuating force Γ. For noise that is uncorrelated in time and has zero mean (as for the noise we are using, cf. (12.7)), the conditional average is determined by the strength C_0 of the noise. Together with the conditional average of the deterministic part from above, this results in the evolution equation for the PDF of the stochstastically driven SWIFT–HOHENBERG equation:

$$\frac{\partial}{\partial t} f = -\frac{\partial}{\partial \psi}\Big(\big(\varepsilon\psi - \psi^3 - \langle(\Delta+1)^2\psi|\psi, \boldsymbol{x}, t\rangle\big) f\Big) + \frac{C_0}{2}\frac{\partial^2}{\partial \psi^2} f \tag{14.3}$$

Here, f is shorthand for $f(\psi, \boldsymbol{x}, t)$. The derivation of this equation utilizes series expansion for small times as well as properties of the noise and is in principle straightforward, albeit a bit lengthy; thus, we refer the interested reader to HAKEN (1983, sec. 6.3, pp. 170ff.) where a detailed account is given in a more general form. The only unclosed term in this equation is the conditional average of $(\Delta+1)^2\psi$ which we will estimate from ensembles obtained from the direct numerical simulations that we discussed in chapters 12 and 13.

14.1.1 Symmetry Considerations

Due to the periodic boundary conditions we assume, the forced SWIFT–HOHENBERG system is statistically homogeneous in all spatial directions. Thus, the statistics do not depend on $\boldsymbol{x}$, and the evolution equation (14.3) becomes

$$\frac{\partial}{\partial t} f(\psi, t) = -\frac{\partial}{\partial \psi}\Big(\underbrace{\big(\varepsilon\psi - \psi^3 - \langle(\Delta+1)^2\psi|\psi, t\rangle\big)} f(\psi, t)\Big) + \frac{C_0}{2}\frac{\partial^2}{\partial \psi^2} f(\psi, t) \tag{14.4a}$$

$$=: \quad -\frac{\partial}{\partial \psi}\Big(D(\psi, t) f(\psi, t)\Big) + \frac{C_0}{2}\frac{\partial^2}{\partial \psi^2} f(\psi, t) \quad . \tag{14.4b}$$

The evolution equation of the PDF of ψ therefore takes the form of a FOKKER–PLANCK equation with the drift term $D(\psi, t)$ and with constant diffusion term C_0.

For statistically stationary systems, the conditional average as well as the PDF do not depend on the time t, i. e. $f = f(\psi)$ and $D = D(\psi)$, and thus $\frac{\partial}{\partial t} f = 0$. In this case a stationary solution of the FOKKER–PLANCK equation is

$$f(\psi) = \mathcal{N} \exp\left(\int_{-\infty}^{\psi} \mathrm{d}\psi' \, \frac{D(\psi')}{C_0/2}\right) \quad , \tag{14.5}$$

which can easily be confirmed by substitution into (14.4). Here, $\mathcal{N} = \mathcal{N}(C_0)$ is a constant that ensures the normalization $\int_{-\infty}^{\infty} \mathrm{d}\psi \, f(\psi) = 1$. Equation (14.5) yields two ways to obtain and compare the PDF of ψ: By directly estimating $f(\psi)$ from the numerics, and by estimating $\langle(\Delta+1)^2\psi|\psi\rangle$ from the numerics and reconstructing $f(\psi)$ according to (14.5). This benchmark will be performed in the next section.

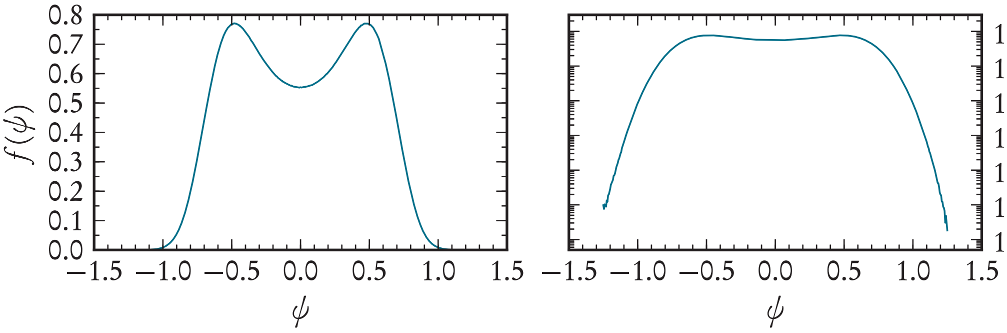

Figure 14.1: *Probability density function of ψ estimated from the direct numerical simulation of the forced* Swift–Hohenberg *equation* (11.3). *The right panel shows the PDF in a logarithmic scale.*

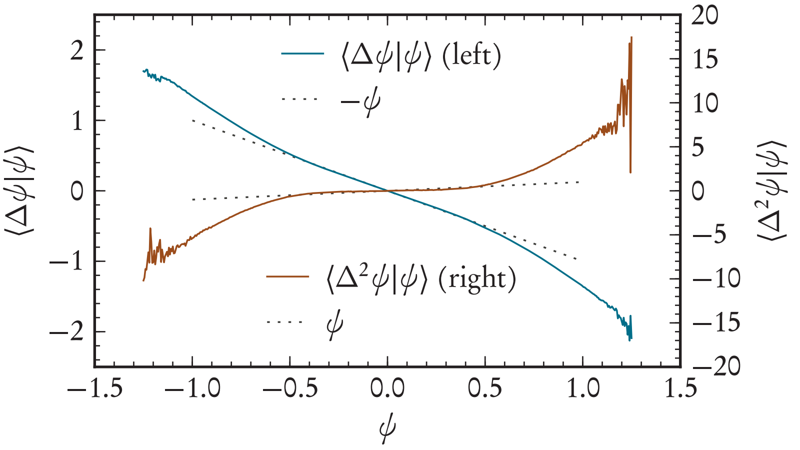

Figure 14.2: *Conditional average of $\Delta\psi$ (left ordinate) and $\Delta^2\psi$ (right ordinate), estimated from numerical simulations. The dotted lines act as a guide to the eye and indicate almost linear conditional averages around $\psi \approx 0$.*

14.2 Numerical Results

We will now use numerical data obtained from ensembles of DNS calculations as proposed in section 13.4 to analyze the statistics of the forced Swift–Hohenberg equation. In figure 14.1 the PDF of ψ is estimated from the numerics. The PDF is bimodal and symmetric, which has to be the case due to the symmetry $\psi \rightarrow -\psi$ of the system. Also the location of the two maxima at $\psi \approx \pm 0.5$ is reasonably justified by the amplitude of the rolls that the system assumes; for the unforced system, the preferred amplitude of sine waves is $A_0 = 0.63$, cf. section 13.2.

When evaluating the reconstructed PDF (14.5), the only unknown expression in the drift term $D(\psi)$ is the conditional average of $(\Delta + 1)^2\psi$. This term can be decomposed as $\langle(\Delta+1)^2\psi|\psi\rangle = \langle\Delta^2\psi|\psi\rangle + 2\langle\Delta\psi|\psi\rangle + \psi$, and the first two terms are shown in figure 14.2.

Figure 14.3: *Terms of the right-hand side of the PDF equation, i. e. conditional average of* $(\Delta+1)^2\psi$ *and the full drift term* $D(\psi)=\varepsilon\psi-\psi^3-\langle(\Delta+1)^2\psi|\psi\rangle$ *with* $\varepsilon=0.3$, *cf.* (14.4). *It is seen that the drift term is dominated by the conditional average.*

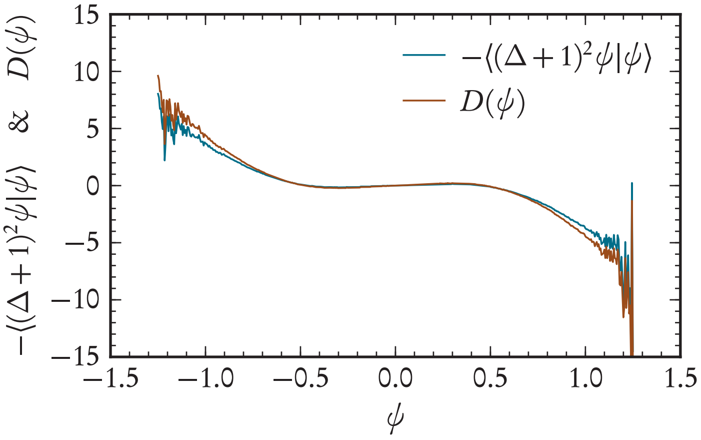

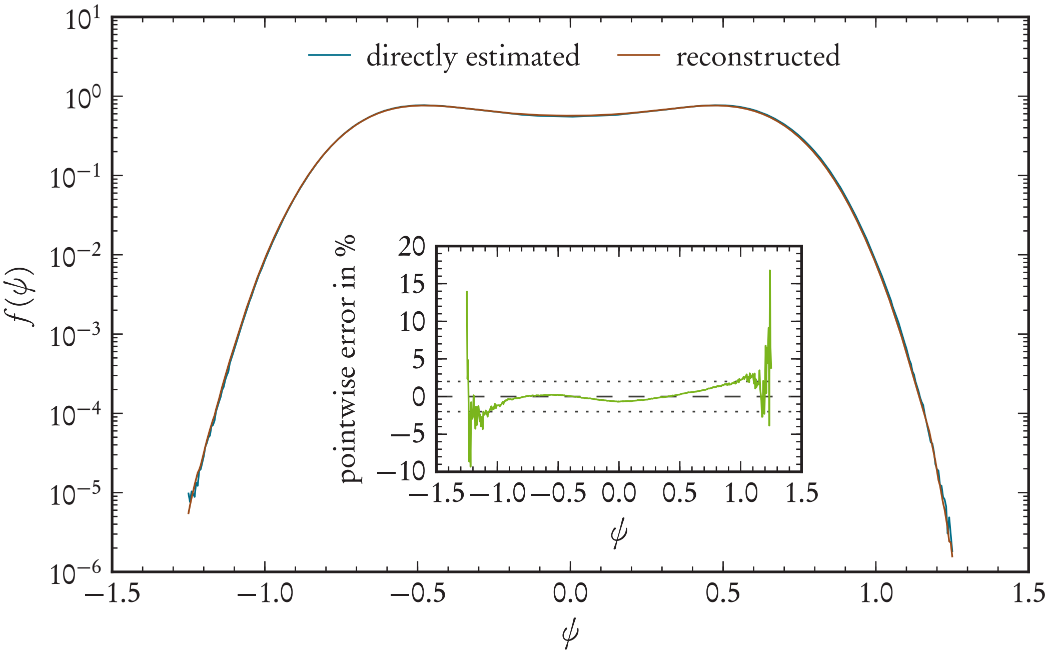

Figure 14.4: *Comparison of the directly estimated PDF of* ψ *and the PDF reconstructed according to* (14.5); *both lines overlap almost completely. The inset shows the pointwise relative error between the two PDFs in percent, i. e.* $100\,\% \times \frac{f_\text{est}-f_\text{rec}}{\frac{1}{2}(f_\text{est}+f_\text{rec})}$.

One observes that in general $\Delta\psi$ is negatively and $\Delta^2\psi$ positively correlated with ψ. Especially in the core region, i. e. around $\psi\approx 0$, the approximate relations $\langle\Delta\psi|\psi\rangle\approx-\psi$ and $\langle\Delta^2\psi|\psi\rangle\approx\psi$ seem to hold, see the dotted lines in the figure. This can be understood when considering plane waves $\varphi=A_0\sin(\boldsymbol{k}\cdot\boldsymbol{x})$, for which the conditional averages can be calculated explicitly to yield $\langle \Delta\varphi|\varphi\rangle = -\boldsymbol{k}^2\varphi$ and $\langle \Delta^2\varphi|\varphi\rangle = \boldsymbol{k}^4\varphi$. As the distribution of possible $\boldsymbol{k}$-vectors is sharply peaked around $|\boldsymbol{k}| = 1$ (cf. figure 13.5), this explains the behavior of the conditional averages close to $\psi = 0$. Further outwards, the conditional averages deviate from this linear behavior due to the dynamics and the noise of the forced SWIFT–HOHENBERG system; in the far ends (i. e., for $|\psi| \gtrsim 1$) the estimation of the conditional averages becomes flawed due to insufficient statistics.

The combined conditional average of $(\Delta+1)^2\psi$ and the resulting drift term $D(\psi)$ are given in figure 14.3, and it is seen that $D(\psi)$ is almost completely dominated by $\langle(\Delta+1)^2\psi|\psi\rangle$, while the additional terms, i. e. $\varepsilon\psi - \psi^3$, only play a minor role for the form of the drift. However, one has to keep in mind that the conditional average implicitly depends on the linear driving and the cubic saturation of the SWIFT–HOHENBERG equation.

By numerically integrating the estimated drift $D(\psi)$ from figure 14.3 as according to (14.5) with $C_0 = 0.4$, we obtain the reconstructed PDF in figure 14.4, where it is shown together with the PDF directly estimated from the data ensemble. The two curves are almost indistinguishable, apart from the outer regions of poor statistics. This is also confirmed by the pointwise relative error in the inset, which is below 1% in the core region of the PDF and only becomes bigger than 2% in the outer regions where the numerical errors grow bigger. We want to emphasize here that no fitting to the estimated PDF was utilized when performing the reconstruction; the only “free” parameter was the *a posteriori* determined normalization constant $\mathcal{N}$. On the other hand, however, the steps leading to the reconstructed PDF (14.5) were exact and did not involve any approximations or assumptions (apart from statistical symmetries). Thus, upon closer consideration it comes as no surprise that the two PDFs generated from the same data set coincide quite well; e. g., in WILCZEK and FRIEDRICH (2009) and WILCZEK *et al.* (2011) a similar method was applied to the vorticity respectively velocity distribution of the three-dimensional NAVIER–STOKES equation and yielded even better agreements. The grade of agreement of course depends on the quality of the data ensemble and how well it fulfills the demanded statistical symmetries.

14.2.1 Model for the Conditional Averages

The shape of the conditional average of $(\Delta+1)^2\psi$ in figure 14.3 as well as the approximately linear behavior of the two conditional averages in figure 14.2 suggests a model up to cubic order:

$$\langle \Delta\psi|\psi\rangle = -\psi + \alpha_3\psi^3 \tag{14.6a}$$

$$\langle \Delta^2\psi|\psi\rangle = \beta_1\psi + \beta_3\psi^3 \tag{14.6b}$$

While the prefactor of the linear term in (14.6a) has been chosen as -1 (cf. figure 14.2), we found that the prefactor of the linear term in $\langle\Delta^2\psi|\psi\rangle$ deviates from the slope 1 that figure 14.2 suggests; thus, we included it as a free parameter via β_1. Fitting the

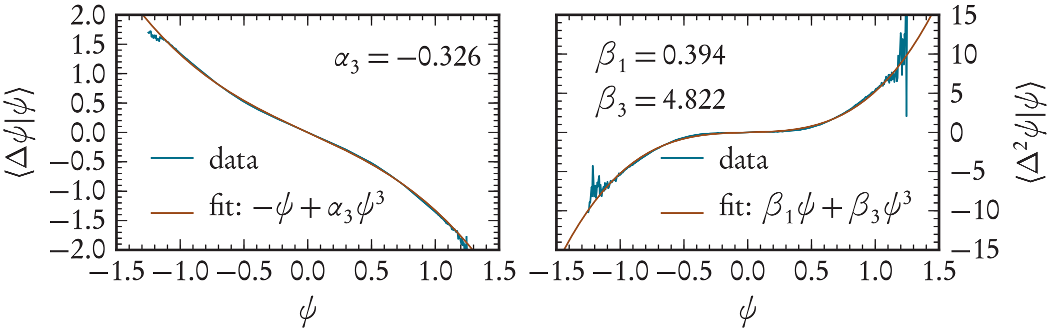

Figure 14.5: *The cubic model* (14.6) *of the conditional averages of* $\Delta\psi$ *(left) and* $\Delta^2\psi$ *(right) fitted to the data obtained from direct numerical simulations via* α_3, β_1 *and* β_3.

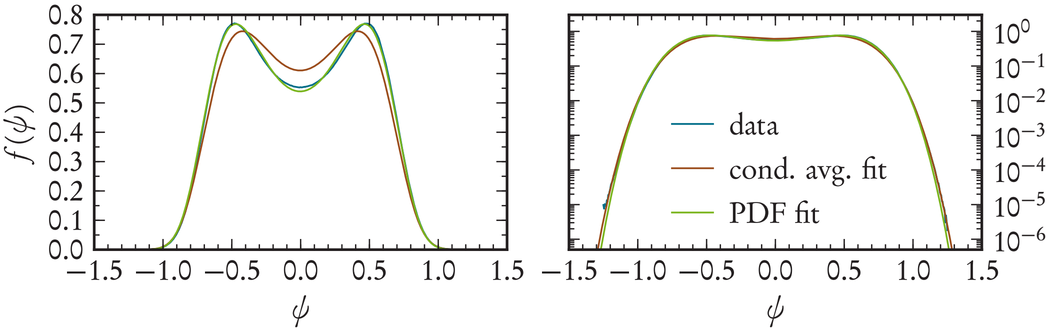

Figure 14.6: *PDF of* ψ *reconstructed from the cubic model as presented in* (14.6) *and figure* 14.5 *(brown curve). The blue curve is the PDF directly estimated from the numerics. The green PDF has been obtained by inserting the model into the PDF reconstruction and fitting this to the directly estimated PDF; the obtained parameters are* $(\alpha_3, \beta_1, \beta_3) = (-9.420 \times 10^{-3}, -7.101 \times 10^{-4}, 4.979)$*. The right panel shows a logarithmic plot of the PDFs.*

model (14.6) to the data, i. e. $\langle\Delta\psi|\psi\rangle$ and $\langle\Delta^2\psi|\psi\rangle$ as estimated from the numerics, gives the results shown in figure 14.5, and indeed it is found that close to $\psi \approx 0$ the slope of $\langle\Delta^2\psi|\psi\rangle$ differs from 1 (cf. the parameters given in the figure). We find that the conditional averages can be described reasonably well with a cubic model. Inserting this model into the PDF reconstruction (14.5) yields the results shown in figure 14.6. While the model is certainly able to capture the general bimodal form of the PDF, there are still deviations between the directly estimated and the modeled PDF (especially in the core regions).

Surprisingly, a different fit method yielded better results for the same model: For the green PDF of figure 14.6 we did not fit the model to the conditional averages, but inserted the model into the PDF reconstruction and then fitted the reconstructed to the estimated

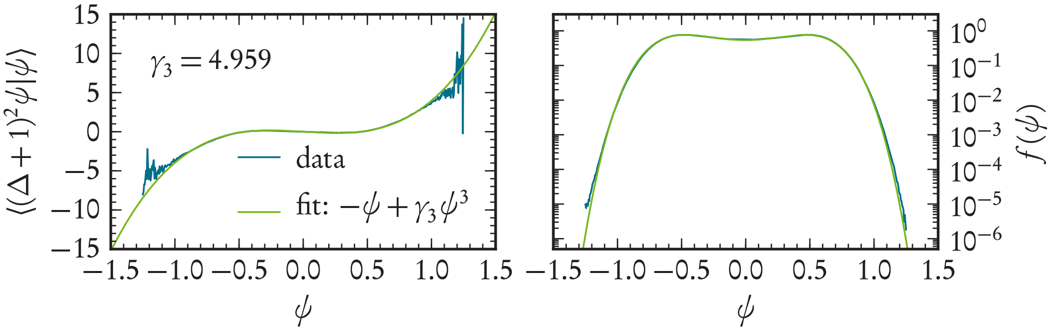

Figure 14.7: *The simplistic model* (14.8) *of the conditional average (left panel) and the logarithmic PDF of ψ reconstructed from this model (right panel). The model was inserted into the reconstructed PDF* (14.5) *which was then fitted to the PDF obtained from DNS via γ_3.*

PDF. This ansatz gives a far better results, as is seen in the agreement between the blue and green curve of figure 14.6; only in the far end the green PDF performs slightly worse than the brown one, as can be seen from the logarithmic plot in the right panel.

When fitting the PDF instead of the single conditional averages of $\Delta\psi$ and $\Delta^2\psi$, one effectively uses the following ansatz for the full conditional average of $(\Delta+1)^2\psi$ (cf. (14.6)):

$$\langle(\Delta+1)^2\psi|\psi\rangle = \langle\Delta^2\psi|\psi\rangle + 2\langle\Delta\psi|\psi\rangle + \psi \tag{14.7a}$$

$$= (\beta_1 - 1)\psi + (2\alpha_3 + \beta_3)\psi^3 \tag{14.7b}$$

Thus, when fitting the PDF and therefore the whole conditional average $\langle(\Delta+1)^2\psi|\psi\rangle$, the parameters α_3 and β_3 are dependent on each other and can be combined into one. Furthermore, the small value of the parameter $\beta_1 = -7.101\times10^{-4}$ (cf. figure 14.6) suggests the following one-parametric cubic model for the conditional average of $(\Delta+1)^2\psi$:

$$\langle(\Delta+1)^2\psi|\psi\rangle = -\psi + \gamma_3\psi^3 \tag{14.8}$$

When inserting this ansatz into (14.5) and fitting the PDF to the data, the results shown in figure 14.7 are obtained. The conditional average as well as the PDF agree very well with the model, and again deviate only in the outer regions of strong noise.[1] Thus, we find that one free parameter γ_3 is enough to characterize the PDF of ψ reasonably well.

---

[1] It is immediately clear that the directly estimated and the modeled PDF deviate mostly in the outer regions: The least-squares fit is obtained by minimizing the L^2-distance between the two functions, and the steep tails of the PDF contribute only negligibly to the L^2-norm. We found that using the L^2-distance of the logarithm of the PDFs yields essentially the same result. The L^2-norm of a function $g(\psi)$ is defined as $||g||^2 = \int d\psi\, g(\psi)^2$.

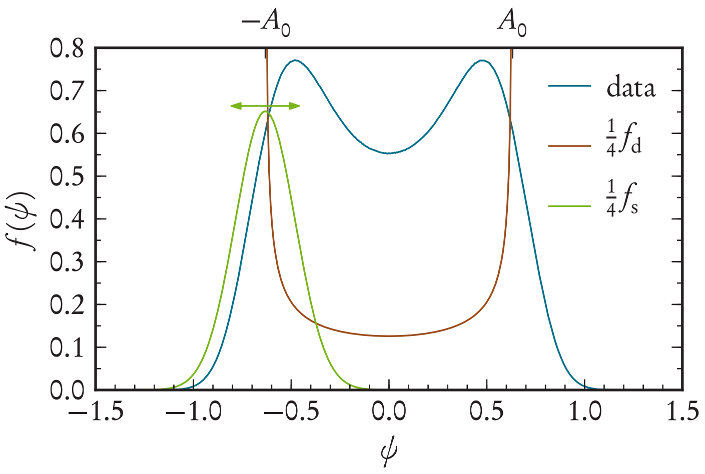

Figure 14.8: *Ansatz functions f_d and f_s (with $\sigma = 0.153$) used in the Gaussian convolution model, cf.* (14.9) *and* (14.10), *together with the PDF obtained from the data. The upper abscissa shows the amplitude of plane waves with $|\boldsymbol{k}| = 1$, i. e. $A_0 = 2\sqrt{\frac{1}{3}\lambda(\boldsymbol{k})} \approx 0.632$, and the green arrow indicates the convolution process.*

14.2.2 Model for the PDF Using Gaussian Convolution

The models presented above contained physical insights because the form of the reconstructed PDF followed directly from the Swift–Hohenberg equation, and only models for $\langle(\Delta+1)^2\psi|\psi\rangle$ had to be provided. In this section, we will briefly present another model that yields a PDF that is qualitatively comparable to the data.

To this end, we propose that the PDF of the stochastically forced Swift–Hohenberg equation is the result of the interplay of two processes: The deterministic dynamics described by the Swift–Hohenberg equation and the stochasticity described by a Gaussian distribution of the noise. In section 13.2.1 we have shown that the deterministic long-term behavior is reasonably well described by plane waves $\psi(\boldsymbol{x}) = A_0 \sin(\boldsymbol{k}\cdot\boldsymbol{x})$. The PDF of plane waves, i. e. the distribution function of a sine, can be calculated explicitly to yield the distribution of the deterministic part:

$$f_\mathrm{d}(\psi) = \Big\langle \delta\left(A_0 \sin(\boldsymbol{k}\cdot\boldsymbol{x}) - \psi\right)\Big\rangle = \frac{1}{V(\Omega)}\int_\Omega \mathrm{d}^2x\, \delta\left(A_0 \sin(\boldsymbol{k}\cdot\boldsymbol{x}) - \psi\right) \tag{14.9a}$$

$$= \begin{cases} \dfrac{1}{\pi}\dfrac{1}{\sqrt{A_0^2 - \psi^2}} & \text{if } |\psi| < A_0 \\ 0 & \text{else} \end{cases} \tag{14.9b}$$

The distribution of the stochastic part, on the other hand, is given by the Gaussian PDF

$$f_\mathrm{s}(\psi) = \frac{1}{\sqrt{2\pi\sigma^2}} \mathrm{e}^{-\frac{\psi^2}{2\sigma^2}} \tag{14.10}$$

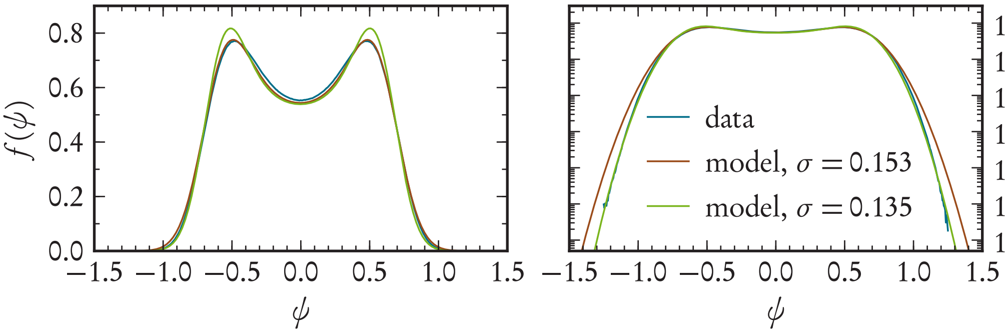

Figure 14.9: *PDF obtained from the convolution model proposed in* (14.9)–(14.11), *together with the directly estimated one; the right panel shows the PDFs logarithmically. The parameter* $\sigma = 0.153$ *has been obtained by minimizing the* L^2*-distance between the modeled and the estimated PDF, while the parameter* $\sigma = 0.135$ *stems from the minimized* L^2*-distance between the logarithms of the two PDFs.*

with the standard deviation σ as a free parameter. Figure 14.8 shows these two PDFs together with the one obtained from the numerics.

The proposed model is that the PDF of the forced SWIFT–HOHENBERG equation is reasonably well described by the convolution of the two aforementioned PDFs:

$$f(\psi) = \left(f_\mathrm{d} * f_\mathrm{s}\right)(\psi) = \int_{-\infty}^{\infty} \mathrm{d}\psi'\, f_\mathrm{d}(\psi')\, f_\mathrm{s}(\psi - \psi') \tag{14.11}$$

This ansatz can be motivated from the fact that for two statistically independent random variables X and Y which have the distribution functions f_X and f_Y, their sum $Z = X + Y$ is distributed as $f_Z = f_X * f_Y$, i. e. as the convolution of the single distributions.[2] It is of course an open question whether or not a decomposition of the random fields of the forced SWIFT–HOHENBERG equation as a sum of a deterministic and a stochastic part (i. e., as $\psi = \psi_\mathrm{d} + \psi_\mathrm{s}$) is possible and how good their statistical independence is fulfilled.

When the ansatz (14.11) is fitted to the estimated PDF via the fit parameter σ, the results shown in figure 14.9 are obtained, and the model fits the data rather well. The bimodal and symmetric form of the PDF is reproduced by construction,[3] and also the asymptotic behavior of the tails of the PDF is captured quite well. There is a difference, though, whether one minimizes the distance between the PDFs or the logarithms of the

---

[2] This can be seen as follows: In general, the sum $Z = X + Y$ of two random variables X and Y is distributed as $f_Z(z) = \int \mathrm{d}x\, \mathrm{d}y\, f_{X,Y}(x,y)\, \delta\big(z - (x+y)\big)$ with the joint distribution $f_{X,Y}(x,y)$. Assuming statistical independence of X and Y, the joint distribution factorizes into $f_{X,Y}(x,y) = f_X(x) f_Y(y)$, and thus, the above expression reduces to $f_Z(z) = \int \mathrm{d}x\, \mathrm{d}y\, f_X(x) f_Y(y)\, \delta\big(z - (x+y)\big) = \int \mathrm{d}x\, f_X(x) f_Y(z-x) = \left(f_X * f_Y\right)(z)$.

[3] The model PDF (14.11) is a convolution of (i) a symmetric and (ii) a symmetric and bimodal PDF, and thus symmetric and bimodal itself.

PDFs: In the first case, the core region of the estimated PDF is reproduced better, while in the latter case the model describes the tails of the PDF almost perfectly. This suggests the view that in the tails of the PDF the GAUSSian behavior of the noise dominates the statistics, while the dynamics of the SWIFT–HOHENBERG system only play a minor role there.

However, we have to emphasize again that this model is purely phenomenological and driven only by the numerical data and not the physics behind the system (apart from the amplitude A_0 of the plane waves that is known from the theory). In particular, we could not directly relate the fitted standard deviations $\sigma \in \{0.153, 0.135\}$ to the strength $C_0 = 0.4$ of the stochastic force.

15 Summary and Conclusion

This part dealt with the pattern forming behavior of convective systems that can be described by the forced Swift–Hohenberg equation and its statistical analysis. In nature and technical applications where the convection is not too turbulent, it is generally found that patterns in the form of rolls emerge. In chapter 11 we gave examples of these patterns and motivated how they can be described by a two-dimensional order parameter field governed by the Swift–Hohenberg equation. We also introduced the stochastically driven Swift–Hohenberg equation, where the idea of impurities of the convective system – e. g., an inhomogeneous heating rate or rough boundaries – enters the order parameter description as a stochastic force. Furthermore, we compared the stripe patterns of both the deterministic and the driven Swift–Hohenberg system which we obtained from direct numerical simulations. The DNS described in chapter 12 is a pseudospectral scheme where the time-stepping treats the linear term implicitly and also takes extra care regarding the fluctuating force.

In chapter 13 we went into the details and consequences of the Swift–Hohenberg system being described by gradient dynamics: As the right-hand side of the evolution equation can be formulated as the functional derivative of the corresponding Lyapunov functional, the deterministic dynamics of the system follow the way that minimizes this functional in a *steepest-descent*-manner. This view leads to a wide range of results. For the preferred patterns of plane waves that are obtained from a linear stability analysis of the Swift–Hohenberg equation, we could calculate the optimal amplitude by minimizing the Lyapunov functional and thereby reproduced the established results, cf. Viñals *et al.* (1991). Furthermore, we showed numerically that the plane waves are reasonably close to true stationary solutions of the Swift–Hohenberg system. For the stocastically driven system, the gradient formulation allowed to construct and solve a functional Fokker–Planck equation that corresponds to the functional Langevin equation that the forced Swift–Hohenberg equation represents, and we thereby could assign a probability to every configuration of the order parameter field. All these partly new, partly reproduced results were then combined to propose a new method to generate statistically stationary ensembles of the stochastically driven Swift–Hohenberg equation: As we can predict the long-term evolution towards local minima of the Lyapunov functional and know the relative frequency of the different minima, this allows us to directly start simulations in states of minimal Lyapunov functional and let the system settle in a statistically stationary state. This takes considerably less computational time compared to a “cold start” from the homogeneous solution. The method does not depend on the exact form of the Lyapunov functional, and therefore we expect it to be easily extended to generate statistically stationary ensembles of any gradient system driven by noise.

With the data set that was produced accordingly, we then proceeded in chapter 14 to give a statistical analysis of the forced Swift–Hohenberg system along the lines of the Lundgren–Monin–Novikov hierarchy already introduced for Rayleigh–Bénard convection in part I. We analyzed the PDF of the Swift–Hohenberg system, this time assigning probabilities to single values of the order parameter and not a whole field configuration. As anticipated, the PDF is symmetric because of the inversion symmetry of the system. Due to the fluctuating force, the evolution equation for this PDF took the form of a Fokker–Planck equation, i. e. a second order partial differential equation, in contrast to the first order equation encountered for the Rayleigh–Bénard case (cf. chapter 3). The only unclosed term that appeared in this formalism was the conditional average of the spatial term, which we estimated from the numerics. The comparison between the PDFs obtained as the solution of the Fokker–Planck equation with the estimated conditional average and the directly estimated PDF yielded satisfactory agreement. Furthermore, the distinct cubic shape of the conditional average suggested different mechanisms at work in the core region respectively the tails of the PDF, and we could show that a simple cubic model of the conditional averages gave results close to the real statistics. An even simpler phenomenological model was introduced that expresses the statistics as the convolution of a PDF describing the deterministic part, which dominates the core region, with a PDF related to the stochastic force which dominates the tails. This one-parametric convolution ansatz yielded reasonable results.

The results obtained from the Lundgren–Monin–Novikov hierarchy in part I gave insight into the average dynamics of the Rayleigh–Bénard system. The present part, on the other hand, gave a description of the pattern formation and the corresponding statistics that can appear in convective systems, and we could reconstruct and model the statistics of the Swift–Hohenberg system and identify the interplay of the responsible deterministic and stochastic processes. Furthermore, as a byproduct we could establish a method to accelerate the generation of ensembles of stochastically driven gradient systems.

Part IV

Summary and Conclusion of the Thesis

In this thesis, we dealt with convective flows, i. e. the motion of a fluid that is heated from below and cooled from above and thus driven by a temperature gradient. We analyzed in three parts the statistics and the dynamics of the flows and of coherent structures therein: In part I we applied statistical methods to the temperature fluctuations of turbulent Rayleigh–Bénard convection, part II introduced a tailored method to examine how turbulent convection is build from coherent structures, and in part III we described the statistics of the structures that emerge near the onset of convection with the help of the stochastic Swift–Hohenberg equation.

In part I, we utilized a technique known from homogeneous isotropic turbulence research – the so-called Lundgren–Monin–Novikov hierarchy or PDF methods – to study the temperature fluctuations of turbulent Rayleigh–Bénard convection. Starting from the basic equations of motion, i. e. the Oberbeck–Boussinesq equations, we derived an exact evolution equation for the probability density function (PDF) of the turbulent temperature field. We then applied the method of characteristics to this first-order partial differential equation and obtained a quasi-Lagrangian description of the average dynamics of the system. This suggested the notion of so-called *conditional particles*, i. e. Lagrangian quasi-particles that are governed by the conditionally averaged flow fields. Thus, starting from a statistical description in terms of the temperature PDF, we could characterize the temperature-resolved average dynamics in the phase space of the system that allowed us to identify the behavior of fluid of different temperatures in different regions of the convection cell.

The conditional averages that appear in this formalism are unclosed terms that had to be estimated from direct numerical simulations of Rayleigh–Bénard convection in three different geometries: Horizontally periodic convection in three and two dimensions and convection in a cylindrical vessel. We found for all three cases that the characteristic curves, i. e. the trajectories of the conditional particles, form concentric closed curves in phase space that reconstruct the general picture of fluid heating up at the bottom, rising to the top, cooling down and sinking to the lower plate again. The two settings with periodic horizontal boundaries exhibited generally a comparable behavior, where the subtle differences were linked to coherent structures that appear in two dimensions, e. g. plume hot spots. As cylindrical convection has another phase space dimension related to the horizontal movement, it featured additional structures that were not present in the former two cases; in particular, we could identify corner flows near the sidewalls of the cylindrical vessel that are only performed by fluid of certain temperatures.

The goal of part II was to identify and understand the structures that are the building blocks of turbulent convection. A method that is able to achieve this is the *proper orthogonal decomposition* (POD) that yields an orthonormal set of basis modes for a given data set of flow fields. Applying this established technique to turbulent convection resulted in modes that give the optimal description of the data in terms of the generalized energy, i. e. kinetic energy plus temperature variance. However, the generalized energy is not physically meaningful, as one effectively mixes quantities of different units. Therefore we tailored the technique towards Rayleigh–Bénard convection so that it instead gives a description of the heat transport. The understanding of the heat transport through the fluid layer in terms of the Nusselt number is one of the key components in Rayleigh–Bénard research.

We then used a data set of two-dimensional convection to benchmark the new method against the usual approach, and could show that the Nusselt-maximizing ansatz performs better in all cases. The description of the time series and the distribution function of the heat transport achieved better results with fewer modes when utilizing lower-dimensional projections on the Nusselt-modes. We could link the better performance to the modes being sensitive to the heat transport: Compared to the usual approach, the Nusselt-modes emphasized localized structures of strong convective heat transport that could subsequently be distinguished, i. e. into plumes that have a high positive heat transport versus blobs of fluid that are being swept in the “wrong” direction (e. g., hot fluid that is forced downwards) and thus have a strongly negative heat transport.

In part III, we analyzed the behavior of the temperature field and its fluctuations near the onset of convection, i. e. far from the turbulent regime that we have considered in the prior parts. To this end, we employed the stochastically forced Swift–Hohenberg equation, which is a nonlinear evolution equation for a two-dimensional order parameter field that is related to the temperature field in horizontal slices of convection. We applied the methods known from part I to derive an equation for the PDF of the order parameter, this time taking the shape of a Fokker–Planck equation due to the noise term. As before, unclosed terms in the form of conditional averages appeared, which we estimated from data obtained through direct numerical simulations. We could thus reconstruct the PDF of the order parameter with the help of the basic equations of motion and link the shape of the PDF to different mechanisms at work in the system. Furthermore, we proposed two simple models – one on the basis of the conditional averages and the PDF methods described above, the other being more phenomenological – that were able to yield reasonable results comparable to the directly estimated PDF.

As a spin-off product of the statistical analysis, the description of the stochastic Swift–Hohenberg system in terms of gradient dynamics (i. e., in a functional formulation) allowed us to propose a method to speed up the generation of data ensembles. We put forward and solved a functional Fokker–Planck equation for the forced Swift–Hohenberg system, which enabled us to assign probabilities to whole configurations of the order parameter field. This in turn made it possible to skip the slow transient initial phases of the dynamics and instead start the numerical simulations in the final stationary states of the system.

Apart from the physical results summarized before, another key aspect of this thesis was the development of methods that were used to analyze convective flows:

Although the framework of PDF methods has been known for some time in pure fluid dynamics as well as in the research on turbulent reactive flows, it had not been adapted towards RAYLEIGH–BÉNARD convection. We have shown that it yields a temperature-resolved description of the dynamics in the convection cell, which is an insightful view of convection that should be pursued further. As an example, the methods presented here could obviously be used to analyze numerical convection data of different flow geometries or in a parameter scan of the RAYLEIGH and the PRANDTL number. This could yield further insights on general mechanisms as well as differences between the different cases. Furthermore, with sufficiently sophisticated measurement tools, it would be interesting to apply the PDF methods to experimental data obtained from simultaneous velocity and temperature measurements.

The description of the NUSSELT-maximizing POD method has been kept as general as possible, and thus it is straightforward to apply the method to different systems that are characterized by response parameters with a strong physical meaning. For example, one could think of a POD method that analyzes the flow of air around the wings of an airplane or the propeller of a wind turbine, and characterize the POD modes in terms of the lift or the drag that is produced. In this way, it should be possible to obtain the flow structures with a major influence on the lift or the drag. Subsequently one can hope to adjust and optimize the wing profiles in order to enhance the desired flow structures and to suppress the unfavored ones, thus increasing the effectiveness.

The functional methods developed for the analysis of the SWIFT–HOHENBERG system can also be extended towards other systems, most easily of course to other gradient dynamics under the influence of noise. But also the PDF analysis may lead to a different view of pattern-forming systems in general, as these are usually coarse-grained models of microscopic behavior (e. g., the pattern formation in thin films is described in the so-called lubrication approximation, which can be thought of as a coarse-graining of the NAVIER–STOKES equations). In this coarsening process the microscopic noise is lost. Thus, in the PDF analysis of the stochastic SWIFT–HOHENBERG equation we performed, the amount of noise that is added to the system may be linked to the amount of smoothing that is applied in the coarse-graining. Therefore, a trade-off between smoothing the microscopic noise while still retaining the relevant large-scale fluctuations in the pattern-forming system may be achieved by fine-tuning the amount of noise in a description by PDF methods. We believe that the analysis of other model equations for pattern formation would benefit from this line of thought.

To bring up another aspect and a further outlook, also the stronger synergy of the three parts of this thesis is expected to yield more insights into the single systems:

As the driving force behind the SWIFT–HOHENBERG system is to minimize the LYAPUNOV functional, a POD approach that measures the LYAPUNOV functional (or, to be more precise, the linear terms therein) is expected to give better results than the usual ansatz. In turn it would be interesting to see how these POD modes compare to the description of the system by a superposition of plane waves, which was already found to be quite satisfactory.

Furthermore, as the modified POD approach was sensible to the convective heat transport, and the PDF method described the mean transport properties of RAYLEIGH–BÉNARD convection, we expect that a combination of these two techniques might provide interesting results. To this end, we suggest to use lower-dimensional projections of convection data onto a subset of the POD modes in the estimation of the conditional averages that are needed for the PDF methods. By this, the mean dynamics and transport properties in the convection cell could be related to the large-scale structures and the small-scale fluctuations that the POD method is able to separate from each other. Thus, we expect that a "hierarchy of heat transport dynamics" could be built to understand the precise role of the structures and their dynamics on different scales.

Also, the PDF analysis of RAYLEIGH–BÉNARD convection with a fluctuating force – which can be motivated from inhomogeneities of the horizontal plates or from internal sources of heat – seems promising: In this case, the structure of the equations would not allow for concentric closed curves in phase space (as were found in part I), as the dynamics in phase space are now subjected to diffusion. It would be interesting to examine how the concentric curves behave when noise is gradually added to the system. The required numerical simulations of the stochastic system can then in turn be sped up with methods alike to the one proposed for the generation of statistical ensembles of the forced SWIFT–HOHENBERG system.

In conclusion, over the course of this thesis we developed statistical methods for the detection of coherent structures and the dynamical behavior of fluid therein. While this does not solve the overarching *turbulence problem*, the methods we developed as well as the insights we obtained from them may prove useful to achieve this distant goal.

Publications in the Context of this Thesis

The following publications were produced during the course of (or are otherwise directly related to) this thesis, sorted in chronological order:

Lülff, Johannes and Wilczek, Michael and Friedrich, Rudolf (2011). Temperature statistics in turbulent Rayleigh–Bénard convection. *New Journal of Physics*, 13(1):015002.

This is the publication resulting from my diploma thesis (Lülff, 2011) that constitutes the basis upon which part I of the present thesis is build. Text and figures of this publication where produced entirely by me.

Friedrich, Rudolf and Daitche, Anton and Kamps, Oliver and Lülff, Johannes and Vosskuhle, Michel and Wilczek, Michael (2012). The Lundgren–Monin–Novikov hierarchy: Kinetic equations for turbulence. *Comptes Rendus Physique*, 13(9–10):929–953.

An invited review article on PDF methods written by my former supervisor Prof. Dr. Rudolf Friedrich († 2012) and his co-workers, where the Rayleigh–Bénard part was contributed by me.

Petschel, Klaus and Stellmach, Stephan and Wilczek, Michael and Lülff, Johannes and Hansen, Ulrich (2013). Dissipation layers in Rayleigh–Bénard convection: A unifying view. *Physical Review Letters*, 110:114502.

Joint work with my second supervisor Prof. Dr. Ulrich Hansen and his co-workers from the geophysics department on a new classification scheme of boundary layers in Rayleigh–Bénard convection; the textual work was done by Klaus Petschel. The present thesis does not go into the details of this publication.

Petschel, Klaus and Stellmach, Stephan and Wilczek, Michael and Lülff, Johannes and Hansen, Ulrich (2015). Kinetic energy transport in Rayleigh–Bénard convection. *Journal of Fluid Mechanics*, 773:395–417.

Joint work with my second supervisor Prof. Dr. Ulrich Hansen and his co-workers on the composition and redistribution of kinetic energy in Rayleigh–Bénard convection, building upon the previous work by Petschel *et al.* (2013). This publication is not detailed in the present thesis.

LÜLFF, JOHANNES and WILCZEK, MICHAEL and STEVENS, RICHARD J. A. M. and FRIEDRICH, RUDOLF and LOHSE, DETLEF (2015). Turbulent Rayleigh–Bénard convection described by projected dynamics in phase space. *Journal of Fluid Mechanics*, 781:276–297.

This is the publication from which part I of this thesis was adapted. It represents original research, and text and figures where produced entirely by me.

LÜLFF, JOHANNES (2015). Describing the heat transport of turbulent Rayleigh–Bénard convection by POD methods. *arXiv e-prints*, 1510.06908. Submitted to *Journal of Fluid Mechanics*.

This publication results from part II and represents original research where all conceptual and textual work was conducted by me. As this publication builds upon and was written after the corresponding part of this thesis, it includes some research not presented here.

Appendix

A PDF Description of RAYLEIGH–BÉNARD Convection: In-depth Analyses

In this section we will present analyses and remarks referring to part I. In particular, this includes figures and technical details that were used in the answers to the referees in the peer review process of the publication that part I is based upon (LÜLFF *et al.*, 2015), but that were deemed too exhaustive to fit into the publication.

A.1 Improvement of the Numerics

In section 4.1 on page 21 we find that the characteristics tend to converge towards limit cycles due to the presence of numerical noise. As this behavior is defective (the characteristics should form closed concentric curves instead), we improved the numerics (i. e., the integration of the characteristics) in the course of the review process of the publication. For reasons of readability, we did not go into the technical details in the publication; nevertheless, we want to include the detailed list of improvements in this appendix:

1. When estimating the conditionally averaged vector field through binning, we enforced the up-down symmetry of the RAYLEIGH–BÉNARD system, thus effectively doubling the amount of statistics.

2. We applied smoothing to the conditionally averaged vector field by convolving the bins with a GAUSSian kernel. Extensive testing suggested a standard deviation of 1.5 bins.

3. We compared a variety of time-stepping schemes and found that the *implicit midpoint rule* (see, e. g., KASTNER-MARESCH (1992)) gave the best results.[1]

4. The field of the probability flux was made divergence-free, i. e. the validity of (4.1) (page 23) was enforced pointwise in the following way: Let $\boldsymbol{q}$ be the phase space velocity, i. e. $\boldsymbol{q} = \begin{pmatrix} \langle u_z | T,z \rangle \\ \langle \Delta T | T,z \rangle \end{pmatrix}$. Then the solenoidality of the probability flux (i. e., (4.1)) reads $\nabla \cdot (\boldsymbol{q} f) = 0$. This was enforced by projecting $\boldsymbol{q} f$ onto its solenoidal

---

[1] As a side note, this time-stepping scheme is also a symplectic integrator when applied to HAMILTONian dynamics.

part by the usual approach, i. e. $\widetilde{qf} = \left(\mathbb{1} - \nabla\Delta^{-1}\nabla\right)(qf)$ with $\nabla \cdot \left(\widetilde{qf}\right) = 0$ (see, e. g., LÜLFF (2011, sec. 2.2.3)). Here, Δ^{-1} stands symbolically for the solution of a POISSON equation, i. e. a POISSON integral.

The modified phase space velocity $\tilde{q}$ corresponding to the solenoidal probability flux $\widetilde{qf}$ was then obtained by division by f, i. e.

$$\tilde{q} = \frac{1}{f}\widetilde{qf} = \frac{1}{f}(\mathbb{1} - \nabla\Delta^{-1}\nabla)(qf) \quad , \tag{A.1}$$

and this $\tilde{q}$ was then used for the integration of the trajectories. It is immediately clear that by construction, $\tilde{q}$ fulfills $\nabla \cdot (\tilde{q}f) = 0$.

This "workaround" of projecting qf and dividing by f is necessary because the solenoidality poses a restriction on the probability flux qf, whereas the phase space velocity q is needed for the integration of the characteristics. We are aware that this procedure implies a bias, because it assumes that only the phase space velocity is defective and responsible for the violation of the solenoidality. But as one cannot expect to unambiguously rectify the two quantities q and f from one equation ($\nabla \cdot (qf) \overset{!}{=} 0$) alone, this bias is in our opinion inevitable.

5. When integrating the trajectories, true bicubic interpolation was applied to sample the conditionally averaged vector field between grid points; prior to this, we used a cubic interpolation in horizontal direction followed by a cubic interpolation in vertical direction (this is different from true bicubic interpolation as it misses certain cross-terms).

The implementation and tuning of these improvements and the post-processing scheme then gave rise to the closed concentric curves we find in section 4.1.

A.2 Comparison of Limit Cycle and Family of Closed Curves

In the discussion of figure 4.5 (page 26) in section 4.1 it is put forward that the faulty limit cycle obtained in the case with noise and the family of closed trajectories obtained by post-processing the data give in general the same picture; furthermore, it is claimed that the limit cycle is one valid member of the family of closed curves, apart from minor imperfections. This comparison is given in figure A.1.

The figure confirms that the limit cycle shown in gray is positioned almost entirely between two adjacent closed circles. Only in the lower left and upper right corners small deviations can be seen. We speculate that these deviations may be attributed to the solenoidal projection (cf. (A.1) in the above section A.1) that may produce unreliable results in these areas: Towards the boundary at $z = 0$, the support of the conditional

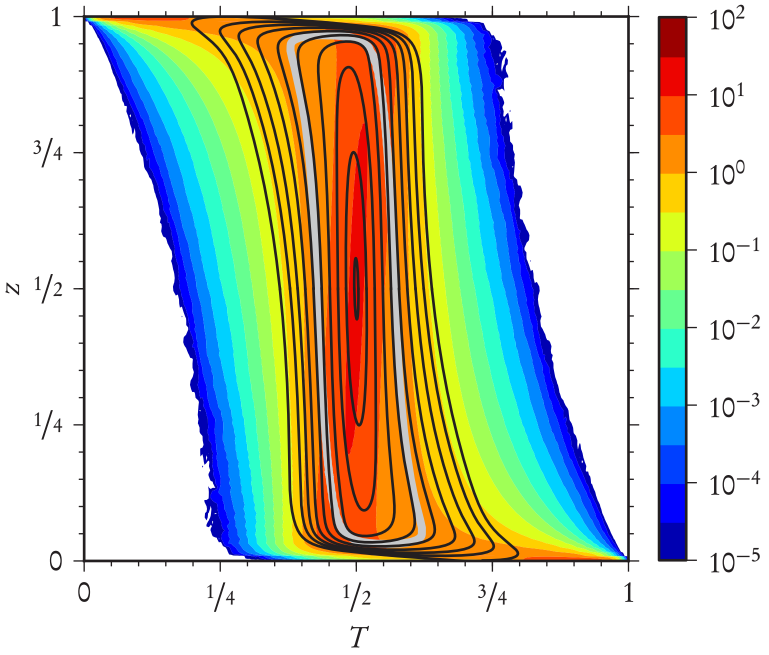

Figure A.1: *Comparison of the faulty limit cycle that is obtained when the noise is not removed from the vector field (in gray) and the family of closed concentric curves that are obtained after post-processing the vector field (in black). Presentation analogous to figures* 4.3 *and* 4.5.

averages changes quickly with z and moves towards $T = 1$ as the temperature PDF contracts towards a δ-function, and thus, in the lower left corner the spatial derivatives of the projection operator $(\mathbb{1} - \nabla\Delta^{-1}\nabla)$ may become flawed (especially the derivative in z-direction). Nevertheless, we deem the alleged limit cycle as a valid, generic member of the family of closed nested loops (modulo minimal imperfections), and it is plausible that the same applies to the Rayleigh–Bénard setups of two-dimensional (section 4.2) and cylindrical convection (section 4.3).

B Proper Orthogonal Decomposition: Proofs and Remarks

This section gives some in-depth calculations and comments that have only been sketched, and especially provides rigorous proofs for observations and statements made in part II.

B.1 From Maximization to Eigenvalue Problem

For a function $\phi(x)$ that maximizes $\left\langle |(q,\phi)|^2 \right\rangle$ under the normalization constraint $||\phi||^2 = 1$ (cf. section 7.1 on page 47), a necessary condition is that ϕ is a stationary point of the LAGRANGian functional

$$\begin{aligned}\mathfrak{L}[\phi] &= \left\langle |(q,\phi)|^2 \right\rangle - \lambda\left((\phi,\phi)-1\right) && \text{(B.1a)}\\ &= \left\langle \int \mathrm{d}x'\,\overline{q}(x')\phi(x') \int \mathrm{d}x'\,\overline{\phi}(x')q(x') \right\rangle \\ &\quad - \lambda\left(\int \mathrm{d}x'\,\overline{\phi}(x')\phi(x') - 1\right) \quad , && \text{(B.1b)}\end{aligned}$$

where λ is a LAGRANGE multiplier that assures normalization. From (B.1a) to (B.1b), $\overline{(q,\phi)} = (\phi,q)$ (with $\overline{\cdot}$ denoting complex conjugation) as well as the definition of the scalar product as $(f,g) = \int \mathrm{d}x'\,\overline{f}(x')g(x')$ has been used. For ϕ to be a stationary point, the variation of $\mathfrak{L}$ with respect to ϕ has to vanish:

$$\frac{\delta}{\delta\phi(x)}\mathfrak{L}[\phi] = 0 \tag{B.2}$$

With the principal rules of differentiation (see also section C.3)

$$\begin{aligned}\frac{\delta\phi(x')}{\delta\phi(x)} &= \delta(x-x') && \text{(B.3a)}\\ \frac{\delta\overline{\phi}(x')}{\delta\phi(x)} &= 0 \quad (\overline{\phi}\text{ is independent of }\phi)^1 && \text{(B.3b)}\\ \frac{\delta q(x')}{\delta\phi(x)} &= 0 \quad (q\text{ is independent of }\phi) && \text{(B.3c)}\end{aligned}$$

---

[1] See, for example, GREINER and REINHARDT (1993, secs. 2.2 and 4.2).

equation (B.2) becomes

$$0 = \frac{\delta}{\delta\phi(x)}\mathfrak{L}[\phi] = \left\langle \int \mathrm{d}x' \overline{q}(x')\delta\left(x - x'\right) \int \mathrm{d}x' \overline{\phi}(x') q(x') \right\rangle \\ - \lambda \int \mathrm{d}x' \overline{\phi}(x')\delta\left(x - x'\right) \quad , \tag{B.4}$$

which simplifies to

$$\left\langle \overline{q}(x) \int \mathrm{d}x' \overline{\phi}(x') q(x') \right\rangle = \lambda \overline{\phi}(x) \quad . \tag{B.5}$$

After reordering, interchanging integration and ensemble average[2] and applying complex conjugation this reads

$$\int \mathrm{d}x' \left\langle q(x)\overline{q}(x')\right\rangle \phi(x') = \lambda\phi(x) \quad , \tag{B.6}$$

which is the eigenvalue problem (7.3) on page 48.

B.2 Mean Energy of the Data Ensemble

From $\lambda_i = \left\langle |(q, \phi^i)|^2 \right\rangle$ (cf. (7.5) on page 48), it follows that the sum of all eigenvalues equals

$$\sum_i \lambda_i = \sum_i \left\langle |(q, \phi^i)|^2 \right\rangle \tag{B.7a}$$

$$= \sum_i \left\langle (q, \phi^i)(\phi^i, q) \right\rangle \tag{B.7b}$$

$$= \sum_i \left\langle \int \mathrm{d}x\, \overline{q}(x)\phi^i(x) \int \mathrm{d}x' \overline{\phi^i}(x') q(x') \right\rangle \tag{B.7c}$$

$$= \left\langle \iint \mathrm{d}x\, \mathrm{d}x' \overline{q}(x) q(x') \sum_i \phi^i(x)\overline{\phi^i}(x') \right\rangle \quad . \tag{B.7d}$$

In (B.7a)–(B.7c), only definitions have been inserted, and in (B.7d) terms have been reordered (it is again assumed that spatial integrals and ensemble averaging commute). Spectral theory now assures that the POD modes ϕ^i, which have been obtained as the eigenfunctions of a Hermitian operator, obey the completeness relation

$$\sum_i \phi^i(x)\overline{\phi^i}(x') = \delta(x - x') \quad . \tag{B.8}$$

---

[2] The arbitrary function ϕ does not depend on the data ensemble $\{q\}$ and therefore "commutes" with the ensemble averaging.

Therefore (B.7) becomes

$$\sum_i \lambda_i = \left\langle \int \mathrm{d}x\, \overline{q}(x) q(x) \right\rangle = \left\langle (q,q) \right\rangle = \left\langle ||q||^2 \right\rangle \quad , \tag{B.9}$$

i. e. the sum of all eigenvalues is the mean energy of the data ensemble.

B.3 Positive Definiteness of $\mathbf{XTX}^\dagger\mathbf{S}$

Multiplying the Eigenvalue problem (7.11) on page 50, i. e.

$$\mathbf{XTX}^\dagger\mathbf{S}\boldsymbol{\phi} = \lambda\boldsymbol{\phi} \quad , \tag{B.10}$$

from the left with $\boldsymbol{\phi}^\dagger\mathbf{S}^\dagger$, one gets

$$\boldsymbol{\phi}^\dagger\mathbf{S}^\dagger\mathbf{XTX}^\dagger\mathbf{S}\boldsymbol{\phi} = \lambda\boldsymbol{\phi}^\dagger\mathbf{S}^\dagger\boldsymbol{\phi} \quad . \tag{B.11}$$

With $v := \mathbf{X}^\dagger\mathbf{S}\boldsymbol{\phi}$ and $\boldsymbol{\phi}^\dagger\mathbf{S}^\dagger\boldsymbol{\phi} = 1$ (cf. (7.16)), this reduces to

$$\lambda = v^\dagger\mathbf{T}v = (v,v)_\mathbf{T} = ||v||^2_\mathbf{T} \geq 0 \quad , \tag{B.12}$$

thus proving the positive definiteness of $\mathbf{XTX}^\dagger\mathbf{S}$ (with $(\cdot,\cdot)_\mathbf{T}$ and $||\cdot||_\mathbf{T}$ being the scalar product and norm induced by $\mathbf{T}$).

B.4 Eigenvalues of $\mathbf{AB}$ and $\mathbf{BA}$

To proof that for general (not necessarily square) matrices[3] $\mathbf{A} \in \mathbb{C}^{m\times n}$ and $\mathbf{B} \in \mathbb{C}^{n\times m}$ the products $\mathbf{AB}$ and $\mathbf{BA}$ have the same non-zero eigenvalues, consider the following $(n+m)\times(n+m)$ block matrices:

$$\mathbf{M} = \begin{pmatrix} \mathbb{0}_{n\times n} & \mathbb{0}_{n\times m} \\ \mathbf{A} & \mathbf{AB} \end{pmatrix} \quad \mathbf{N} = \begin{pmatrix} \mathbf{BA} & \mathbb{0}_{n\times m} \\ \mathbf{A} & \mathbb{0}_{m\times m} \end{pmatrix} \quad \mathbf{Y} = \begin{pmatrix} \mathbb{1}_{n\times n} & \mathbf{B} \\ \mathbb{0}_{m\times n} & \mathbb{1}_{m\times m} \end{pmatrix} \tag{B.13}$$

A simple calculation shows that $\mathbf{YM} = \mathbf{NY}$, or, since $\mathbf{Y}$ is invertible (all eigenvalues of $\mathbf{Y}$ are 1),

$$\mathbf{M} = \mathbf{Y}^{-1}\mathbf{NY} \quad . \tag{B.14}$$

Thus, the matrices $\mathbf{M}$ and $\mathbf{N}$ are *similar* and therefore have the same characteristic polynomial:

$$\left|\lambda\mathbb{1} - \mathbf{M}\right| = \left|\lambda\mathbb{1} - \mathbf{N}\right| \tag{B.15}$$

---

[3] Without loss of generality, we assume $m \leq n$.

Inserting **M** and **N** yields

$$\lambda^n \left|\lambda\mathbb{1} - \mathbf{AB}\right| = \lambda^m \left|\lambda\mathbb{1} - \mathbf{BA}\right| \quad \text{or} \quad \lambda^{n-m} \left|\lambda\mathbb{1} - \mathbf{AB}\right| = \left|\lambda\mathbb{1} - \mathbf{BA}\right| \quad , \tag{B.16}$$

which shows that the n eigenvalues of the bigger matrix **BA** consist of the m eigenvalues of **AB** and $n - m$ additional zeros.

The idea of this proof is due to Butler (2013). Equivalently, the same may be shown by applying Sylvester's determinant theorem (Sylvester, 1851), which states that $\left|\mathbb{1} + \mathbf{AB}\right| = \left|\mathbb{1} + \mathbf{BA}\right|$.

B.5 Comments on the Calculation of Covariance Matrices and its Implementation

As the data ensemble may become very large, the direct implementation of the matrix equations from section 7.2 with a linear algebra library is a bit cumbersome. Often, the data set consists of a collection of one file per snapshot. Then the direct manipulation of **X** may become impossible simply because the matrix becomes too large to fit into the main memory of the computer. To still handle e. g. the temporal covariance matrix $\mathbf{X}^\dagger\mathbf{S}\mathbf{X}$ of the method of snapshots, one could opt to calculate every entry "by hand" – i. e., load pairs of snapshots corresponding to columns of **X** into the memory and calculate their scalar product to obtain one entry of $\mathbf{X}^\dagger\mathbf{S}\mathbf{X}$. While this is certainly possible, it requires a considerable amount of additional management – for example, one has to care about how the matrix equations look like when instead operating on collections of vectors. Also, the calculation of the POD modes $\mathbf{\Phi}$ as a linear combination of the snapshots contained in **X** becomes unhandy, not least because it requires a huge amount of swapping between memory and disk space as all snapshots have to be separately loaded from disk to obtain a single POD mode.

After extensive testing, we found that the fastest and most concise numerical implementation can be achieved by utilizing so-called *memory-mapped* matrices (or arrays), which are available in many programming languages. With memory-mapped arrays, a big file on the hard disk can be manipulated as a regular array, and the required parts of the array are loaded from disk into the memory by the operating system as needed. As the operating system is also in charge of caching parts of the arrays, this is usually orders of magnitude faster than the ansatz proposed above; but most importantly, one can operate on the whole matrices, thus enabling a direct implementation of the equations derived in section 7.2. This means that in the numerical implementation, the single snapshots contained in single files have first to be copied into columns of the memory-mapped matrix **X**; after that, the program does not have to care about swapping, caching, copying between disk and memory etc., as this is all done in the background by the operating system.

Also, it should be noted that the big $N_x \times N_x$ matrix $\mathbf{S}$ does not have to reside in memory with all N_x^2 entries, because in virtually all cases it is not dense but (blockwise) diagonal. Thus only $\mathcal{O}(N_x)$ entries have to be stored, and most linear algebra libraries contain special methods to efficiently handle (blockwise) diagonal matrices.

B.6 Energy Contained in the Projection of a Single Snapshot

We want to show that the energy contained in a single snapshot, projected onto N_p POD modes, is rising monotonically with the number N_p of modes used (cf. discussion of figure 8.6 on page 67). To this end, we examine the energy contained in the projection of an arbitrary (say, the i-th) snapshot, i. e.

$$E^{N_p}(t_i) = \left(\tilde{\boldsymbol{q}}^i\right)^\dagger \mathbf{S}\tilde{\boldsymbol{q}}^i \quad , \tag{B.17}$$

where $\tilde{\boldsymbol{q}}^i$ is the i-th column of the projected data set $\tilde{\mathbf{X}}$:

$$\begin{aligned} \tilde{\boldsymbol{q}}^i &= \tilde{\mathbf{X}}\boldsymbol{e}_i &\text{(B.18a)}\\ &= \mathbf{X}\mathbf{T}\tilde{\mathbf{C}}\tilde{\mathbf{C}}^\dagger \boldsymbol{e}_i &\text{(B.18b)}\\ &= \mathbf{X}\mathbf{T}\mathbf{C}\mathbf{R}^{N_p}\left(\mathbf{R}^{N_p}\right)^\dagger \mathbf{C}^\dagger \boldsymbol{e}_i &\text{(B.18c)} \end{aligned}$$

Here, only definitions from section 7.5 have been substituted. Inserting $\tilde{\boldsymbol{q}}^i$ into (B.17) and identifying the eigenvalue problem $\mathbf{X}^\dagger\mathbf{S}\mathbf{X}\mathbf{T}\mathbf{C} = \mathbf{C}\boldsymbol{\Lambda}$ and the orthonormality relation $\mathbf{C}^\dagger\mathbf{T}\mathbf{C} = \mathbb{1}$, we arrive at

$$\begin{aligned} E^{N_p}(t_i) &= \boldsymbol{e}_i^\dagger \mathbf{C}\mathbf{R}^{N_p}\left(\mathbf{R}^{N_p}\right)^\dagger \boldsymbol{\Lambda}\mathbf{R}^{N_p}\left(\mathbf{R}^{N_p}\right)^\dagger \mathbf{C}^\dagger \boldsymbol{e}_i &\text{(B.19a)}\\ &=: \boldsymbol{v}^\dagger \boldsymbol{\Lambda}\boldsymbol{v} &\text{(B.19b)} \end{aligned}$$

with the vector $\boldsymbol{v} := \left(\mathbf{C}\mathbf{R}^{N_p}\left(\mathbf{R}^{N_p}\right)^\dagger\right)^\dagger \boldsymbol{e}_i \in \mathbb{C}^{N_t}$. Since $\boldsymbol{\Lambda}$ is a diagonal matrix composed of the non-negative eigenvalues λ_i, writing the previous vector-matrix-vector product as a sum over the entries reads

$$\begin{aligned} E^{N_p}(t_i) &= \sum_{j=1}^{N_t} \overline{v_j}\lambda_j v_j &\text{(B.20a)}\\ &= \sum_{j=1}^{N_t} \lambda_j |v_j|^2 \quad . &\text{(B.20b)} \end{aligned}$$

The energy of an N_p-dimensional projection of a single snapshot can therefore be written as a sum of non-negative terms.

To show that this sum is monotonically growing with N_p, we note that the matrix $\mathbf{C}\mathbf{R}^{N_p}\left(\mathbf{R}^{N_p}\right)^{\dagger}$ is the same as the matrix $\mathbf{C}$ but with the last $N_t - N_p$ *columns* replaced by zeros; thus, the last $N_t - N_p$ *rows* of its conjugate transpose and therefore also the last $N_t - N_p$ entries of v are zero. Consequently, the previous sum actually consists of only N_p terms:

$$E^{N_p}(t_i) = \sum_{j=1}^{N_p} \underbrace{\lambda_j |v_j|^2}_{\geq 0} \tag{B.21}$$

This concludes the proof that $E^{N_p}(t_i)$ is monotonically growing with N_p.

B.7 Heat Transport Maximizing POD in Three Dimensions

In chapter 9, we developed and tested the POD that maximizes the convective heat transport for Rayleigh–Bénard convection in two dimensions. Although the velocity field is two-dimensional, due to incompressibility the horizontal velocity depends on the vertical one, and thus, we can restrict ourselves to only handle the vertical velocity component. Therefore, the snapshots consisting of temperature and vertical velocity fully determine the fluid state at each time instant. As a consequence, the newly defined scalar product that measures the convective heat transport uses all the information contained in the snapshots, which is also reflected in the fact that the matrix $\mathbf{S}$ defining the scalar product (cf. (9.3) on page 70) has only non-zero eigenvalues.

This situation changes when considering convection in three dimensions. Here, the incompressible fluid is fully determined by specifying the fields of temperature and two velocity components, say one horizontal and the vertical one. The snapshots take (in a blockwise fashion) the form

$$q^i = \left(T^i, u_x^i, u_z^i\right)^{\mathrm{T}} \in \mathbb{R}^{3n_x} \quad , \tag{B.22}$$

and the whole data matrix is

$$\mathbf{X} = \begin{pmatrix} T^1 & \dots & T^{N_t} \\ u_x^1 & \dots & u_x^{N_t} \\ u_z^1 & \dots & u_z^{N_t} \end{pmatrix} \in \mathbb{R}^{3n_x \times N_t} \quad . \tag{B.23}$$

The Nu$^{\mathrm{c}}$-maximizing scalar product matrix then reads

$$\mathbf{S} = \frac{1}{2n_x} \begin{pmatrix} \mathbb{0} & \mathbb{0} & \mathbb{1} \\ \mathbb{0} & \mathbb{0} & \mathbb{0} \\ \mathbb{1} & \mathbb{0} & \mathbb{0} \end{pmatrix} \in \mathbb{R}^{3n_x \times 3n_x} \quad , \tag{B.24}$$

which has the eigenvalues $\pm 1/2n_x$ and 0, each n_x-fold. Due to the eigenvalues 0, the matrix **S** is not non-degenerate any more and does not have full rank; in the induced scalar product and thus in the covariance matrix, information about the horizontal velocity component is lost.

This does not pose a problem, though, and it does not necessarily mean that the temporal covariance matrix becomes rank deficient: In section 7.4 it was established that the temporal covariance matrix $\mathbf{X}^\dagger\mathbf{S}\mathbf{X}\mathbf{T}$ has full rank as long as all matrices have full rank and $\operatorname{rank}\mathbf{S} > \operatorname{rank}\mathbf{T}$. In the case discussed here, this reasoning has to be slightly adapted as **S** is rank deficient. To this end, consider the above matrices without the horizontal part, i. e.

$$\widehat{\mathbf{X}} = \begin{pmatrix} T^1 & \dots & T^{N_t} \\ u_z^1 & \dots & u_z^{N_t} \end{pmatrix} \in \mathbb{R}^{2n_x \times N_t} \tag{B.25}$$

and

$$\widehat{\mathbf{S}} = \frac{1}{2n_x} \begin{pmatrix} \mathbb{0} & \mathbb{1} \\ \mathbb{1} & \mathbb{0} \end{pmatrix} \in \mathbb{R}^{2n_x \times 2n_x} \quad . \tag{B.26}$$

It is easy to see that the covariance matrices are identical, i. e.

$$\mathbf{X}^\dagger\mathbf{S}\mathbf{X}\mathbf{T} = \widehat{\mathbf{X}}^\dagger\widehat{\mathbf{S}}\widehat{\mathbf{X}}\mathbf{T} \quad . \tag{B.27}$$

Since the reasoning from section 7.4 directly applies to the "hatted" matrices, it follows that $\mathbf{X}^\dagger\mathbf{S}\mathbf{X}\mathbf{T}$ has full rank when $\widehat{\mathbf{X}}$ has full rank and $\operatorname{rank}\widehat{\mathbf{S}} > \operatorname{rank}\mathbf{T}$, i. e. $2n_x > N_t$. In this case, the maximal number of N_t non-zero eigenvalues of the covariance matrix is obtained, and no problematic eigenvalues 0 appear.[4]

To put it in other words, the snapshots *lacking the horizontal part* have to be linearly independent. This could be violated for snapshots that have identical temperature and vertical velocity parts and only differ in the horizontal velocities, which we consider irrelevant because it is a pathological and not well-behaved case.

Although the information about the horizontal velocity components is lost in the covariance matrix, the horizontal velocity is still present in the POD modes and in the lower-dimensional projections, because these are constructed as linear combinations of the snapshots (cf. (9.6) and (7.33)). In a sense, the POD preserves the linear relation between the velocity components – e. g., when all the snapshots have a preferred direction of rotation in the horizontal plane (think of rotating convection), the POD modes will display the same horizontal rotation.

---

[4] As a reminder, full rank means only non-zero eigenvalues.

C Swift–Hohenberg Equation: Additional Comments

This section will give additional comments and explanations regarding the Swift–Hohenberg equation analyzed in part III.

C.1 Quadratic Nonlinearity in the Swift–Hohenberg Equation and the Connection to the Rayleigh–Bénard System

The Swift–Hohenberg equation with an additional quadratic nonlinearity reads

$$\frac{\partial}{\partial t}\psi(\boldsymbol{x},t)=\varepsilon\psi(\boldsymbol{x},t)-(\Delta+1)^2\psi(\boldsymbol{x},t)-\psi(\boldsymbol{x},t)^3+\delta\,\psi(\boldsymbol{x},t)^2 \quad , \tag{C.1}$$

see e. g. Bestehorn (2006, sec. 9.4.5). The quadratic term breaks the symmetry $\psi\rightarrow-\psi$, and additionally to the usual stripes also hexagonal as well as localized patterns are obtained, cf. figure C.1. Although the hexagonal pattern was already found in the early convection experiments by Bénard (1901), hexagons are generally not found in the *pure* Rayleigh–Bénard system but require special prerequisites like a Marangoni-esque surface instability or an internal heating. This is also the reason why we will not consider a quadratic nonlinearity in this thesis.

Figure C.1: *Stationary solution of the Swift–Hohenberg equation with additional quadratic nonlinearity that displays an ordered hexagonal structure. The parameters are* $\varepsilon=0.3$, $\delta=1.0$ *and* $\Omega=[0,16\pi]\times[0,16\pi]$, *and the remaining parameters are as in section* 13.4*ff.*

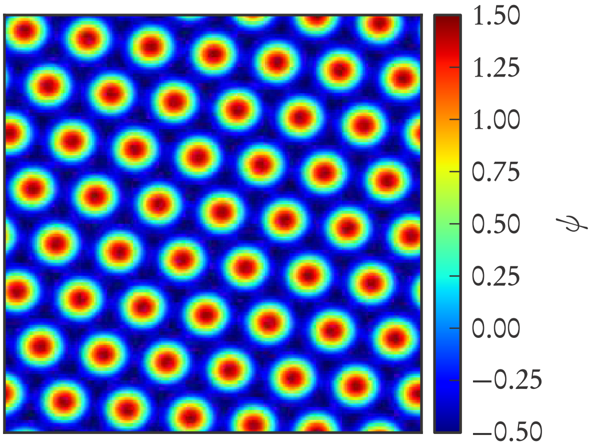

It is mentioned by KRAFT and GUREVICH (2015) that the addition of an offset

$$\psi \to \psi + \frac{\delta}{3} \tag{C.2}$$

transforms (C.1) into

$$\frac{\partial}{\partial t}\psi = \left(\varepsilon + \frac{\delta^2}{3}\right)\psi - (\Delta+1)^2\psi - \psi^3 + \frac{\delta}{3}\left(\varepsilon - 1 + \frac{2\delta^2}{9}\right) \tag{C.3a}$$

$$=: \varepsilon'\psi - (\Delta+1)^2\psi - \psi^3 + Y \quad , \tag{C.3b}$$

i. e. the quadratic term has the same effect on the dynamics and the patterns of the SWIFT–HOHENBERG equation as an inhomogeneity Y.[1] As the order parameter ψ is related to the temperature distribution in a horizontal plane of RAYLEIGH–BÉNARD convection, the inhomogeneity Y connects nicely to the observation that with internal heating, RAYLEIGH–BÉNARD convection may display hexagonal patterns – internal heating amounts to an inhomogeneity in the temperature part of the OBERBECK–BOUSSINESQ equations. In fact, hexagonal structures are often obtained in RAYLEIGH–BÉNARD convection when the up-down symmetry is broken, which is the case for both a quadratic nonlinearity and internal heating. Also, in the experiments by BÉNARD (1901) the up-down symmetry was broken due to different boundary conditions at the bottom and the top, which led (together with a MARANGONI-like surface instability) to the hexagonal patterns that were observed.

C.2 Creating GAUSSian Noise with Correlation

In order to generate a GAUSSian noise field $\Gamma(\boldsymbol{x})$ with a prescribed correlation function, i. e.

$$\left\langle \Gamma(\boldsymbol{x})\Gamma(\boldsymbol{x}+\boldsymbol{r})\right\rangle \overset{!}{=} c(\boldsymbol{r}) \quad , \tag{C.4}$$

we make use of the WIENER–KHINCHIN theorem. It states that the FOURIER transform of the correlation function $c(\boldsymbol{r})$ is the spectral density (i. e., the squared absolute value of the FOURIER transform) of the noise field, and therefore the absolute value of the FOURIER-transformed noise field is

$$\left|\mathscr{F}\left[\Gamma(\boldsymbol{x})\right](\boldsymbol{k})\right| = \sqrt{\mathscr{F}\left[c(\boldsymbol{r})\right](\boldsymbol{k})} \quad . \tag{C.5}$$

---

[1] Equation (C.3) is widely used in the context of nonlinear optics. There, the order parameter field ψ is connected to the light field in an optical resonator, and the inhomogeneity Y is an injection field (TLIDI *et al.*, 2009).

By choosing the yet undetermined complex phases of $\mathscr{F}\left[\Gamma(\boldsymbol{x})\right]$ as $\mathrm{e}^{\mathrm{i}\phi}$ where $\phi=\phi(\boldsymbol{k})$ are random numbers uniformly distributed in the interval $[0,2\pi)$, we can construct a noise field $\Gamma(\boldsymbol{x})$ that obeys (C.4) as

$$\Gamma(\boldsymbol{x})=\mathscr{F}^{-1}\left[\sqrt{\mathscr{F}\left[c(\boldsymbol{r})\right]}\,\mathrm{e}^{\mathrm{i}\phi}\right] \quad . \tag{C.6}$$

The central limit theorem then guarantees that $\Gamma(\boldsymbol{x})$ follows a GAUSSian distribution, as the inverse FOURIER transform in (C.6) can effectively be seen as the sum of independent random variables with different (but finite) variances. Additionally, certain assumptions have to hold regarding the form of the spectral density, such as a faster-than-algebraic decay.

In general, (C.6) allows the generation of random fields with an arbitrary correlation function, as long as its FOURIER transform is known (or can be computed numerically). In part III, we use the choice

$$c(\boldsymbol{r})=C_0\mathrm{e}^{-\frac{r^2}{2l^2}} \tag{C.7}$$

for which the FOURIER transform is know analytically,

$$\mathscr{F}\left[c(\boldsymbol{r})\right]=C_0 l^2\mathrm{e}^{-\frac{k^2l^2}{2}} \quad , \tag{C.8}$$

and which also shows an exponential decay. Thus, noise with correlation as in (C.7) can easily be generated. In fact, as the pseudospectral scheme employs $\mathscr{F}[\Gamma]$ instead of Γ itself (cf. (12.4) in section 12.1), the inverse FOURIER transform in (C.6) is redundant, and the correlated noise can be generated without actually calculating FOURIER transformations numerically. Furthermore, because $c(\boldsymbol{r})$ has slope zero at $\boldsymbol{r}=0$, the noise field $\Gamma(\boldsymbol{x})$ is differentiable, which is convenient for the pseudospectral scheme.

C.3 Variational Calculus in a Nutshell

The variational calculus deals with mappings of the form

$$L\,:\,V\rightarrow\mathbb{R} \quad , \tag{C.9}$$

where V is a vector space containing functions; in part III and also for the remainder of this section, we consider $V=C^4(\Omega)$, i. e. the set of all bounded functions from a compact two-dimensional set $\Omega\subset\mathbb{R}^2$ to the real numbers that have continuous fourth derivatives[2] that are also bounded. The mapping L, also called a *functional*, therefore assigns a real number $L[f]$ to each function $f(\boldsymbol{x})\in V$, and the calculus of variations examines how this value changes when the function f changes. Here, the function $f(\boldsymbol{x})$

---

[2] This is because the SWIFT–HOHENBERG equation contains a fourth derivative, i. e. $\Delta^2\psi$.

can be thought of as an infinite-dimensional vector with a continuous index $x \in \Omega$, as opposed to a finite-dimensional vector $\boldsymbol{f} = (f_i) \in \mathbb{R}^n$ with a discrete index $i \in \{1, 2, \ldots, n\}$. As an example, the functional $L[f] = \int_\Omega d^2y\, f(y)$ is proportional to the mean value of f; an more elaborate example is the LYAPUNOV functional (13.7) on page 106 that chapter 13 deals with.

The functional derivative of a functional $L[f]$ can be defined as the limit of a difference quotient:

$$\frac{\delta L[f(y)]}{\delta f(x)} := \lim_{\epsilon \to 0} \frac{L\big[f(y) + \epsilon\delta(y-x)\big] - L\big[f(y)\big]}{\epsilon} \tag{C.10}$$

While the functional $L[f]$ is a scalar, the functional derivative $\frac{\delta L[f(y)]}{\delta f(x)}$ yields a function that depends on x.

Speaking in terms of the analogy of $f(y)$ being an infinite-dimensional vector indexed by the continuous index y, the expression $f(y) + \epsilon\delta(y-x)$ means disturbing the "x-th" entry of the vector f by ϵ, or, to put it in other words, $f(y)$ is disturbed in the "direction" $\delta(y-x)$. In finite dimensions, the analogue would be $f_i + \epsilon\delta_{ij}$, i. e. disturbing the vector $\boldsymbol{f}$ in the direction of the j-th coordinate, and the limit of the corresponding difference quotient becomes the derivative of the function L at position $\boldsymbol{f}$ in the direction $\boldsymbol{e}_j$.

Although the definition (C.10) of the functional derivative is mathematically precise, it is not handy to work directly with the difference quotient. Therefore, we will now give a number of rules how to calculate functional derivatives, where $\frac{\delta}{\delta f(x)}$ denotes the functional derivative with respect to $f(x)$. In the following, $F : \mathbb{R} \to \mathbb{R}$ is an arbitrary[3] function of a scalar.

I. $f(x)$ and $f(y)$ are independent for $x \neq y$:

$$\frac{\delta f(y)}{\delta f(x)} = \delta(x-y) = \delta(y-x) \tag{C.11}$$

The finite-dimensional analogue would be $\frac{df_i}{df_j} = \delta_{ij}$.

II. Functional derivative and integral commute for functionals of the form $L[f] = \int_\Omega d^2y\, F\big(f(y)\big)$:

$$\frac{\delta L[f]}{\delta f(x)} = \frac{\delta}{\delta f(x)} \int_\Omega d^2y\, F\big(f(y)\big) = \int_\Omega d^2y\, \frac{\delta}{\delta f(x)} F\big(f(y)\big) \tag{C.12}$$

III. The functional derivative obeys a chain rule:

$$\frac{\delta F\big(f(y)\big)}{\delta f(x)} = F'\big(f(y)\big)\, \frac{\delta f(y)}{\delta f(x)} \overset{\mathrm{I}}{=} F'\big(f(y)\big)\, \delta(x-y) \tag{C.13}$$

---

[3] We assume all functions and functionals appearing in this section to be well-behaved.

This allows to use the usual rules of differentiation, e. g. calculate the derivative *locally*

$$\frac{\delta f(y)^n}{\delta f(x)} = n f(y)^{n-1}\,\delta(x-y) \quad , \tag{C.14}$$

or together with rule II *globally* (or, in other words, in a *weak* sense):

$$\frac{\delta}{\delta f(x)} \int_\Omega \mathrm{d}^2 y \, \sin f(y) \overset{\text{II}}{=} \int_\Omega \mathrm{d}^2 y \, \delta(x-y) \cos f(y) = \cos f(x) \tag{C.15}$$

IV. The functional derivative of a “regular” derivative (i. e., gradient) ∇f obeys the rule

$$\frac{\delta \nabla f(y)}{\delta f(x)} = \nabla \frac{\delta f(y)}{\delta f(x)} = \nabla \delta(x-y) \quad , \tag{C.16}$$

i. e. functional derivative and regular derivative commute.[4] This states that a function f and its gradient ∇f are dependent.

The gradient of the δ-function, $\nabla \delta(x-y)$, can be evaluated globally through *integration by parts*, for example:

$$\int_\Omega \mathrm{d}^2 y \, g(y) \nabla \delta(x-y) \overset{\text{i.p.}}{=} -\int_\Omega \mathrm{d}^2 y \, \delta(x-y) \nabla g(y) = -\nabla g(x) \tag{C.17}$$

Here we assumed that the boundary term of the integration by parts vanishes, i. e. $\int_{\partial\Omega} \mathrm{d}A \, g(y)\,\delta(x-y) = 0$; this is fulfilled for periodic boundaries or by demanding that the functions vanish on the boundary $\partial\Omega$ of the volume Ω.

To give an example, these rules can be combined to evaluate functional derivatives of the form $\int_\Omega \mathrm{d}^2 y \, G\big(\nabla f(y)\big)$ with an arbitrary function $G : \mathbb{R}^2 \to \mathbb{R}$:

$$\begin{aligned}
\frac{\delta}{\delta f(x)} \int_\Omega \mathrm{d}^2 y \, G\big(\nabla f(y)\big) &= \int_\Omega \mathrm{d}^2 y \, (\nabla G)\big(\nabla f(y)\big) \cdot \frac{\delta \nabla f(y)}{\delta f(x)} && \text{(II, III)} \quad \text{(C.18a)} \\
&= \int_\Omega \mathrm{d}^2 y \, (\nabla G)\big(\nabla f(y)\big) \cdot \nabla \delta(x-y) && \text{(IV)} \quad \text{(C.18b)} \\
&= -\int_\Omega \mathrm{d}^2 y \, \delta(x-y) \, \nabla \cdot \Big((\nabla G)\big(\nabla f(y)\big)\Big) && \text{(i. p.)} \quad \text{(C.18c)} \\
&= -(\Delta G)\big(\nabla f(x)\big)\, \Delta f(x) && \text{(C.18d)}
\end{aligned}$$

---

[4] In a mathematically more precise context, an expression like $\nabla\delta$ would have to be defined in a distributional sense. For the sake of simplicity, we will follow the physicist’s practice to not strictly distinguish between regular functions and distributions; however, one has to keep in mind that an expression like $\nabla\delta$ only makes sense under an integral, i. e. in a weak formulation.

In the first equality, rule III has been used two times for the two arguments of the function G, i. e. for the two components of ∇f; we have thus calculated the total functional derivative of G. In the last step, we calculated the (total) divergence of the expression $(\nabla G)\big(\nabla f(y)\big)$ by performing the usual chain rule, which resulted in the derivative $\nabla^2 f = \Delta f$ of the inner function ∇f. In contrast to that, the expression $(\nabla G)\big(\nabla f(y)\big)$ means that the gradient of G is evaluated at position $\nabla f(y)$, i. e. the gradient does not act on the inner function $\nabla f(y)$.

As a further example and the actual application we are aiming at, we consider the Lyapunov functional (13.7)

$$\mathscr{L}[\psi] = \int_\Omega \mathrm{d}^2x' \left(-\frac{\varepsilon}{2}\psi(x')^2 + \frac{1}{4}\psi(x')^4 + \frac{1}{2}\big(\Delta\psi(x') + \psi(x')\big)^2 \right) \tag{C.19}$$

for a bounded function $\psi : C^4(\Omega) \to \mathbb{R}$. When calculating the functional derivative of $\mathscr{L}[\psi]$, the first two terms can be evaluated trivially:

$$\frac{\delta\mathscr{L}[\psi]}{\delta\psi(x)} = -\varepsilon\psi(x) + \psi(x)^3 + \frac{1}{2}\frac{\delta}{\delta\psi(x)}\int_\Omega \mathrm{d}^2x' \,\big(\Delta\psi(x') + \psi(x')\big)^2 \tag{C.20}$$

The functional derivative of the remaining term is calculated as follows:

$$\begin{aligned}
&\frac{1}{2}\frac{\delta}{\delta\psi(x)}\int_\Omega \mathrm{d}^2x' \,\big(\Delta\psi(x') + \psi(x')\big)^2 && && \text{(C.21a)}\\
&\quad= \int_\Omega \mathrm{d}^2x' \,\big(\Delta\psi(x') + \psi(x')\big)\big(\Delta\delta(x-x') + \delta(x-x')\big) && \text{(II, III, IV)} && \text{(C.21b)}\\
&\quad= \int_\Omega \mathrm{d}^2x' \,\big(\Delta\psi(x') + \psi(x')\big)\Delta\delta(x-x') \;+\; \Delta\psi(x) + \psi(x) && \text{(eval. } \delta(\cdot)\text{)} && \text{(C.21c)}\\
&\quad= \Delta^2\psi(x) + \Delta\psi(x) \;+\; \Delta\psi(x) + \psi(x) && (2\times \text{i. p.}) && \text{(C.21d)}\\
&\quad= (\Delta + 1)^2\psi(x) && && \text{(C.21e)}
\end{aligned}$$

Hints for the undertaken steps are given after the respective equations. By substituting this into (C.20) it becomes clear that $-\frac{\delta\mathscr{L}[\psi]}{\delta\psi(x)}$ results in the correct right-hand side of the unforced Swift–Hohenberg equation, cf. (11.1) on page 99.

List of Figures

1.1 Three-dimensional convection with periodic horizontal boundaries . . . 2
1.2 Two-dimensional convection with periodic horizontal boundaries 3
1.3 Four consecutive snapshots of two-dimensional convection with periodic horizontal boundaries 7

4.1 Snapshot of the temperature field in three-dimensional RAYLEIGH–BÉNARD convection 21
4.2 Height-resolved profiles of the first four standardized moments of the temperature distribution for three-dimensional convection 22
4.3 Concentric closed characteristics found for three-dimensional convection after removing imperfections 24
4.4 Characteristics followed backwards in time for three-dimensional convection 25
4.5 RB cycle of the characteristics for three-dimensional convection 26
4.6 RB cycle for three-dimensional convection together with phase space speed 27
4.7 Temperature field for two-dimensional convection with periodic horizontal boundary conditions 28
4.8 First four standardized moments of temperature for two-dimensional convection 29
4.9 RB cycle of the characteristics for two-dimensional convection, together with the temperature PDF 30
4.10 RB cycle of the characteristics for two-dimensional convection, together with the phase space speed 31
4.11 Snapshot of the temperature field in three-dimensional convection in a cylinder 32
4.12 First four standardized moments of the temperature distribution for convection in a cylinder 33
4.13 RB cycle of the characteristics for convection in a cylinder 34
4.14 Vector field governing the characteristics in phase space for convection in a cylinder 36

6.1 Proper orthogonal decomposition in two dimensions 46

8.1 Two-dimensional data set of RAYLEIGH–BÉNARD convection 61
8.2 Eigenvalues of POD modes 63
8.3 Examples of POD modes 64
8.4 Sum of the first n eigenvalues 65
8.5 Projection of the data set onto the first four modes 66
8.6 Time series of full data set and projections 67

9.1 Eigenvalues of the Nu-modes 73
9.2 Examples of Nu-modes 74
9.3 Time series of the convective heat transport 76
9.4 Heat transport that is contained in the i-th Nu- respectively E-mode . . 77
9.5 Heat transport of Nu- and E-modes 77
9.6 Projection of one snapshot onto different number of Nu-modes 78
9.7 Time series of full data set and projections onto Nu-modes 80
9.8 Heat transport of positive Nu-modes 80
9.9 Time series of full data set and projections onto E-modes 81
9.10 L^2-norm of projected time series 82
9.11 Local convective heat transport of a single snapshot 83
9.12 Local convective heat transport of a projection onto the positive modes 84
9.13 PDF of local convective heat transport of projections onto positive Nu-modes 84
9.14 PDF of local convective heat transport of projections onto Nu-modes . 85
9.15 PDF of local convective heat transport of projections onto E-modes . . 85
9.16 Higher moments of the PDFs of local convective heat transport obtained from projections 86
9.17 Time series of the amplitudes 88
9.18 PDFs of the time series of the amplitudes 89
9.19 Power spectra of the time series of the amplitudes 90

11.1 Examples of pattern formation in convection 97
11.2 *Undulatus* type clouds 98
11.3 Example of patterns formed by the SWIFT–HOHENBERG equation 100

12.1 Numerical solution of the stochastically driven SWIFT–HOHENBERG equation 103

13.1 Competition of linear driving versus nonlinear saturation in the SWIFT–HOHENBERG equation 107
13.2 LYAPUNOV functional of plane waves in dependence on their amplitude . 108
13.3 LYAPUNOV functional, optimal amplitude and growth rate of plane waves in dependence on their wave number 109

13.4 Temporal evolution of the unforced SWIFT–HOHENBERG equation, starting from plane waves 110
13.5 Probability to obtain plane waves in the stochastically forced SWIFT–HOHENBERG equation 112
13.6 Long-term behavior of the forced SWIFT–HOHENBERG equation 113
13.7 LYAPUNOV functional of the discrete wave vectors in a periodic domain . 114
13.8 Probability of plane waves for discrete wave vectors 114
13.9 Five most probable plane wave configurations 115
13.10 Exemplary time series of the LYAPUNOV functional 116

14.1 Probability density function of ψ 121
14.2 Conditional average of $\Delta\psi$ and $\Delta^2\psi$ 121
14.3 Conditional average and drift term as a function of ψ 122
14.4 Reconstructed and directly estimated PDF of ψ 122
14.5 Cubic model fitted to the conditional averages of $\Delta\psi$ and $\Delta^2\psi$ 124
14.6 PDF reconstructed from cubic model of the conditional averages 124
14.7 PDF reconstructed from a simplistic model 125
14.8 Ansatz functions used in the GAUSSian convolution 126
14.9 PDF obtained from the convolution model 127

A.1 Limit cycle obtained with noise, and closed concentric curves obtained after post-processing 143

C.1 Hexagonal solution of the SWIFT–HOHENBERG equation with additional quadratic nonlinearity 153

List of Tables

9.1 Number of E- and Nu-modes needed to obtain a specified percentage of convective heat transport . . . 79

13.1 Number of ensemble members for each initial condition of the forced SWIFT–HOHENBERG equation . . . 115
13.2 Details of the numerical simulations for the ensemble calculation of the forced SWIFT–HOHENBERG equation . . . 116

Bibliography

Ahlers, Guenter and Grossmann, Siegfried and Lohse, Detlef (2009). Heat transfer and large scale dynamics in turbulent Rayleigh–Bénard convection. *Reviews of Modern Physics*, 81(2):503–537. [p. 15, 69]

Ahlers, Guenter and He, Xiaozhou and Funfschilling, Denis and Bodenschatz, Eberhard (2012). Heat transport by turbulent Rayleigh–Bénard convection for $\mathrm{Pr} \simeq 0.8$ and $3 \times 10^{12} \lesssim \mathrm{Ra} \lesssim 10^{15}$: aspect ratio $\Gamma = 0.5$. *New Journal of Physics*, 14(10):103012. [p. 15]

Angot, Philippe and Bruneau, Charles-Henri and Fabrie, Pierre (1999). A penalization method to take into account obstacles in incompressible viscous flows. *Numerische Mathematik*, 81(4):497–520. [p. 22]

Aranson, Igor S. and Kramer, Lorenz (2002). The world of the complex Ginzburg–Landau equation. *Reviews of Modern Physics*, 74:99–143. [p. 118]

Argyris, John and Faust, Gunter and Haase, Maria and Friedrich, Rudolf (2010). *Die Erforschung des Chaos*. Springer, Berlin / Heidelberg, 2nd revised edition. [p. 98]

Bailon-Cuba, Jorge and Emran, Mohammad S. and Schumacher, Jörg (2010). Aspect ratio dependence of heat transfer and large-scale flow in turbulent convection. *Journal of Fluid Mechanics*, 655:152–173. [p. 15, 47, 63, 83, 92]

Bailon-Cuba, Jorge and Schumacher, Jörg (2011). Low-dimensional model of turbulent Rayleigh–Bénard convection in a cartesian cell with square domain. *Physics of Fluids*, 23(7):077101. [p. 47]

Bénard, Henri (1901). Les tourbillons cellulaires dans une nappe liquide. – Méthodes optiques d'observation et d'enregistrement. *Journal de Physique Théorique et Appliquée*, 10(1):254–266. Cited after Chandrasekhar (1981). [p. 1, 97, 98, 153, 154]

Bestehorn, Michael (2006). *Hydrodynamik und Strukturbildung*. Springer, Berlin / Heidelberg. [p. 117, 153]

Bodenschatz, Eberhard and Pesch, Werner and Ahlers, Guenter (2000). Recent developments in Rayleigh–Bénard convection. *Annual Review of Fluid Mechanics*, 32(1):709–778. [p. 98]

BOUSSINESQ, JOSEPH V. (1903). *Théorie Analytique de la Chaleur*, volume 2. Gauthier-Villars, Paris. [p. 5, 16]

BUTLER, DAVID (2013). Eigenvalue magic tricks. *Seminar at the School of Mathematical Sciences, University of Adelaide*, `http://www.adelaide.edu.au/mathslearning/play/seminars/evalue-magic-tricks-handout.pdf`. [p. 148]

CALZAVARINI, ENRICO and LOHSE, DETLEF and TOSCHI, FEDERICO and TRIPICCIONE, RAFFAELE (2005). Rayleigh and Prandtl number scaling in the bulk of Rayleigh–Bénard turbulence. *Physics of Fluids*, 17(5):055107. [p. 40]

CHANDRASEKHAR, SUBRAHMANYAN (1981). *Hydrodynamic and Hydromagnetic Stability*. Dover Publications, New York. [p. 98, VII]

CHILLÀ, FRANCESCA and SCHUMACHER, JÖRG (2012). New perspectives in turbulent Rayleigh–Bénard convection. *The European Physical Journal E: Soft Matter and Biological Physics*, 35:1–25. [p. 15]

CHING, EMILY S. C. (1993). Probability densities of turbulent temperature fluctuations. *Physical Review Letters*, 70(3):283–286. [p. 15, 40]

CHING, EMILY S. C. and GUO, H. and SHANG, XIAO-DONG and TONG, PENGER and XIA, KE-QING (2004). Extraction of plumes in turbulent thermal convection. *Physical Review Letters*, 93:124501. [p. 15]

COOLEY, JAMES W. and TUKEY, JOHN W. (1965). An algorithm for the machine calculation of complex Fourier series. *Mathematics of Computation*, 19(90):297–301. [p. 103]

COURANT, RICHARD and HILBERT, DAVID (1962). *Methods of Mathematical Physics Volume II*. Wiley-Interscience. [p. 18]

CROSS, MICHAEL C. and HOHENBERG, PIERRE C. (1993). Pattern formation outside of equilibrium. *Reviews of Modern Physics*, 65(3):851–1112. [p. 98]

FLIESSBACH, TORSTEN (1992). *Mechanik*. BI Wissenschaftsverlag. [p. 71]

FRIEDRICH, RUDOLF and DAITCHE, ANTON and KAMPS, OLIVER and LÜLFF, JOHANNES and VOSSKUHLE, MICHEL and WILCZEK, MICHAEL (2012). The Lundgren–Monin–Novikov hierarchy: Kinetic equations for turbulence. *Comptes Rendus Physique*, 13(9–10):929–953. [p. 15, 17]

GASTEUIL, YOANN and SHEW, WOODROW L. and GIBERT, MATHIEU and CHILLÀ, FRANCESCA and CASTAING, BERNARD and PINTON, JEAN-FRANCOIS (2007). Lagrangian temperature, velocity, and local heat flux measurement in Rayleigh–Bénard convection. *Physical Review Letters*, 99(23):234302. [p. 15]

Greiner, Walter and Reinhardt, Joachim (1993). *Theoretische Physik Band 7A: Feldquantisierung*. Verlag Harri Deutsch. [p. 145]

Grossmann, Siegfried and Lohse, Detlef (2000). Scaling in thermal convection: a unifying theory. *Journal of Fluid Mechanics*, 407:27–56. [p. 6, 15]

Grossmann, Siegfried and Lohse, Detlef (2001). Thermal convection for large Prandtl numbers. *Physical Review Letters*, 86(15):3316–3319. [p. 15, 69]

Grossmann, Siegfried and Lohse, Detlef (2011). Multiple scaling in the ultimate regime of thermal convection. *Physics of Fluids*, 23(4):045108. [p. 15]

Grossmann, Siegfried and Lohse, Detlef (2012). Logarithmic temperature profiles in the ultimate regime of thermal convection. *Physics of Fluids*, 24(12):125103. [p. 15]

Haken, Hermann (1975). Cooperative phenomena in systems far from thermal equilibrium and in nonphysical systems. *Reviews of Modern Physics*, 47:67–121. [p. 98]

Haken, Hermann (1983). *Synergetics: Introduction and advanced topics*. Springer, Berlin / Heidelberg. [p. 120]

Härdle, Wolfgang and Müller, Marlene and Sperlich, Stefan and Werwatz, Axel (2004). *Nonparametric and Semiparametric Models*. Springer Series in Statistics. Springer, Berlin / Heidelberg. [p. 89]

Hernández-García, Emilio and San Miguel, Maxi and Toral, Raúl and Viñals, Jorge (1992). Noise and pattern selection in the one-dimensional Swift–Hohenberg equation. *Physica D*, 61:159–165. [p. 103]

Hohenberg, Pierre C. and Halperin, Bertrand I. (1977). Theory of dynamic critical phenomena. *Reviews of Modern Physics*, 49:435–479. [p. 118]

Holmes, Philip and Lumley, John L. and Berkooz, Gal (1996). *Turbulence, Coherent Structures, Dynamical Systems and Symmetry*. Cambridge University Press. [p. 47, 48, 59, IX, X]

Jentzen, Arnulf and Kloeden, Peter E. (2009). The numerical approximation of stochastic partial differential equations. *Milan Journal of Mathematics*, 77:205–244. [p. 102]

Karhunen, Kari (1946). Zur Spektraltheorie stochastischer Prozesse. *Annales Academiæ Scientiarum Fennicæ Series A1*, 34. Cited after Holmes *et al.* (1996). [p. 45]

Kastner-Maresch, Alois E. (1992). The implicit midpoint rule applied to discontinuous differential equations. *Computing*, 49(1):45–62. [p. 141]

Keetels, Geert H. and D'Ortona, Umberto and Kramer, W. and Clercx, Herman J. H. and Schneider, Kai and van Heijst, Gertjan J. F. (2007). Fourier spectral and wavelet solvers for the incompressible Navier–Stokes equations with volume-penalization: Convergence of a dipole-wall collision. *Journal of Computational Physics*, 227(2):919–945. [p. 22]

Kraft, Alexander and Gurevich, Svetlana V. (2015). Time-delayed feedback control of spatio-temporal self-organized patterns in dissipative systems. *Private communication, to be published*. [p. 154]

Loève, Michel (1945). Functions aléatoire de second ordre. *Comptes Rendus de l'Académie des Sciences, Paris*, 220. Cited after Holmes *et al.* (1996). [p. 45]

Lohse, Detlef and Toschi, Federico (2003). Ultimate state of thermal convection. *Physical Review Letters*, 90:034502. [p. 40]

Lohse, Detlef and Xia, Ke-Qing (2010). Small-scale properties of turbulent Rayleigh–Bénard convection. *Annual Review of Fluid Mechanics*, 42(1):335–364. [p. 15]

Lülff, Johannes (2011). *Statistische Eigenschaften turbulenter Rayleigh–Bénard-Konvektion*. Diplomarbeit, Westfälische Wilhelms-Universität Münster. [p. 2, 13, 97, 101, 137, 142]

Lülff, Johannes (2015). Describing the heat transport of turbulent Rayleigh–Bénard convection by POD methods. *arXiv e-prints*, 1510.06908. Submitted to *Journal of Fluid Mechanics*. [p. 9, 43, 92]

Lülff, Johannes and Wilczek, Michael and Friedrich, Rudolf (2011). Temperature statistics in turbulent Rayleigh–Bénard convection. *New Journal of Physics*, 13(1):015002. [p. 13, 16, 17, 21]

Lülff, Johannes and Wilczek, Michael and Stevens, Richard J. A. M. and Friedrich, Rudolf and Lohse, Detlef (2015). Turbulent Rayleigh–Bénard convection described by projected dynamics in phase space. *Journal of Fluid Mechanics*, 781:276–297. [p. 8, 13, 141]

Lumley, John L. and Poje, Andrew (1997). Low-dimensional models for flows with density fluctuations. *Physics of Fluids*, 9(7):2023–2031. [p. 47]

Lundgren, Thomas S. (1967). Distribution functions in the statistical theory of turbulence. *Physics of Fluids*, 10(5):969–975. [p. 17]

Mecke, Klaus and Rauscher, Markus (2005). On thermal fluctuations in thin film flow. *Journal of Physics: Condensed Matter*, 17(45):S3515. [p. 118]

Monin, Andrei S. (1967). Equations of turbulent motion. *Journal of Applied Mathematics and Mechanics (Prikladnaya Matematika i Mekhanika)*, 31(6):1057–1068. [p. 17]

NOVIKOV, EVGENY A. (1968). Kinetic equations for a vortex field. *Soviet Physics-Doklady*, 12(11):1006–1008. [p. 17]

O'BEIRNE, GREG (2009). Picture of *undulatus* clouds. *Wikimedia Commons*, `https://commons.wikimedia.org/wiki/File:CloudRipples_gobeirne.jpg`. Published under Creative Commons License. [p. 98]

OBERBECK, ANTON (1879). Über die Wärmeleitung der Flüssigkeiten bei Berücksichtigung der Strömungen infolge von Temperaturdifferenzen. *Annalen der Physik und Chemie*, 7:271–292. [p. 5, 16]

ORSZAG, STEVEN A. (1971). On the elimination of aliasing in finite-difference schemes by filtering high-wavenumber components. *Journal of the Atmospheric Sciences*, 28:1074. [p. 102]

PEARSON, KARL (1901). On lines and planes of closest fit to systems of points in space. *Philosophical Magazine Series 6*, 2(11):559–572. [p. 45]

PETSCHEL, KLAUS and STELLMACH, STEPHAN and WILCZEK, MICHAEL and LÜLFF, JOHANNES and HANSEN, ULRICH (2013). Dissipation layers in Rayleigh–Bénard convection: A unifying view. *Physical Review Letters*, 110:114502. [p. 15, 137]

PETSCHEL, KLAUS and WILCZEK, MICHAEL and BREUER, MARTIN and FRIEDRICH, RUDOLF and HANSEN, ULRICH (2011). Statistical analysis of global wind dynamics in vigorous Rayleigh–Bénard convection. *Physical Review E*, 84(2):026309. [p. 15, 69]

POPE, STEPHEN B. (1984). Calculations of a plane turbulent jet. *American Institute of Aeronautics and Astronautics Journal*, 22(7):896–904. [p. 17]

POPE, STEPHEN B. (1985). PDF methods for turbulent reactive flows. *Progress in Energy and Combustion Science*, 11:119–192. [p. 17, 19]

POPE, STEPHEN B. (2000). *Turbulent Flows*. Cambridge University Press, Cambridge, England. [p. 17]

RAYLEIGH, LORD (JOHN W. STRUTT) (1916). On convection currents in a horizontal layer of fluid, when the higher temperature is on the under side. *Philosophical Magazine*, 32(192):529–546. [p. 1, 98]

ROWLEY, CLARENCE W. (2001). *Modeling, Simulation, and Control of Cavity Flow Oscillations*. PhD thesis, California Institute of Technology. [p. 50, 54, 58]

ROWLEY, CLARENCE W. and COLONIUS, TIM and MURRAY, RICHARD M. (2004). Model reduction for compressible flows using POD and Galerkin projection. *Physica D*, 189(1–2):115–129. [p. 50]

SARRA, SCOTT A. (2003). The method of characteristics with applications to conservation laws. *Journal of Online Mathematics and its Applications*, 3:1–6. [p. 18]

SCHMALZL, JÖRG and BREUER, MARTIN and WESSLING, STEPHAN and HANSEN, ULRICH (2004). On the validity of two-dimensional numerical approaches to time-dependent thermal convection. *Europhysics Letters*, 67(3):390–396. [p. 29]

SCHNEIDER, KAI (2005). Numerical simulation of the transient flow behaviour in chemical reactors using a penalisation method. *Computers & Fluids*, 34(10):1223–1238. [p. 22]

SCHUMACHER, JÖRG (2009). Lagrangian studies in convective turbulence. *Physical Review E*, 79(5):056301. [p. 15]

SHANG, XIAO-DONG and TONG, PENGER and XIA, KE-QING (2008). Scaling of the local convective heat flux in turbulent Rayleigh–Bénard convection. *Physical Review Letters*, 100:244503. [p. 15]

SHISHKINA, OLGA and STEVENS, RICHARD J. A. M. and GROSSMANN, SIEGFRIED and LOHSE, DETLEF (2010). Boundary layer structure in turbulent thermal convection and its consequences for the required numerical resolution. *New Journal of Physics*, 12(7):075022. [p. 22, 25, 28]

SIROVICH, LAWRENCE (1987a). Turbulence and the dynamics of coherent structures, parts I–III. *Quarterly of Applied Mathematics*, XLV(3):561–590. [p. 52]

SIROVICH, LAWRENCE (1987b). Turbulence and the dynamics of coherent structures, part II: Symmetries and transformations. *Quarterly of Applied Mathematics*, XLV(3):573–582. [p. 59]

SIROVICH, LAWRENCE and PARK, H. (1990). Turbulent thermal convection in a finite domain: Part I. Theory. *Physics of Fluids A*, 2(9):1649–1658. [p. 59]

SMITH, TROY R. and MOEHLIS, JEFF and HOLMES, PHILIP (2005). Low-dimensional modelling of turbulence using the proper orthogonal decomposition: A tutorial. *Nonlinear Dynamics*, 41(1–3):275–307. [p. 47]

STEVENS, RICHARD J. A. M. (2011). The numerical data set of three-dimensional Rayleigh–Bénard convection in a cylindrical vessel was generated with the method presented in VERZICCO and CAMUSSI (2003). *Private communication.* [p. 13]

STEVENS, RICHARD J. A. M. and VAN DER POEL, ERWIN P. and GROSSMANN, SIEGFRIED and LOHSE, DETLEF (2013). The unifying theory of scaling in thermal convection: the updated prefactors. *Journal of Fluid Mechanics*, 730:295–308. [p. 15]

SUGIYAMA, KAZUYASU and NI, RUI and STEVENS, RICHARD J. A. M. and CHAN, TAK SHING and ZHOU, SHENG-QI and XI, HENG-DONG and SUN, CHAO and GROSSMANN, SIEGFRIED and XIA, KE-QING and LOHSE, DETLEF (2010). Flow reversals in thermally driven turbulence. *Physical Review Letters*, 105(3):034503. [p. 28, 62]

SWIFT, JACK and HOHENBERG, PIERRE C. (1977). Hydrodynamic fluctuations at the convective instability. *Physical Review A*, 15(1):319–328. [p. 99, 100, 106]

SYLVESTER, JAMES JOSEPH (1851). On the relation between the minor determinants of linearly equivalent quadratic functions. *Philosophical Magazine Series 4*, 1(4):295–305. [p. 148]

TLIDI, MUSTAPHA and VLADIMIROV, ANDREI G. and PIEROUX, DIDIER and TURAEV, DMITRY (2009). Spontaneous motion of cavity solitons induced by a delayed feedback. *Physical Review Letters*, 103:103904. [p. 154]

VAN DER POEL, ERWIN P. and OSTILLA-MÓNICO, RODOLFO and VERZICCO, ROBERTO and LOHSE, DETLEF (2014). Effect of velocity boundary conditions on the heat transfer and flow topology in two-dimensional Rayleigh–Bénard convection. *Physical Review E*, 90:013017. [p. 16]

VAN DER POEL, ERWIN P. and STEVENS, RICHARD J. A. M. and LOHSE, DETLEF (2011). Connecting flow structures and heat flux in turbulent Rayleigh–Bénard convection. *Physical Review E*, 84(4):045303. [p. 15, 69]

VAN DER POEL, ERWIN P. and STEVENS, RICHARD J. A. M. and LOHSE, DETLEF (2013). Comparison between two- and three-dimensional Rayleigh–Bénard convection. *Journal of Fluid Mechanics*, 736:177–194. [p. 16, 29, 30]

VERZICCO, ROBERTO and CAMUSSI, ROBERTO (2003). Numerical experiments on strongly turbulent thermal convection in a slender cylindrical cell. *Journal of Fluid Mechanics*, 477:19–49. [p. 31, XII]

VIÑALS, JORGE and HERNÁNDEZ-GARCÍA, EMILIO and SAN MIGUEL, MAXI and TORAL, RAÚL (1991). Numerical study of the dynamical aspects of pattern selection in the stochastic Swift–Hohenberg equation in one dimension. *Physical Review A*, 44(2):1123–1133. [p. 108, 109, 129]

WILCZEK, MICHAEL and DAITCHE, ANTON and FRIEDRICH, RUDOLF (2011). On the velocity distribution in homogeneous isotropic turbulence: correlations and deviations from Gaussianity. *Journal of Fluid Mechanics*, 676:191–217. [p. 15, 17, 123]

WILCZEK, MICHAEL and FRIEDRICH, RUDOLF (2009). Dynamical origins for non-Gaussian vorticity distributions in turbulent flows. *Physical Review E*, 80(1):016316. [p. 15, 17, 123]

YAKHOT, VICTOR (1989). Probability distributions in high-Rayleigh number Bénard convection. *Physical Review Letters*, 63(18):1965–1967. [p. 15, 40]

Ich danke…

… *meinen Gutachtern und dem Prüfungskommitee*, allen voran Prof. Rudolf Friedrich, der leider viel zu früh verstorben ist, sowie Prof. Ulrich Hansen und Prof. Detlef Lohse.

… *meiner Arbeitsgruppe „Selbstorganisation und Komplexität“*, zunächst unter der Leitung von Prof. Rudolf Friedrich, dann unter Prof. Uwe Thiele.

… *meinen Betreuern*, insbesondere Michael Wilczek, der nach dem Tod von Prof. Friedrich meine fachliche Betreuung vorwiegend übernommen hat, sowie Oliver Kamps und Svetlana Gurevich, die mir als Postdocs der Gruppe immer mit Rat und Tat zur Seite standen.

… *meinen Bürokollegen und denen der Nachbarbüros* für unzählige Fragen und Diskussionen. Es kann hier zwar nicht jeder einzeln aufgezählt werden, aber die Richtigen werden sich angesprochen fühlen.

… *meinen Koautoren* für die Arbeit, die sie in die Veröffentlichungen gesteckt haben, die während dieser Promotion entstanden sind.

… *meinen Korrekturlesern.*

… *der Deutschen Forschungsgemeinschaft und dem Center for Nonlinear Science* für die Finanzierung, unter anderem von vielen Auslandsreisen und Konferenzen, und für die damit verbundenen zahlreichen Erfahrungen.

… *der Zafernahütte* für die vielen Abenteuer im Kleinwalsertal, die ich mit Arbeitskollegen während der AG-Seminare erleben durfte.

… *meinen Eltern und meinen Schwestern* für alles.

… *Meli* für die seelische und moralische Unterstützung in der schwierigen Endphase, und für Deine unglaublich positive Grundeinstellung, mit der Du mich immer mitgerissen hast.

… *Steffi* für die Ablenkung bei unzähligen Kaffeepausen und entspannten Feierabendbieren, und für Deine Begeisterungsfähigkeit, die mich immer motiviert hat.

… *Jule* für drei gemeinsame Jahre.

… *meinen Freunden*, auf die ich mich immer verlassen konnte.

… *meinen Kletterleuten* für den sportlichen Ausgleich.

… *meiner Band* für die Möglichkeit, Stress abzubauen.

… *der Uni Münster, dem Institut für Theoretische Physik, und meinen Komilitonen.*